



HAL
open science

Model catalysts for water splitting studied operando using X-ray Diffraction and X-ray Absorption Spectroscopy

Mathilde Bouvier

► **To cite this version:**

Mathilde Bouvier. Model catalysts for water splitting studied operando using X-ray Diffraction and X-ray Absorption Spectroscopy. Material chemistry. Institut Polytechnique de Paris, 2021. English. NNT : 2021IPPAX124 . tel-03662469

HAL Id: tel-03662469

<https://theses.hal.science/tel-03662469>

Submitted on 9 May 2022

HAL is a multi-disciplinary open access archive for the deposit and dissemination of scientific research documents, whether they are published or not. The documents may come from teaching and research institutions in France or abroad, or from public or private research centers.

L'archive ouverte pluridisciplinaire **HAL**, est destinée au dépôt et à la diffusion de documents scientifiques de niveau recherche, publiés ou non, émanant des établissements d'enseignement et de recherche français ou étrangers, des laboratoires publics ou privés.

Model catalysts for water splitting studied operando using X-ray Diffraction and X-ray Absorption Spectroscopy

Thèse de doctorat de l'Institut Polytechnique de Paris
préparée à l'École Polytechnique
(Laboratoire de Physique de la Matière Condensée)

École doctorale n°626 Ecole Doctorale de
l'Institut Polytechnique de Paris (ED IP Paris)

Spécialité de doctorat: Chimie

Thèse présentée et soutenue à Palaiseau, le 10/12/2021, par

Mathilde Bouvier

Composition du Jury :

Elena Savinova Professeur, Université de Strasbourg (– ICPEES)	Présidente
Eric Sibert Chargé de recherche, Université de Grenoble Alpes (– LEPMI)	Rapporteur
Benedikt Lassalle-Kaiser Scientifique de ligne, Synchrotron SOLEIL	Rapporteur
Aurélien Habrioux Maître de conférence, Université de Poitiers (– IC2MP)	Examineur
Philippe Allongue Directeur de recherche, École Polytechnique (– LPMC)	Directeur de thèse
Fouad Maroun Directeur de recherche, École Polytechnique (– LPMC)	Co-Directeur de thèse

Abstract

Water splitting into oxygen and hydrogen is a promising route for renewable energies conversion and storage. Iron group oxides (Fe, Ni, Co) have interesting catalytic properties towards water oxidation into oxygen (OER) in alkaline electrolytes, and they are amongst the best candidates for a large-scale deployment of this energy conversion technology. The development of efficient catalysts involves their synthesis and the understanding of the reaction mechanisms of water oxidation at the surface of such materials. In this work we investigate the structure and chemical state of OER model catalysts - cobalt, iron and mixed cobalt-iron oxide layers with a well-defined structure, composition and morphology - by simultaneously using surface X ray diffraction (SXRD) and X ray absorption spectroscopy (XAS). We show that this approach allows a deeper interpretation of observations and yields new insights into the OER mechanisms. In the case of pure cobalt oxides obtained by epitaxial electrodeposition on a single crystal substrate Au(111), our results show that spinel cobalt oxide $\text{Co}_3\text{O}_4(111)$ and oxyhydroxide $\text{CoOOH}(001)$ exhibit different structural and oxidation state changes induced by potential, corresponding to distinct surface transformation. A sub-nm skin layer is formed on Co_3O_4 before OER onset and its oxidation state is +3. In the case of CoOOH , no skin layer is observed and the small oxidation state variations with potential is due to changes of the H surface coverage. In the case of mixed $\text{CoFeO}_y(111)$ spinel oxide thin films electrodeposited on Au(111) with an iron content ranging between 15% and 50%, we find similarities with Co_3O_4 , including structural changes and Co^{2+} surface atoms experiencing oxidation to Co^{3+} with potential while Fe redox state remains unchanged. The comparison of these results with those obtained for both Co_3O_4 and Fe_3O_4 crystalline oxides yields insights into the role of Fe doping in OER activity improvement of Co_3O_4 . We further present a second preparation method where oxide films are obtained by anodic oxidation of an electrodeposited ultrathin ($\leq 1\text{nm}$) epitaxial metal film (Co, Fe, CoFe alloys of variable compositions). The nm thickness of the anodic oxides affords higher sensitivity in potential induced redox changes determination and the preparation method allows a more flexible tuning of the Co/Fe ratio in the oxide. The oxidation state changes in these samples are examined in light of the results obtained for their crystalline analogues, to which they are also compared in terms of composition, catalytic activity and operando behaviour. By studying well-defined Co, Fe and mixed CoFe oxides systems, we establish correlation between structural properties and oxidation state changes that are used to identify the OER active phase and to discuss the reaction mechanism.

Résumé

La décomposition électrochimique de l'eau en oxygène et hydrogène est un moyen énergétiquement efficace de convertir et stocker l'électricité issue d'énergies renouvelables. Les oxydes du groupe Fer (Fe, Ni, Co) présentent des propriétés catalytiques intéressantes vis à vis de la réaction d'oxydation de l'eau en oxygène (OER) en milieu alcalin, et sont parmi les meilleurs candidats pour un déploiement à grande échelle de cette stratégie de conversion des énergies renouvelables. Le développement de catalyseurs efficaces implique leur synthèse et la compréhension des mécanismes réactionnels de l'oxydation de l'eau à leur surface. Dans ce travail, nous étudions la structure et l'état chimique de catalyseurs modèles pour l'OER, des films minces d'oxydes de cobalt, de fer et d'oxydes mixtes cobalt-fer, ayant une structure, composition et morphologie bien définies. Pour cela nous utilisons simultanément la diffraction de rayons X de surface et la spectroscopie d'absorption de rayons X. Nous montrons que cette approche permet une interprétation plus approfondie des observations faites et apporte un nouvel éclairage sur les mécanismes de l'OER. Dans le cas des oxyde de cobalt purs obtenus par électrodépôt épitaxié sur un substrat monocristallin Au(111), nos résultats montrent que le potentiel appliqué à l'électrode induit des changements structuraux et de degré d'oxydation différents chez l'oxyde de cobalt de structure spinelle $\text{Co}_3\text{O}_4(111)$ et chez l'oxyhydroxyde $\text{CoOOH}(001)$, ce qui correspond à des transformations de surface différentes. Une peau d'épaisseur inférieur au nanomètre se forme à la surface de Co_3O_4 avant l'OER, et son degré d'oxydation vaut +3. Dans le cas de CoOOH , on n'observe pas de peau et les faibles variations de degré d'oxydation induites par le potentiel sont liées à des variations de taux de couverture d'hydrogène à la surface. Les films minces d'oxydes mixtes $\text{CoFeO}_y(111)$ de structure spinelle dont la teneur en Fer varie de 15% à 50% sont également obtenus par électrodépôt sur Au(111). Dans leur cas, on observe des similitudes avec Co_3O_4 , notamment des modifications structurales et l'oxydation avec le potentiel des atomes de Co^{2+} de surface en Co^{3+} , tandis que l'état d'oxydation du fer reste inchangé. La comparaison de ces résultats avec ceux obtenus pour les oxydes cristallins Co_3O_4 et Fe_3O_4 apporte des informations sur le rôle du dopage en Fer dans l'amélioration des propriétés catalytiques de Co_3O_4 . Nous présentons de plus une deuxième méthode de préparation où les films d'oxydes sont obtenus par oxydation anodique d'un film épitaxié ultramince ($\leq 1\text{nm}$) de métal (Co, Fe, alliages Co/Fe the compositions variables) obtenu par électrodépôt. L'épaisseur nanométrique des oxydes anodiques permet une plus grande sensibilité dans la détermination des changements redox induits par le potentiel, et la méthode de préparation offre une plus grande flexibilité dans le choix du ratio Co/Fe dans l'oxide. Les variations de degré d'oxydation dans ces matériaux sont examinées à la lumière des résultats obtenus pour les analogues

cristallins, auxquels ils sont également comparés en termes de composition, d'activité catalytique et de comportement operando. En étudiant des systèmes d'oxydes bien définis de Co, Fe, et mixtes CoFe, nous pouvons établir des corrélations entre propriétés structurales et de variations de degré d'oxydation, qui sont utilisées pour identifier la phase active pour la réaction de l'OER et discuter de son mécanisme réactionnel.

Remerciements

J'aimerais d'abord adresser mes remerciements aux membres du jury pour avoir accepté d'évaluer ce travail de thèse. Je remercie Mr Eric Sibert et Mr Benedikt Lassalle d'avoir pris le temps de lire et commenter en détails ce manuscrit, et pour les discussions riches et intéressantes qui en ont découlé. Un remerciement particulier à Mr Benedikt Lasalle pour ses conseils et sa sollicitude concernant l'après thèse. Merci également à Mme Elena Savinova et Mr Aurélien Habrioux pour les commentaires et discussions lors de la soutenance et pour être venus y assister en personne malgré les conditions sanitaires particulières.

J'aimerais également remercier Mr Alesandro Coati et Mme Virginie Lair pour avoir accepté de faire partie de mon comité d'évaluation de mi-thèse, et spécialement Mme Virginie Lair qui m'a suivie en tant qu'enseignante à Chimie Paris et au cours du Master PSL Energy.

Je suis très reconnaissante à mes deux encadrants de thèse, Philippe Allongue et Fouad Maroun, de m'avoir permis de participer à ce projet de recherche. Dès les premiers entretiens au laboratoire j'ai senti votre implication dans ce projet et j'ai su que je serais bien encadrée et suivie en travaillant avec vous.

J'aimerais remercier Philippe Allongue pour m'avoir poussée à toujours être rigoureuse scientifiquement, à toujours faire mieux et aller plus loin dans l'analyse et l'interprétation de résultats. Merci pour votre disponibilité en particulier pendant la période de rédaction, pour les discussions scientifiques, toujours intéressantes, les suggestions d'articles, et votre présence pour les runs synchrotron à Soleil !

Je ne pourrais pas remercier assez Fouad Maroun pour son immense implication dans mon projet de thèse. Rien n'aurait été possible sans tout le temps et l'énergie que vous avez investi dans ce projet ! Que ce soit la préparation des runs, les nuits au synchrotron, les problèmes de manips que vous réussissez toujours à arranger, mais aussi les discussions et réflexions sur l'analyse des données ou leur interprétation, votre aide m'a été très précieuse pendant ces 3 ans. Merci de m'avoir fait confiance pour beaucoup d'aspects, j'ai énormément appris et ai été très heureuse d'avoir la chance de travailler avec vous !

Ce travail de thèse s'inscrit dans un projet plus large qui inclut notamment Ivan Pacheco Bubi du laboratoire PMC et le groupe d'Olaf Magnussen à l'Université de Kiel. Je remercie Ivan pour m'avoir appris à faire les dépôts d'oxydes, aidée dans la préparation des runs synchrotrons et aidée/supportée pendant ces derniers. J'aimerais aussi remercier les collaborateurs de l'université de Kiel, Olaf Magnussen, Jochim Stettner, Finn Reikowski, Tim

Wiegmann et Canrong Qui, pour m'avoir appris beaucoup sur la diffraction de rayons X de surface, pour leur participation et aide au cours des runs synchrotron et pour les discussions scientifiques sur les résultats. Merci en particulier à Tim et Jackey d'être venus en France à Soleil pour m'aider, j'ai beaucoup aimé travailler avec vous !

Comme une majeure partie de mes résultats concerne des mesures réalisées sur ligne de lumière synchrotron, je n'aurais pas pu réaliser ces expériences sans l'aide précieuse des scientifiques de ligne : à DESY sur la ligne P23 où Dimitri Novikov et Azat Khadiev ont toujours été présents pour la mise en place et la résolution de problèmes, et à Soleil sur la ligne DiffAbs où Dominique Thiaudière a passé du temps à nous former sur l'utilisation de la ligne, Solenn Reguer a été très présente et à l'écoute pour nous aider et améliorer l'utilisation de la ligne, ainsi que Cristian Mocuta et Philippe Joly. J'ai également eu la chance de recevoir de l'aide de scientifiques du laboratoire PMC, notamment de Sandrine Tusseau-Nunez pour la diffraction de Rayons X, et d'Isabelle Maurin pour discuter des résultats de XAS et DRX.

De manière plus large j'aimerais remercier tous les membres du groupe Electrochimie et Couches Minces, et tous les membres du laboratoire PMC, qui ont toujours été très agréables, accueillants et sympathiques avec moi. J'ai beaucoup aimé travailler 3 ans dans ce laboratoire, et c'est en grande partie grâce à vous. Merci à Elodie, Sophie et Hopheybea pour leur aide sur les aspects administratifs mais aussi pour avoir été des co-bureaux aussi attentionnées ! J'ai aussi eu la chance d'être entourée dans le laboratoire de doctorants, post-doctorants et jeunes chercheurs, géniaux, avec qui je garde de supers souvenirs de pauses midi avec de grandes discussions, de pauses cafés, de Uno, de matchs de foot, de pique-niques, soirées jeux, bars, PMU de Lozère, restaurants et autres. Merci pour le soutien quotidien, la bonne humeur et vos encouragements en fin de troisième année qui m'ont beaucoup aidé. J'ai été très heureuse de rencontrer autant de personnes gentilles, drôles et différentes, j'espère que l'on gardera contact !

Merci enfin à ma famille pour m'avoir toujours soutenue !

Table of Contents

Abstract	2
Chapter 1: Introduction	10
1.1 Context	10
1.2 Principle of electrochemical water splitting.....	10
1.3 Transition metal oxide catalysts for Oxygen Evolution Reaction in alkaline medium	12
1.4 Studying OER catalysts under operating conditions	21
1.5 Model catalysts	27
1.6 Objectives of the thesis	31
1.7 Bibliography	32
Chapter 2: Experimental and methods	40
2.1 Samples preparation	40
2.2 SXRD: methodology and data treatment.....	45
2.3 X-Ray Absorption Spectroscopy: methodology and data treatment	55
2.4 Lab characterizations	69
2.5 Bibliography	70
Chapter 3: Epitaxial Co oxide thin films	72
3.1 Introduction	72
3.2 Structure of Co_3O_4 and CoOOH	75
3.3 Results.....	76
Characterization of as prepared Co_3O_4 and CoOOH deposits.....	76
Characterizations of the oxide films with synchrotron-based techniques	80
Oxides structure and Co oxidation state dependence with potential	82
Catalytic activity of Co_3O_4 and CoOOH :	88
3.4 Discussion	89
Oxidation of $\text{Co}_3\text{O}_4(111)$: a skin effect.....	89
Oxidation of $\text{CoOOH}(001)$: a deprotonation effect	94
Co oxides surface oxidation state and OER activity.....	97
3.4 Conclusions	98
3.5 Bibliography	98
3.6 Appendix.....	103
Chapter 4: Fe doped Co oxide thin films	108
4.1 Introduction	108
4.2 Characterizations of as prepared samples up to immersion	110
Structure of $\text{Co}_{1-x}\text{Fe}_x\text{O}_y$ layers	110
Morphology of $\text{Co}_{1-x}\text{Fe}_x\text{O}_y$ layers	113
Cobalt and iron oxidation state in $\text{Co}_{1-x}\text{Fe}_x\text{O}_y$ oxide films.....	114
4.3 Operando characterizations	117

Potential induced structural changes	117
Co and Fe oxidation state changes with potential	123
4.4 Composition dependence of catalytic properties	127
Catalytic activity of Fe-doped Co_3O_4 :	127
OER activity and skin layer.....	130
4.5 Conclusion	133
4.6 Bibliography	133
4.7 Appendix.....	137
Chapter 5: Anodic oxides	142
5.1 Introduction	142
5.2 Structure of Co and Fe metals.....	143
5.3 Results.....	144
Monitoring Co/Fe electrodeposition and anodic oxidation	144
Characterization of Co and Fe anodic oxides	147
Characterizations of alloys films and oxides	148
Catalytic properties of $\text{Co}_{100-x}\text{Fe}_x\text{O}_y$ films	155
Potential induced spectroscopic changes	156
5.4 Discussion	157
Oxidation of $\text{Co}_{100-x}\text{Fe}_x\text{O}_y$ oxides	157
OER activity and amount of Co^{3+} / Fe^{3+} in the surface region	161
Anodic and crystalline oxides: comparison	162
5.5 Conclusion	164
5.6 Bibliography	165
5.7 Appendix.....	167
General conclusion and perspectives.....	172

Chapter 1: Introduction

1.1 Context

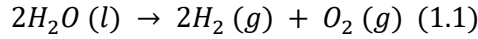
The combined effects of increasing energy needs, the depletion of fossil fuel resources and the need to reduce our greenhouse gas emissions in order to limit the consequences of global warming are encouraging a diversification of our energy sources. The mobility and energy sectors are particularly concerned by these issues because they mostly rely on the use of fossil fuels. Among the different alternatives considered, the energy based on hydrogen offers several advantages.

Hydrogen can be used to provide energy for several applications, for instance to generate electricity in fuel cells via an electrochemical process or to generate heat via H_2 combustion. Fuel cells are energy conversion systems that convert chemical energy into electrical energy by oxidation of a fuel, hydrogen. During this operation, the electrochemical reaction produces water but no greenhouse gas [1]. To generate heat and thereby mechanical power, direct hydrogen combustion in air in an internal combustion engine represents an environmentally friendly alternative to gasoline [2]. Hydrogen is also an interesting way to store energy since unlike intermittent energy sources such as sun or wind, hydrogen can be stored permanently and is readily available in case of need to power fuel cells and produce electricity [2].

Hydrogen is therefore an energy carrier, and it can be produced from several energy sources. Especially hydrogen production by water splitting is an interesting electrochemical process with which H_2 can be synthesized from water, an abundant resource, and without CO_2 emissions. Since it uses an abundant resource, it is extremely interesting from an environmental point of view. When conducted in aqueous electrolyte, it takes place in ambient conditions, between room temperature and $\sim 200^\circ C$ [95], at atmospheric pressure. It only requires electricity to apply a potential difference to the system. Electricity from different sources may be used to supply water splitting electrochemical cells. For instance, it may come from renewable resources, and the as-produced hydrogen is consequently referred to “green hydrogen”, or from nuclear energy, producing “pink hydrogen”, etc. Compared to hydrogen synthesized from fossil fuels by steam reforming, water splitting is significantly eco-friendlier if supplied by the appropriate electricity source.

1.2 Principle of electrochemical water splitting

The water splitting process is the decomposition of liquid water into hydrogen and oxygen gas, following the reaction:

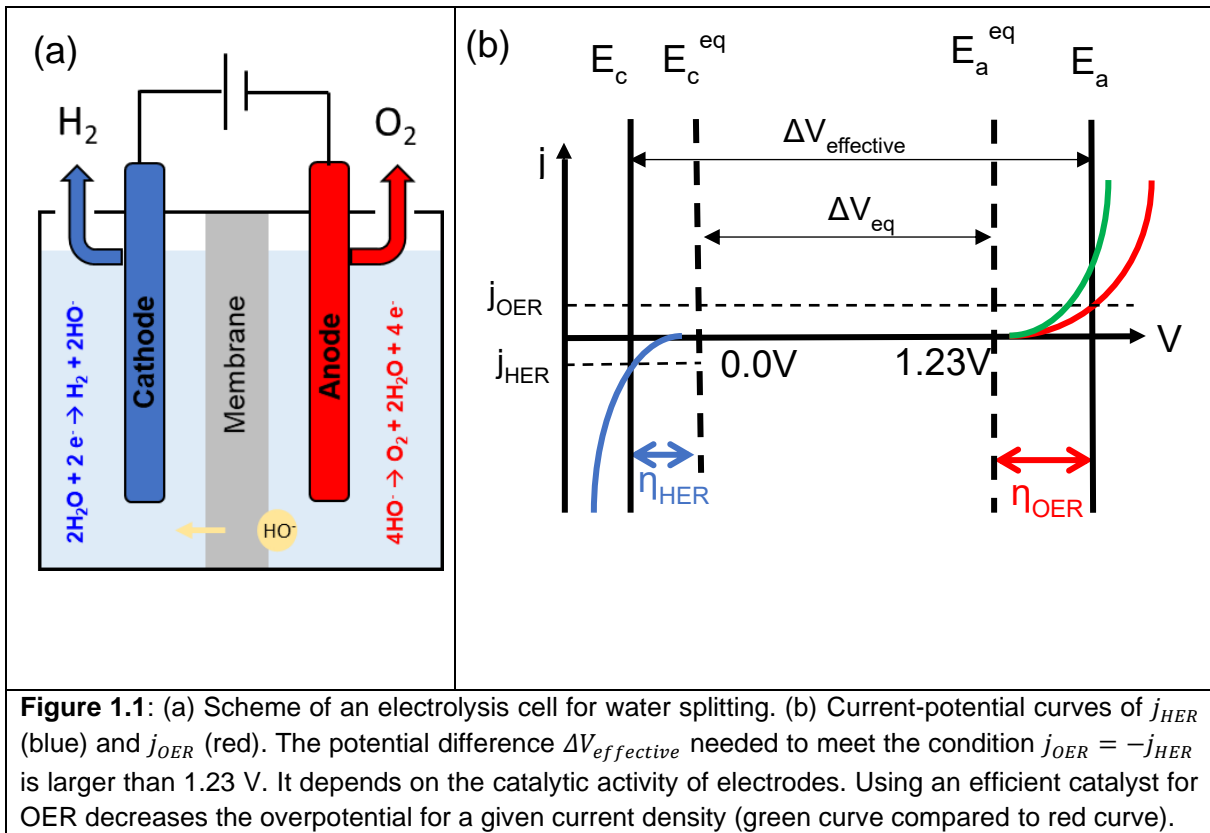


This reaction takes place in an electrolysis cell, of which a scheme is shown in **Figure 1.1a**. It is composed of an anode and a cathode immersed in an electrolyte, and connected to a power supply. Indeed, the reaction requires an input of energy in order to drive the process. In electrochemical water splitting, the reaction is driven by a difference of potential ΔV between the anode and the cathode. Different aqueous electrolytes can be used, that are generally separated in three types: acidic, neutral and alkaline electrolytes. In this work we especially focus on electrochemical water splitting in alkaline electrolytes.

During the electrolysis process, water is reduced into hydrogen at the cathode via Hydrogen Evolution Reaction (HER) (1.2) which standard potential is $E_c^0 = 0 \text{ VRHE}$. At the anode, water is oxidized into oxygen via the Oxygen Evolution Reaction (OER) (1.3) which standard potential is $E_a^0 = 1.23 \text{ VRHE}$.



The thermodynamic voltage difference between the anode and the cathode required for the electrolysis cell to operate is therefore: $\Delta V_{eq} = E_a^0 - E_c^0 = 1.23 - 0 = 1.23 \text{ V}$.



Each reaction presents its own current (j) – voltage (V) characteristic. It is experimentally an

exponential law of the applied voltage: $j_{HER} = j_{HER}^0 \exp(b_{HER}(V - E_c^0))$ and $j_{OER} = j_{OER}^0 \exp(b_{OER}(V - E_a^0))$ where b are the Tafel slope and j^0 are exchange current densities. Tafel slopes are depending on the mechanism of the reaction [3] and the exchange currents account for the kinetics of the reaction. **Figure 1.1b** shows current density – voltage curves of a water splitting system, plotting both j_{HER} (blue) and j_{OER} (red) current densities as a function of applied potential. It illustrates that the minimum voltage to split water is larger than the thermodynamic voltage of 1.23 V. In reality one has to account for potential losses due to the exponential dependence with the voltage. The difference between the thermodynamically determined half reaction potential ((1.2) or (1.3)) and the potential necessary to drive a specific current density at the electrode is defined as an overpotential, called η_{OER} at the anode and η_{HER} at the cathode. The overpotentials that need to be provided to the system in order to produce a given current density $j_{OER} = -j_{HER}$ are shown in **Figure 1.1b** (dashed horizontal lines). As a consequence, a potential difference $\Delta V_{effective} > \Delta V_{eq}$ should be applied between the anode and the cathode of the electrolyser in order to obtain the current density $j_{OER} = -j_{HER}$.

To reduce the overpotential and therefore $\Delta V_{effective}$, the reactions at both the anode and the cathode should be optimized in order to produce hydrogen with the least amount of energy possible. For this purpose, catalysts are added to the anode and cathode. The red curve on **Figure 1.1b** corresponds to a poor OER catalyst compared to the green curve that would be obtained with an efficient OER catalyst. With a good catalyst, the overpotential to drive a current density j_{OER} is reduced and a smaller $\Delta V_{effective}$ is mandatory in order to reach an identical current density.

1.3 Transition metal oxide catalysts for Oxygen Evolution Reaction in alkaline medium

As schematized in **Fig. 1.1b**, the overpotentials are especially important at the anode side where OER takes place. The OER is a slow reaction [4] compared to that of the HER ($j_{OER}^0 \ll j_{HER}^0$), i.e. it requires a large overpotential to meet the condition $j_{OER} = -j_{HER}$. The reason is that OER is a complex four electrons transfer process. The OER is therefore responsible for the main energy losses within water splitting electrolyzers [5], which justifies studying this reaction and developing efficient sustainable catalysts.

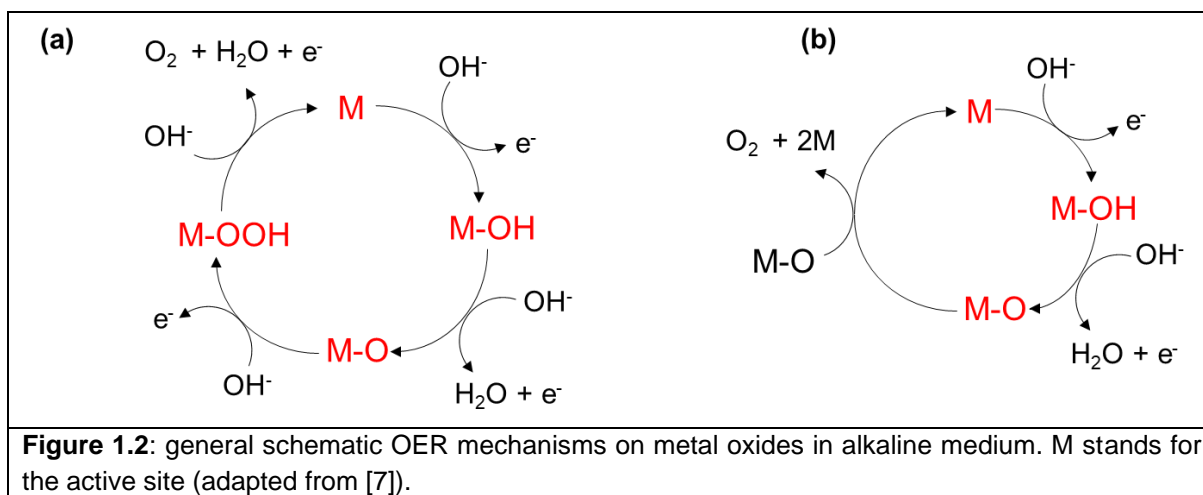
A large variety of materials are considered as potential candidates to catalyse efficiently OER [6]. Below is a non-exhaustive list of the most commonly studied OER catalysts:

- Noble metal-based materials such as Ir or Ru metals, alloys and oxides.

- Earth abundant transition metal oxides or hydroxides, including Ni, Fe, Co, Mn, Ti, Cu, Pb based materials and any composites made of the combination of two or several of these metals.
- Perovskite oxides/hydroxides (of the form ABO_3 , with A a rare-earth or an alkaline element, and B is generally a transition metal)
- Metal phosphate, borides... where the metal is generally a transition metal
- Carbon based materials like carbon nanotubes or graphene

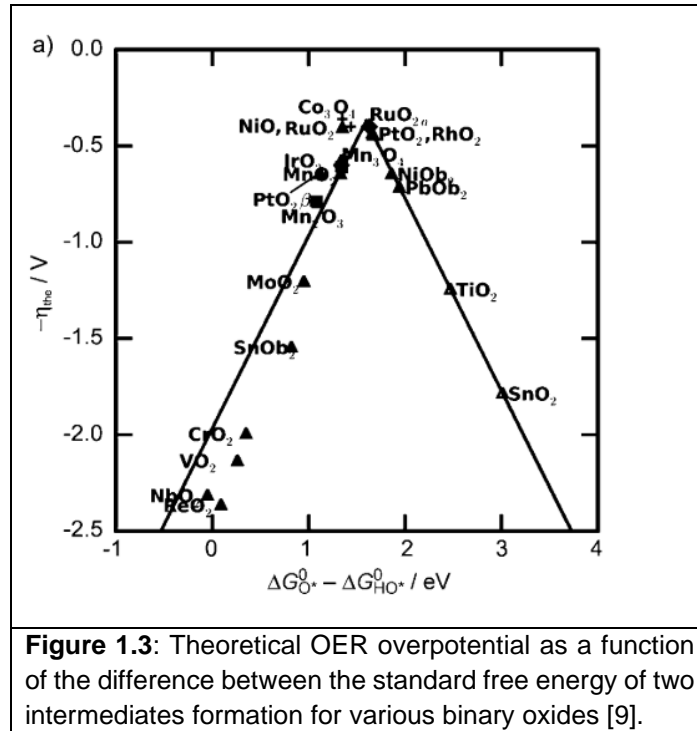
Comparing the catalytic activity of OER catalysts

In this work we will especially focus on transition metal oxide catalysts for OER. A general OER mechanism scheme for metal oxides in alkaline medium is shown in **Figure 1.2**, where M refers as the active site. Two pathways are presented starting from M species, with the same first two steps: adsorption of HO^- on the active site by oxidation of the hydroxide anion, followed by M-O formation by coupled proton and electron removal from M-OH. In pathway (a) [8], a M-OOH intermediate is formed by HO^- nucleophilic attack on M-O and M oxidation, and O_2 is further released after proton coupled electron transfer. In pathway (b) [3], 2 neighbouring M-O species react together to directly form O_2 .



In general, the active site M is considered as the metal cation. A universal descriptor for the catalytic activity of OER catalysts was described by Man et al. [9]. It is based on the difference between the energies of M-OH intermediate formation (first OER step) and M-OOH formation (third OER step), that correspond to the rate-determining step. From a computational point of view, the activity of OER catalysts (for example the overpotential) can be determined by DFT calculations, and compared to OER descriptors. For example, Man et al. [3] used the universal OER descriptor mentioned above to correlate the overpotential of several crystalline oxide compounds, showing a volcano plot illustrated in **Fig. 1.3**. The catalysts at the top of the volcano have a higher overpotential and the optimal value of the OER descriptor. These

conditions are found for Ru oxide RuO_2 , close to PtO_2 , RhO_2 , NiO and Co_3O_4 oxides. Other transition metal oxides like TiO_2 , MoO_2 or CrO_2 fall on the foot of the volcano and do not fulfil the conditions to be good OER catalysts. From an experimental point of view however, the overpotential of a given metal oxide may depend on several factors that are not taken into account in computational works. Such volcano plots therefore cannot therefore be considered as universal OER activity trends.



Experimentally, the OER activity of a catalyst is characterized by measuring the corresponding current – voltage curve (see **Fig. 1.1**). As discussed above, the current generally follows an exponential law of the potential: $j_{OER} = j_{OER}^0 \exp(b(V - E_a^0))$, where the Tafel slope b , which is related to the reaction path [3]. Indeed, $1/b$ is inversely proportional to the number of transferred electrons before and during the rate determining step. It may be used to identify the electron transfer that is the rate determining step [7]. The latter is therefore often used to characterize the OER mechanism at a catalyst. Apart from the mechanistic aspect, a low Tafel slope may be desirable since it corresponds to a faster increase in current density for a similar of overpotential. However, it is not enough in itself to evaluate the OER activity of a catalyst. The OER activity is by contrast directly proportional to the exchange current j_{OER}^0 and, two catalysts with similar Tafel slopes may give very different OER currents at a given overpotential. descriptor of the intrinsic activity of a catalyst is the Turn Over Frequency (TOF) that indicates the number of O_2 molecules a catalytic site produces per second. In the case of OER which is a four electrons transfer process, its expression is:

$$TOF = \frac{j}{4eN} \quad (1.4)$$

With j the current density at a given overpotential, e the elementary charge and N the number of active sites for the reaction. The current density j at a given potential as well as N should be normalized by the active surface area of the catalyst. However, how this normalization is performed varies a lot in the literature. A normalization with respect to geometrical surface area or metal load, is valuable from an applied viewpoint but is not accurate. True benchmarking of different catalysts requires normalizing the current with respect to the Electrochemical Surface Area (ECSA) of the catalyst. Different methods exist for this purpose, including capacitance, BET or microscopy measurements [10]. However, a reliable ECSA determination is not easy and erroneous ECSA estimation may affect substantially the OER activity measured for a catalyst. This also applies for the overpotential η at a fixed current density j that should consider the ECSA of the material. Similarly, determining the true number of active sites N for the reaction is not straightforward and even more complicated than determining the ECSA.

Together with the Tafel slope and the TOF, the above mentioned overpotential necessary to flow a given current density and current density measured at a given potential are amongst the most used OER activity metrics. However, a fair comparison of OER activity is difficult to establish, depending on the indicator chosen and the way the current is normalized. In the following, we will focus on the catalysts' activity in neutral-alkaline electrolyte, which is more favourable for OER than acidic conditions [6]. The stability of the catalyst in alkaline medium is therefore another parameter to consider when evaluating the performances of a catalyst. The comparison of the overpotentials required to reach a given current density measured at $t=0$ and at $t=2h$ are for example a way to evaluate the stability of the catalyst in OER conditions [11].

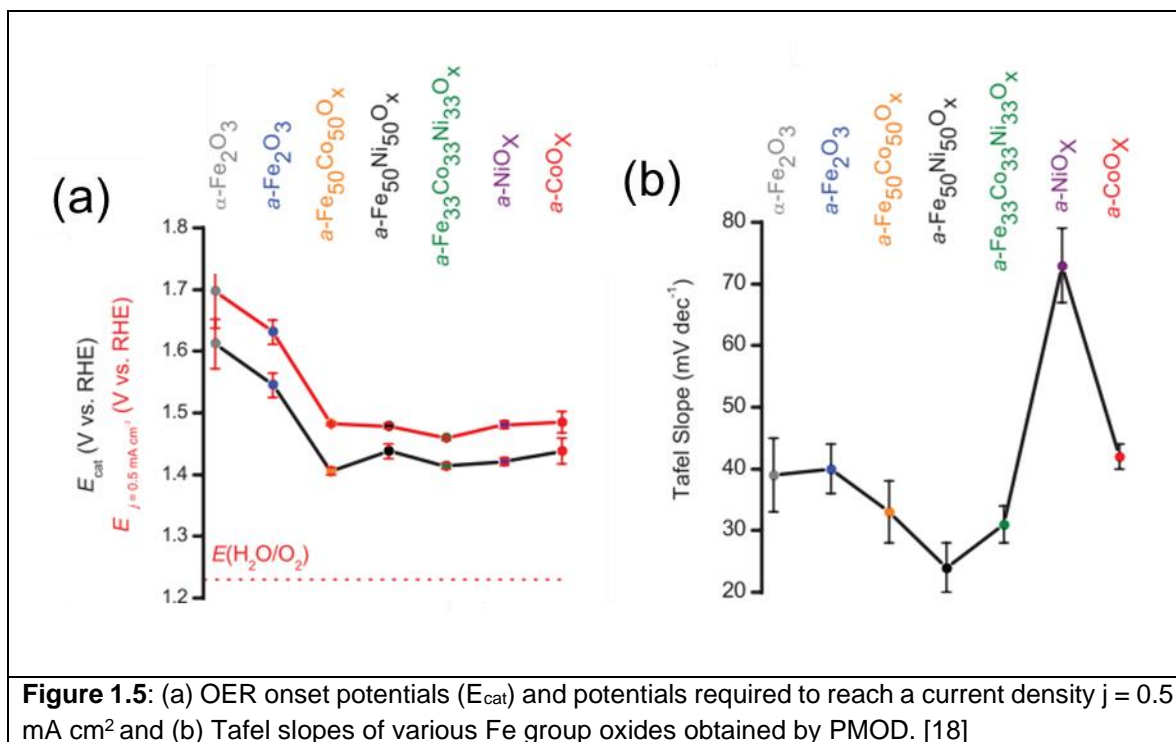
Benchmarking studies of transition metal oxide catalysts

To address the issue of uncertainties in experimental OER activity comparison, some research groups have carried out benchmarking studies using consistent protocols to accurately compare the activity of several OER catalysts. For example, Mc Crory et al. [11-13] have compared the OER activity in alkaline medium (1M NaOH) of 26 electrodeposited metal oxides, made of single or binary or ternary metals including Co Fe, Ni, Cu, La, Mn, Ir, Ru, etc. The activity metrics they used to evaluate the activity of the catalysts are the overpotential needed to reach a current density of 10mA/cm² per geometrical surface area, measured at both $t=0h$ and at $t=2h$ in order to additionally estimate the stability of the catalyst, as illustrated in **Fig. 1.4 a** and **b** (zoom in the white zone). The ECSA and roughness factor RF were estimated by determining the double-layer capacitance of the system from CV and are included in the figure as a colour scale for each data point. The general trend is a higher catalytic activity of noble

It is generally accepted that noble metal oxides are better OER catalysts than other transition metal oxides [14], however in a sustainability viewpoint, it is essential to use earth abundant catalyst materials. The above studies indicate that the activity of iron group oxides (Fe, Ni, Co) oxides is rather close to that of Ir or Ru oxides, which makes them good candidates for durable OER electrocatalysts.

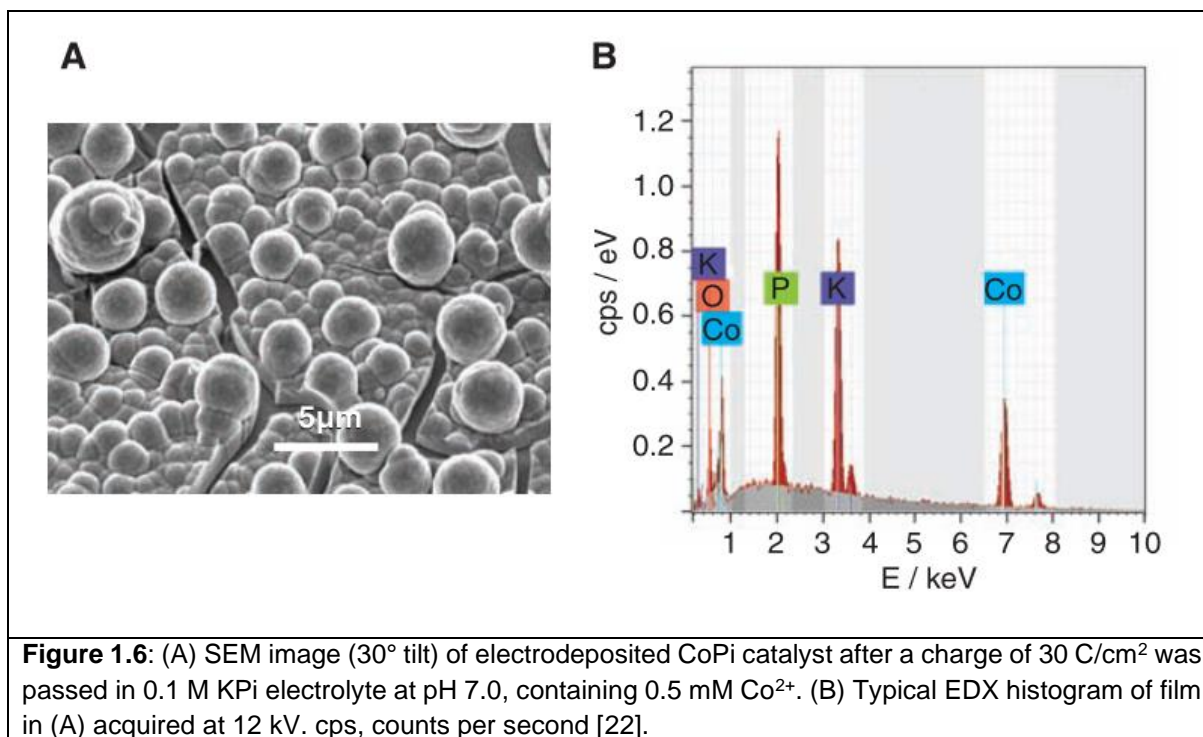
Iron group oxides catalysts

The OER activity of Fe group oxides both as single metal oxide or oxyhydroxide CoO_x , FeO_x and NiO_x and binary/ternary metal oxides CoFe , CoNi , FeNi , CoFeNi has been investigated by different groups [15-19]. In these studies, oxide or oxyhydroxide catalysts of different compositions were prepared either by electrodeposition or photochemical metal organic deposition (PMOD), and similar metal loadings were used in order to accurately compare the catalyst activity of each oxide. Regarding the single metal oxides, Smith et al. [17,18] found similar OER activities for PMOD prepared Ni and Co oxides, based on the OER onset overpotential (where the Tafel regime becomes linear) and the overpotential needed to reach a current density of 0.5 mA/cm^2 , at least 100mV lower than the one measured for FeO_x . Morales et al. [19] determined the following activity trend: $\text{CoO}_x > \text{NiO}_x > \text{FeO}_x$, based on the TOF and the ECSA corrected current density at an overpotential of 0.35V. However, Burke et al. [15] found that the TOF of electrodeposited FeO_xH_y oxyhydroxide is higher than that of CoO_xH_y , itself higher than the one of NiO_xH_y . They attributed the usually low OER activity measured for Fe oxides to their poor electrical conductivity, and mentioned that at higher overpotential, Fe oxide becomes more conductive, leading to higher OER activity. Even though whether Fe oxides are good OER catalysts is debated, it is accepted that Fe addition in Co or Ni oxides improves greatly their activity. This was observed in all studies mentioned above, where either mixed FeNi or [15,17] or CoFe [19] oxides had the best OER activities. This is also the reason why the high OER activity sometimes measured for Ni oxide is attributed in some studies to the presence of Fe impurities in commercial electrolyte medium [15,20,21]. **Fig. 1.5a** shows overpotentials at OER onset and at 0.5 mA/cm^2 of PMOD prepared Co, Fe and Ni oxides, together with their Tafel slopes in **(b)** [18]. Fe oxides present relatively low Tafel slopes ($\sim 40 \text{ mV/decade}$) in spite of their high overpotentials, while Ni has a notably higher Tafel ($\sim 70 \text{ mV/decade}$). Fe addition decreases both the overpotentials and the Tafel slopes of mixed oxides compared to the pure ones. Even if they are composed of two metals of high OER activity, mixed CoNi oxides are found less or as good as catalysts as single Co or Ni oxides [15,19].



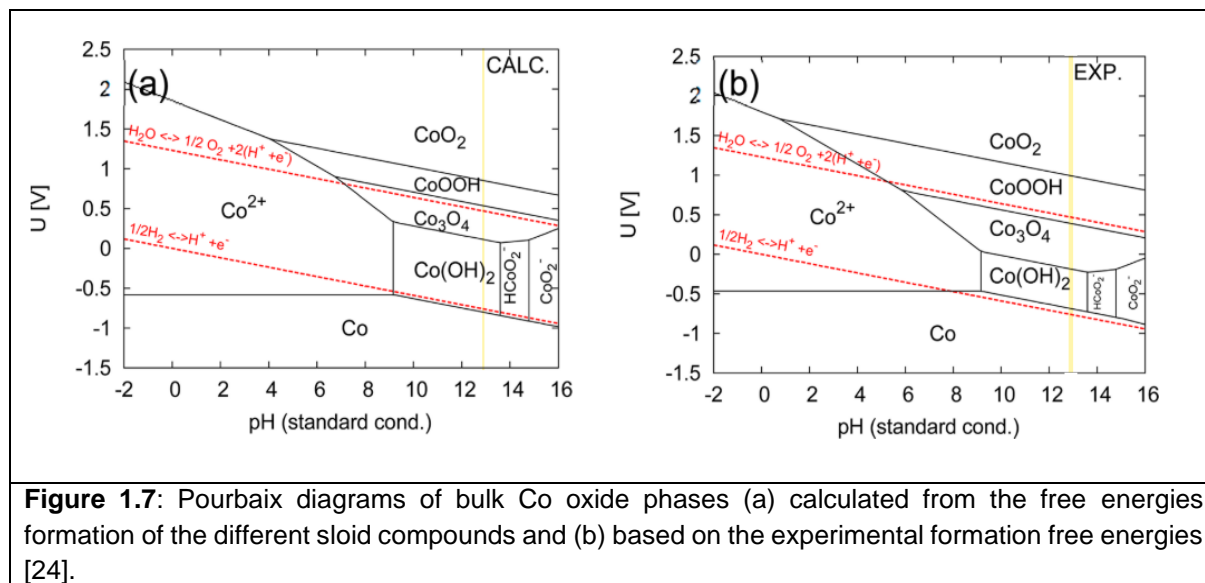
Cobalt oxides catalysts

In this work we especially focus on Co and CoFe based oxides. One of the most OER active Co based oxide catalyst was reported by Nocera et al. [22]. It is obtained by electrodeposition of Co(II) salts in pH7 potassium phosphate buffer (KPi) solution on different substrates like ITO or FTO, and often referred as CoPi or CoCat. The as-formed precipitate is an amorphous oxide/hydroxide of micrometer thickness (see **Fig. 1.6a**) which contains Co, K, P and O atoms with Co:K:P in a ratio 2:1:1 (see **Fig. 1.6b**). It exhibits good OER activity and stability in neutral pH with an OER onset starting at 0.28V. In a further mechanistic study by electrokinetic and ^{18}O isotope experiments [23], the authors showed that phosphate plays a critical role in OER mechanism since the Tafel slope is greatly increased in its absence. The OER mechanism they described involves an equilibrium between Co(III) and Co(IV) species maintained by phosphate species, followed by a limiting chemical step involving O-O bond coupling. However, CoCat is not a well-defined oxide since it contains a notable amount of phosphorus and potassium.



The activity of pure Co oxide catalysts has been investigated by computational methods including DFT studies. In this case, the use of defined crystalline cobalt oxides is required, as well as a specific orientation of the surface in contact with the electrolyte. **Figure 1.7** compares Pourbaix diagrams of cobalt oxides determined from (a) DFT calculated Co oxides formation free energies [24] and (b) experimental formation free energies [25]. At pH 13 (yellow lines) the Co oxides considered are Co(OH)₂ at low potentials, Co₃O₄, CoOOH and CoO₂ at high potentials. The top red line shows the potential at which OER theoretically takes place. At potentials where OER experimentally occurs (> 1.4V for example), CoOOH is found to be the most thermodynamically stable phase and is supposed to be the active phase for OER. CoOOH(01 $\bar{1}$ 2) surface was found to be the most stable one in OER conditions [24]. The OER on Co₃O₄(001) and CoOOH(01 $\bar{1}$ 2) surfaces was investigated by Norksov et al. [26] using DFT simulations, which found similar overpotentials for the two surfaces that they attributed to similar Co coordination environment of the active sites. More recently, Creazzo et al. [27,28] performed DFT calculations combined with molecular dynamics (DFT-MD) which take into account specifically the H₂O dynamics at the oxide-electrolyte interface, in order to correlate more closely to experimental conditions. They studied both Co₃O₄(110) and CoOOH(0001) surfaces and found that if water participates in OER mechanism, Co₃O₄(110) overpotential is consequently lower than that of CoOOH(0001). They however did not include HO⁻ in their simulations. The computational studies described above evidence that the most stable crystalline oxides in OER conditions are Co₃O₄ and CoOOH, however they do not yield a clear

understanding regarding their relative OER activity, especially since they consider several distinct surface orientations for these oxides.



The OER properties of Co_3O_4 and CoOOH have been widely studied experimentally in alkaline medium. Their reported activity largely depends on the morphology, surface area, oxide composition (oxidation state, presence of defects or oxygen vacancies) or substrate used [29, 30]. These oxides can indeed be prepared with several methods such as sol-gel [31], hydrothermal [32], or solvothermal [33] synthesis, or direct electrodeposition in different media [34] which lead to the formation of nanoparticles, nanosheets or thin films. In the studies of references [35,36], the OER activity (overpotential) of Co_3O_4 nanoparticles increases with decreasing particle sizes which is associated to their larger surface area as well as the increase of Co oxidation state with decreasing particle sizes. An increase in the nanoparticles surface area by an order of magnitude was found to decrease the overpotential by approximately 50 mV. The substrate can also influence OER activity, as measured by Bell et al. [37] who showed that the TOF of Co oxide depends on the metal substrate it is electrodeposited on: it decreases with decreasing electronegativity of the substrate. It is therefore not straightforward to compare the catalytic activity of the different Co oxides, due to the various parameters that may influence the measurement. An attempt to reliably compare Co_3O_4 and CoOOH OER activity was reported by Liu et al. [38] who synthesized $\text{CoOOH}(001)$ and $\text{Co}_3\text{O}_4(111)$ by respectively electrochemical oxidation or thermal decomposition of an electrodeposited $\text{Co}(\text{OH})_2(001)$ film on $\text{Au}(111)$. The OER activity of Co_3O_4 and CoOOH were compared by Tafel analysis in O_2 saturated 1M KOH electrolyte. The Tafel slopes of both oxides were found close to 55 - 60 mV/decade. The OER activity (current density and overpotentials) of the two materials becomes similar when taking their ECSA into account, while it is notably different if not.

Consequently, great care in the morphology of the materials and the experimental conditions should be taken in order to compare the OER activity of different oxides.

1.4 Studying OER catalysts under operating conditions

The OER mechanisms shown in **Figure 1.2** are simplified and theoretical reaction pathways, which do not take into account the chemistry of the metal center M: which atoms is it bonded to? what is its oxidation state? To which oxide structure/phase does it correspond to? It has indeed been demonstrated that the composition, morphology, structure or oxidation state of the catalysts is dependent on the applied potential [39]. In addition, a critical point in creating efficient catalysts is identifying the active site for the reaction. This refers to the group of atom(s) where $\text{H}_2\text{O}/\text{HO}^-$ is split into O_2 which atomic environment and local structure are key parameters to determine. The evolution of the physical and chemical parameters characterizing the active site(s) can only be probed in situ, in electrochemical conditions. Characterizations under reaction conditions also called operando characterizations refer to characterizing the catalyst in OER conditions, while measuring its activity at the same time. It allows establishing relationships between the activity of a catalyst and structural or chemical parameters probed with a relevant characterization technique.

Several characterization techniques have been used in operando condition in order to probe different physical parameters of the catalysts. This includes vibrational techniques like Raman spectroscopy, Infrared (IR) spectroscopy and X-ray techniques, such as Photoelectron spectrometry (XPS), Mossbauer spectroscopy or X-Ray Absorption Spectroscopy (XAS), as well as X-ray Diffraction (XRD), scanning probe microscopies, such as AFM, SEM, and liquid TEM. Each of these techniques, when used in operando conditions provides different type of information. Selected examples of their use for the study of Co/Fe oxides catalysts for OER are given below.

IR spectroscopy: this vibrational technique gives information about chemical bonds and helps identifying the reactants, products and reaction intermediates. Time resolved IR spectroscopy experiment is sometimes necessary when reaction intermediates have short lifetimes. Zhang et al. for instance [40], evidenced the formation of two reaction intermediates with different temporal behaviour, which they assigned to two different catalytic sites on crystalline Co_3O_4 nanoparticles during photoelectrochemical OER. They associated the first one, a Co(III) superoxide, to a site where a fast OER mechanism takes place, and the second one, a Co(IV)=O species, to a slow OER site.

Raman spectroscopy: this technique is especially valuable since it is surface sensitive, it can provide structural fingerprints by which phases can be identified, as well as chemical bonds. For example, Yeo et al. [37] followed the Raman peaks of a Co_3O_4 sample obtained by

electrodeposition on a rough Au substrate during a potential sweep. With increasing potential, they observed the attenuation of peaks belonging to Co_3O_4 (shown with dashed vertical lines in **Fig. 1.8a**) and the formation of another peak at 579 cm^{-1} (see **Fig. 1.8a**) that they ascribed to CoOOH .

Near-Ambient-Pressure XPS (NAPXPS): XPS is also a surface sensitive technique which allows identifying the elemental composition of a material as well as the chemical state and electronic state of the elements present in the material. XPS usually requires UHV conditions but operando measurements using (Near) Ambient-Pressure XPS can be performed with the adequate setup and sample preparation. This technique enabled Favaro et al. [41] to study in situ Co_3O_4 and biphasic $\text{Co}_3\text{O}_4/\text{Co}(\text{OH})_2$ samples deposited by plasma-enhanced atomic layer deposition (PE-ALD) on a Si substrate. They compared XPS spectra obtained under increasing polarizations until OER potential and found that Co_3O_4 and $\text{Co}(\text{OH})_2$ are converted into CoOOH at OER potential (see **Fig. 1.8b**). The chemical-structural transformation is complete in the case of the biphasic sample while it only concerns 5 \AA (over 40) in the case of Co_3O_4 . The appearance of new spectral features in $\text{Co}2\text{p}$ and $\text{O}1\text{s}$ spectra at OER potential (green highlighted area in **Fig. 1.8b**) was assigned to the formation of Co^{4+} centres.

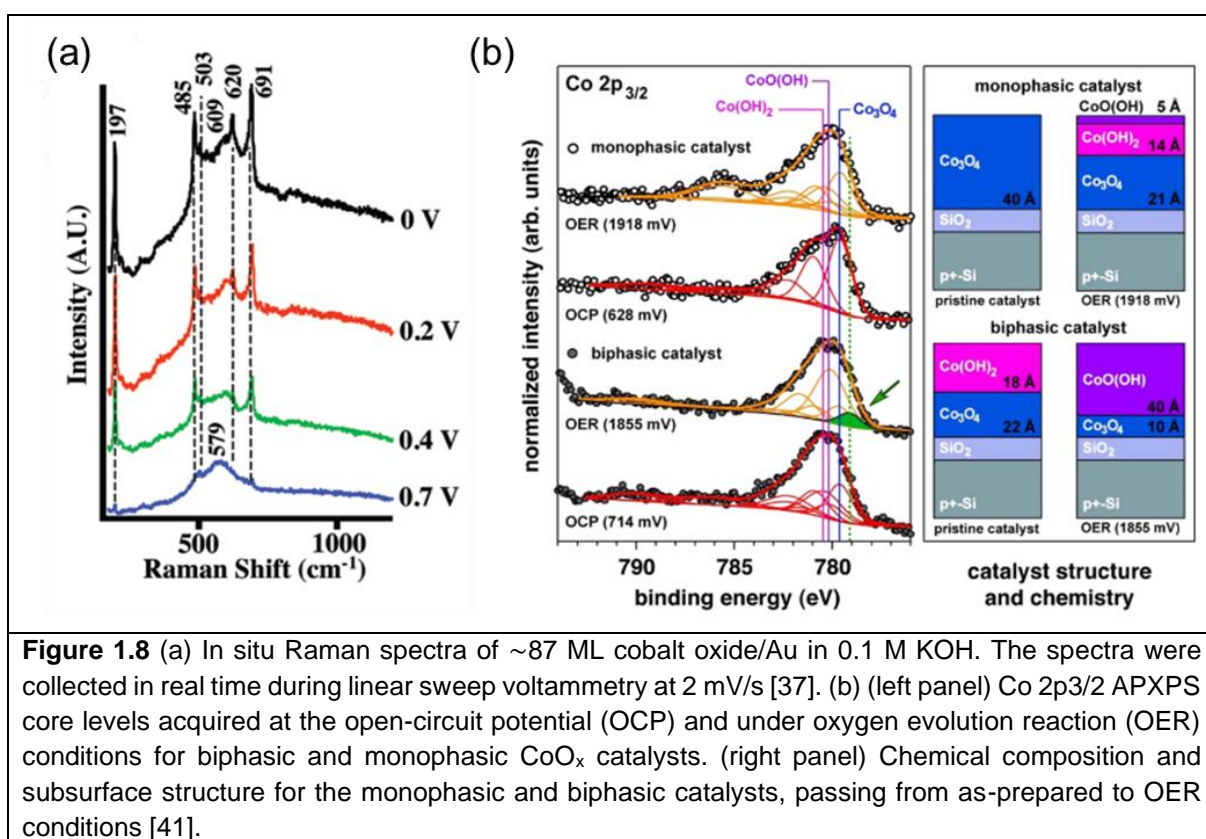


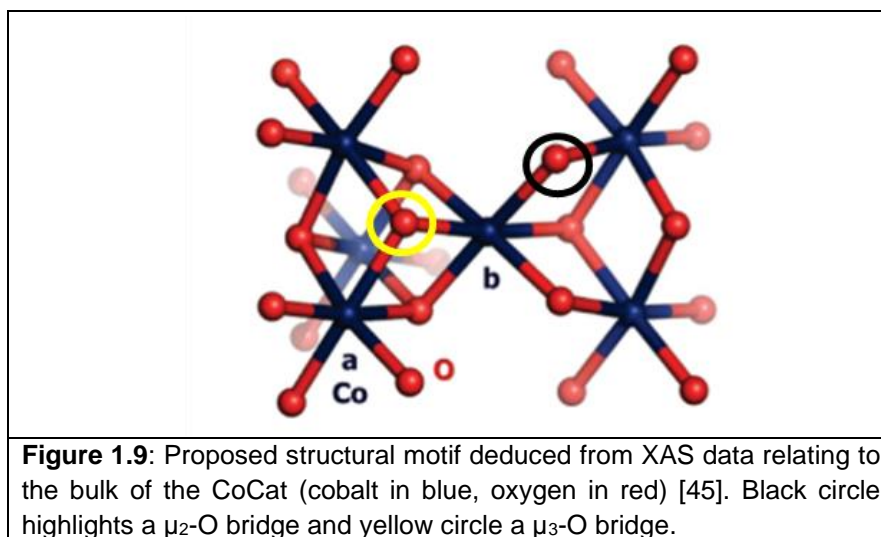
Figure 1.8 (a) In situ Raman spectra of ~ 87 ML cobalt oxide/Au in 0.1 M KOH . The spectra were collected in real time during linear sweep voltammetry at 2 mV/s [37]. (b) (left panel) $\text{Co} 2\text{p}_{3/2}$ APXPS core levels acquired at the open-circuit potential (OCP) and under oxygen evolution reaction (OER) conditions for biphasic and monophasic CoO_x catalysts. (right panel) Chemical composition and subsurface structure for the monophasic and biphasic catalysts, passing from as-prepared to OER conditions [41].

Transmission Electron Microscopy (EC-TEM): For operando TEM experiments, the sample is installed into a thin layer electrochemical cell. This emerging technique was used to study

crystalline Co_3O_4 nanoparticles during OER in alkaline medium [32]. After immersion in electrolyte and potential sweeps in pre OER and OER regime, the authors observed an irreversible amorphization of the Co_3O_4 nanoparticles: the outer part of the particles is transformed into a less dense cobalt oxide phase of nanometric size, suggested to be an amorphous CoO_xH_y phase. The Co_3O_4 structure is not found again after electrochemical measurements.

X-ray Absorption Spectroscopy: XAS has been widely used in literature to measure the metal center oxidation state under operating conditions - using the XANES part of a XAS spectrum – and the local environment (bond distances, coordination number) of the atom – using the EXAFS part of the spectrum. This is a powerful technique is bulk sensitive and compatible with operando conditions because it uses relatively high energy X-rays (7-8 keV for probing Co and Fe K-edges) which penetration depth is a few 100 μm . Electrochemical cells with very thin electrolyte layers and controlled electrolyte flow have been designed in order to limit the attenuation of the beam in liquid electrolyte [42,43]. “Quasi in situ XAS” [44] instead of “operando XAS” is a particular method where the electrochemical is freeze quenched in liquid N_2 and stored at low temperature for further XAS measurements. This approach assumes that the structure of the catalyst in operando conditions is preserved by rapid freezing. The advantage is that high quality EXAFS may be measured at low temperature [44].

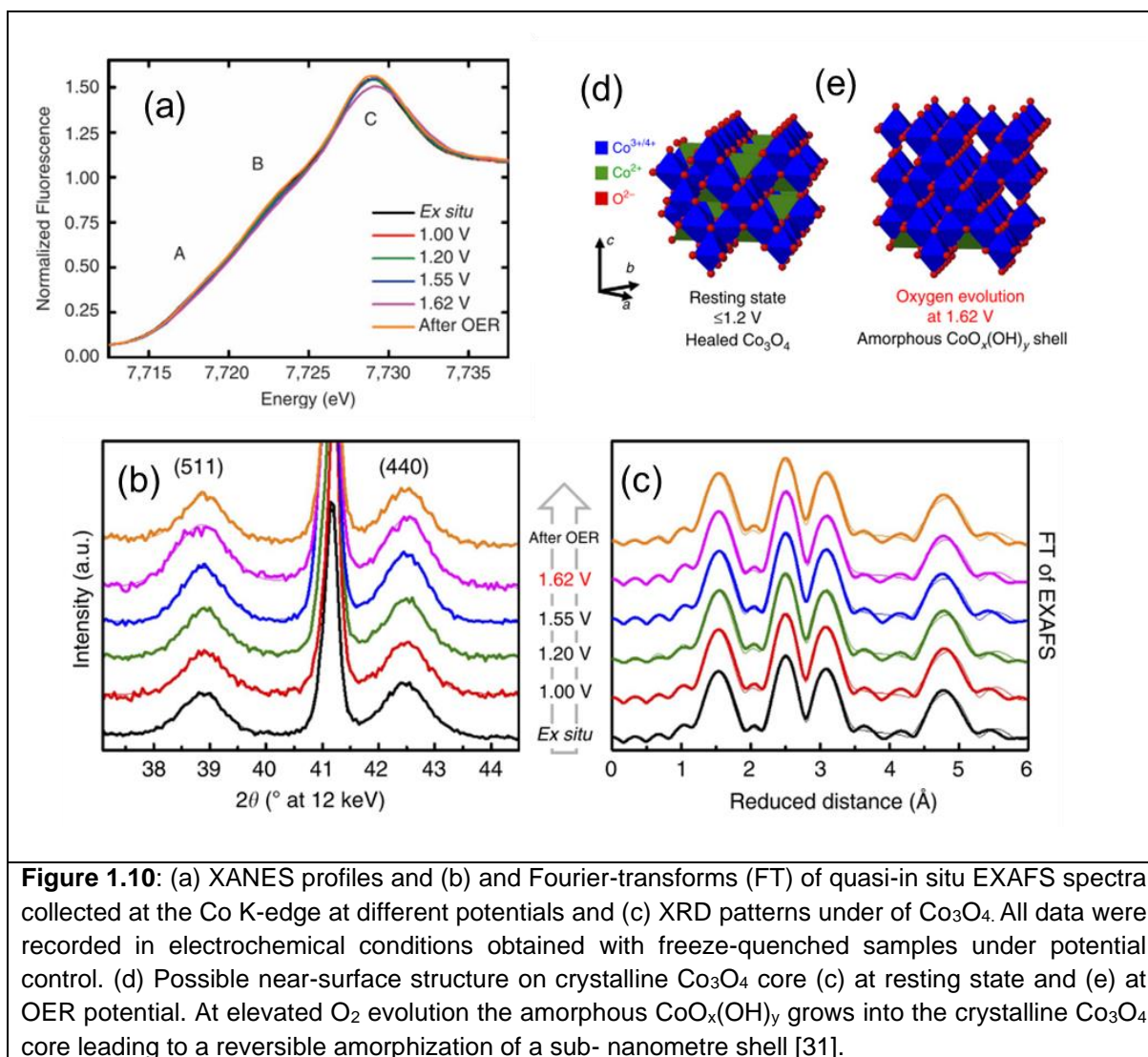
The CoCat sample mentioned above was characterized by XAS, first ex-situ [45] then at OCP and polarized at 1.25V [46]. Ex-situ, the geometry around Co atoms was identified as a near-octahedral environment where Co is coordinated to 6 oxygen atoms as illustrated in **Figure 1.9**. The material consists of oxygen sharing CoO_6 units and this structure is conserved at 1.25V [46]. This local environment is therefore believed to be the active phase for OER. By comparison with reference spectra, the oxidation state of CoCat was found close to +3 ex situ and increases once polarized at 1.25V, indicating an oxidation state higher than +3 under reaction conditions. This was further investigated in an operando study of CoCat films using XAS, UV visible absorption and time-resolved mass spectrometry [44]. Shifts of the main absorption edge towards higher energies with increasing potential were observed, showing an increase of Co oxidation state from Co(II) to Co(III) between 0.8V and 1.0-1.2V, which further increases from Co(III) to Co(IV) when increasing potential. They found that these transitions are accompanied by changes in Co-Co and Co-O environment and claimed that the Co atoms undergoing oxidation state changes are located at the edges of motifs of six-fold coordinated Co (such as the Co atom highlighted with an “a” in **Figure 1.9**). At OER onset, they found 20% of Co(IV) in the film and proposed that at least two adjacent Co(IV) are required to create an active site where O-O bond formation occurs.



Regarding non-amorphous Co oxides, Bergmann et al. [31] used the freeze quenched approach to characterize at different potentials a nanocrystalline Co_3O_4 film deposited by spin coating on glassy carbon electrode. As prepared, the oxidation state of Co_3O_4 is between +2 and +3 as expected for this oxide. With increasing potential, the authors observed a slight increase of Co mean oxidation state (see **Fig. 1.10a**) and changes in Co coordination shell (see **Fig. 1.10b**): more octahedrally coordinated Co ions are present at 1.62V. After OER, XANES and EXAFS spectra are very similar to the as prepared sample, suggesting that the changes occurring during OER are reversible. They suggested the transformation, at OER potential, of surface Co_3O_4 to an octahedrally coordinated CoO_xH_y phase, as illustrated in **Fig.1.10e**. This conclusion is however in discrepancy with former studies which show that Co oxidation takes place progressively with potential and not during OER. In a later study, they combined quasi in situ XAS and DFT calculations to compare the transformation in neutral electrolyte and under OER condition of four well-defined catalysts: rock salt CoO, wurtzite CoO, spinel Co_3O_4 and CoOOH [47]. For all materials, the formation of a surface CoO_xH_y layer considered as the OER active phase was observed. Analysis of O K-edge spectra revealed for all samples the presence at OER potential of a characteristic feature of octahedral environment. They proposed the existence of two active sites for OER in these oxides. The first one is associated to a fast OER mechanism (low Tafel slope) and involves motifs where oxygen atoms are bonded to two neighbouring Co (μ_2 -O bridges, highlighted in black in **Fig.1.10a**). The second mechanism implies oxygen atoms bonded to three neighbouring Co (μ_3 -O bridges, highlighted in yellow in **Fig.1.10b**), and corresponds to slow OER (high Tafel slope).

Operando XAS studies involving slightly modified Co oxides, such as CoOOH nanosheets [51], oxygen vacancies rich Co_3O_4 [52], Co_3O_4 samples where tetrahedral Co^{2+} and octahedral Co^{3+} were substituted by Zn^{2+} and Al^{3+} OER inactive cations [53], or $\text{Co}_3\text{O}_4/\text{CoO}$ core shells [54],

have also been carried out, and confirm the general trend of the formation of a CoOOH like species at OER potential, with an octahedral type of environment.



Operando XAS characterizations have also been employed in order to study the role of Fe in OER mechanism at the surface of CoFe oxides [48]. For example, for amorphous CoFeOx oxides, Smith et al. [49] proposed a multiple active site mechanism, with two type of sites. The first active sites is made a μ_2 -O bridge between two Co atoms, which are oxidized up to Co^{4+} upon potential application. The second site involves a μ_2 -O bridge between Co^{2+} and Fe^{3+} , where Co^{2+} is oxidized, and Fe remains Fe^{3+} . However, Fe oxidation to $\text{Fe}^{>3+}$ at OER potential was measured by Boettcher et al. [50] who studied $\text{Co}_{0.8}\text{Fe}_{0.2}\text{O}_x\text{H}_y$ and $\text{Co}_{0.6}\text{Fe}_{0.4}\text{O}_x\text{H}_y$ oxyhydroxides. They proposed two mechanisms on CoFe oxyhydroxides: (i) an OER mechanism where Co-Fe is the active site, without Co^{4+} formation; (ii) a mechanism with Fe as the active site and involving $\text{Fe}^{>3+}$ species.

X-ray diffraction (XRD): For crystalline materials, XRD is a powerful technique to determine structural changes. It is also well suited for operando characterizations since at synchrotron facilities it is performed with high energy X-Rays (>18 keV for example). In these conditions, real electrochemical conditions can be accessed, with the sample covered by a rather thick electrolyte since the beam attenuation by the electrolyte is consequently smaller at high energy [55]. In addition, XRD measurements can be performed with a grazing incidence (referred as grazing incidence XRD, GIXRD, or Surface XRD, SXRD), which allows to be more specifically sensitive to the surface of the material where structural changes are expected to take place. For example, Bergmann et al. [31] combined operando GIXRD to their quasi in situ XAS measurements on nanocrystalline Co_3O_4 . Before OER, they did not observe any change in the structure of the oxide, however at OER potential, they measured a decrease in Co_3O_4 coherence length, that they associated to the formation of Co_3O_4 crystallite into the CoO_xH_y active phase for OER (see **Fig.1.10c**) Since they did not observe the formation of other XRD feature, they suggested that this phase is X-Ray amorphous. After OER, the initial Co_3O_4 coherence length was recovered, indicating that this structural transformation is reversible. This was not the case for other Co oxides CoO and CoOOH [47] for which irreversible structural changes were measured. Such reversible amorphization was also measured by Reikowski et al. [56] on epitaxial Co_3O_4 (111) thin film obtained by electrodeposition. They performed operando surface X-Ray Diffraction measurements where the oxide Bragg peak was monitored during potential cycles in pre OER and OER regimes, enabling to determine the changes in crystallite sizes and lattice constants induced by potential. A reversible and continuous decrease of the sizes of the crystallites takes place several hundred of mV before OER potential, together with a compression of the lattice unit cell. This was interpreted as the progressive formation of an amorphous phase at the surface of Co_3O_4 crystallites, which thickness is close to 1 nm at OER potential. Since these changes start at a potential close to $\text{Co}_3\text{O}_4/\text{CoOOH}$ thermodynamic equilibrium, the formation of this surface layer, hereafter called skin layer, could be related the $\text{Co}_3\text{O}_4/\text{CoOOH}$ phase transition rather than OER. An epitaxial $\text{CoOOH}(001)$ thin film was investigated with the same method, and they found no skin layer because its structure was completely stable in a wide potential window including OER.

The selected examples described above show that operando characterizations have yielded substantial insights into understanding the chemical state, phase, and oxidation state of the active site for OER in Co and CoFe oxides. Especially XAS has the advantage of providing insight into the local environment and oxidation state of the metal cation, which play a critical role in OER mechanism. XRD is essential to study crystalline samples, and proves to be especially useful in the case of Co based oxides since operando studies mainly converge to show that these oxides undergo structural transformations under OER conditions. These

transformations correspond to the formation of a new phase where the metal oxidation state is higher than in the bulk. However, the reversible nature of this transformation is debated and seems to depend on the oxide phase. The different studies also do not agree on the potential at which it is formed (at OER potential or progressive potential induced formation) and on its nature (amorphous or crystalline, CoOOH-like phase or species with a higher oxidation state).

1.5 Model catalysts

The aim of operando characterizations of OER catalysts is to establish relationships between the activity of an oxide surface and other parameters that may play a role in OER activity, such as the structure or the chemical state of a catalyst. However, we have seen in **section 1.3** that determining properly the activity of a catalyst may present several issues, especially linked to the poor knowledge of the real electrochemical surface area of the surfaces. In most of the operando studies detailed in **1.4**, the ECSA is not known, therefore the density of surface (active) sites cannot be estimated. In addition, the exact composition and state of the surface (atomic arrangement, presence of defects, edge sites and their density), which cannot be estimated may have an important role in the catalytic activity of the surface.

To establish structural and chemical -property relationships at the atomic scale, identify and study the active site(s) for OER and make comparable activity comparisons, ideal or model systems are therefore required.

What is a model catalyst?

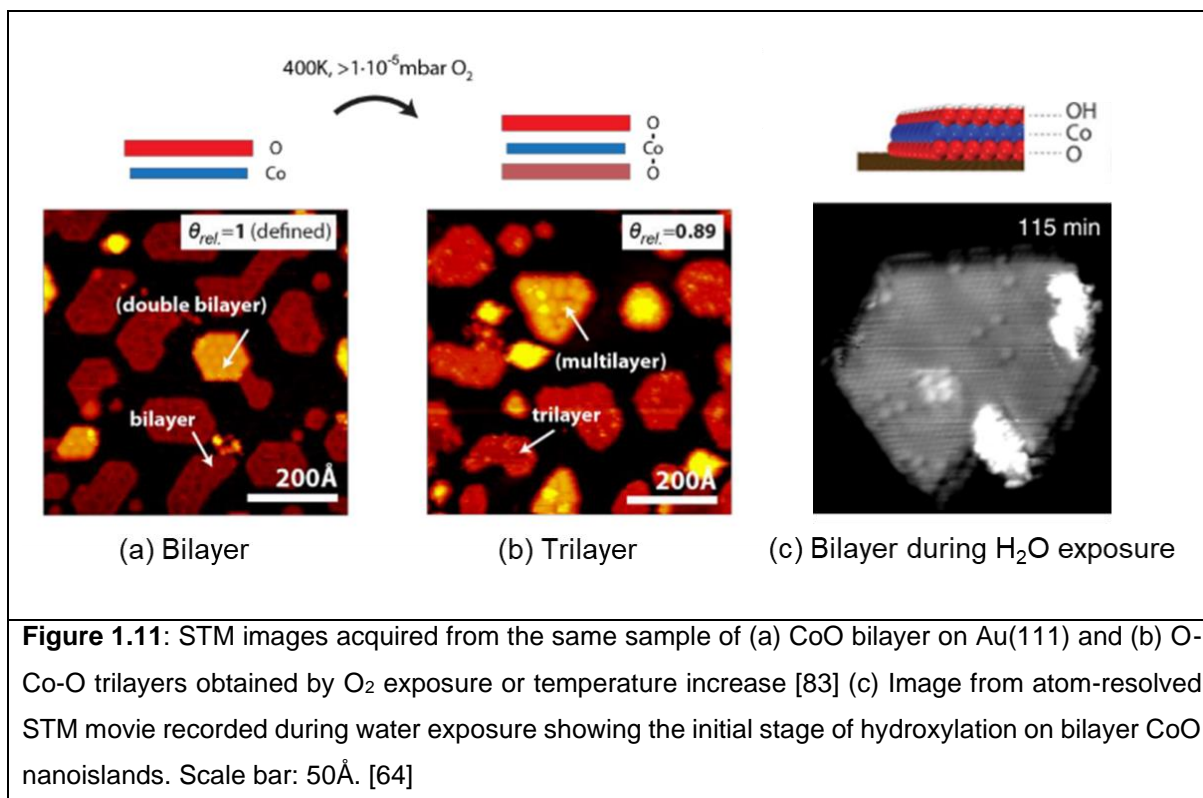
The purpose of model catalyst systems is to understand a catalytic process, using a catalyst material as well defined and defect free as possible. The defects properties of a catalyst surface should be controlled since they may influence greatly the catalytic reaction mechanism [57]. For this purpose, the model catalysts should ideally be prepared as planar as possible with atomically-defined surfaces having a low defect density. They are generally either single crystal electrodes or thin epitaxial films grown on a single crystal substrate [58]. The great advantage of this approach is that a structure – property relationship may be established because the sample surface consists of one type of catalytic sites (if one neglects defects such as atomic steps, point defects). In addition, one may study the influence of a possible surface reconstruction [59]. In the case of single crystal, a standard preparation is performing cycles sputtering / annealing in the UHV to clean the surface. In the case of epitaxial thin oxide films, different preparations may be used, such as Physical Vapor Deposition (PVD) processes, Chemical Vapor Deposition (CVD) processes, Molecular beam epitaxy (MBE), or electrodeposition [58,60]. With these methods, the oxide is generally prepared from a single crystal or grown on a single crystal substrate and adopts its crystalline structure. This allows

having oxide with a well-defined atomic structure and orientation, an atomically defined morphology and high purity [58]. The aim is also to obtain as thin films as possible so that minor changes in their structure, composition or chemical state can be probed. With their special features, these catalysts are indeed suitable for several characterization techniques such as XRD, surface sensitive techniques like XPS or microscopy techniques like STM or AFM, which allow to establish a complete characterization.

In the literature, little operando studies using Co and Fe oxides model catalysts to investigate OER mechanism exist. Model catalysts studies have mainly focused on studying the stability of the catalysts by characterizing them before and after OER or investigating the adsorption of molecules such as H₂O at their surface. A few examples of Co and Fe oxides model catalysts studies are given below, showing different preparation methods.

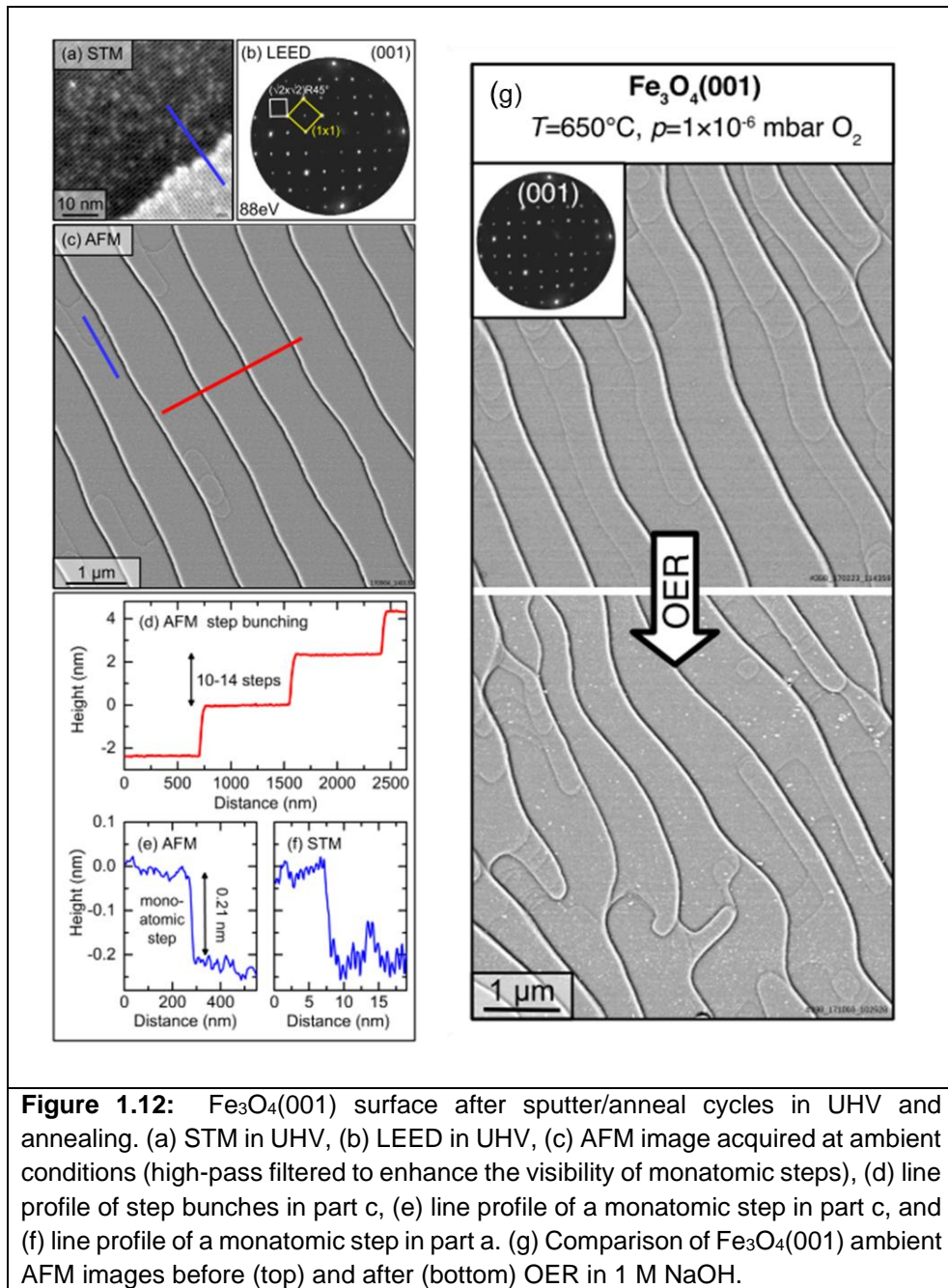
Co oxides epitaxial thin films by PVD

Faisal et al. [61] prepared 6 nm thick Co₃O₄(111) films on sputtered- annealed Ir(100) single crystal substrate. The preparation takes place in an ultra-high vacuum (UHV) chamber and involves Co physical vapor deposition at a specific oxygen pressure. LEED was used to check the crystallographic orientation of the as-prepared film and its composition was verified with XPS. Lauritsen et al. [62,63] reported the synthesis of CoO nanoislands exposing (111) plane on Au(111) substrate in UHV, Co being deposited with an electron beam evaporator in O₂ atmosphere. This method yields 1.7 Å thick CoO bilayer (see STM image in **Fig. 1.11a**). By increasing either the annealing temperature or the O₂ exposure, 2.9 Å thick O-Co-O trilayers are obtained (**Fig. 1.11b**), on which a hydroxyl overlayer was identified. Based on the lattice parameter, XPS analysis indicating a Co³⁺ oxidation state and the coverage of the hydroxyl overlayer, they suggest a CoOOH_{0.33} structure. Co-O bilayer nanoislands (**Fig.1.11a**) have been characterized by STM and XPS before and after ten cycles in OER regime in alkaline medium [63]. After OER, the sample is composed of surface hydroxylated O-Co-O trilayers (as in **Fig.1.11b**). This organization was also obtained when exposing CoO bilayer to liquid water. In another work where they studied with in situ STM the hydroxylation of such bilayers by exposing the surface to vapour H₂O, they found that the islands edges are active sites for water dissociation (see **Fig.1.11c**) and proposed based on DFT calculations that these sites may also act as active sites for OER [64].



Fe oxides single crystal electrodes

Müllner et al. [65] prepared two well-defined Fe₃O₄ model surfaces Fe₃O₄(001) and Fe₃O₄(110) using Fe₃O₄ single crystals, sputtered and annealed in a UHV chamber. **Figure 1.12** shows LEED pattern (b) and microscopic characterizations of Fe₃O₄(001) surface in UHV (a) and at ambient conditions (c). It is composed of wide terraces separated by 10-14 atomic steps (d), and atomic step are sometimes visible (e-f). The two Fe₃O₄ surfaces were found to be stable after several cycles in 1 M NaOH based on the comparison of AFM images recorded before and after OER (see example in **Fig. 1.12g** for Fe₃O₄(110)). However, XPS post characterizations indicated a slight overoxidation of Fe, that the authors attributed to the oxidation of Fe²⁺ atoms in the near surface region to Fe³⁺.



Cobalt oxides epitaxial layers by electrodeposition:

Electrodeposition of metallic epitaxial films [66-68] and epitaxial metal oxide films [34,69,70] on a single crystal substrate is now a mature method, easy to implement in ambient conditions. Recently, Switzer et al. developed electrodeposition methods to synthesize epitaxial $\text{Co}_3\text{O}_4(111)$ [34] and $\text{Fe}_3\text{O}_4(111)$ [69,70] films on a single crystal substrate. Crystalline Co_3O_4 films are obtained by electrochemical oxidation of Co^{2+} complexes in aqueous alkaline electrolyte. The deposition yields ~25 nm thick Co_3O_4 crystallites, that grow with a (111) orientation on Au(100) substrate. Crystalline Fe_3O_4 films are prepared by electrochemical reduction of a Fe^{3+} complex in alkaline electrolyte, which results in 300 nm thick films. The

films are electrodeposited on a Ni(111) substrate and gives (111) oriented Fe_3O_4 . In both cases, no post treatment is required since the method directly yields crystalline films.

$\text{Co}_3\text{O}_4(111)$ and $\text{CoOOH}(001)$ thin films investigated in the operando SXR D study [56] mentioned above were prepared with a method adapted from the work of Switzer et al [34]. According to AFM characterizations, this method yields well-defined 20-30 nm thick $\text{Co}_3\text{O}_4(111)$ packed crystallites and atomically flat 10-20 nm $\text{CoOOH}(001)$ islands both covering completely the Au(111) surface. Since their ECSA can be determined with microscopy techniques, their OER activities can be compared properly and related to their operando structural modifications. If their ECSA is taken into account, the catalytic activity of $\text{Co}_3\text{O}_4(111)$ and $\text{CoOOH}(100)$ is very similar. Morphological characterizations indicate that few edge sites are present on CoOOH surface, they concluded that it is mainly composed of $\mu_3\text{-O(H)}$ sites, where oxygen atoms are bonded to 3 neighbouring Co. This surface is the OER active surface since CoOOH structure does not change in a large potential range including OER potential window. The active OER surface for $\text{Co}_3\text{O}_4(111)$ is a non-crystalline phase, likely containing defects with $\mu_2\text{-O(H)}$ sites, according to [31]. It would therefore seem that $\mu_3\text{-O(H)}$ are as active sites for OER as $\mu_2\text{-O(H)}$, which are generally associated with fast OER and considered as the most active sites for cobalt oxides [45,47].

1.6 Objectives of the thesis

In this thesis we aim at developing a better understanding of the reaction mechanisms of water oxidation at the surface of earth abundant metal oxide catalysts. For this purpose, we use model catalysts and characterize them in the electrochemical environment, under operating conditions. To address the issue of the lack of consistency in determining and comparing the activity as well as the density of active sites of different OER catalysts, we employ oxide thin films with a well-defined structure, composition and morphology as model catalysts. These are epitaxial cobalt, iron and cobalt-iron oxides layers, obtained by electrodeposition on a single crystal substrate.

We use both surface X-ray diffraction (SXR D) and X-ray absorption spectroscopy (XAS) to investigate the oxide structure and the mean oxidation state of the metal(s) in the catalysts. These parameters have a critical importance in the OER mechanism on Co/Fe oxides surfaces because (i) the materials surface can undergo structural transformations in the pre-OER and OER regimes and (ii) oxidation of metal cations is expected to occur with increasing potentials while OER mechanism involves changes in their oxidation state. In dedicated electrochemical cells, both characterization techniques are well suited for operando electrochemical measurements because they involve X-rays of high energy that can penetrate deep enough in

the electrolyte without being strongly attenuated. This is especially true for XRD, while the XAS X-ray energies become more limiting. Therefore, they mimic well the operating conditions of the catalysts. The operando characterization of such model catalysts for water splitting allows to correlate the potential induced structural and oxidation state variations of the catalysts with their OER activity to gain an as accurate as possible determination of the catalyst surface state at OER potential. We aim at a better understanding of OER mechanism on their surface, together with an identification of the active sites.

We first focus in **chapter 3** on epitaxial pure cobalt oxides $\text{Co}_3\text{O}_4(111)$ and $\text{CoOOH}(001)$, for which we reproduce the measurements of [68] and extend the surface state characterization during OER by performing simultaneously operando XAS measurements. In **chapter 4**, we expand the XAS and SXRD operando characterization to a well-defined system of mixed CoFeO_y (111) spinel oxides thin films with an iron content ranging between 15% and 50%, obtained by electrodeposition on $\text{Au}(111)$. The behaviour of the mixed oxides is compared to the results obtained for pure crystalline Co_3O_4 and Fe_3O_4 spinel oxides. **Chapter 5** focuses on oxide films obtained by a second preparation method which consists in the anodic oxidation of an electrodeposited ultrathin ($\leq 1\text{nm}$) epitaxial metal film (Co, Fe, CoFe alloys of variable compositions). This system steps slightly away from the model catalyst systems because the oxides are not structurally well defined but offers several advantages such as a higher sensitivity in redox changes determination and more flexible tuning of the Co/Fe ratio in the oxide.

1.7 Bibliography

- [1] Roger, I.; Shipman, M. A.; Symes, M. D. Earth-Abundant Catalysts for Electrochemical and Photoelectrochemical Water Splitting. *Nature Reviews Chemistry*. 2017. <https://doi.org/10.1038/s41570-016-0003>.
- [2] Breeze, P. Hydrogen Energy Storage. *Power Syst. Energy Storage Technol.* **2018**, 69–77. <https://doi.org/10.1016/b978-0-12-812902-9.00008-0>.
- [3] Bockris, J. O. M. Kinetics of Activation Controlled Consecutive Electrochemical Reactions: Anodic Evolution of Oxygen. *J. Chem. Phys.* **1956**, 24 (4), 817–827. <https://doi.org/10.1063/1.1742616>.
- [4] Li, S.; Thomas, A. *Emerged Carbon Nanomaterials from Metal-Organic Precursors for Electrochemical Catalysis in Energy Conversion*; Elsevier Inc., 2019. <https://doi.org/10.1016/B978-0-12-814558-6.00012-5>.
- [5] Walter, M. G.; Warren, E. L.; McKone, J. R.; Boettcher, S. W.; Mi, Q.; Santori, E. A.; Lewis, N. S. Solar Water Splitting Cells. *Chem. Rev.* **2010**, 110 (11), 6446–6473. <https://doi.org/10.1021/cr1002326>.

- [6] Tahir, M.; Pan, L.; Idrees, F.; Zhang, X.; Wang, L.; Zou, J. J.; Wang, Z. L. Electrocatalytic Oxygen Evolution Reaction for Energy Conversion and Storage: A Comprehensive Review. *Nano Energy* **2017**, *37* (February), 136–157. <https://doi.org/10.1016/j.nanoen.2017.05.022>.
- [7] Song, F.; Bai, L.; Moysiadou, A.; Lee, S.; Hu, C.; Liardet, L.; Hu, X. Transition Metal Oxides as Electrocatalysts for the Oxygen Evolution Reaction in Alkaline Solutions: An Application-Inspired Renaissance. *J. Am. Chem. Soc.* **2018**, *140* (25), 7748–7759. <https://doi.org/10.1021/jacs.8b04546>.
- [8] Dau, H.; Limberg, C.; Reier, T.; Risch, M.; Roggan, S.; Strasser, P. The Mechanism of Water Oxidation: From Electrolysis via Homogeneous to Biological Catalysis. *ChemCatChem* **2010**, *2* (7), 724–761. <https://doi.org/10.1002/cctc.201000126>.
- [9] Man, I. C.; Su, H. Y.; Calle-Vallejo, F.; Hansen, H. A.; Martínez, J. I.; Inoglu, N. G.; Kitchin, J.; Jaramillo, T. F.; Nørskov, J. K.; Rossmeisl, J. Universality in Oxygen Evolution Electrocatalysis on Oxide Surfaces. *ChemCatChem* **2011**, *3* (7), 1159–1165. <https://doi.org/10.1002/cctc.201000397>.
- [10] Trasatti, S.; Petrii, O. A. Real surface area measurements in electrochemistry. *J. Electroanal. Chem.* **1992**, *327*, 353–376. [https://doi.org/10.1016/0022-0728\(92\)80162-W](https://doi.org/10.1016/0022-0728(92)80162-W).
- [11] Jung, S.; McCrory, C. C. L.; Ferrer, I. M.; Peters, J. C.; Jaramillo, T. F. Benchmarking nanoparticulate metal oxide electrocatalysts for the alkaline water oxidation reaction. *J. Mater. Chem. A* **2016**, *4* (8), 3068–3076. <https://doi.org/10.1039/c5ta07586f>.
- [12] McCrory, C. C. L.; Jung, S.; Peters, J. C.; Jaramillo, T. F. Benchmarking heterogeneous electrocatalysts for the oxygen evolution reaction. *J. Am. Chem. Soc.* **2013**, *135* (45), 16977–16987. <https://doi.org/10.1021/ja407115p>.
- [13] McCrory, C. C. L.; Jung, S.; Ferrer, I. M.; Chatman, S. M.; Peters, J. C.; Jaramillo, T. F. Benchmarking Hydrogen Evolving Reaction and Oxygen Evolving Reaction Electrocatalysts for Solar Water Splitting Devices. *J. Am. Chem. Soc.* **2015**, *137* (13), 4347–4357. <https://doi.org/10.1021/ja510442p>.
- [14] Matsumoto, Y.; Sato, E. Electrocatalytic properties of transition metal oxides for oxygen evolution reaction. *Mater, Chem, Phys.*, **1986**, *14*, 397. [https://doi.org/10.1016/0254-0584\(86\)90045-3](https://doi.org/10.1016/0254-0584(86)90045-3).
- [15] Burke, M. S.; Zou, S.; Enman, L. J.; Kellon, J. E.; Gabor, C. A.; Pledger, E.; Boettcher, S. W. Revised Oxygen Evolution Reaction Activity Trends for First-Row Transition-Metal (Oxy)hydroxides in Alkaline Media. *J. Phys. Chem. Lett.* **2015**, *6* (18), 3737–3742. <https://doi.org/10.1021/acs.jpcllett.5b01650>.
- [16] Stevens, M. B.; Enman, L. J.; Batchellor, A. S.; Cosby, M. R.; Vise, A. E.; Trang, C. D. M.; Boettcher, S. W. Measurement techniques for the study of thin film heterogeneous water oxidation electrocatalysts. *Chem. Mater.* **2017**, *29* (1), 120–140. <https://doi.org/10.1021/acs.chemmater.6b02796>.
- [17] Smith, R. D. L.; Prévot, M. S.; Fagan, R. D.; Trudel, S.; Berlinguette, C. P. Water oxidation catalysis: Electrocatalytic response to metal stoichiometry in amorphous metal oxide films containing iron, cobalt, and nickel. *J. Am. Chem. Soc.* **2013**, *135* (31), 11580–11586. <https://doi.org/10.1021/ja403102j>.

- [18] Smith, R. D. L.; Prévot, M.S.; Fagan, R.D.; Zhang, Z.; Sedach, P.A.; Jack Siu, M.K.; Trudel, S.; Berlinguette, C.P. Photochemical Route for Accessing Amorphous Metal Oxide Materials for Water Oxidation Catalysis. *Science* **2013**, *340* (April), 60–63.
- [19] Morales-Guio, C. G.; Liardet, L.; Hu, X. Oxidatively Electrodeposited Thin-Film Transition Metal (Oxy)hydroxides as Oxygen Evolution Catalysts. *J. Am. Chem. Soc.* **2016**, *138* (28), 8946–8957. <https://doi.org/10.1021/jacs.6b05196>.
- [20] Corrigan, D. A. The Catalysis of the Oxygen Evolution Reaction by Iron Impurities in Thin Film Nickel Oxide Electrodes. *J. Electrochem. Soc.* **1987**, *134* (2), 377–384. <https://doi.org/10.1149/1.2100463>.
- [21] Trotochaud, L.; Young, S. L.; Ranney, J. K.; Boettcher, S. W. Nickel-Iron oxyhydroxide oxygen-evolution electrocatalysts: The role of intentional and incidental iron incorporation. *J. Am. Chem. Soc.* **2014**, *136* (18), 6744–6753. <https://doi.org/10.1021/ja502379c>.
- [22] Kanan, M. W.; Nocera, D. G. In situ formation of an oxygen-evolving catalyst in neutral water containing phosphate and Co²⁺. *Science* (80-.). **2008**, *321* (5892), 1072–1075. <https://doi.org/10.1126/science.1162018>.
- [23] Surendranath, Y.; Kanan, M. W.; Nocera, D. G. Mechanistic studies of the oxygen evolution reaction by a cobalt-phosphate catalyst at neutral pH. *J. Am. Chem. Soc.* **2010**, *132* (46), 16501–16509. <https://doi.org/10.1021/ja106102b>.
- [24] Bajdich, M.; García-Mota, M.; Vojvodic, A.; Nørskov, J. K.; Bell, A. T. Theoretical investigation of the activity of cobalt oxides for the electrochemical oxidation of water. *J. Am. Chem. Soc.* **2013**, *135* (36), 13521–13530. <https://doi.org/10.1021/ja405997s>.
- [25] Pourbaix, M.; Zhang, H.; Pourbaix, A. Presentation of an Atlas of Chemical and Electrochemical Equilibria in the Presence of a Gaseous Phase. *Mater. Sci. Forum* **1997**, *251–254*, 143–148. <https://doi.org/10.4028/www.scientific.net/msf.251-254.143>.
- [26] Garcia-Mota, Monica; Bajdich, Michal; Viswanathan, Venkatasubramanian; Vojvodic, Aleksandra; Bell, Alexis; Korskov, J. K. Importance of Correlation in Determining Electrocatalytic Oxygen Evolution Activity on Cobalt Oxides. *J. Phys. Chem. C* **2012**, *116*, 21077–21082. <https://doi.org/10.1021/jp306303y>.
- [27] Creazzo, F.; Oxygen evolution reaction at cobalt oxides/water interfaces: heterogeneous electrocatalysis by DFT-MD simulations & metadynamics. Other. Université Paris-Saclay, **2020**
- [28] Creazzo, F.; Galimberti, D. R.; Pezzotti, S.; Gageot, M. P. DFT-MD of the (110)-Co₃O₄ cobalt oxide semiconductor in contact with liquid water, preliminary chemical and physical insights into the electrochemical environment. *J. Chem. Phys.* **2019**, *150* (4). <https://doi.org/10.1063/1.5053729>.
- [29] Deng, X.; Tüysüz, H. Cobalt-oxide-based materials as water oxidation catalyst: Recent progress and challenges. *ACS Catal.* **2014**, *4* (10), 3701–3714. <https://doi.org/10.1021/cs500713d>.
- [30] Fabbri, E.; Haberer, A.; Waltar, K.; Kötz, R.; Schmidt, T. J. Developments and Perspectives of Oxide-Based Catalysts for the Oxygen Evolution Reaction. *Catal. Sci. Technol.* **2014**, *4* (11), 3800–3821. <https://doi.org/10.1039/c4cy00669k>.

- [31] Bergmann, A.; Martinez-Moreno, E.; Teschner, D.; Chernev, P.; Gliech, M.; De Araújo, J. F.; Reier, T.; Dau, H.; Strasser, P. Reversible amorphization and the catalytically active state of crystalline Co₃O₄ during oxygen evolution. *Nat. Commun.* **2015**, *6*. <https://doi.org/10.1038/ncomms9625>.
- [32] Ortiz Peña, N.; Ihiwakrim, D.; Han, M.; Lassalle-Kaiser, B.; Carencio, S.; Sanchez, C.; Laberty-Robert, C.; Portehault, D.; Ersen, O. Morphological and Structural Evolution of Co₃O₄ Nanoparticles Revealed by in Situ Electrochemical Transmission Electron Microscopy during Electrocatalytic Water Oxidation. *ACS Nano* **2019**, *13* (10), 11372–11381. <https://doi.org/10.1021/acsnano.9b04745>.
- [33] He, S.; Huang, Y.; Huang, J.; Liu, W.; Yao, T.; Jiang, S.; Tang, F.; Liu, J.; Hu, F.; Pan, Z.; Liu, Q. Ultrathin CoOOH Oxides Nanosheets Realizing Efficient Photocatalytic Hydrogen Evolution. *J. Phys. Chem. C* **2015**, *119* (47), 26362–26366. <https://doi.org/10.1021/acs.jpcc.5b09442>.
- [34] Koza, J. A.; He, Z.; Miller, A. S.; Switzer, J. A. Electrodeposition of crystalline Co₃O₄-A catalyst for the oxygen evolution reaction. *Chem. Mater.* **2012**, *24* (18), 3567–3573. <https://doi.org/10.1021/cm3012205>.
- [35] Seo, B.; Sa, Y. J.; Woo, J.; Kwon, K.; Park, J.; Shin, T. J.; Jeong, H. Y.; Joo, S. H. Size-Dependent Activity Trends Combined with in Situ X-ray Absorption Spectroscopy Reveal Insights into Cobalt Oxide/Carbon Nanotube-Catalyzed Bifunctional Oxygen Electrocatalysis. *ACS Catal.* **2016**, *6* (7), 4347–4355. <https://doi.org/10.1021/acscatal.6b00553>.
- [36] Esswein, A. J.; Mcmurdo, M. J.; Ross, P. N.; Bell, A. T.; Tilley, T. D. Size-dependent activity of Co₃O₄ nanoparticle anodes for alkaline water electrolysis. *J. Phys. Chem. C* **2009**, *113* (33), 15068–15072. <https://doi.org/10.1021/jp904022e>.
- [37] Yeo, B. S.; Bell, A. T. Enhanced activity of gold-supported cobalt oxide for the electrochemical evolution of oxygen. *J. Am. Chem. Soc.* **2011**, *133* (14), 5587–5593. <https://doi.org/10.1021/ja200559j>.
- [38] Liu, Y. C.; Koza, J. A.; Switzer, J. A. Conversion of electrodeposited Co(OH)₂ to CoOOH and Co₃O₄, and comparison of their catalytic activity for the oxygen evolution reaction. *Electrochim. Acta* **2014**, *140*, 359–365. <https://doi.org/10.1016/j.electacta.2014.04.036>.
- [39] Jiang, H.; He, Q.; Zhang, Y.; Song, L. Structural Self-Reconstruction of Catalysts in Electrocatalysis. *Acc. Chem. Res.* **2018**, *51* (11), 2968–2977. <https://doi.org/10.1021/acs.accounts.8b00449>.
- [40] Zhang, M.; De Respinis, M.; Frei, H. Time-resolved observations of water oxidation intermediates on a cobalt oxide nanoparticle catalyst. *Nat. Chem.* **2014**, *6* (4), 362–367. <https://doi.org/10.1038/nchem.1874>.
- [41] Favaro, M.; Yang, J.; Nappini, S.; Magnano, E.; Toma, F. M.; Crumlin, E. J.; Yano, J.; Sharp, I. D. Understanding the Oxygen Evolution Reaction Mechanism on CoO_x using Operando Ambient-Pressure X-ray Photoelectron Spectroscopy. *J. Am. Chem. Soc.* **2017**, *139* (26), 8960–8970. <https://doi.org/10.1021/jacs.7b03211>.
- [42] Van Oversteeg, C. H. M.; Doan, H. Q.; De Groot, F. M. F.; Cuk, T. In situ X-ray absorption spectroscopy of transition metal based water oxidation catalysts. *Chem. Soc. Rev.* **2017**, *46* (1), 102–125. <https://doi.org/10.1039/c6cs00230g>.

- [43] Choi, Y. W.; Mistry, H.; Roldan Cuenya, B. New insights into working nanostructured electrocatalysts through operando spectroscopy and microscopy. *Curr. Opin. Electrochem.* **2017**, *1* (1), 95–103. <https://doi.org/10.1016/j.coelec.2017.01.004>.
- [44] Risch, M.; Ringleb, F.; Kohlhoff, M.; Bogdanoff, P.; Chernev, P.; Zaharieva, I.; Dau, H. Water oxidation by amorphous cobalt-based oxides: In situ tracking of redox transitions and mode of catalysis. *Energy Environ. Sci.* **2015**, *8* (2), 661–674. <https://doi.org/10.1039/c4ee03004d>.
- [45] Risch, M.; Khare, V.; Zaharleva, I.; Gerencser, L.; Chernev, P.; Dau, H. Cobalt-oxo core of a water-oxidizing catalyst film. *J. Am. Chem. Soc.* **2009**, *131* (20), 6936–6937. <https://doi.org/10.1021/ja902121f>.
- [46] Kanan, M. W.; Yano, J.; Surendranath, Y.; Dincă, M.; Yachandra, V. K.; Nocera, D. G. Structure and valency of a cobalt-phosphate water oxidation catalyst determined by in situ X-ray spectroscopy. *J. Am. Chem. Soc.* **2010**, *132* (39), 13692–13701. <https://doi.org/10.1021/ja1023767>.
- [47] Bergmann, A.; Jones, T. E.; Martinez Moreno, E.; Teschner, D.; Chernev, P.; Gliech, M.; Reier, T.; Dau, H.; Strasser, P. Unified structural motifs of the catalytically active state of Co(oxyhydr)oxides during the electrochemical oxygen evolution reaction. *Nat. Catal.* **2018**, *1* (9), 711–719. <https://doi.org/10.1038/s41929-018-0141-2>.
- [48] Feng, C.; Faheem, M. B.; Fu, J.; Xiao, Y.; Li, C.; Li, Y. Fe-Based Electrocatalysts for Oxygen Evolution Reaction: Progress and Perspectives. *ACS Catal.* **2020**, *10* (7), 4019–4047. <https://doi.org/10.1021/acscatal.9b05445>.
- [49] Smith, R. D. L.; Pasquini, C.; Loos, S.; Chernev, P.; Klingan, K.; Kubella, P.; Mohammadi, M. R.; Gonzalez-Flores, D.; Dau, H. Spectroscopic identification of active sites for the oxygen evolution reaction on iron-cobalt oxides. *Nat. Commun.* **2017**, *8* (1). <https://doi.org/10.1038/s41467-017-01949-8>.
- [50] Enman, L. J.; Stevens, M. B.; Dahan, M. H.; Nellist, M. R.; Toroker, M. C.; Boettcher, S. W. Operando X-Ray Absorption Spectroscopy Shows Iron Oxidation Is Concurrent with Oxygen Evolution in Cobalt–Iron (Oxy)hydroxide Electrocatalysts. *Angew. Chemie - Int. Ed.* **2018**, *57* (39), 12840–12844. <https://doi.org/10.1002/anie.201808818>.
- [51] Zhou, J.; Wang, Y.; Su, X.; Gu, S.; Liu, R.; Huang, Y.; Yan, S.; Li, J.; Zhang, S. Electrochemically accessing ultrathin Co (oxy)-hydroxide nanosheets and: Operando identifying their active phase for the oxygen evolution reaction. *Energy Environ. Sci.* **2019**, *12* (2), 739–746. <https://doi.org/10.1039/c8ee03208d>.
- [52] Xiao, Z.; Huang, Y. C.; Dong, C. L.; Xie, C.; Liu, Z.; Du, S.; Chen, W.; Yan, D.; Tao, L.; Shu, Z.; Zhang, G.; Duan, H.; Wang, Y.; Zou, Y.; Chen, R.; Wang, S. Operando Identification of the Dynamic Behavior of Oxygen Vacancy-Rich Co₃O₄ for Oxygen Evolution Reaction. *J. Am. Chem. Soc.* **2020**, *142* (28), 12087–12095. <https://doi.org/10.1021/jacs.0c00257>.
- [53] Wang, H. Y.; Hung, S. F.; Chen, H. Y.; Chan, T. S.; Chen, H. M.; Liu, B. In Operando Identification of Geometrical-Site-Dependent Water Oxidation Activity of Spinel Co₃O₄. *J. Am. Chem. Soc.* **2016**, *138* (1), 36–39. <https://doi.org/10.1021/jacs.5b10525>.

- [54] Tung, C. W.; Hsu, Y. Y.; Shen, Y. P.; Zheng, Y.; Chan, T. S.; Sheu, H. S.; Cheng, Y. C.; Chen, H. M. Reversible adapting layer produces robust single-crystal electrocatalyst for oxygen evolution. *Nat. Commun.* **2015**, *6*, 1–9. <https://doi.org/10.1038/ncomms9106>.
- [55] Chang, C. J.; Zhu, Y.; Wang, J.; Chen, H. C.; Tung, C. W.; Chu, Y. C.; Chen, H. M. In situ X-ray diffraction and X-ray absorption spectroscopy of electrocatalysts for energy conversion reactions. *J. Mater. Chem. A* **2020**, *8* (37), 19079–19112. <https://doi.org/10.1039/d0ta06656g>.
- [56] Reikowski, F.; Maroun, F.; Pacheco, I.; Wiegmann, T.; Allongue, P.; Stettner, J.; Magnussen, O. M. Operando Surface X-ray Diffraction Studies of Structurally Defined Co₃O₄ and CoOOH Thin Films during Oxygen Evolution. *ACS Catal.* **2019**, *9* (5), 3811–3821. <https://doi.org/10.1021/acscatal.8b04823>.
- [57] Libuda, J.; Schauermaun, S.; Laurin, M.; Schalow, T.; Freund, H. J. Model Studies in Heterogeneous Catalysis. From Structure to Kinetics. *Monatshefte fur Chemie* **2005**, *136* (1), 59–75. <https://doi.org/10.1007/s00706-004-0249-8>.
- [58] Weber, M. L.; Gunkel, F. Epitaxial Catalysts for Oxygen Evolution Reaction: Model Systems and Beyond. *JPhys Energy* **2019**, *1* (3). <https://doi.org/10.1088/2515-7655/ab1577>.
- [59] Grumelli, D.; Wiegmann, T.; Barja, S.; Reikowski, F.; Maroun, F.; Allongue, P.; Balajka, J.; Parkinson, G. S.; Diebold, U.; Kern, K.; Magnussen, O. M. Electrochemical Stability of the Reconstructed Fe₃O₄ (001) Surface. *Angew. Chemie* **2020**, *132* (49), 22088–22092. <https://doi.org/10.1002/ange.202008785>.
- [60] Brummel, O.; Libuda, J. Electrifying Oxide Model Catalysis: Complex Electrodes Based on Atomically-Defined Oxide Films. *Catal. Letters* **2020**, *150* (6), 1546–1560. <https://doi.org/10.1007/s10562-019-03078-x>.
- [61] Faisal, F.; Bertram, M.; Stumm, C.; Cherevko, S.; Geiger, S.; Kasian, O.; Lykhach, Y.; Lytken, O.; Mayrhofer, K. J. J.; Brummel, O.; Libuda, J. Atomically Defined Co₃O₄(111) Thin Films Prepared in Ultrahigh Vacuum: Stability under Electrochemical Conditions. *J. Phys. Chem. C* **2018**, *122* (13), 7236–7248. <https://doi.org/10.1021/acs.jpcc.8b00558>.
- [62] Walton, A. S.; Fester, J.; Bajdich, M.; Arman, M. A.; Osiecki, J.; Knudsen, J.; Vojvodic, A.; Lauritsen, J. V. Interface Controlled Oxidation States in Layered Cobalt Oxide Nanoislands on Gold. *ACS Nano* **2015**, *9* (3), 2445–2453. <https://doi.org/10.1021/acsnano.5b00158>.
- [63] Fester, J.; Walton, A.; Li, Z.; Lauritsen, J. V. Gold-Supported Two-Dimensional Cobalt Oxyhydroxide (CoOOH) and Multilayer Cobalt Oxide Islands. *Phys. Chem. Chem. Phys.* **2017**, *19* (3), 2425–2433. <https://doi.org/10.1039/c6cp07901f>.
- [64] Fester, J.; Makoveev, A.; Grumelli, D.; Gutzler, R.; Sun, Z.; Rodríguez-Fernández, J.; Kern, K.; Lauritsen, J. V. The Structure of the Cobalt Oxide/Au Catalyst Interface in Electrochemical Water Splitting. *Angew. Chemie - Int. Ed.* **2018**, *57* (37), 11893–11897. <https://doi.org/10.1002/anie.201804417>.
- [65] Müllner, M.; Riva, M.; Kraushofer, F.; Schmid, M.; Parkinson, G. S.; Mertens, S. F. L.; Diebold, U. Stability and Catalytic Performance of Reconstructed Fe₃O₄ (001) and Fe₃O₄ (110) Surfaces during Oxygen Evolution Reaction. *J. Phys. Chem. C* **2019**, *123* (13), 8304–8311. <https://doi.org/10.1021/acs.jpcc.8b08733>.

- [66] Jurca, H. F.; Damian, A.; Gougoud, C.; Thiaudière, D.; Cortès, R.; Maroun, F.; Allongue, P. Epitaxial Electrodeposition of Fe on Au(111): Structure, Nucleation, and Growth Mechanisms. *J. Phys. Chem. C* **2016**, *120* (29), 16080–16089. <https://doi.org/10.1021/acs.jpcc.5b12771>.
- [67] Allongue, P.; Maroun, F.; Jurca, H. F.; Tournerie, N.; Savidand, G.; Cortès, R. Magnetism of Electrodeposited Ultrathin Layers: Challenges and Opportunities. *Surf. Sci.* **2009**, *603* (10–12), 1831–1840. <https://doi.org/10.1016/j.susc.2008.11.040>.
- [68] Allongue, P.; Cagnon, L.; Gomes, C.; Gündel, A.; Costa, V. Electrodeposition of Co and Ni/Au(1 1 1) Ultrathin Layers. Part I: Nucleation and Growth Mechanisms from in Situ STM. *Surf. Sci.* **2004**, *557* (1–3), 41–56. <https://doi.org/10.1016/j.susc.2004.03.016>.
- [69] Gudavarthy, R. V.; Gorantla, S.; Mu, G.; Kulp, E. A.; Gemming, T.; Eckert, J.; Switzer, J. A. Epitaxial Electrodeposition of Fe₃O₄ on Single-Crystal Ni(111). *Chem. Mater.* **2011**, *23* (8), 2017–2019. <https://doi.org/10.1021/cm2002176>.
- [70] Kulp, E. A.; Kothari, H. M.; Limmer, S. J.; Yang, J.; Gudavarthy, R. V.; Bohannon, E. W.; Switzer, J. A. Electrodeposition of Epitaxial Magnetite Films and Ferrihydrite Nanoribbons on Single-Crystal Gold. *Chem. Mater.* **2009**, *21* (21), 5022–5031. <https://doi.org/10.1021/cm9013514>.

Chapter 2: Experimental and methods

2.1 Samples preparation

In this work, different types of oxides have been studied: cobalt oxides, iron oxides and mixed cobalt-iron oxides. Each type of oxide may be prepared either by direct oxide electrodeposition on a single crystal substrate or by anodic oxidation of a metal layer, itself electrodeposited on the substrate.

Substrate preparation and chemicals

The substrate is a top hat-shaped Au(111) single crystal (MaTeck) with an orientation uncertainty of $<0.1^\circ$. Before deposition, it is cleaned in a 1:2 mixture of 30 % H_2O_2 and 96 % H_2SO_4 (both *Carlo Erba*, RSE) and then flame-annealed using a butane torch.

$\text{Co}(\text{NO}_3)_2$ (*Merck*, $> 99.0\%$), L-tartrate (*Sigma-Aldrich*, ACS reagent, $> 99.5\%$), NaOH (*Merck*, ACS reagent, Fe content $< 0.00005\%$), Triethanolamine (*Sigma Aldrich*, assay $\geq 99\%$, Co and Fe contents $\leq 1\text{ mg/kg}$), FeCl_3 (*Sigma-Aldrich*, reagent grade $\geq 98\%$), CoCl_2 (*Sigma-Aldrich*, ACS reagent 99-102 %, Fe content $\leq 50\text{ mg/kg}$), FeSO_4 (*Sigma Aldrich*, ACS reagent $\geq 99\%$), CoSO_4 (*Merck*, assay $\geq 99\%$, Fe content $< 0.0005\%$), NaClO_4 (ACS reagent $\geq 98\%$, Co and Fe contents respectively $\leq 5\text{ mg/kg}$ and $\leq 3\text{ mg/kg}$) and Milli-Q water are used to prepare deposition solutions.

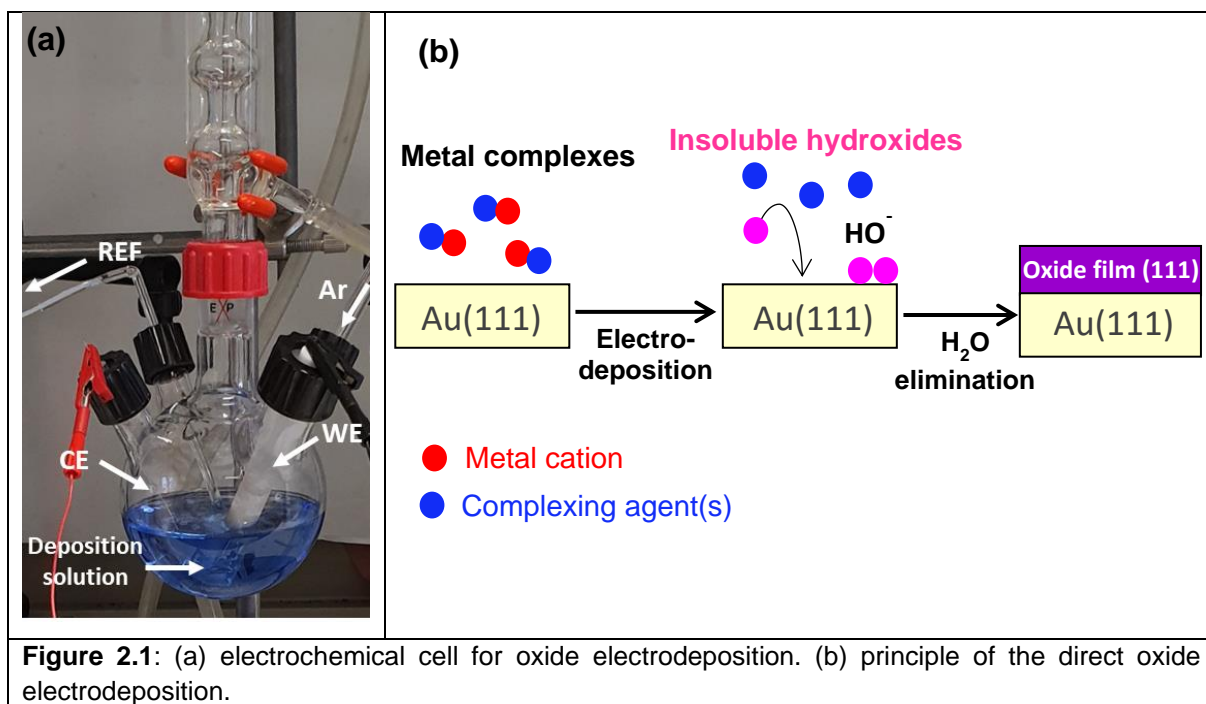
Pellets made of Co_3O_4 , CoO, Fe_3O_4 , Fe_2O_3 and FeO commercial powders (5% metal powder 95% cellulose in weight, *Sigma-Aldrich*, 99.5 %) are used as reference samples for XANES.

Direct oxide electrodeposition on Au(111)

For this one step electrodeposition synthesis, the deposition solution is placed in an electrochemical reflux cell, shown in **Fig 2.1a**. The working electrode is the Au(111) substrate, positioned in a sample holder, so as to expose the top (111) surface and the vertical edges to the solution. A Pt wire serves as counter electrode and a Mercury Sulphate Electrode (MSE) reference electrode is connected to the cell. A reflux column is mounted on top of the cell, since the electrodeposition should take place at reflux temperature in order to increase the crystallinity of the deposits. The deposition is performed under argon atmosphere (solution purging for more than 30 minutes) in order to prevent oxygen presence in the solution that could oxidize cobalt or iron ions in solution.

To prepare the deposition solution, a solution containing a metallic (Co/Fe) salt and a complexing agent is added to a NaOH basic solution. The principle of the direct oxide

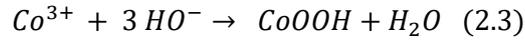
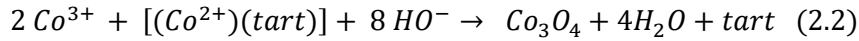
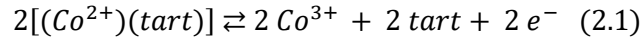
electrodeposition is illustrated in **Fig.2.1b**. The metal complex(es) formed in the deposition solution is oxidized (anodic electrodeposition) or reduced (cathodic electrodeposition) when applying a potential at the electrode. This destabilizes the metal complex and the oxidized/reduced cations precipitate at the substrate surface in the presence of HO^- ions, forming an oxide. After deposition, the sample holder is removed from the cell and the sample is rinsed with milli Q-water to remove electrolyte drying on the sample surface with the formation of NaOH crystals.



The deposition conditions (salt, complexing agent, concentrations, deposition potentials, temperature) depend on the type of oxide we want to synthesize. They are summarized below for each oxide type.

- **Cobalt oxides**

The anodic deposition process is adapted from the one used by Switzer et al. for the growth of Co_3O_4 [15]. A solution containing 1 mM $\text{Co}(\text{NO}_3)_2$ (metallic salt) and 1.2 mM L-tartrate (tart, complexing agent) is added to an alkaline NaOH solution. Depending on the NaOH concentration, we found that one can either obtain the cobalt oxide Co_3O_4 (for 1M NaOH) or the cobalt oxyhydroxide CoOOH (for 5M NaOH). The metallic complex is oxidized by applying at the electrode a potential of $-0.55V_{\text{MSE}}$ for Co_3O_4 and $-0.5V_{\text{MSE}}$ for CoOOH . The complex is destabilized and the oxidized cations precipitate at the surface to form a deposit. Switzer et al. proposed a two step mechanism shown in (2.1) – (2.2). In the case of CoOOH , we suggest a two step mechanism also given by (2.1) – (2.3).

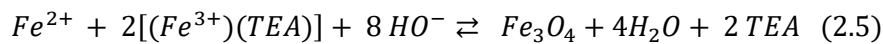
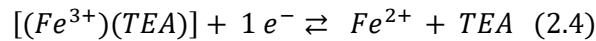


The deposition is stopped after a charge of a few mC (1 to 10 generally) is passed, resulting in oxide layers 5 to 40 nm thick.

For intermediate NaOH concentrations, the deposition often yields two mixed phases containing both CoOOH and Co₃O₄. Increasing the deposition potential may affect the crystallinity and the grains morphology of the deposits. These aspects are examined in details in the PhD thesis of Ivan Pacheco Bubi.

- **Pure iron oxide**

Iron oxide Fe₃O₄ is obtained by direct cathodic electrodeposition, using a process adapted from Switzer et al. [16]. A solution containing 10 mM FeCl₃ (metallic salt) and 12 mM Triethanolamine (TEA, complexing agent) is added to a basic solution of 2M NaOH. Once the deposition solution temperature is stabilized at 80°C, the metallic complex is reduced to Fe²⁺ by applying a potential of -1.41VMSE at the electrode. The complex is destabilized and the reduced cations precipitate at the surface to form a deposit, supposedly according to the mechanism given in (2.4) and (2.5).



The deposition is stopped after a charge of a few mC (5 to 20 generally) is passed, resulting in oxide layers 15 to 50 nm thick.

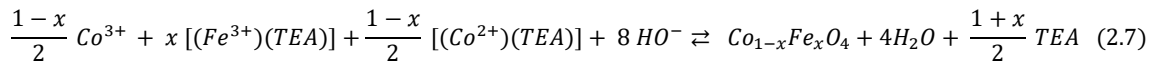
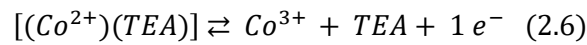
- **Mixed cobalt iron oxides**

Mixed cobalt iron oxides (Co_{1-x}Fe_xO_y) can be obtained by either cathodic or anodic processes using CoCl₂ and FeCl₃ as metallic salts and TEA as complexing agent in an alkaline NaOH solution. The cathodic deposition process is adapted from the work of Switzer et al. [17] while the anodic process was developed in our group during the PhD of Ivan Pacheco-Bubi. Both processes lead to deposits with a low coverage on a Au(111) substrate. The cathodic route allows growing Fe rich mixed oxides, while the anodic one allows growing Co-rich mixed oxides.

The anodic process is compatible with deposition on an oxyhydroxide CoOOH buffer layer which greatly improves the growth modes of Co_{1-x}Fe_xO_y because continuous and relatively flat

thin films are obtained in this case. Unfortunately, the cathodic route is not compatible with use of a CoOOH buffer layer as substrate. These findings are examined in details in the PhD thesis of Ivan Pacheco Bubi.

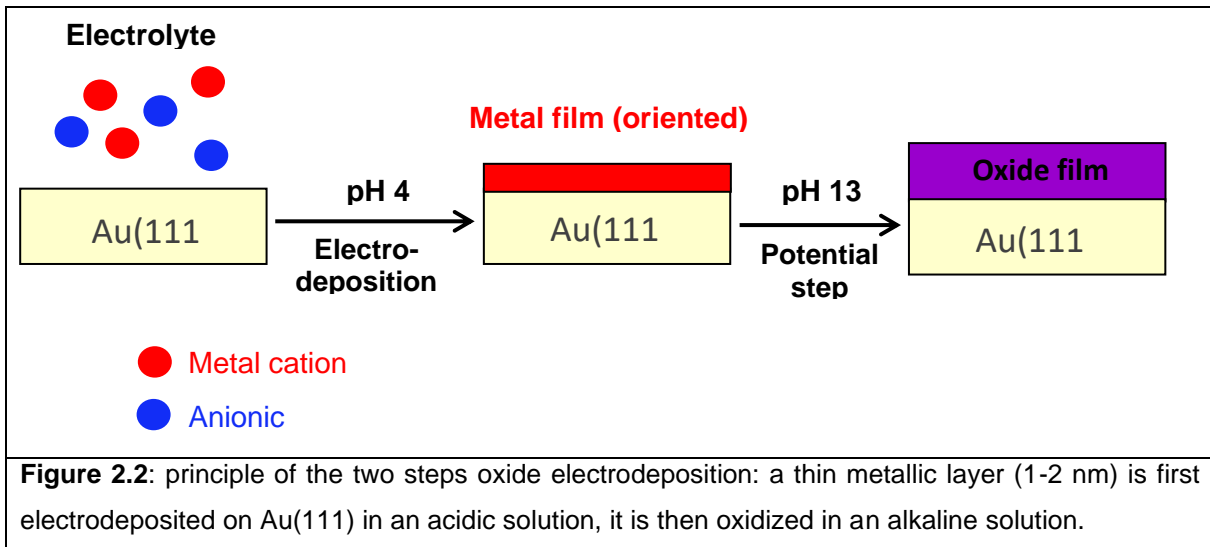
All $Co_{1-x}Fe_xO_y$ oxides presented in this work are actually bilayers $Co_{1-x}Fe_xO_y/CoOOH$ deposited on Au(111) using the anodic electrodeposition method. The concentration of $CoCl_2$ and $FeCl_3$ in the deposition solution varies between 1 and 2 mM; TEA concentration is set to be in slight excess compared to the metallic salts and a 1M NaOH solution is used. The metallic complex is oxidized by applying at the electrode a potential of $-0.5V_{MSE}$. The oxidation and precipitation of the oxide at the surface of the working electrode is supposedly occurring according to the mechanisms in (2.6) - (2.7).



The deposition is stopped after a charge of a charge of 15 to 30 mC is passed, resulting in oxide layers 10 to 40 nm thick.

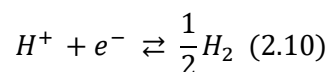
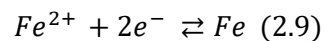
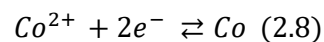
Anodic oxides films on Au(111)

The sample preparation is a two-step process. The principle of the procedure is illustrated in **Fig. 2.2**. The Au(111) substrate surface is in contact with a solution containing metallic salt(s), a supporting electrolyte and which pH is adjusted to 3.5 - 4. The metal cations are reduced when applying a potential at the electrode, and migrate to the working electrode where they deposit as an epitaxial metallic film. The cell is then flushed with a pH 4 metal free electrolyte solution to remove any traces of the metal cations. Next, an alkaline 0.1 M NaOH solution (pH 13) is introduced in the cell. These steps are performed under potential control in order to keep the film metallic. The latter is then oxidized by stepping the potential at $0.4V_{Ag/AgCl}$ in pH 13 electrolyte, resulting in an oxide thin film that is not crystalline. All solutions are kept under argon atmosphere. In practice, the preparation is conducted at the beamline in the electrochemical cell used for XAS/XRD measurements (see **Fig.2.16**), which allows characterizing the epitaxial metal layer before its anodic oxidation.



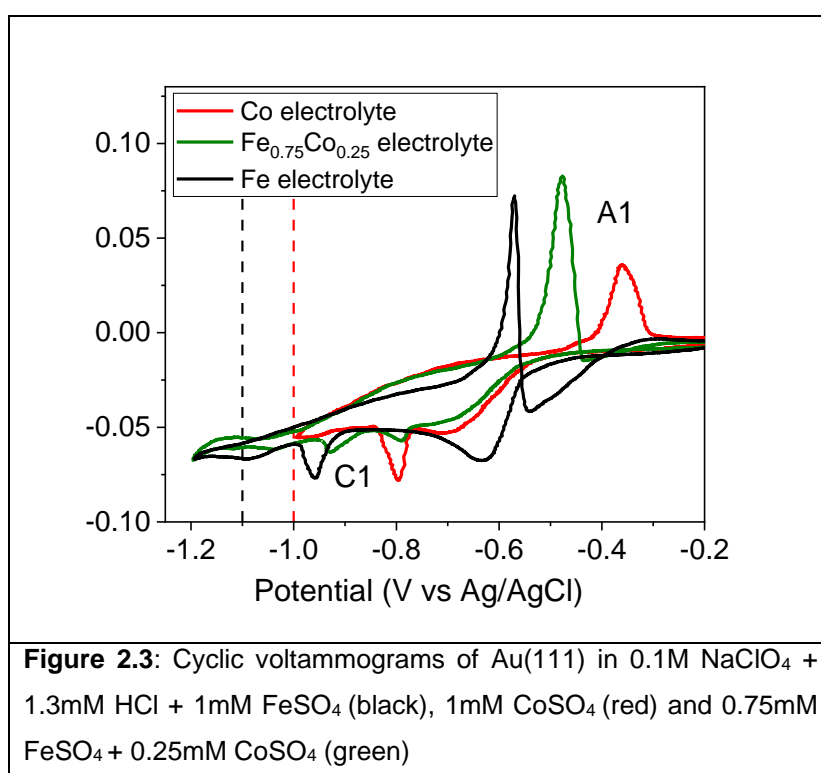
The deposition conditions (concentrations, deposition potentials) depend on the type of oxide we want to synthesize. The deposition solution contains x mM FeSO_4 and $1-x$ mM CoSO_4 with x in $[0-1]$ corresponding to the desired Co/Fe ratio in the metal film. 0.1 M NaClO_4 and 1.3 mM HCl are also present in the solution, to ensure the conductivity of the solution and adjust its pH to 3.5-4.

Cyclic voltammograms of Au(111) in $0.1\text{MNaClO}_4 + 1.3\text{mMHCl} + 1\text{mM FeSO}_4$ (black), 1mM CoSO_4 (red) and $0.75\text{mM FeSO}_4 + 0.25\text{mM CoSO}_4$ (green) are shown in **Fig.2.3**. The CVs present one main cathodic peak C1 between $\sim -0.8 V_{\text{Ag}/\text{AgCl}}$ (Co electrolyte) and $-0.95 V_{\text{Ag}/\text{AgCl}}$ (Fe electrolyte) and one anodic peak which position varies between $\sim -0.6 V_{\text{Ag}/\text{AgCl}}$ (Fe electrolyte) and $-0.35 V_{\text{Ag}/\text{AgCl}}$ (Co electrolyte). They correspond to Co/Fe deposition on the negative sweep and Co/Fe dissolution on the positive sweep proceeding according to (2.8) and (2.9). The cathodic wave around $-0.7V_{\text{Ag}/\text{AgCl}}$ stands for the hydrogen evolution reaction (2.10) [18-19].



For the deposition of metallic films, the deposition potential is chosen negative to the cathodic peak, as shown by the dashed line on the figure (red: Co films, black: Fe containing films). Co films are electrodeposited at $-1.0 V_{\text{Ag}/\text{AgCl}}$ and Fe containing films are electrodeposited at $-1.1V_{\text{Ag}/\text{AgCl}}$. The deposit thickness depends on the deposition time. It is calibrated in a trial and error procedure by performing deposition/dissolution routines and calculating the charge under the metal dissolution peak A1. This allows to deposit metallic layers of a chosen thickness. In

general, a few (3 to 8) metal monolayers were electrodeposited for deposition times of 20 to 100 seconds. For Co films, the deposition is stopped by stepping the potential at $-0.7 \text{ V}_{\text{Ag}/\text{AgCl}}$ where the film is stable against dissolution. This potential is kept during the exchange with Co free electrolyte and it is shifted to $-0.9 \text{ V}_{\text{Ag}/\text{AgCl}}$ after introducing NaOH solution. In the case of Fe containing films, the deposition is stopped by manually exchanging the solution to Co/Fe free electrolyte while the potential is kept at -1.1 V because stepping to a higher potential might dissolve the film. The NaOH solution is introduced at this same potential and the membrane of the cell is installed at the end of the exchange with NaOH solution. All films are oxidized by stepping the potential to $0.4 \text{ V}_{\text{Ag}/\text{AgCl}}$ while the membrane is inflated.



2.2 SXRD: methodology and data treatment

In X-ray Diffraction experiments, a crystalline material is illuminated with a monochromatic X-ray beam of wavelength λ . Since X-rays wavelength is in the same order of magnitude as the interatomic distances in crystals, interferences of scattered rays occur, leading to a pattern of measured intensity from which the crystal structure can be reconstructed. The XRD background given in this section is mainly based on [2]-[4].

Diffraction conditions

Let us consider a crystal, made of periodical blocks of atoms repeated in space. The smallest repeating block of atoms that enables to reconstruct the crystal is the crystal unit cell. It is defined as a parallelepiped and six lattice parameters that are shown on **Fig.2.4**: the lengths of the unit cell a , b , c and the angles between them α , β , γ . The crystal lattice may be reconstructed by infinite repetition of the unit cell.

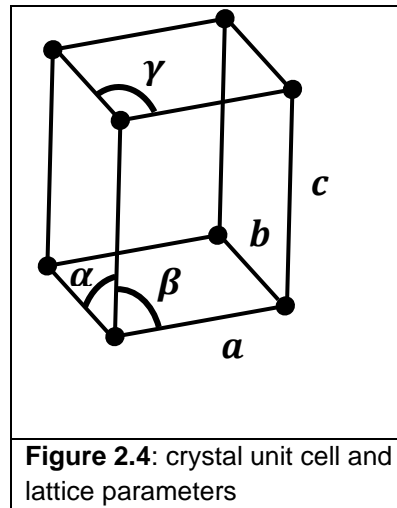


Figure 2.4: crystal unit cell and lattice parameters

The crystal is made of different set of atom planes of different orientations. The orientation of a plane is described by three Miller indices h, k, l . A plane identified as (h, k, l) intercepts the three points a/h , b/k and c/l (or a multiple integer of it). The interatomic distance between each (h, k, l) plane is d_{hkl} .

In XRD experiment, it is convenient to use the reciprocal space, instead of the real space described above. The crystal reciprocal lattice is obtained by Fourier transform of the crystal real space lattice. For a unit cell of volume V , the reciprocal lattice unit cell parameters are: $a^* = \frac{b^*c}{V}$, $b^* = \frac{a^*c}{V}$, $c^* = \frac{b^*a}{V}$. Each set of (h, k, l) planes in the real lattice correspond to one (h, k, l) 3D point in reciprocal space and the distance d_{hkl}^* between two (h, k, l) points in the reciprocal space is $d_{hkl}^* = \frac{1}{d_{hkl}}$.

Each of the 3D (h, k, l) points of the reciprocal space has its own intensity that depends on the electronic density around the atoms of the planes. The reciprocal lattice of a crystal can be visualized as 3D map of the reciprocal space.

Figure 2.5a shows a scheme of the scattering geometry for an XRD experiment. The incident X-ray beam of wavelength λ can be described by a wave vector \vec{k}_i along the incident beam direction, which magnitude is $\frac{2\pi}{\lambda}$. The scattered beam of same magnitude (elastic scattering is

supposed in our experiments) propagates in the direction \vec{k}_f . The scattering vector \vec{q} is defined as $\vec{q} = \vec{k}_f - \vec{k}_i$. For \vec{k}_f to have a significant intensity, \vec{k}_i and \vec{k}_f should interfere constructively. The condition for this is that \vec{q} equals a reciprocal lattice vector of the crystal ie $\vec{q} = h\vec{a}^* + k\vec{b}^* + l\vec{c}^*$. This is the Laue condition.

This condition can be illustrated by the Ewald construction shown in **Fig.2.5b**. It allows to determine which lattice planes will give a diffracted signal for a given incident beam of wavelength λ . The Ewald sphere in reciprocal space contains the origin of the reciprocal lattice and has a radius $\frac{1}{\lambda}$. It is the location of all possible extremities of $\vec{q} = \vec{k}_f - \vec{k}_i$ vector for all scattered beam directions possible. (h, k, l) diffraction peaks will be observed only if the sphere cuts through a point (h, k, l) of the reciprocal lattice.

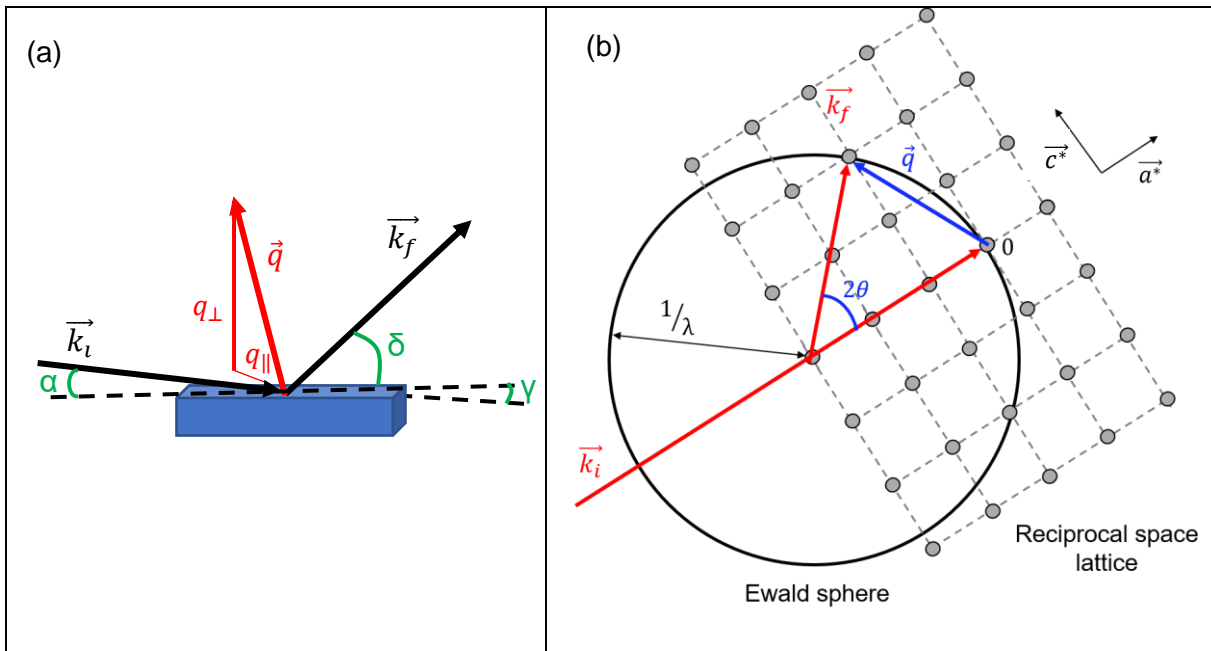


Figure 2.5: (a) scattering geometry for XRD measurements \vec{k}_i , is the incident X-ray beam wave vector and \vec{k}_f the scattered wave vector. The scattering vector \vec{q} is defined as $\vec{q} = \vec{k}_f - \vec{k}_i$ and can be decomposed into out-of-plane q_{\perp} and in plane q_{\parallel} contributions. (b) Ewald construction that shows the planes for which a diffracted signal can be measured for a given wavelength λ .

As illustrated in **Fig.2.5b**, if the angle between \vec{k}_f and \vec{k}_i is 2θ , θ is the incidence angle and the magnitude of \vec{q} is $\frac{2 \sin(\theta)}{\lambda}$. If the diffraction conditions are fulfilled, the magnitude of the scattering vector \vec{q} is also d_{hkl}^* which leads to Bragg's law: $\lambda = 2 \sin(\theta) d_{hkl}$.

Laboratory XRD experiment often consist in measuring the diffracted intensity during θ - 2θ scans. The detector has a circular trajectory cutting through the (h, k, l) points of the reciprocal space that are along the c^* direction, which means that it probes the (h, k, l) planes parallel to

the surface of the sample. The resulting XRD pattern shows a peak of measured intensity when the detector passes through a reciprocal lattice point.

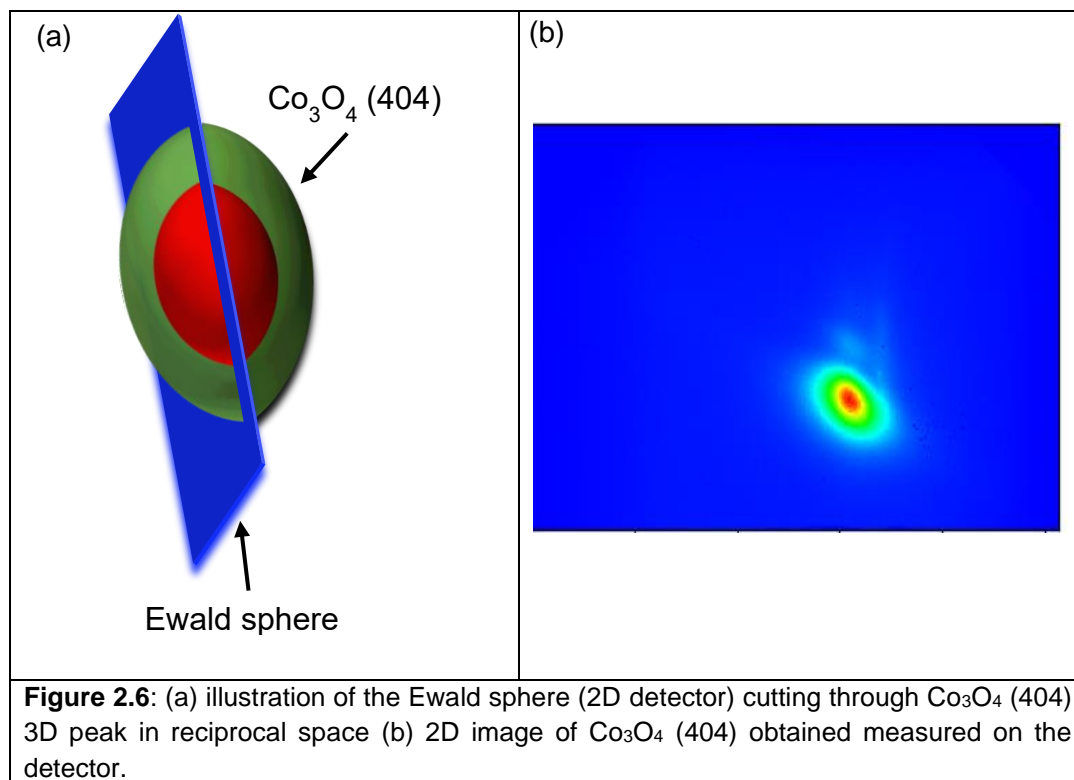
In the SXRD experiments we performed at synchrotron beamlines, a 2D detector is used to measure the diffracted intensity signal. For an incident X-ray beam of fixed wavelength λ , the detector is moved along the Ewald sphere in order to access the different Bragg peaks of the crystal. Each Bragg peak corresponds to one detector-sample position and to one (h, k, l) set of planes. In order to do so, the 2D detector is mounted on a diffractometer arm that has two degrees of freedom, that are defined by the angles δ (detector height) and γ (detector azimuth angle) (see **Fig.2.5a**). The third degree of freedom is given by the sample's rotation around its normal, defined by the angle φ , and the X-ray beam hits the sample with an angle of incidence α . A Bragg peak position corresponds to a given 2D detector position identified by a set of $(\alpha, \gamma, \delta, \varphi)$ values. For example, for an incident X-ray beam of wavelength $\lambda = 0.661 \text{ \AA}$ and an incident angle $\alpha = 0.4^\circ$, $\text{Co}_3\text{O}_4(404)$ peak can be found at: $\delta = 22.4^\circ$ and $\gamma = 15.4^\circ$ while φ depends on the sample alignment. When the detector is placed at the position of the Bragg peak, the recorded signal will be a cut through the 3D (h, k, l) point in the reciprocal space, as illustrated in **Fig.2.6a**. The detector thus gives a 2D cut of the reciprocal space (**Fig.2.6b**) and the diffraction pattern of the whole crystal can be interpreted as a 3D map of the reciprocal space lattice.

The smaller λ the more diffracted planes are accessible, and the smaller the radius of curvature of the Ewald sphere is. In SXRD measurements, λ is chosen small which means a high energy X-ray beam, so that the sphere might be approximated as a flat plane cutting through the Bragg peaks.

During experiments at the beamline and for a posteriori data analysis, previous considerations are used to convert from angle space (angles of the detector arm, as shown in **Fig.2.5a**) to reciprocal space and from detector raw pixel data to q space. **Figure 2.5a** shows that the scattering vector \vec{q} might be decomposed into two components: its in plane projection q_{\parallel} and its out of plane projection q_{\perp} . The 2D cut of the peak imaged on the detector can be described in terms of q_{\parallel} and q_{\perp} coordinates. These transformations are operated by a Python software developed by colleagues at Kiel university, together with the data treatment procedure described in the following section. I used this software for SXRD experiments analysis and a similar software in Labview language written by Fouad Maroun for combined SXR and XAS operando measurements analysis.

The samples studied during SXR measurements are all deposited on a Au(111) substrate. It is convenient to use the hexagonal reciprocal lattice of Au(111) to express the positions of the

oxides peaks. The (h, k, l) reciprocal space in the Au(111) coordinate system is used at the beamline to navigate into the reciprocal space and access the Bragg peaks.



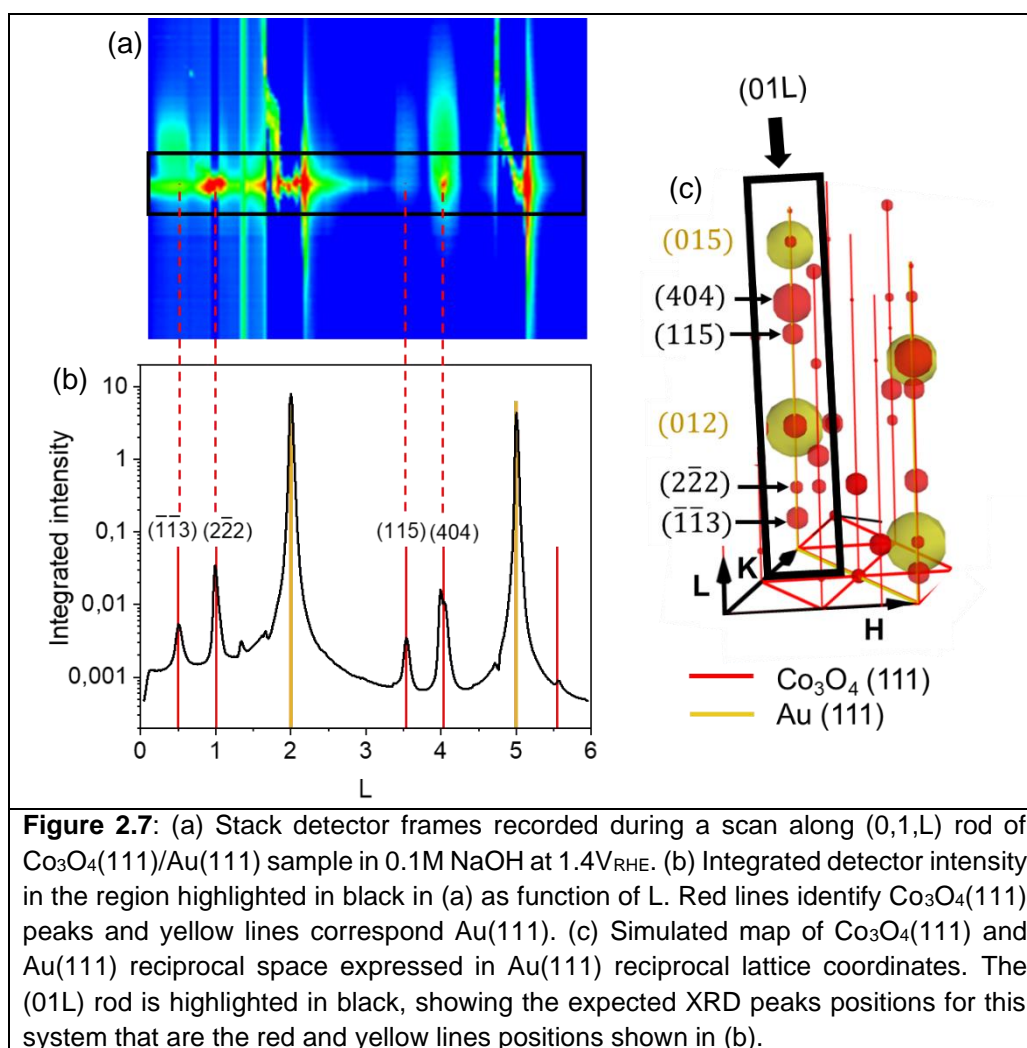
SXRD measurements and data treatment

In this work, two main type of measurement have been performed at SXRD beamlines. They are described below.

- **L-scans**

This type of measurement aims at studying the structure of the deposits by imaging slices of the reciprocal space. For this, the detector is moved along one of the reciprocal space coordinates, for example along the L axis at fixed H and K values, and 2D images are recorded every 0.02 L step. The latter measurement will be referred as L-scans in the following. **Figure 2.7** illustrates the result of a $(0,1,L)$ scan for $\text{Co}_3\text{O}_4(111)/\text{Au}(111)$ sample recorded at $1.4V_{\text{RHE}}$ in 0.1M NaOH. All 351 raw images of the scan have been stacked to reconstruct the 3D representation of the $(0,1,L)$ rod shown in **(a)**. To prevent damaging the detector, automatic attenuators are used during the scan, which explains the sudden decrease/increase in intensity in the images around intense Au(111) peaks. To extract useful information from this scan, it is convenient to represent the integrated intensity on the region of interest of the detector (represented as a black square on **Fig.2.7a**) as a function of L and correct for the attenuator

values, as illustrated in **Fig.2.7b**. The obtained experimental diffraction pattern can be compared with the expected L position of the $\text{Co}_3\text{O}_4(111)$ and $\text{Au}(111)$ Bragg peaks. The reciprocal space simulation of such system is shown on **Fig.2.7c**. The $(0,1,L)$ rod is highlighted in black and the different diffraction peaks expected are given. The hexagonal $\text{Au}(111)$ reciprocal space coordinate system is used but the indices of the Bragg peaks of Co_3O_4 refers to the conventional cubic unit cell. Red spheres stand for $\text{Co}_3\text{O}_4(111)$ and yellow one for $\text{Au}(111)$. Four intense $\text{Co}_3\text{O}_4(111)$ peaks and 2 $\text{Au}(111)$ peaks are expected. Their positions are indexed with the same colours on **Fig.2.7b**.



- **Operando monitoring of Bragg peaks**

For these measurements, the detector is fixed and positioned at a Bragg peak position. Peaks such as $\text{Co}_3\text{O}_4(404)$ or (113) and $\text{CoOOH}(105)$ or (107) are chosen for they present a sufficiently large intensity and are accessible at the working energy.

Chapter 2

The aim of the measurement is to determine the dependence with potential of the oxide structure. The principle and methods are the same as the ones described in [5]. Images of the 2D Bragg peak are recorded every second during a cyclic voltammogram at 5 or 10 mV/s. The in plane and out-of-plane strains ε_{\parallel} and ε_{\perp} are derived from the peak in-plane and out-of-plane positions. Their expression is given in (2.11) and (2.12) with $q_{\parallel,th}$ and $q_{\perp,th}$ the peak positions that correspond to the literature value of the lattice parameter of the studied oxide.

$$\varepsilon_{\parallel} = \frac{q_{\parallel,th} - q_{\parallel}}{q_{\parallel}} \quad (2.11)$$

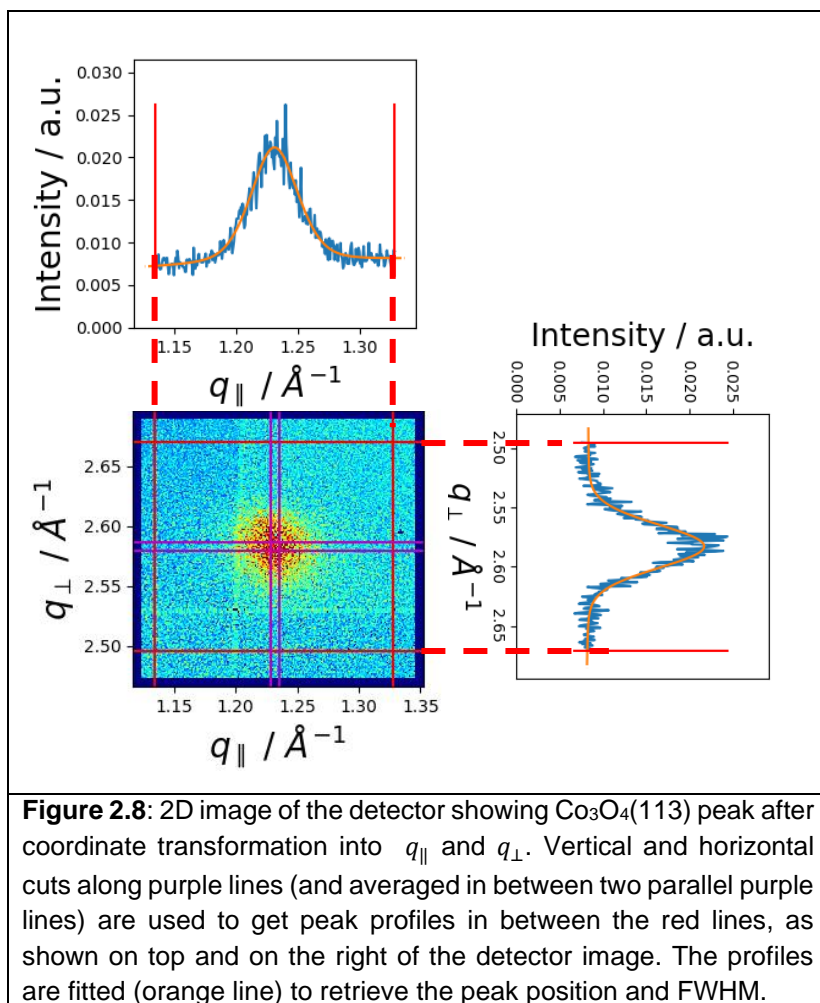
$$\varepsilon_{\perp} = \frac{q_{\perp,th} - q_{\perp}}{q_{\perp}} \quad (2.12)$$

The in plane and out-of-plane coherence lengths d_{\parallel} and d_{\perp} are derived from the in plane and out-of-plane full width at half maximum $FWHM_{\parallel}$ and $FWHM_{\perp}$ of the peak, as give equations (2.13) and (2.14). The coherence lengths d_{\perp} and d_{\parallel} respectively provide the average height and width of the crystallites forming the films.

$$d_{\perp} = \frac{2\pi}{FWHM_{\perp}} \quad (2.13)$$

$$d_{\parallel} = \frac{2\pi}{FWHM_{\parallel}} \quad (2.14)$$

To extract these parameters from the detector 2D frames, fits of peak profiles from cuts along the out-of-plane and in-plane directions are performed for each image. The process is illustrated in **Fig.2.8**: out-of-plane and in-plane cuts are averaged over 10 detector pixel rows, these are the rows in between the two purple lines for each direction. The peak profiles are the resulting averaged detector intensities along q_{\parallel} and q_{\perp} for pixels in between the red lines (top and right plots on **Fig.2.8**). The peak profiles are then fitted by Lorentzian, Gaussian or pseudo-Voigt functions, from which the peak position and the FWHM of the peaks are extracted and used to calculate ε and d .



In the following, we will especially focus on the in-plane and out-of-plane relative changes in strain and crystallite sizes during potential sweeps. The changes are relative to the strain or coherence length value measured at the lowest potential of the sweep and will be referred as $\Delta d_{\perp}, \Delta d_{\parallel}, \Delta \varepsilon_{\perp}$ and $\Delta \varepsilon_{\parallel}$. Since detector and sample are fixed during these measurements, the resolution of this method allows detection of relative strain changes in the order of $\sim 10^{-4}$ and ~ 0.1 nm for crystallite size changes.

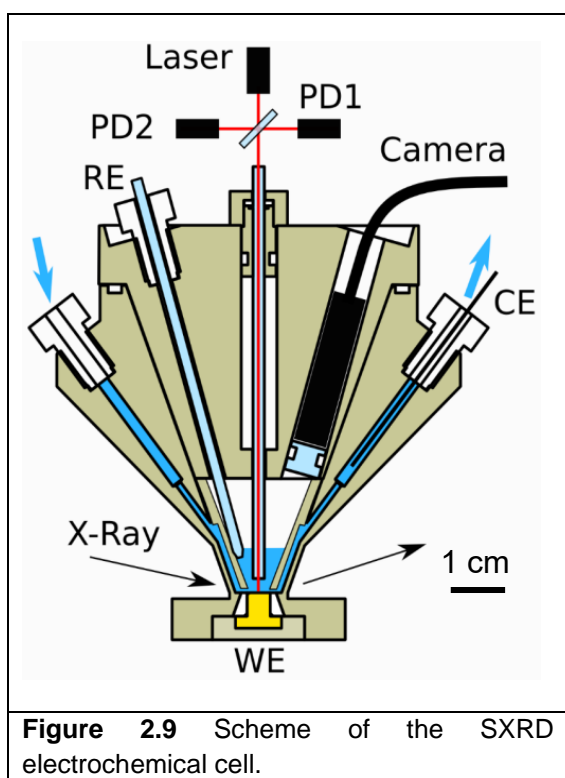
Operando SXR D measurements: setup and procedure

Operando SXR D measurements were performed at two different beamlines:

- at ESRF synchrotron, ID03 beamline (photon energy 22.5 keV, photon flux 4×10^{11} counts/s, beam size 250 μm width \times 30 μm height)
- at DESY synchrotron, P23 beamline (photon energy 18 keV, photon flux 2×10^{13} counts/s, beam size 200 μm width \times 10 μm height).

SXR D characterizations are performed in an electrochemical cell dedicated to in situ characterizations that was designed and built by Finn Reikowski from Kiel University [5]. The

potential was controlled with a potentiostat using a Ag/AgCl reference electrode and a Pt wire as counter electrode. All potentials are quoted against the relative hydrogen electrode (RHE) potential. The electrolyte circulation is controlled by a remote pump system that allows a controlled and continuous electrolyte flux within the cell (circulation speed from 5 to 500 $\mu\text{L/s}$). **Figure 2.9** shows a scheme of the SXRD cell (vertical cut) that highlights its different components. The Au(111) substrate on which an oxide film is electrodeposited (WE) is placed at the bottom of the cell. It is sealed with a Teflon cone so that only the top (111) surface is in contact with the electrolyte that flows from left to right (blue arrows) via the pump system. The reference electrode (RE) is put inside a glass capillary to prevent electrolyte contamination and the counter electrode is placed at the electrolyte outlet to avoid contamination. The cell is equipped with an optical reflectivity system (laser and photodiodes) that does not perturb the measurements. Finally, a camera is used to check the effective operation of the cell: detect leaks, verify that the sample's surface and the reference electrode are in contact with the electrolyte or monitor the formation of O_2 bubbles at the sample's surface at higher OER current.



The X-ray path is shown with black arrows on **Fig.2.9**. In this zone, the X-ray beam goes through a 1 mm thick cell wall. The cell is made of PEEK, which is stable in the presence of X-rays and which attenuation length is slightly higher to that of water [1]. At an incident X-ray energy of 18 keV, the attenuation length of water/PEEK is 11 mm and the path of the beam through the PEEK and the electrolyte layer is ~ 7 mm (the wall of the cell is 1 mm thick). This

results in an acceptable intensity loss due to cell and electrolyte absorption, making it possible to have a free electrolyte surface on top of the sample. In this cell, electrochemical measurements at high OER currents can be performed, especially since the electrolyte circulation can minimize O_2 bubbles accumulation at the sample surface. It can also remove radicals that may be formed by the incident X-ray beam.

Figure 2.10a shows a picture of the setup used for operando XRD measurements at P23 beamline. The cell was mounted on a heavy load six-circle diffractometer, and a 2D LAMBDA 750k GaAs detector was used to monitor X-ray diffraction signal. The picture focuses on the cell described above, together with the remote pump system connected to the reservoirs. The whole setup is mounted on a hexapod that serves for sample alignment. A light blue arrow shows the direction of the incident X-ray beam. The 2D XRD detector is out the picture field, it is mounted on the diffractometer arm visible at the back of the picture. **Fig.2.10b** pictures a scheme of the scattering geometry, showing how the angles α , δ , γ and φ are defined. For measurements at grazing incidence, α was fixed either at 0.34° or 1° .

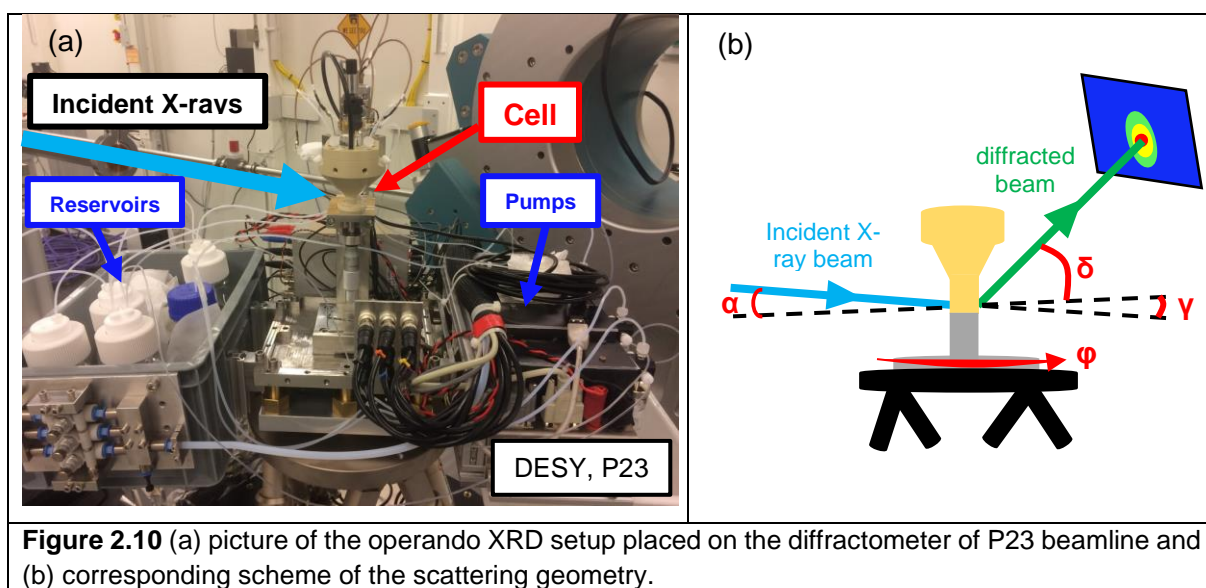


Figure 2.10 (a) picture of the operando XRD setup placed on the diffractometer of P23 beamline and (b) corresponding scheme of the scattering geometry.

During the experiment, the samples are mounted in air in the SXRD cell and aligned in order to be centered into the X-ray beam. X-ray reflectivity and L-scans are first performed in air to establish the material phase and orientation. The sample is then put in contact with the electrolyte and potential control is established at $1.4V_{RHE}$ (within the potential stability domains of the studied oxides). The electrolyte is a 0.1M NaOH solution (pH 13) kept under Argon atmosphere, that is typically exchanged at a rate of $5 \mu\text{L/s}$, using the remote-controlled pump system. The same structural characterizations are performed again at $1.4V_{RHE}$ in 0.1M NaOH to make sure of the stability of the sample in the experimental conditions. Next, the structural changes during potential sweeps are determined from the changes of a Bragg peak. For SXRD measurements, images of the 2D Bragg peak are recorded every 1 second during a cyclic

voltammogram at 10 or 5 mV/s. For combined XAS/XRD measurements at DiffAbs beamline (SOLEIL), the integration time of the 2D images of Bragg peaks is 5 seconds, which is fast enough to monitor the structural changes while sweeping the applied potential at a rate of 5 mV/s.

2.3 X-Ray Absorption Spectroscopy: methodology and data treatment

In X-ray Absorption Spectroscopy experiments, a material is illuminated with an X-ray beam which energy is swept. The absorption of X-rays of specific energy by the material is investigated. The XAS background in this section is based on [6]-[9].

X-ray Absorption Spectroscopy: principle

Figure 2.11 illustrates XAS principle. It first involves the excitation of a core electron which can be promoted into an unoccupied atomic or molecular level or to an unbound state, the continuum. This transition is created by the absorption of an X-ray photon which energy is set to the ionization energy of the core electron. Each atom has its own corresponding ionization energy, which makes XAS an atom specific method. A de-excitation follows the absorption of the core electron that has left a core-hole. The latter is filled by a higher-level core electron and a fluorescent X-ray or Auger electron is emitted. The fluorescent X-ray energy is equal to the difference between the two core levels of the atom, while the Auger photoelectron is promoted to the continuum.

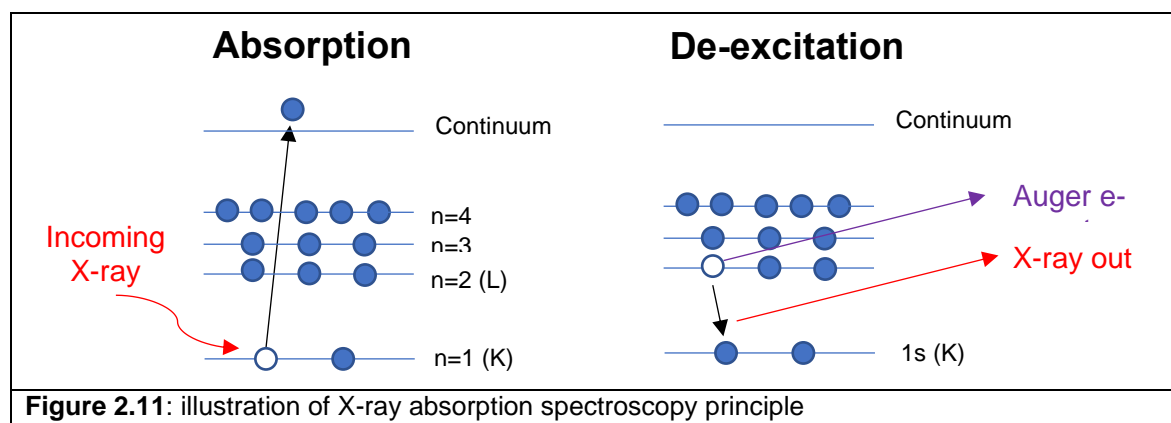


Figure 2.12a shows the basic experimental configuration for XAS measurements. The sample is illuminated with an X-ray beam which intensity I_0 is recorded. Either the transmitted I_t or fluorescent I_f X-rays intensity are measured while the incident X-ray energy is varied in the energy region of interest. For a sample of thickness t , Beer Lambert's law can be applied: $\ln\left(\frac{I_0}{I_t}\right) = \mu t$. For dilute or thin samples, the absorption coefficient μ is proportional to the ratio

of fluorescence and incident X-rays: $\mu(E) \sim \frac{I_f}{I_0}$. XAS spectra show the absorption coefficient intensity as a function of the photon energy.

All the XAS measurements presented in this work were recorded in fluorescence mode. This means that a fluorescence detector was placed near the sample (see Figure 2.1) and fluorescence spectra were recorded every 5 seconds while increasing the incident X-ray energy. **Figure 2.12b** shows an example of fluorescence spectrum recorded during the experiment. The left peak located at 6.9 keV corresponds to Co K-alpha fluorescent line and the right peak comes from the incident X-ray beam. For each energy, the Cobalt peak area (grey shaded area on the spectrum) is integrated. It is then divided by the intensity of the incident X-ray to give a XAS spectrum: $\mu = f(E)$.

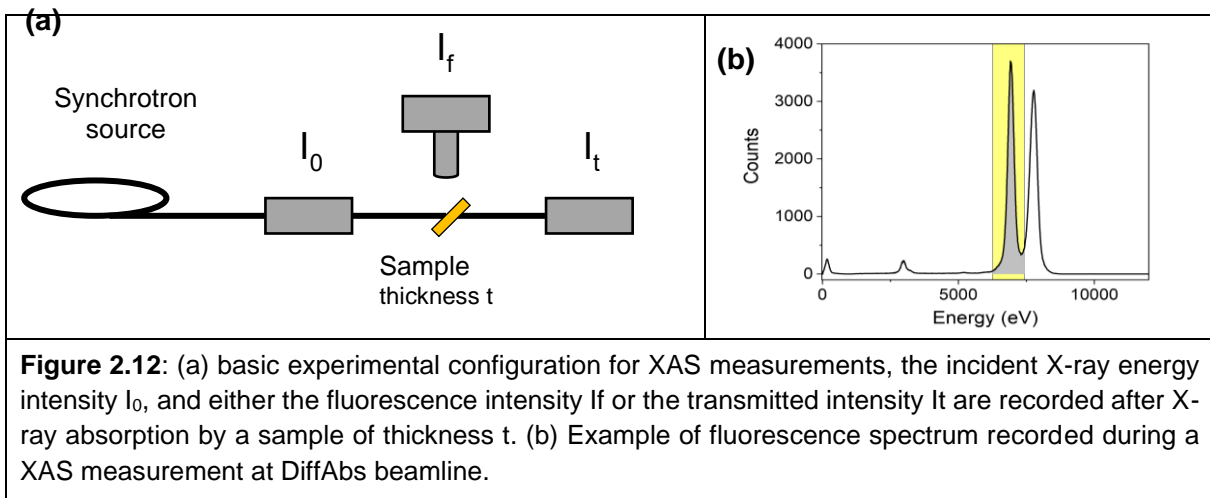
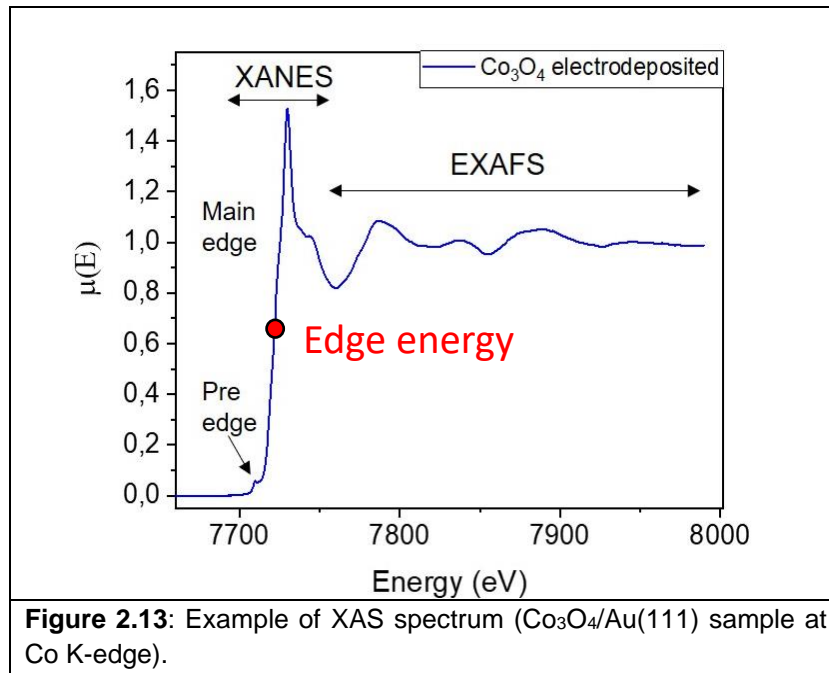


Figure 2.13 shows an example of XAS spectrum of a $\text{Co}_3\text{O}_4/\text{Au}(111)$ sample, recorded at Co K-edge. The word K-edge is used to characterize an excited electron which belongs to the K-shell. A XAS spectrum is composed of two energy regions: the XANES region (X-ray Absorption Near Edge Structure, at ± 50 eV around the edge energy) and the EXAFS region (Extended X-ray Absorption Fine Structure, 50 to 1000 eV above the edge). As shown in **Fig.2.13**, the XANES region is generally composed of a pre-edge which precedes a main absorption edge. An absorption edge occurs when a core electron absorbs an amount of energy higher or equal to its binding energy: it goes from core level to continuum.

The EXAFS region presents oscillations, they give information about the local structure around the probed atom type. During the XAS process, the ejection of a core electron in the continuum is followed by the emission and a photo-electron. This photoelectron can be scattered by neighbouring atoms. The outgoing and scattered waves will interfere, resulting in constructive and destructive interferences. This will make the probability of absorption to oscillate.



In the following we will mainly be interested in the edge energy of the XANES spectra. Indeed, the edge energy is sensitive to the formal oxidation state of the element probed. The more oxidized is the element the higher is its edge energy, since it is more difficult to remove a core electron from an oxidized species. The pre-edge shape is sensitive to site coordination and disorder.

Normalization of XANES spectra

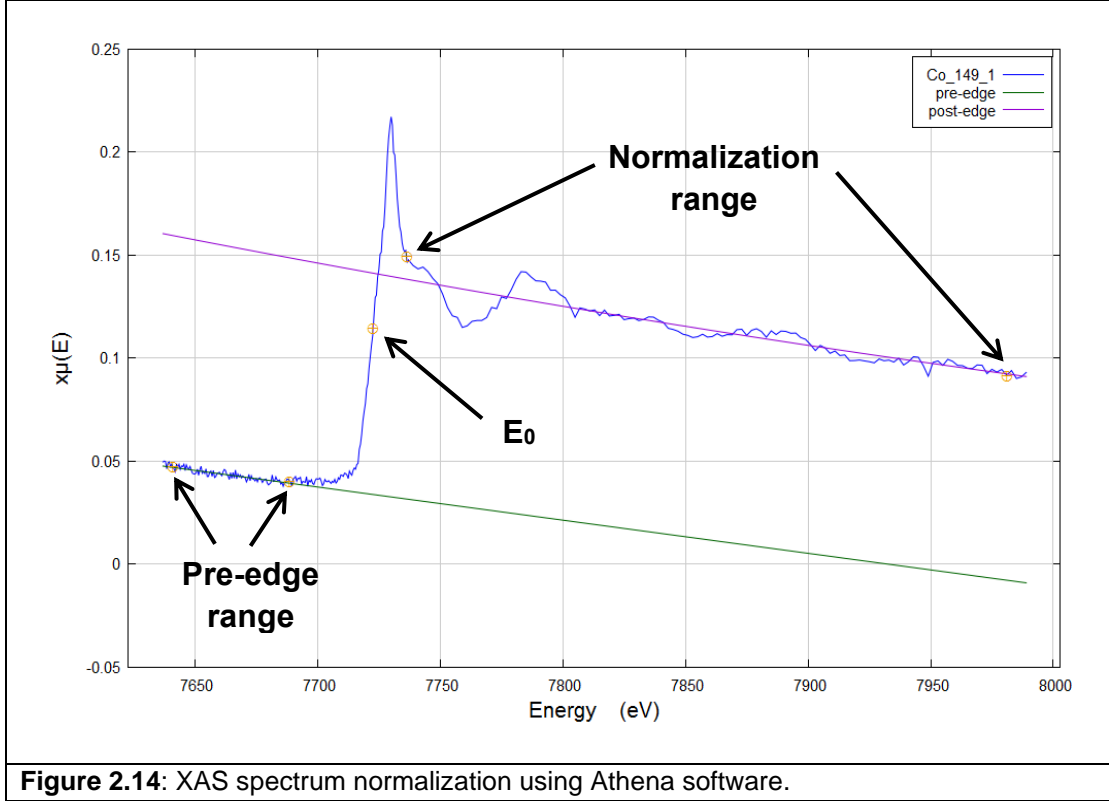
XANES spectra were recorded at Co K-edge between 7.64 keV and 7.82 keV and at Fe K-edge between 7.05 keV and 7.23 keV. Raw spectra need to be normalized and baseline corrected before data analysis. Athena software was used for this [10]. As shown in **Fig.2.14**, a pre-edge (green line), defined as a linear background in the pre-edge energy range is first subtracted to the spectrum. Then, a post-edge (purple line) is subtracted to the spectrum. It is defined as a spline background in the range of the spectrum located after the edge (this approximates the background in this range with an adjustable function defined by a polynomial expression which order can be chosen between 1 and 3). For both the pre-edge and post-edge, the user determines the range boundaries (orange points in **Fig.2.14**) to define the slope of the function. E_0 is the edge energy, it can be firstly approximated by the maximum of the first derivative of the spectrum or as the energy at half height of the edge.

The spectrum is then normalized by the software using a normalization constant $\mu_0(E_0)$ calculated as:

$$\mu_0(E_0) = \text{Post edge function}(E_0) - \text{Pre edge function}(E_0) \quad (2.15)$$

The normalization constant is used to calculate the normalized spectrum $\mu(E)_{normalized}$:

$$\mu(E)_{normalized} = \frac{\mu(E)_{raw} - (pre\ edge\ function + post\ edge\ function)}{\mu_0(E_0)} \quad (2.16)$$



With the normalized spectrum, the K-edge energy E_{edge} is determined using the integral method [11] according to Eq. (2.17) where μ_1 and μ_2 define the edge region boundaries in the normalized XANES spectrum. We used $\mu_1 = 0.15$ and $\mu_2 = 1$ to avoid contributions respectively from the pre-peak and absorption peak.

$$E_{edge} = \frac{1}{\mu_2 - \mu_1} \int_{\mu_1}^{\mu_2} E(\mu) d\mu \quad (2.17)$$

For some spectra in Chapter 5 that present a high pre-peak contribution, the lower boundary μ_1 was changed to 0.35 in order to avoid this contribution.

Co and Fe oxidation state calibration

In order to link E_{edge} and the Co/Fe oxidation states (hereafter called α), XANES spectra of reference samples are recorded. We use Co_3O_4 , CoO , FeO , Fe_3O_4 and Fe_2O_3 commercial powders diluted in cellulose (5% in weight) and pressed as pellets. The obtained XAS spectra are corrected for self-absorption and the corresponding edge energy is determined using the

method described above in order to establish a calibration plot that links α and the Co/Fe edge energy.

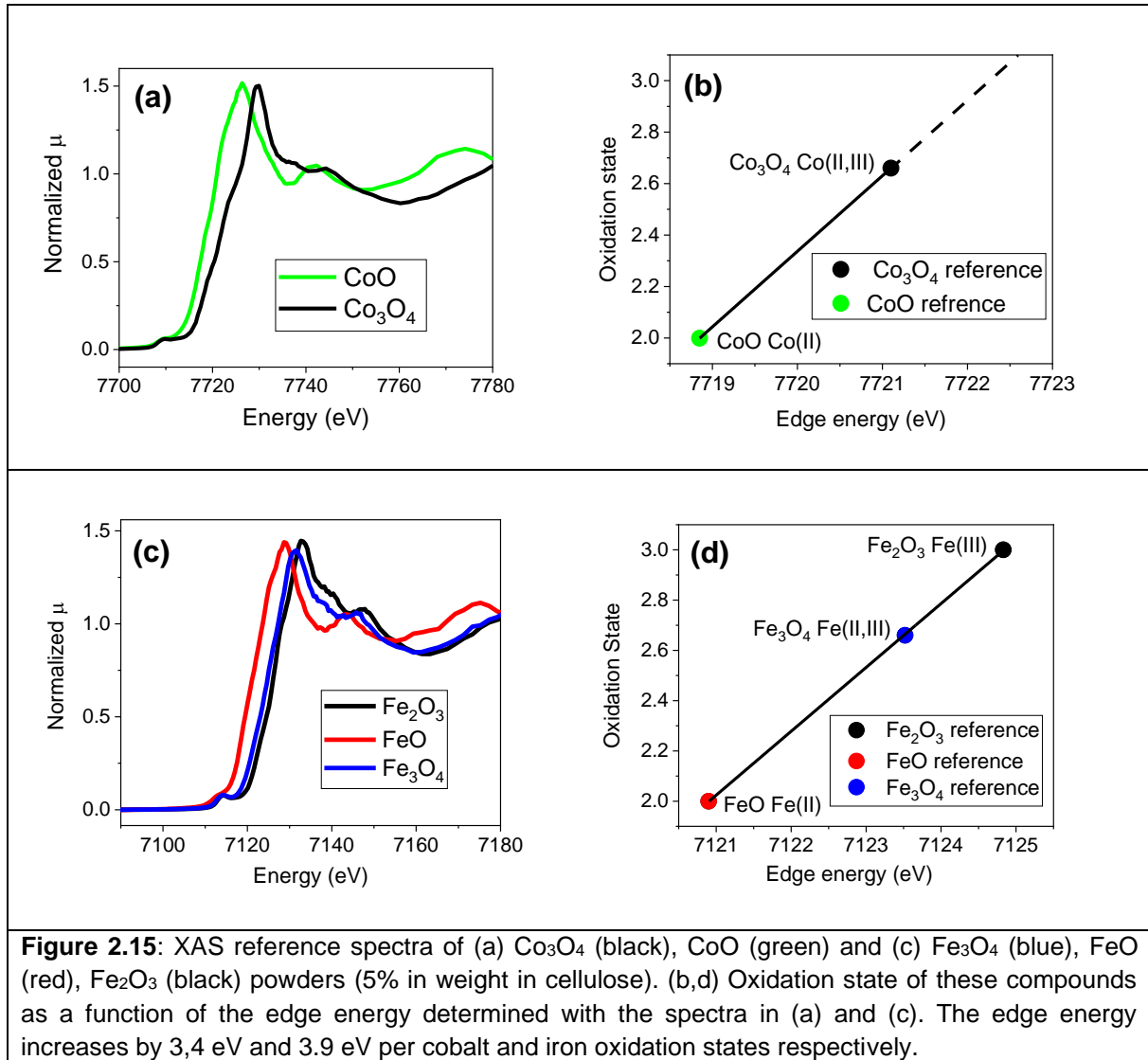


Figure 2.15a shows the Co K-edge XANES spectra of CoO (green line) and Co_3O_4 (black line), which edge energy E_{edge} is determined with the integral method: $E_{edge} = 7718.85 \text{ eV}$ for CoO (Co oxidation state +2) and $E_{edge} = 7721.1 \text{ eV}$ for Co_3O_4 (oxidation state 2.66). **Figure 2.15b** is a plot of the Co oxidation state as a function of E_{edge} . The inverse of the slope gives a 3.4 eV increase per cobalt oxidation state. This plot is used to convert the experimentally measured E_{edge} of deposits into an average Co oxidation state. The same process is used for Fe oxidation state: Fe_2O_3 (black), Fe_3O_4 (blue) and FeO (black) Fe K-edge XANES spectra presented in **Fig.2.15c** respectively give $E_{edge} = 7124.83 \text{ eV}$ (Fe +3), 7123.52 eV (Fe +2.66) and 7120.9 eV (Fe +2). The plot in **Fig.2.15d** results in a 3.9 eV increase per Fe oxidation state.

The K-edge shift per oxidation state for Co and Fe is in relatively good agreement with values found in the literature using the same edge determination method. A 2.3 eV/oxidation state shift and 4.6 eV/oxidation state for Co and Fe K-edge are respectively found by Dau and co-workers [12], [13], while Calvillo et al. found 3.0 eV/oxidation state for Co and 3.5 eV/oxidation state for Fe [20]. Using the same data processing for EXAFS spectra of similar oxides available on IXAS XAFS database [14] yields shifts between 2.5 and 5 eV/oxidation state for Co K-edge and between 4 and 5.5 eV/oxidation state for Fe K-edge. The measured value of the shift might depend on the energy calibration of the beamline, the purity and dilution of the compound (accuracy of the compound oxidation state, auto-absorption correction). Since we rely on the latter parameter for our measurements, that give calibration close to other experimental values, the calibrations obtained with the plots shown in **Fig2.15** will be used for the following.

Cell and setup for operando measurements

Operando XAS and XRD studies were performed at SOLEIL DiffAbs beamline using a photon energy between 7 keV and 8 keV, and a beam size of 250x300 μm^2 . The electrochemical cell used for operando XAS/XRD measurements had been previously designed and built in PMC lab for similar operando studies [19]. **Figure 2.16** displays a scheme (vertical cut) of this electrochemical cell. A Teflon cone is protecting the side walls of the Au crystal to only expose its top (111) surface (WE). The sample and its cone are mounted on a support which height is adjustable. The counter and reference electrodes are placed above the inlet and outlet of the cell. The geometry of the cell differs from the SXRD one because we use a smaller X-ray energy and the electrolyte attenuation length is smaller. At 8 keV, the X-ray attenuation length by water is ca. 1mm [1]. As a consequence, it is important to minimize the electrolyte thickness in order to have a strong enough X-ray signal and a good sensibility. In the XAS cell, a 12 μm extendable polypropylene foil is fixed on top of the sample to close the cell. The inlet and outlet of the cell are connected to reservoirs and the remote-controlled pump system is used to fill/empty the cell (total volume ~5 mL). The electrolyte layer thickness above the sample is monitored by adding or removing small electrolyte quantities (50 to 200 μL) to the cell which inflates or deflates the membrane. The inflated state is represented with the black dashed line and the deflated state corresponds to the black plane line. The X-ray path is shown with black arrows. During the experiments, the state (deflated or inflated) of the membrane was monitored using an external camera in the beamline hutch. In the XAS cell, electrochemical measurements may be performed with or without the polypropylene foil. Measurements without the polymer membrane allow higher OER currents and better electrochemical conditions since the electrolyte layer on top of the sample is thicker. However, for operando measurements combining XAS and XRD, the electrochemical measurements have to be performed with the polymer window on.

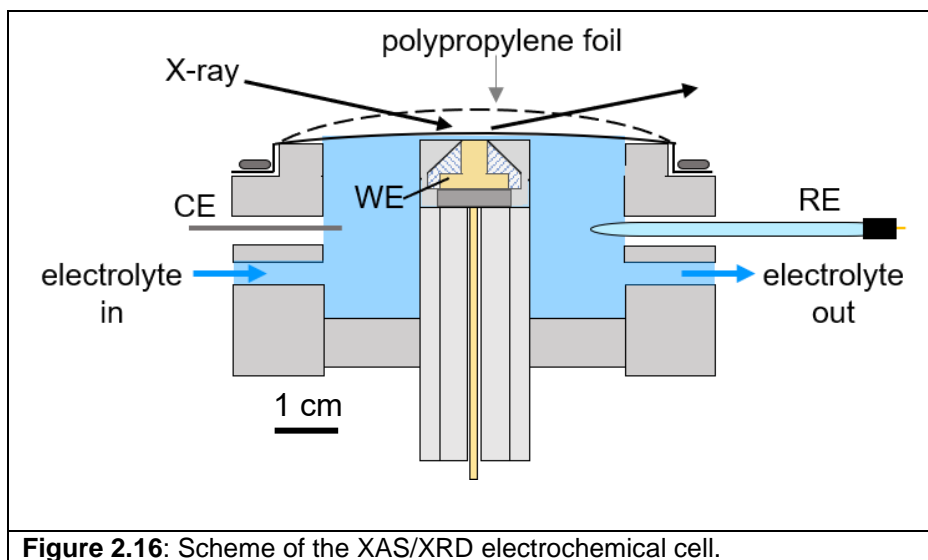


Figure 2.16: Scheme of the XAS/XRD electrochemical cell.

Figure 2.17a shows the setup (cell, reservoirs, pumps) mounted on the beamline 6 circles diffractometer in kappa geometry. As also depicted on the scheme of **Fig.2.17b**, the sample surface is horizontal and aligned parallel to the incident X ray beam prior to the measurements. XAS measurements were performed in fluorescence mode using a 4-element SDD fluorescence detector placed just above the sample surface at 90° with respect to the incident X ray beam. For XRD measurements, a 2D detector XPAD S140 was used to capture the diffraction peaks. The XRD detector angles are defined in the same manner as for the SXRD cell in **Fig2.10b**. A fixed incidence angle α of 4° was used for XRD and XAS measurements maximizing the footprint of the beam on the sample.

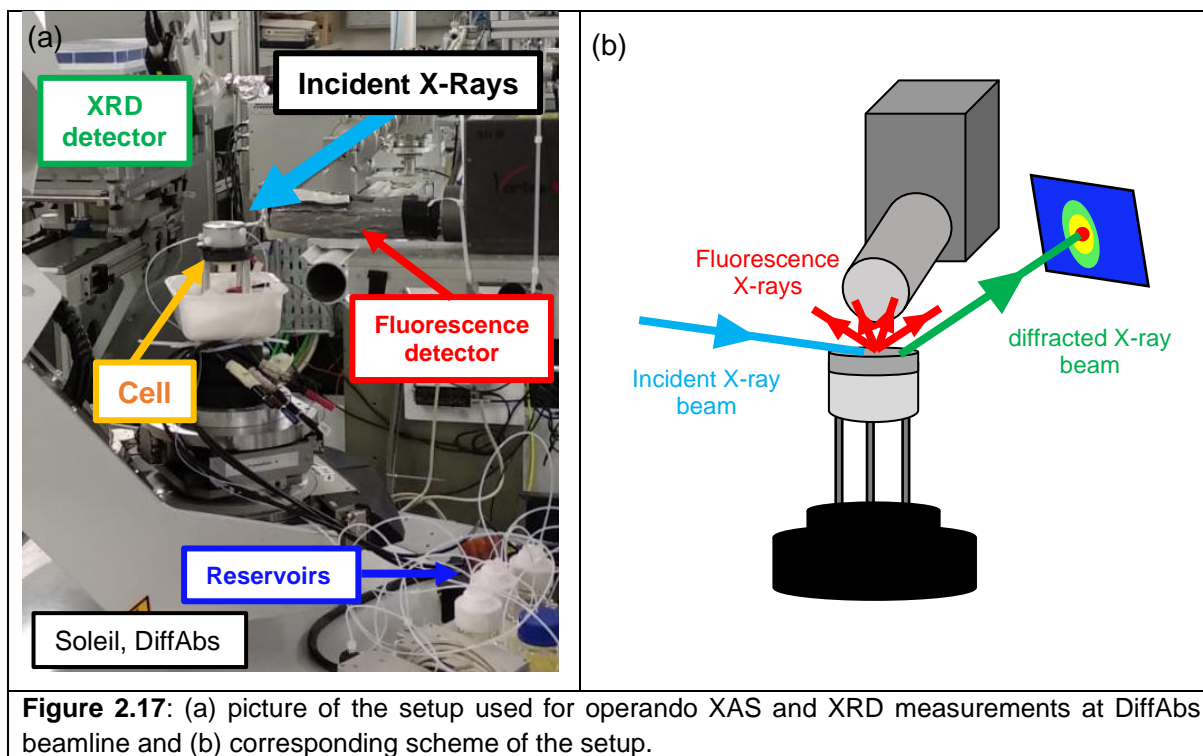
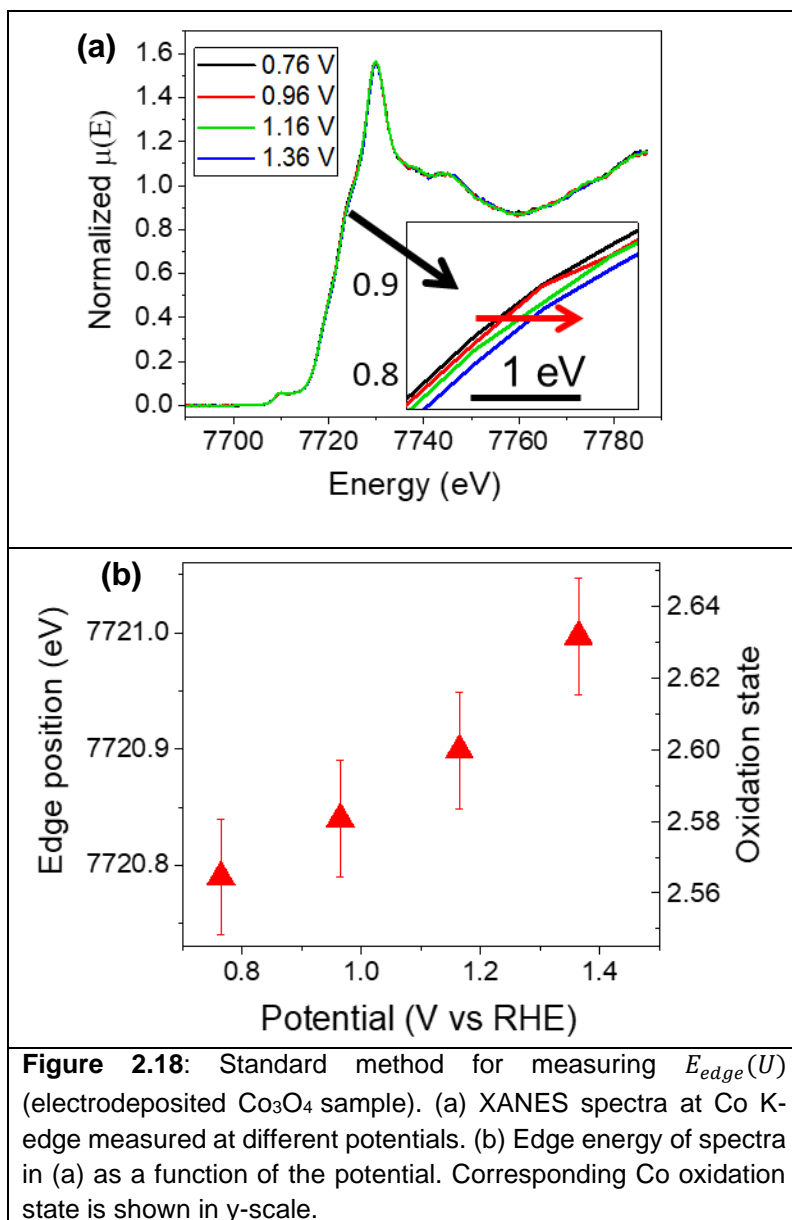


Figure 2.17: (a) picture of the setup used for operando XAS and XRD measurements at DiffAbs beamline and (b) corresponding scheme of the setup.

Determination of the oxide state as a function of potential

The main purpose of the operando XAS measurements is to study potential induced Co and Fe oxidation state changes in pre-OER and OER regime. Two methods have been applied to monitor the metal oxidation states changes with potential. This section explains these methods, especially details one of them and justifies its use in order to realize real operando measurements.

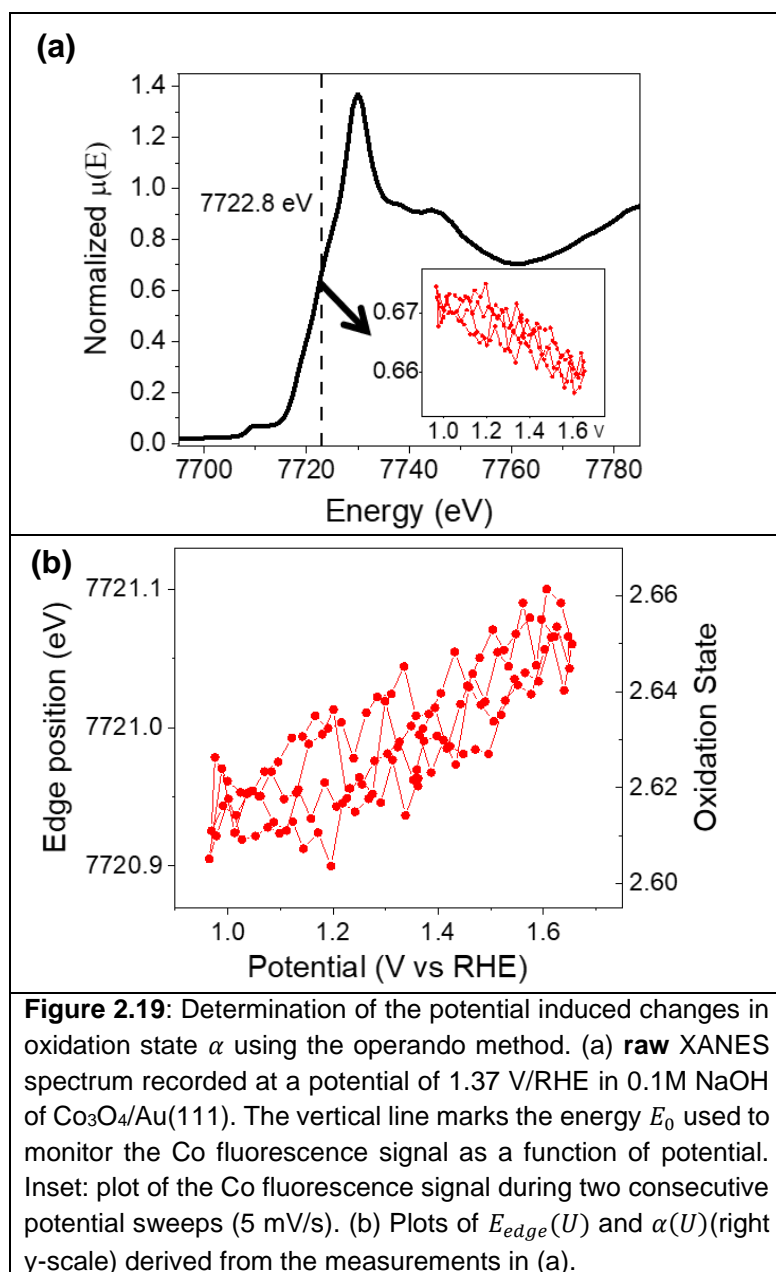
Figure 2.18 illustrates the most common method used in literature for measuring the edge energy as a function of potential $E_{edge}(U)$. Full XANES spectra are recorded at different potentials (see **Fig.2.18a** where the data concern an electrodeposited $\text{Co}_3\text{O}_4/\text{Au}(111)$ sample). For each potential U , E_{edge} is obtained from the XANES spectrum with the integral method described above. The inset highlights the edge region showing a slight shift of Co K-edge towards higher energies. **Figure 2.18b** displays the plot $E_{edge}(U)$ and the right y-scale gives the Co oxidation state using the calibration plot in **Fig.2.15**. Prior to each spectrum measurement the membrane is inflated to renew the electrolyte on top of the sample then deflated to optimize the fluorescence signal. This method is not too difficult to implement but has the drawback of being time consuming since recording one full XAS spectrum takes approximately 20 minutes. Because of this, acquiring more points as than those in **Fig. 2.18b** is possible but practically not doable each time. In addition, this method is only sensitive to the electrochemical steady state of the sample which makes it difficult to correlate with features in the voltammograms.



As shown in **Fig. 2.18a**, we are measuring very slight changes in edge energy, so we need a very sensitive method to be able to monitor it with high precision. For these reasons, we tested and used a second method that allows an operando determination of the oxidation state. It is illustrated in **Figure 2.19** and is referred as operando method in the following of the section. Measurements on an electrodeposited $\text{Co}_3\text{O}_4/\text{Au}(111)$ sample are used as example. A complete XANES spectrum is first recorded at a potential of $1.37 \text{ V}_{\text{RHE}}$ (**Fig. 2.19a**). The sample is then irradiated at a fixed X-ray energy $E_0 = 7722.8 \text{ eV}$, chosen close to E_{edge} , and the Co fluorescence signal is monitored while the applied potential is scanned at a rate of 5 mV/s . The inset of **Fig. 2.19a** gives the potential dependence of the cobalt fluorescence signal measured during two consecutive potential cycles between 0.97 V and $1.67 \text{ V}_{\text{RHE}}$. The decrease of the fluorescence signal towards positive potentials is due to the Co edge energy shifts towards

higher energies. Dividing the fluorescence signal by the *local* slope of the XANES spectrum (at the energy $E_0 = 7722.8 \text{ eV}$) yields the *shift* ΔE_{edge} of the XANES spectrum with applied potential. This is a good approximation since the edge shift is small and the spectrum is rather linear in this energy range. To plot $E_{edge}(U)$, as is shown in **Fig. 2.19b**, one must account for the value of $E_{edge}(U = 1.37V)$ which is determined after analysing the normalized spectrum in **Fig.2.19a**. The right y-scale of **Fig. 2.19b** gives the corresponding value of α using the calibration plot in **Fig. 2.15b**.

Compared to the usual method, this one thus presents the advantage that $E_{edge}(U)$ or $\alpha(U)$ is measured with a high potential resolution in short time: it takes ca. 30 min in total for recording one full XAS spectrum and the two potential sweeps with a point every 25 mV, i.e., 16 times more points than in the first method.



The reliability of the method has been tested. It is emphasized that the choice of E_0 is not affecting the final determination of $E_{edge}(U)$ provided E_0 is chosen not too far from E_{edge} , which means that it is taken within the rise of the Co/Fe K-edge. **Figure 2.20a** shows the raw XANES spectrum (not normalized) of a $\text{Co}_3\text{O}_4/\text{Au}(111)$ sample recorded at 1.37 V. The insets are plots of the Co fluorescence signal as a function of applied potential (sweep rate 5 mV/s). The two plots are measured at $E_0 = 7719.8$ eV and 7722.8 eV which are within the Co edge region. **Figure 2.20b** demonstrates that the plots $E_{edge}(U)$ measured at the two energies E_0 are perfectly overlapping. **Figures 2.20c** and **2.20d** show the same as **Figures 2.20a** and **b** for a $\text{CoOOH}/\text{Au}(111)$ sample. The fluorescence signal variations with potential in the edge region are measured at $E_0 = 7722$ eV and 7724 eV and also give very close $E_{edge}(U)$ plots.

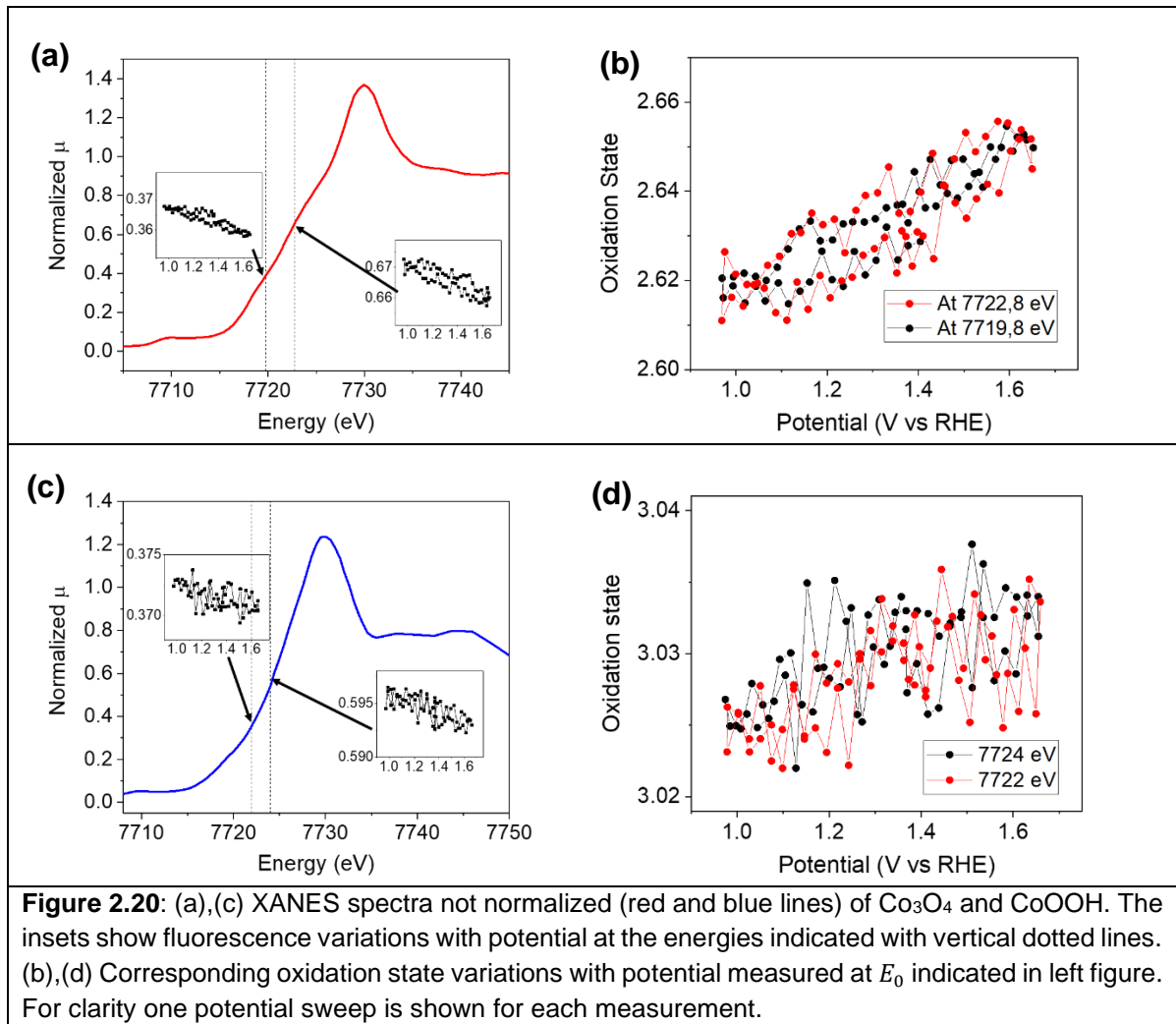
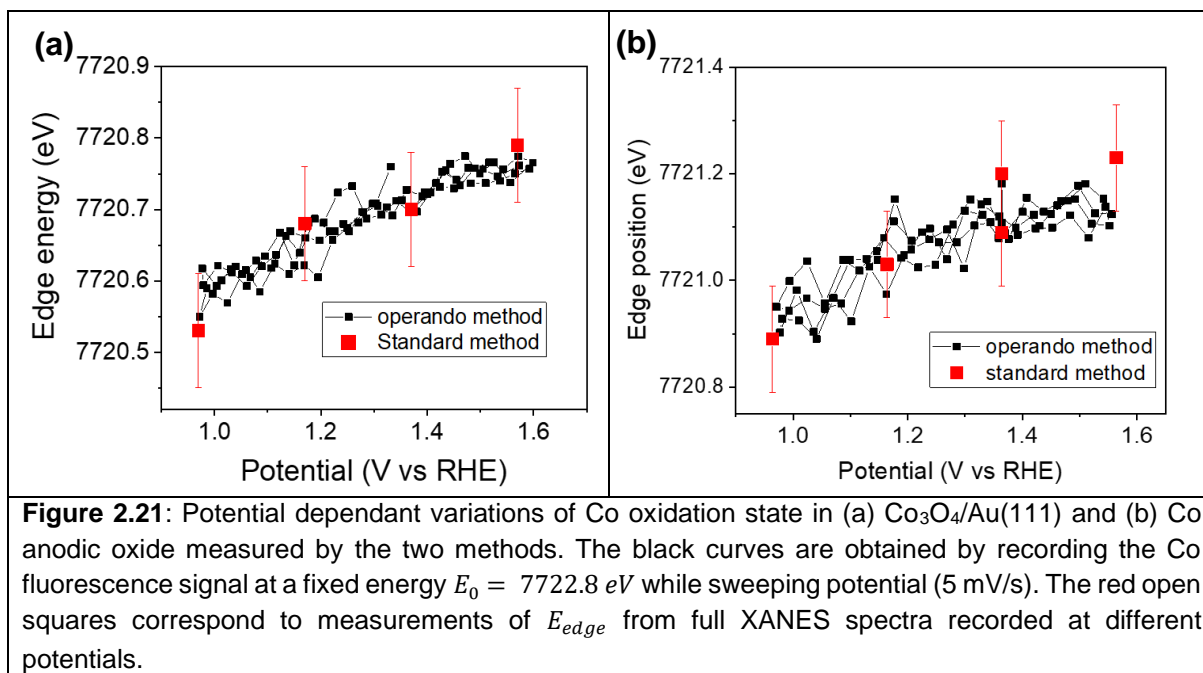


Figure 2.21 compares the results obtained with the two methods described above: measuring full XANES spectra at different potentials (illustrated in **Fig. 2.18**) and measuring the fluorescence signal at a fixed energy E_0 , chosen close to E_{edge} (illustrated in **Fig. 2.19**). The two kinds of determinations have been conducted on a 21 nm thick $\text{Co}_3\text{O}_4/\text{Au}(111)$ sample (a) and a Co anodic oxide obtained after oxidizing a 8ML $\text{Co}(001)/\text{Au}(111)$ thin film (b). Prior to the measurement the electrolyte is renewed and the fluorescence signal is optimized. Filled black squares are data obtained with the operando method (2 potential sweeps) and open squares with the standard method. For both samples, a good agreement is found between the two methods, if one accounts for the fact that the standard method gives the steady state value of α . In addition, in the example of **Fig. 2.19b**, the operando measurements show that the edge energy saturate at potentials more positive than 1.4V. This behaviour cannot be deduced from the standard method. Moreover, it is clear from **Fig. 2.19** that the uncertainty of the measured value is significantly smaller for the operando method.



In this section, it was demonstrated that the operando method proposed in this work is robust (i.e. not sensitive to the choice of E_0) and offers a high potential resolution within a short measurement time and better signal over noise ratio.

Combined XAS and XRD measurements

For combined XAS and XRD measurements, XAS and XRD data shown in this work are acquired sequentially at different beam energies E . Operando XAS data are recorded as explained below at a beam energy chosen close to E_{edge} . For operando SXRD measurements, a beam energy E outside of Co and Fe absorption K-edge regions has been chosen in order to improve XRD intensity signal and minimize measurements noise. They were recorded at $E = 7.83 \text{ keV}$ for all samples except for Fe_3O_4 for which an energy $E = 7.24 \text{ keV}$ (outside of Fe K-edge region) was chosen. The reason for this is that the Bragg peak intensity varies significantly in the edge energy region and is slightly larger at E outside and higher than E_{edge} . This is illustrated by **Figure 2.22** which shows the integrated intensity of $\text{Co}_3\text{O}_4(113)$ Bragg peak during a scan in energy in Co K-edge region. The position of 2D detector was tuned so that it follows the Bragg peak at each energy.

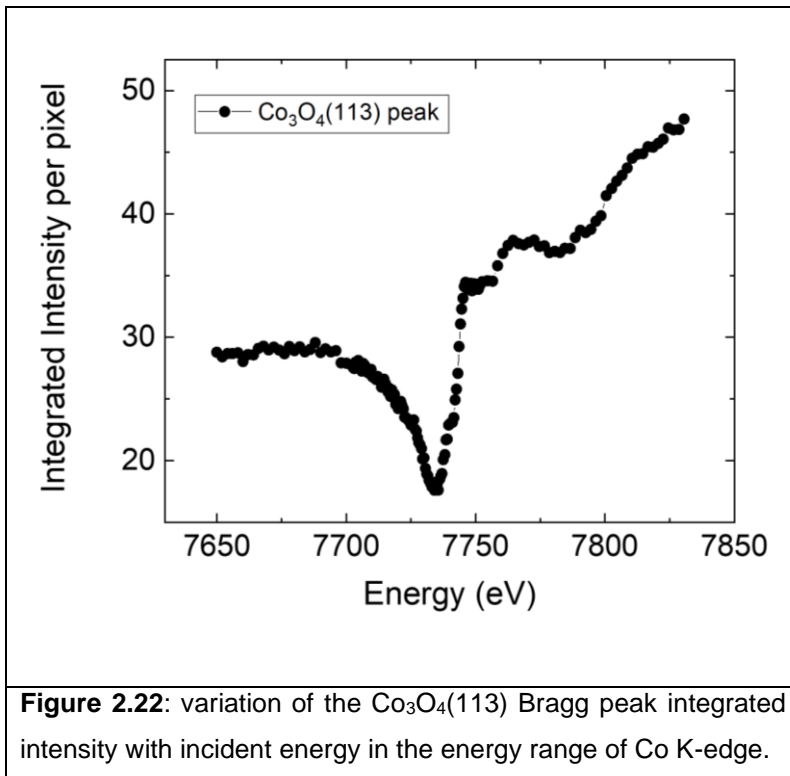
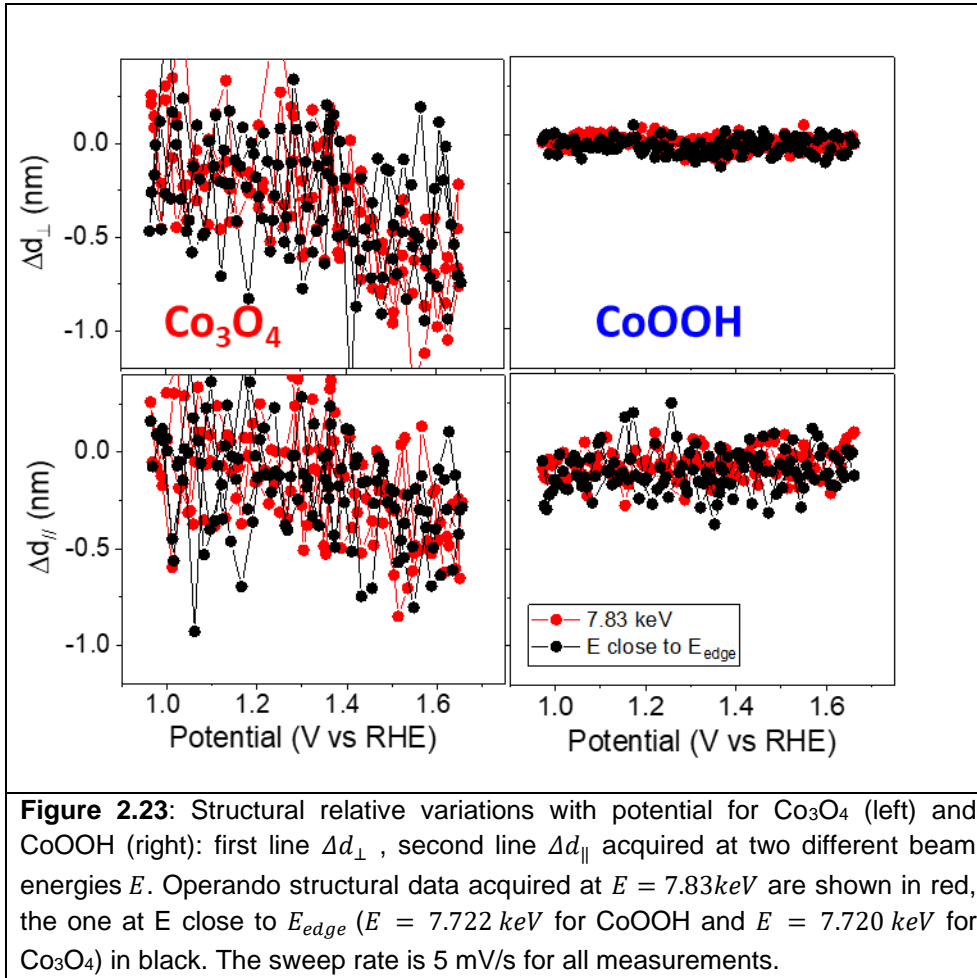


Figure 2.22: variation of the $\text{Co}_3\text{O}_4(113)$ Bragg peak integrated intensity with incident energy in the energy range of Co K-edge.

Bellow we show that sequential acquisition can however be safely trusted for the correlations between XAS and XRD discussed in chapters 3 and 4. **Figure 2.23** shows operando structural variations (Δd_{\parallel} , Δd_{\perp}) measured at two different beam energies: $E = 7.83 \text{ keV}$ higher than E_{edge} and E close to E_{edge} ($E = 7.772 \text{ keV}$ for CoOOH (right column) and $E = 7.720 \text{ keV}$ for Co_3O_4 (left column)). The latter data (black) present more data scattering than the former (red), but both show the same behaviour. This means that XRD operando measurements can be safely correlated to operando XAS even though they are not acquired simultaneously. This is true all the more since the samples undergo reproducible and reversible structural changes with no sizeable modification of their morphology and structure.



2.4 Lab characterizations

X-ray Diffraction

The structure of deposits prepared by direct electrodeposition on Au(111) in the reflux cell is characterized by XRD (θ - 2θ) before measurements at the beamline. A Rigaku Smartlab X-ray diffractometer with a rotating anode Cu $K\alpha$ radiation source ($\lambda = 0.154\text{ nm}$) is used for this purpose. X-ray diffraction patterns were obtained using a parallel beam configuration, a Ge(220) double bounce monochromator on the incident beam side and a Hypix-3000 2D detector used in 1D mode.

Wide ($15^\circ - 75^\circ$) θ - 2θ scans inform about the phase and epitaxy of the deposits. Narrow θ - 2θ scans (17° - 23°) in the angular region of Co_3O_4 (111), CoOOH (003) and Fe_3O_4 (111) peaks also give the phase of the deposit and are used to determine the thickness t of the deposits, using Scherrer equation (2.18). The crystallites mean height are linked to the FWHM of the peaks, to the Bragg angle θ and the incident X-ray wavelength λ .

$$t = \frac{0.9 * \lambda}{FWHM(2\theta) * \cos(\theta)} \quad (2.18)$$

Atomic Force Microscopy (AFM)

The morphology of deposits is investigated using a PicoSPM (Agilent) AFM operating in the AC Mode. Sharp silicon tips (μmasch , nominal tip radius ≈ 8 nm, cone angle 40° , spring constant ≈ 45 N m $^{-1}$, resonance frequency ≈ 190 kHz) were used for high-resolution. Different regions of the samples are imaged with image sizes ranging from 5 μm to 500 nm to verify the homogeneity of the deposit. AFM measurements allow to obtain to determine the roughness factor of the deposits, based on the mean island's width and geometry.

Scanning Electron Microscopy (SEM) and Energy Dispersive X-ray spectroscopy (EDX)

SEM images of the deposits prepared by direct electrodeposition are obtained using a Hitachi S4800 microscope equipped with field effect gun and operating between 3 and 10kV. The SEM is equipped with an SDD fluorescence detector for EDX characterizations. These were performed with a fixed current at 20 kV. Bilayer $\text{Co}_{1-x}\text{Fe}_x\text{O}_y/\text{CoOOH}$ samples obtained by direct electrodeposition on Au(111) (see **section 2.1**) were characterized by EDX before and after $\text{Co}_{1-x}\text{Fe}_x\text{O}_y$ deposition in order to determine the iron content in the top mixed CoFe oxide layer (see Appendix of **chapter 4**).

2.5 Bibliography

- [1] Henke, B. L.; Gullikson, E. M.; Davis, J. C. X-ray interactions: Photoabsorption, scattering, transmission, and reflection at $E = 50\text{-}30,000$ eV, $Z = 1\text{-}92$. *Atomic Data and Nuclear Data Tables*. **1993**, 181–342. <https://doi.org/10.1006/adnd.1993.1013>.
- [2] Guinier, A. Théorie et technique de la radiocristallographie, Dunod, Paris, **1964**.
- [3] Robinson, I. K.; Tweet, D.J.; Surface X-ray diffraction. *Rep. Prog. Phys.* **1992**, 55, 599-651. <https://doi.org/10.1088/0034-4885/55/5/002>.
- [4] Bordet, P. Rappels de Cristallographie, EDP Sciences, Les Ulis, **2008**, *Collection SFN 9*, 1–17. <https://doi.org/10.1051/sfn:2008002>
- [5] Reikowski, F.; Maroun, F.; Pacheco, I.; Wiegmann, T.; Allongue, P.; Stettner, J.; Magnussen, O. M. Operando Surface X-ray Diffraction Studies of Structurally Defined Co_3O_4 and CoOOH Thin Films during Oxygen Evolution. *ACS Catal.* **2019**, 9 (5), 3811–3821. <https://doi.org/10.1021/acscatal.8b04823>.
- [6] Penner-Hahn, J.E., X-ray Absorption Spectroscopy. In eLS, John Wiley & Sons, Ltd (Ed.). <https://doi.org/10.1038/npg.els.0002984>.
- [7] Sakura Pascarelli, Fundamentals of X-ray Absorption Fine Structure: basic principles, European Synchrotron Radiation Facility, Grenoble, HERCULES, **2017**
- [8] Bruce Ravel, Introduction to X-ray Absorption Spectroscopy, Columbia University, Sept. **2015**

- [9] Schnor, C. S., Ridgway, M.C., Introduction to X-Ray Absorption Spectroscopy in [Springer Series in Optical Sciences](#) 190, **2015**
- [10] Ravel, B.; Newville, M. ATHENA, ARTEMIS, HEPHAESTUS: Data analysis for X-ray absorption spectroscopy using IFEFFIT. *J. Synchrotron Radiat.* **2005**, *12* (4), 537–541. <https://doi.org/10.1107/S0909049505012719>.
- [11] Dau, H.; Liebisch, P.; Haumann, M. X-ray absorption spectroscopy to analyze nuclear geometry and electronic structure of biological metal centers-potential and questions examined with special focus on the tetra-nuclear manganese complex of oxygenic photosynthesis. *Anal. Bioanal. Chem.* **2003**, *376* (5), 562–583. <https://doi.org/10.1007/s00216-003-1982-2>.
- [12] Bergmann, A.; Martinez-Moreno, E.; Teschner, D.; Chernev, P.; Gliech, M.; De Araújo, J. F.; Reier, T.; Dau, H.; Strasser, P. Reversible amorphization and the catalytically active state of crystalline Co₃O₄ during oxygen evolution. *Nat. Commun.* **2015**, *6*. <https://doi.org/10.1038/ncomms9625>.
- [13] Smith, R. D. L.; Pasquini, C.; Loos, S.; Chernev, P.; Klingan, K.; Kubella, P.; Mohammadi, M. R.; Gonzalez-Flores, D.; Dau, H. Spectroscopic identification of active sites for the oxygen evolution reaction on iron-cobalt oxides. *Nat. Commun.* **2017**, *8* (1). <https://doi.org/10.1038/s41467-017-01949-8>.
- [14] IXAS XAFS database, service of the International X-ray Absorption Society, available at: <http://ixs.iit.edu/database/>
- [15] Koza, J. A.; He, Z.; Miller, A. S.; Switzer, J. A. Electrodeposition of crystalline Co₃O₄-A catalyst for the oxygen evolution reaction. *Chem. Mater.* **2012**, *24* (18), 3567–3573. <https://doi.org/10.1021/cm3012205>.
- [16] Gudavarthy, R. V.; Gorantla, S.; Mu, G.; Kulp, E. A.; Gemming, T.; Eckert, J.; Switzer, J. A. Epitaxial electrodeposition of Fe₃O₄ on single-crystal Ni(111). *Chem. Mater.* **2011**, *23* (8), 2017–2019. <https://doi.org/10.1021/cm2002176>.
- [17] He, Z.; Koza, J. A.; Mu, G.; Miller, A. S.; Bohannan, E. W.; Switzer, J. A. Electrodeposition of Co_xFe_{3-x}O₄ epitaxial films and superlattices. *Chem. Mater.* **2013**, *25* (2), 223–232. <https://doi.org/10.1021/cm303289f>.
- [18] Reikowski, F.; Maroun, F.; Di, N.; Allongue, P.; Ruge, M.; Stettner, J.; Magnussen, O. M. In situ surface X-ray diffraction study of ultrathin epitaxial Co films on Au(111) in alkaline solution. *Electrochim. Acta* **2016**, *197*, 273–281. <https://doi.org/10.1016/j.electacta.2016.01.052>.
- [19] Jurca, H. F.; Damian, A.; Gougaud, C.; Thiaudière, D.; Cortès, R.; Maroun, F.; Allongue, P. Epitaxial Electrodeposition of Fe on Au(111): Structure, Nucleation, and Growth Mechanisms. *J. Phys. Chem. C* **2016**, *120* (29), 16080–16089. <https://doi.org/10.1021/acs.jpcc.5b12771>.
- [20] Calvillo, L.; Carraro, F.; Vozniuk, O.; Celorrio, V.; Nodari, L.; Russell, A. E.; Debellis, D.; Fermin, D.; Cavani, F.; Agnoli, S.; Granozzi, G. Insights into the durability of Co-Fe spinel oxygen evolution electrocatalysts: Via operando studies of the catalyst structure. *J. Mater. Chem. A* **2018**, *6* (16), 7034–7041. <https://doi.org/10.1039/c7ta10892c>.

Chapter 3: Epitaxial Co oxide thin films

3.1 Introduction

For the purpose of understanding their catalytic activity for the Oxygen Evolution Reaction (OER), cobalt oxides catalysts have been the subject of numerous experimental [1-20,25-27, 30-33] and computational [12,21-24,32-34] studies. Especially experimental works in operando conditions have been widely used to probe the variations of some key parameters during the OER process [4-19, 30-32]. As the currently known OER mechanism on Co oxide involves changes in Co oxidation state and coordination sphere, many of the operando studies used X-ray absorption spectroscopy (XAS) since it may be employed in operando conditions on a large variety of samples and yield the Co oxidation state and the local atomic environment. The general trends derived from these measurements at Co K-edge are: (i) an increase of Co mean oxidation state with increasing potential for CoCat [8,13], CoO and Co₃O₄ [11,12,15,16,18], CoOOH bulk and nanosheets [12, 19, 32] and (ii) small changes in Co coordination shell in OER conditions [11,12, 15].

The surface of these different oxides is terminated by oxygen atoms or hydroxyl groups which are coordinated to Co atoms by either 2 or 3 bonds: they are referred as μ_2 -O(H) and μ_3 -O(H) sites respectively. The CoCat, which is among the most active Co based catalysts for OER [25] is also thought to be the more disordered. Since a disordered phase is expected to contain the highest density of μ_2 -O(H), the μ_2 -O(H) bridges are considered to be the most active sites for OER [26]. Strasser et al. [12] associated μ_2 -O(H) bridges to a fast OER mechanism while a slow OER would take place on μ_3 -O sites. According to their analysis of electrochemical and XAS measurements on different Cobalt oxides, μ_2 -O(H) sites are associated to high Co³⁺-O bond electrochemical reducibility, unlike μ_3 -O sites, which are decisive for high OER activity. Zhang et al. [5] used time resolved FTIR spectroscopy to study Co₃O₄ nanocrystalline particles during photocatalytic OER, and evidenced the formation of two reaction intermediates which correspond to two different catalytic sites, one associated to a fast OER mechanism and one to a slow mechanism. **Figure 3.1**, that is taken from their work [5], illustrates the different steps of these two mechanisms ((a) fast and (b) slow) in a neutral electrolyte. The reaction intermediates they identified by time resolved FTIR spectroscopy are highlighted in yellow.

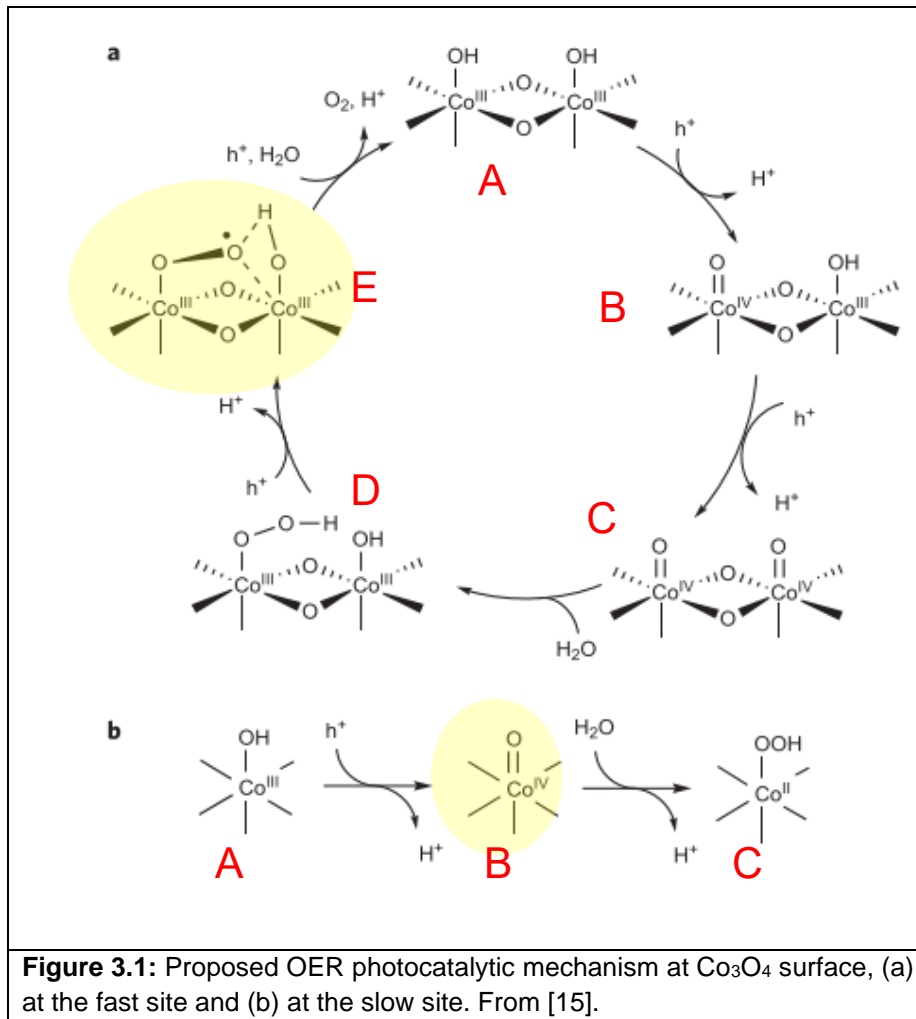


Figure 3.1: Proposed OER photocatalytic mechanism at Co_3O_4 surface, (a) at the fast site and (b) at the slow site. From [15].

The fast mechanism takes place at a $\mu_2\text{-O}$ site where two O-bridged $\text{Co}^{\text{III}}\text{-OH}$ groups (A) are first converted into intermediate B containing one Co^{IV} group, then into intermediate C with two $\text{Co}^{\text{IV}}\text{=O}$ groups. Bulk water nucleophilic addition to one of the Co^{IV} follows, and results in O – O bond formation and reduction of the two Co in Co^{III} . Intermediate D is transformed into the superoxide intermediate E, identified by the authors. O_2 is then released, concomitantly as H_2O attack to reform A. This light pulse assisted mechanism takes place within 300 ms. The difference with the slow mechanism (b) lies in the absence of an O-bridged adjacent $\text{Co}^{3+}\text{-OH}$ group at the initial active site. In this case, the oxidizing power of isolated $\text{Co}^{\text{IV}}\text{=O}$ intermediate (B) is lowered and H_2O deprotonation is required for its addition to B, which makes this reaction step consequently slower than in the fast mechanism.

This OER scheme involves the formation of Co^{4+} species as reaction intermediates and numerous experimental works searched evidences for such species in OER conditions. For example, operando XPS measurements on Co_3O_4 associate the apparition of features at low binding energy in the Co 2p XPS spectrum measured at OER potential to the formation of Co^{4+} at the oxide surface [30]. The apparition of Co^{4+} signal was observed by EPR characterizations

of CoCat catalyst at potentials above 1.1V [36,37]. The authors found that the intensity of this signal increases with potential, while Co^{2+} signal decreases, and estimated that approximately 10% of Co^{4+} were present in the material at 1.34V. Pasquini et al. [32] studied CoCat catalyst with operando Raman spectroscopy and described the region of Co-O vibrations by Gaussian bands of potential-dependent amplitudes. They assigned the $\text{Co}^{3+} \rightarrow \text{Co}^{4+}$ transition to a linear combination of these bands' amplitudes, in relation to previous operando XAS measurements. In the latter, a mean oxidation state of ~ 3.25 was determined for CoCat at OER potentials, implying the presence of approximately 20% Co^{4+} in the material. [8] Combining XAS with UV visible absorption and time-resolved mass spectroscopy to track the OER kinetics, Dau et al. proposed a four stages OER scheme at μ_2 -O sites by CoCat, involving (i) a dynamic interconversion between three species containing Co(II,III), Co(III) and Co(III,IV), (ii) formation of an active site by encounter of two or more Co(IV) ions, (iii) O-O bond formation step followed by Co reduction at the active site, and (iv) Co re-oxidation to return to equilibrium conditions[8]. In this picture, Co^{4+} and Co^{3+} co-exist at the catalyst surface and are in constant equilibrium. To interpret operando XAS data, the mean cobalt oxidation state at OER potential is often referred as $\text{Co}^{3+/4+}$ [8,11,12,32]. This is for example the case in the study of CoOOH nanosheets in which the Co oxidation state was found higher than 3 under OER conditions, interpreted as the formation of a CoO_2 reaction intermediates [32]. Strasser et al. [11] described the reversible formation of an amorphous $\text{CoO}_x(\text{OH})_y$ reaction zone at the surface of crystalline Co_3O_4 , resulting from the oxidation of surface Co^{2+} ions into Co^{3+} , and in which Co^{4+} can be incorporated via the deprotonation of μ_i -O bridges between Co ions. Since this phase is limited to the surface of the crystallites, the corresponding XAS spectra they measured show a very slight increase of Co mean oxidation state.

The quantitative interpretation of XAS data is therefore far from being straightforward since the XAS signal originates from the entire oxide film whereas the modifications are expected to take place at or very near to the oxide surface. In fact, the structure of the oxide may be restructuring in OER condition. Such a restructuring has for instance been reported and documented for Co_3O_4 using operando XRD [11,14]. In this case, extracting the information related with surface atoms is a challenging task especially when the active surface area of the catalyst cannot be reliably determined and presents different crystallographic facets with a large number of surface site types. In this context, the use of well-defined catalysts materials appears very interesting to facilitate the interpretation of the XAS measurements.

In particular, our group used operando Surface X-ray Diffraction to study the structural behaviour of epitaxial $\text{Co}_3\text{O}_4(111)$ and $\text{CoOOH}(001)$ thin films [14]. It was demonstrated that the transformation of Co_3O_4 surface region also occurs in the case of epitaxial films, and that it is reversible with potential, in agreement with [11]. This near surface region called skin layer

is structurally disordered and it is the OER active phase. On the contrary, no significant structural changes were measured in the case of CoOOH(001) films, which catalytic activity was found to be similar to that of Co₃O₄(111).

In this chapter, we study in operando conditions, the potential dependence of the cobalt average oxidation state in epitaxial Co₃O₄(111) and CoOOH(001) thin films (10-30 nm) electrodeposited on Au(111) using in combination X-ray absorption spectroscopy (XAS) and structural characterizations, based on Surface X-Ray Diffraction (SXR). In the case of Co₃O₄, results evidence close correlation between the increase of the Co oxidation state in pre-OER regime and the simultaneous restructuring of the near surface region, i.e. the so-called above-mentioned skin layer. In the case of CoOOH, which surface is perfectly stable, a smaller increase of the cobalt oxidation state is measured. Data are quantitatively analysed to discuss the oxidation state of Co atoms at the surface of oxides.

3.2 Structure of Co₃O₄ and CoOOH

Figure 3.2a shows the atomic structure of CoOOH (heterogenite) which has a trigonal structure. Along the (001) direction, CoOOH presents a layered structure. There are 3 CoOOH molecules per hexagonal unit cell (shown with a black rectangle on **Fig. 3.2a**), which lattice parameters are: $a_{CoOOH} = 0.285 \text{ nm}$ and $c_{CoOOH} = 13.15 \text{ nm}$. Each layer is composed of one CoOOH molecule, and the distance between two CoOOH layers, i.e. the distance between two Co planes, is 0.438 nm. A CoOOH layer consists of one plane of Co³⁺ sandwiched between two planes of O²⁻ ions. These trilayers are bonded together via O-H-O bridges. Each O²⁻ ion is therefore coordinated with three Co³⁺ ions, leading to a μ_3 -O site, and to one H atom that ensures the cohesion between trilayers, while Co³⁺ are in octahedral sites. Each bulk Co atom is thus six-fold coordinated with OH_{0.5} groups, where the H_{0.5} expresses that the H atoms are shared between two trilayers. On average, the cobalt oxidation state is therefore: $\alpha_{bulk} = 3$ because each OH_{0.5} is connected to 3 Co ions. At the surface, the oxygen groups (O or OH) of the topmost plane have no partners above and the top Co atoms present an oxidation state α_{surf} which depends on the protonation state of the topmost O-atomic plane. For a fully protonated surface, $\alpha_{surf} = 2.5$ and for a fully deprotonated surface, $\alpha_{surf} = 3.5$. A schematic illustration of CoOOH(001) surface plane(s) is shown in **Fig.3.2b**, alternatively fully OH and O terminated. The different Co planes contained in a unit cell shown in (a) are highlighted with a yellow parallelogram.

Co₃O₄ is a cubic spinel compound. **Fig.3.2c** expresses its structure in a hexagonal unit cell, with c_{hex} parallel to the cubic (111) direction. This representation is convenient since it uses the same orientation as the hexagonal Au(111) substrate. In this case, the Co₃O₄ unit cell

(shown with a black rectangle) has the following lattice parameters: $a_{\text{Co}_3\text{O}_4_{\text{hex}}} = \frac{a_{\text{Co}_3\text{O}_4_{\text{cubic}}}}{\sqrt{2}} = 5.716 \text{ nm}$ and $c_{\text{Co}_3\text{O}_4_{\text{hex}}} = c_{\text{Co}_3\text{O}_4_{\text{cubic}}} * \sqrt{3} = 14.00 \text{ nm}$. There are 6 Co_3O_4 molecules per hexagonal unit cell. Co_3O_4 contains both Co^{2+} (light blue) and Co^{3+} (dark blue): Co^{2+} are in tetrahedral sites and Co^{3+} in octahedral sites. Oxygen planes sandwich two types of Co layers: one with Co^{3+} only and one containing both Co^{2+} and Co^{3+} . Co_3O_4 can be written as $\text{Co}^{2+}_1\text{Co}^{3+}_2\text{O}_4$ giving a mean Co oxidation state of 2.66. **Fig.3.2d** illustrates the atomic arrangement of the Co planes in $\text{Co}_3\text{O}_4(111)$, showing in yellow the atoms contained in a unit cell.

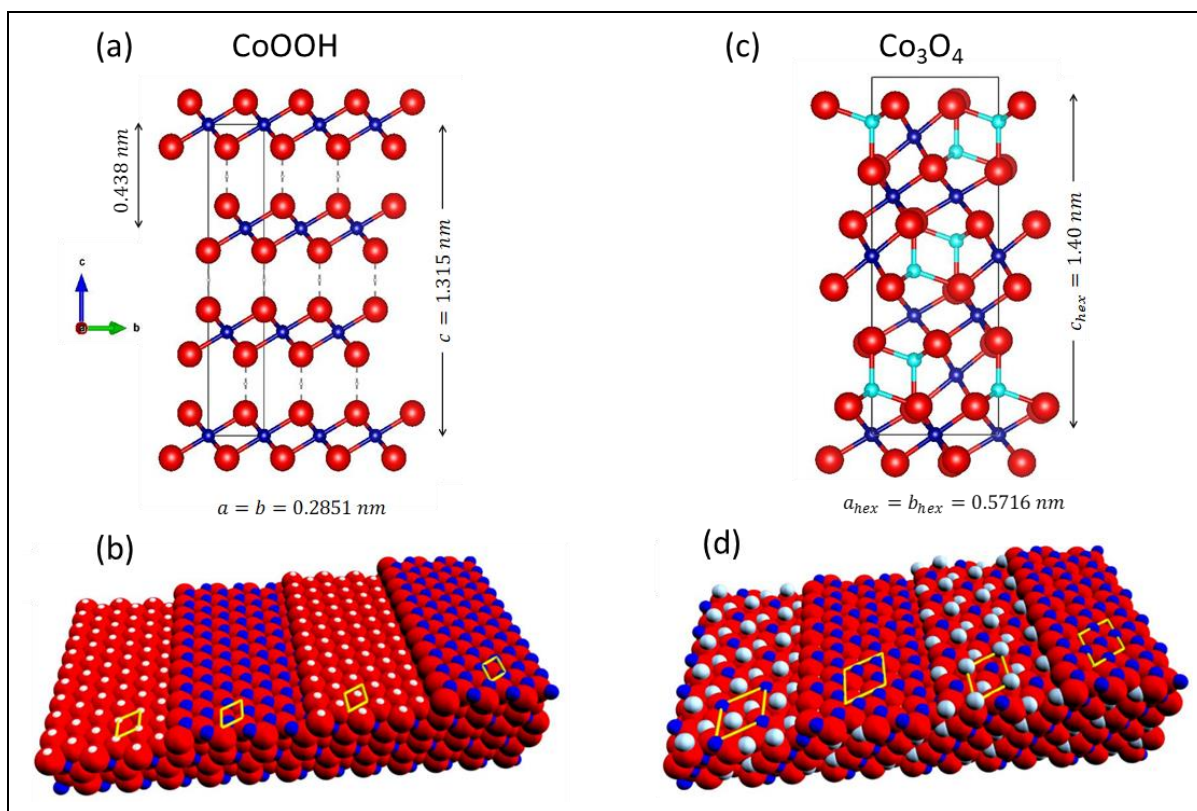


Figure 3.2: Unit cells of (a) $\text{CoOOH}(001)$ and (c) $\text{Co}_3\text{O}_4(111)$ oxides. Co^{2+} are shown in light blue, Co^{3+} in dark blue, O in red and H in white (the ionic radius is used to represent elements). The cell parameters along a, b and c directions are given, together with the distance between two atomic planes along the (001) direction in a CoOOH unit cell. Schematic illustration of the atomic arrangement in the hexagonally ordered planes of (b) $\text{CoOOH}(001)$ and (d) $\text{Co}_3\text{O}_4(111)$, showing edge steps. In electrolyte, the topmost plane of the oxides is most likely terminated by oxygen or hydroxyls groups. Highlighted in yellow are the different Co planes of the unit cells shown in (a) and (c).

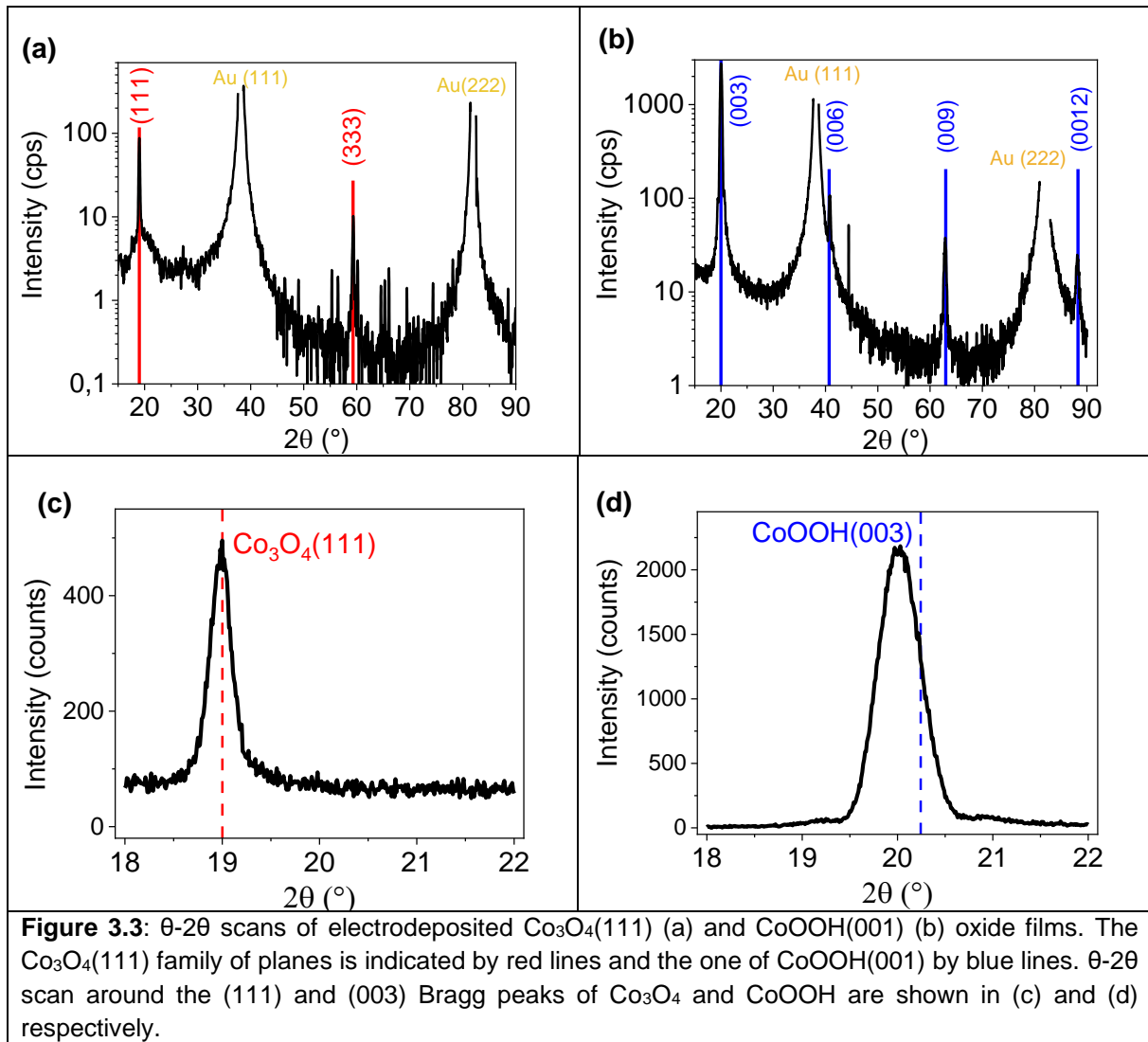
3.3 Results

Characterization of as prepared Co_3O_4 and CoOOH deposits

Co_3O_4 and CoOOH are obtained by direct electrodeposition on $\text{Au}(111)$ substrate. Details of the electrodeposition method are given in **section 2.5**.

Figure 3.3 shows XRD θ - 2θ scans of Co_3O_4 and CoOOH deposits (a) and (b) in a wide angular range (2θ between 15° and 90°) for Co_3O_4 and CoOOH respectively. In **Fig.3.3a** peaks are observed at 19° and 59.3° , they correspond to (111) and (333) peaks of spinel Co_3O_4 with a faced centred unit cell. In **Fig.3.3b**, peaks at 20° , 40.8° , 62.9° and 88.2° are found, they are respectively assigned to (003),(006),(009) and (0012) of CoOOH with an hexagonal unit cell. This indicates that the Co_3O_4 and CoOOH deposits are crystalline and respectively grow with a (111) and (001) orientation on Au(111) substrate. $\text{Co}_3\text{O}_4(222)$ and $\text{Co}_3\text{O}_4(444)$ peaks are not visible because they are located close to the Au(111) and Au(222) peaks of the substrate. As no other peaks are present on Co_3O_4 and CoOOH diffractograms, the oxides are pure phases with a well-defined orientation.

The epitaxial growth of the oxides on Au(111) is probably linked to the identical in-plane hexagonal symmetry of Au(111), $\text{Co}_3\text{O}_4(111)$ and $\text{CoOOH}(001)$. In addition, the in-plane lattice constant of Au(111) ($a_{\text{Au}} = 0.2884 \text{ nm}$) is very close to the one of $\text{CoOOH}(001)$ ($a_{\text{CoOOH}} = 0.2851 \text{ nm}$) and is almost twice that of $\text{Co}_3\text{O}_4(111)$ ($a_{\text{Co}_3\text{O}_4} = 0.5716 \text{ nm} = 2 * 0.2858 \text{ nm}$). This corresponds to a small in-plane lattice mismatch between substrate and deposit.



For a more detailed structure determination, θ - 2θ in a narrow region around $\text{Co}_3\text{O}_4(111)$ and $\text{CoOOH}(003)$ peaks (θ between 18 and 22°) are shown in **Fig.3.3c** and **d**. While the position of $\text{Co}_3\text{O}_4(111)$ peak is very close to the expected $\text{Co}_3\text{O}_4(111)$ peak position (dashed red line), the position of the $\text{CoOOH}(003)$ peak is shifted towards lower 2θ values compared to the theoretical $\text{CoOOH}(003)$. This indicates an out of plane strain of $\sim +1\%$ for CoOOH deposits and almost no out of plane strain for Co_3O_4 deposits. Higher order peaks of the oxides show similar behaviours. The crystallite out-of-plane size, i.e. the average crystallite height is estimated from the FWHM of the $\text{CoOOH}(003)$ and $\text{Co}_3\text{O}_4(111)$ peaks using Scherrer formula. For example, in **Fig.3.3c** and **d**, $\text{Co}_3\text{O}_4(111)$ and $\text{CoOOH}(003)$ peak FWHMs respectively equal 0.29° and 0.44° which yield 28.2 nm and 18.3 nm.

Figure 3.4 displays typical AFM images of CoOOH (XRD crystallite height: 15 nm) and Co_3O_4 (XRD crystallite height: 22 nm) deposits along with a horizontal cross-section through the image at the position shown with arrows.

The CoOOH film (**Fig. 3.4a**) consists of wide and rather shallow islands, with stepped facets. The steps are 0.4 to 0.5 nm high which is consistent with the distance between two atomic planes along the (001) direction of CoOOH (0.438 nm). The islands have a pyramidal shape which height (4 – 9 nm) is smaller than the XRD average crystallite height, suggesting that a continuous CoOOH layer is present below the pyramidal islands visible in the AFM images. These observations evidence that CoOOH deposits are approximately bidimensional layers, with an electrochemical surface area (ECSA) very close to the geometrical area of the substrate. Consequently, the roughness factor (RF), defined as the ratio of the ECSA and the sample geometrical area, is ~ 1 for this sample.

The Co₃O₄ deposit (**Fig. 3.4b**) presents a comparatively rougher morphology with tightly packed triangular islands (30 nm to 70 nm wide). One notices that the Co₃O₄ islands adopt two preferential orientations separated by 180°, as highlighted by the two red triangles on **Fig.3.4b**. Their edges are approximately parallel to six in plane axis, which is consistent with the hexagonal symmetry of the Co₃O₄(111) on Au(111) planes. The profile below the AFM image shows that the average islands height (between the island top and the deeper dips between the islands that would correspond to the substrate surface) is approximately 20 nm, very close to the value of XRD average crystallite height. The profile also shows that the grains tops are rather flat. As explained in **Appendix A3.1**, we model the Co₃O₄ (111) islands as triangular prisms to estimate the ECSA of the sample. This model yields an ECSA that is approximately 1.75 times higher than the geometrical surface area of the substrate (RF ~ 1.75).

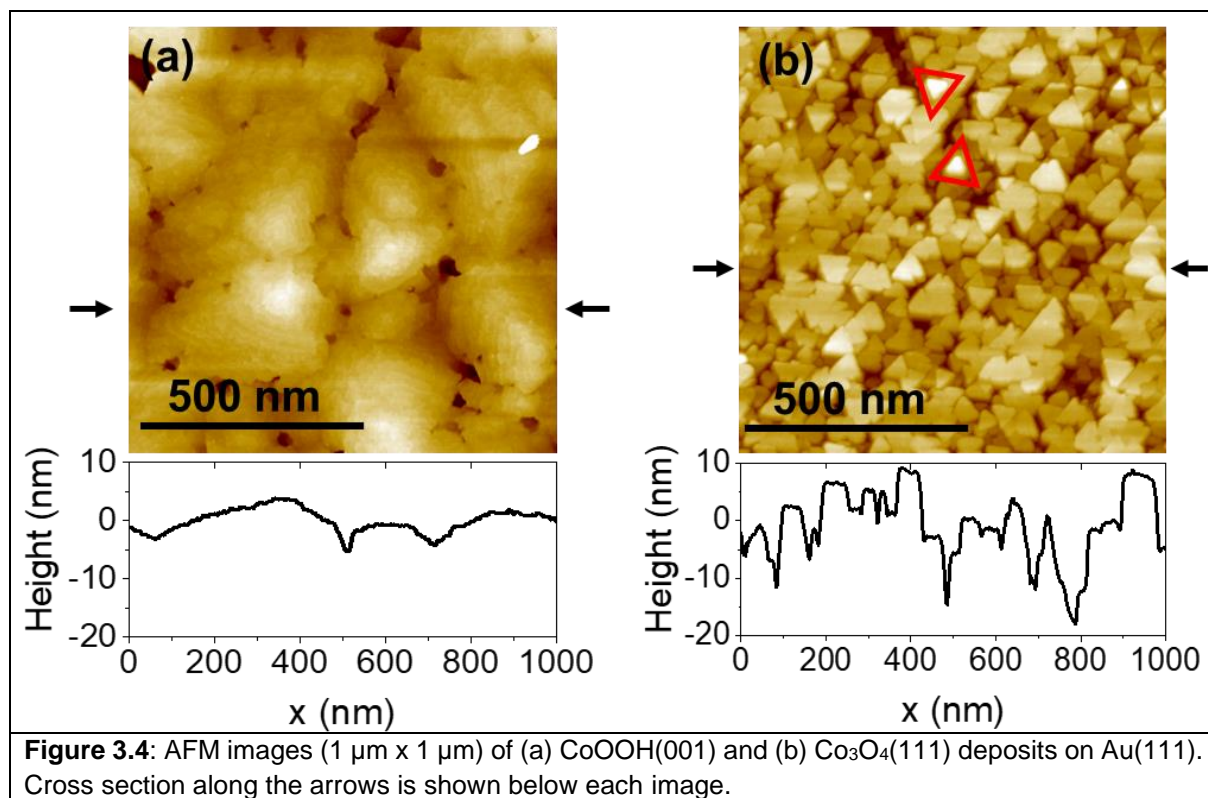


Figure 3.4: AFM images ($1\ \mu\text{m} \times 1\ \mu\text{m}$) of (a) CoOOH(001) and (b) Co₃O₄(111) deposits on Au(111). Cross section along the arrows is shown below each image.

Characterizations of the oxide films with synchrotron-based techniques

Two Co₃O₄ and two CoOOH samples have been fully characterized by SXRD and XAS at DiffAbs beamline (SOLEIL), both in air and in a 0.1M NaOH electrolyte. **Table 3.1** collects the list of these samples together with their principal morphological, structural and spectroscopic parameters.

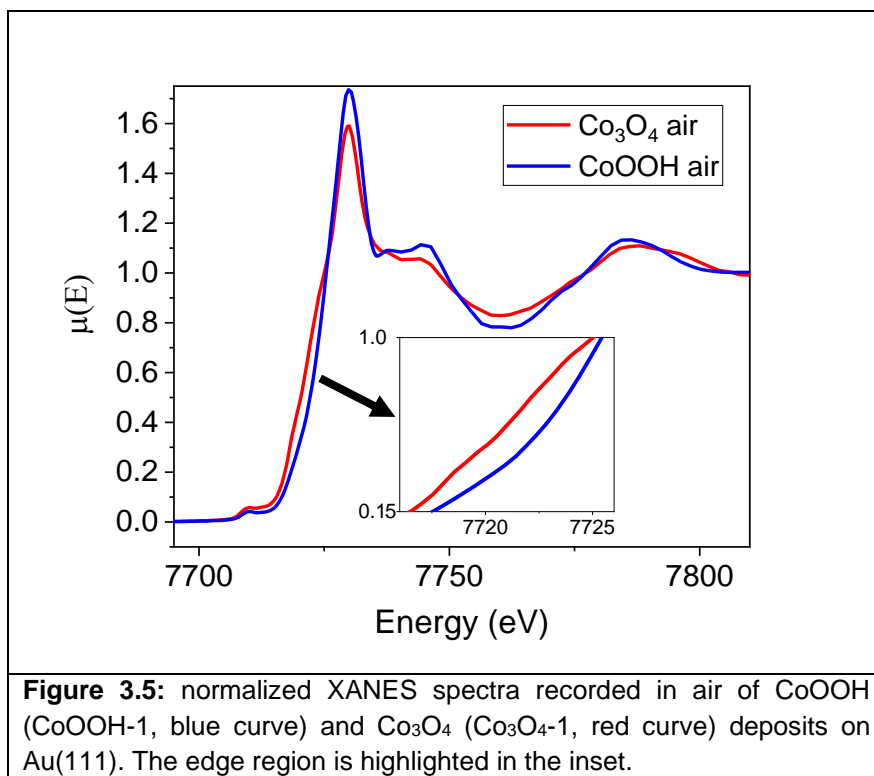
Table 3.1: Main structural, spectroscopic and morphological parameters of as prepared samples in air and in parenthesis in 0.1M NaOH at 0.97V: the first 2 columns give the structural parameters (in-plane and out-of-plane crystallite sizes), the next 2 columns give the spectroscopic parameters (E_{edge} and α). E_{edge} is determined with an accuracy of ± 0.1 eV and $\alpha \pm 0.03$. The last column gives the roughness factor (RF), defined as the ratio of the ECSA and the sample geometrical area, determined with AFM.

Sample	d_{\perp} (nm)	d_{\parallel} (nm)	E_{edge} (eV)	α	RF
Co ₃ O ₄ - 1	22	21	7720.69 (7720.95)	2.54 (2.62)	1.75
Co ₃ O ₄ - 2	29	21	7720.56 (7720.84)	2.5 (2.58)	n.a.
CoOOH - 1	15	29	7722.36 (7722.37)	3.02 (3.03)	1
CoOOH - 2	17	35	7722.30 (7722.34)	3.0 (3.02)	1

The SXRD characterizations conducted in air at the synchrotron confirm the epitaxial relationship between the electrodeposited oxides and Au(111). As detailed in **chapter 2.2**, the in-plane and out-of-plane crystallite sizes d_{\parallel} and d_{\perp} of the deposits are determined by analysing

2D images of oxides Bragg peaks. The structural parameters given here are extracted from $\text{Co}_3\text{O}_4(113)$ and $\text{CoOOH}(105)$ Bragg peaks images. d_{\perp} is the same parameter as the average XRD crystallite height determined with θ - 2θ scans, and both values agree well for the samples given in **Table 3.1**.

Figure 3.5 displays normalized XANES spectra measured in air at Co K-edge of as prepared Co_3O_4 and CoOOH deposits. The general shape of these spectra is consistent with that reported for the respective oxides in the literature [11,16,18,20,22]. One main difference between the two spectra is a larger Co edge energy of CoOOH (blue curve) as compared to Co_3O_4 (red curve). One also notes differences in the amplitude of oscillations for energies larger than 7.74 keV. This is most probably related to the different average coordination shells around the Co atoms within the two oxides. Using the method detailed in chapter **2.3**, the edge energies are found to be $E_{edge} = 7720.69 \pm 0.1$ eV and 7722.36 ± 0.1 eV, respectively for the Co_3O_4 -1 and CoOOH -1 layers. These values are converted into an average cobalt oxidation state α using the calibration plot shown in **Fig.2.15**, which respectively result in $\alpha = 2.54 \pm 0.03$ and $\alpha = 3.02 \pm 0.03$. Very similar values are found for the two Co_3O_4 and the two CoOOH samples respectively (see **Table 3.1**). **Table 3.1** also gives the α values measured when the samples are polarized at a potential of 0.97 V_{RHE} (in a solution of 0.1M NaOH). A value of α very close to 3 for CoOOH agrees very well with expectations. In the case of Co_3O_4 , α departs significantly from the expected 2.66 in air and comes closer to this ideal value after immersion in the electrolyte solution. This may be due to oxygen vacancies present in the as prepared sample which density may change upon sample immersion in the electrolyte.



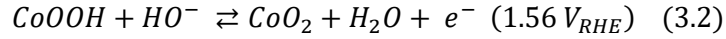
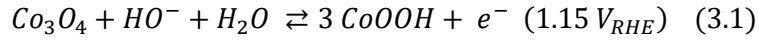
Oxides structure and Co oxidation state dependence with potential

The potential dependence of both the structure and the Co oxidation state of the oxides were studied in the XAS/XRD cell using the procedure described in chapter 2.3. We focus here on the pre-OER (0.97 – 1.6 V_{RHE}) and OER (1.6 - 1.67V_{RHE}) regimes by monitoring the oxides Bragg peaks changes and the Co fluorescence signal at a fixed incident X-ray energy around E_{edge} during potential sweeps between 0.97V and 1.67V.

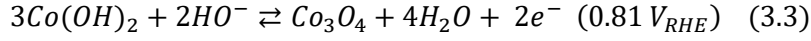
Figure 3.6 presents the cyclic voltammograms in 0.1 M NaOH electrolyte of the two oxides together with the analysis of operando XAS and SXRD data. The left and right columns respectively deal with Co₃O₄ (red) and CoOOH (blue). The reference state is that measured at 0.97V_{RHE}. The CVs, structural and oxidation state changes have been monitored during two potential sweeps at 5 mV/s. The filled and open symbols are data points of the first and second potential cycle respectively. Their overlap shows that the measurements are reproducible. The thick lines are polynomial fits to guide eye through the data points of the two cycles.

The XAS and SXRD operando data were recorded during CVs with the polymer membrane on. They are very similar to that measured without the membrane, except for a slightly higher ohmic drop, due to the thinner electrolyte layer on top of the sample. Oxygen Evolution Reaction onset potential is 1.6V_{RHE} (grey shaded area). Dashed lines define the thermodynamic stability domains [28] of the different cobalt oxides at pH 13. They are defined by the following redox reactions (Ref. 28):

Chapter 3



Co_3O_4 stability domain extends negative to the potential window shown here, and is limited by reaction (3.3):



In the pre-OER regime the CV of Co_3O_4 presents a pair of positive and negative waves at 1.52V which is consistent with the literature [2,11,27-29]. Only one redox wave around 1.15 V is visible in the CV of CoOOH and is also observed in that of Co_3O_4 .

The variations of Co oxidation state with potential $\alpha(U)$ are presented in **Figs 3.6c** and **d**. These plots show that $\alpha(U)$ increases continuously with increasing potential and that the main difference between the two types of oxides is a lower amplitude of the relative variation of α for CoOOH ($\frac{\Delta\alpha}{\alpha} \approx 0.3\%$) than for Co_3O_4 ($\frac{\Delta\alpha}{\alpha} \approx 1.5\%$). The variations are linear for CoOOH, while for Co_3O_4 the curve $\alpha(U)$ increases approximately linearly above 1.1 V. (These data were acquired with the operando procedure detailed in **Chap. 2, section 3**, and similar trends in Co oxidation state variations with potential were measured using the standard method detailed in chapter 2 (see an example in **Appendix A3.2**).

The lower part of the figure deals with the structural changes: the relative out-of-plane and in-plane crystallite sizes variations $\Delta d_{\perp}(U)$ and $\Delta d_{\parallel}(U)$ are respectively shown in **Figs. 3.6e** and **f** and **Figs. 3.6g** and **h**). In the case of $\text{Co}_3\text{O}_4(111)$, Δd_{\perp} and Δd_{\parallel} both decrease as a function of potential before OER potential (1.6V). Between 0.97V and 1.1-1.2 V, the crystallite size remains stable. At higher potentials, the crystallite size decreases in the direction parallel and perpendicular to the surface plane. The variations are almost linear with no specific changes at OER potential. At OER potential, $\Delta d_{\perp} = -0.5 \text{ nm}$ and $\Delta d_{\parallel} = -1 \text{ nm}$. This process is completely reversible since the initial crystallite dimensions are recovered while sweeping the potential back to 0.97V.

In parallel to above variations of the crystallite dimensions, a decrease of the lattice unit cell volume $\Delta V_{bulk}(U)$ is measured (**Figs. 3.6i** and **3.6j**) defined as $\Delta V_{bulk}\% = \Delta\varepsilon_{\perp}\% + 2\Delta\varepsilon_{\parallel}\%$ ($\Delta\varepsilon_{\perp}(U)$ and $\Delta\varepsilon_{\parallel}(U)$ are plotted separately in **Appendix A3.3**). The fact that ΔV_{bulk} decreases means that the unit cell volume contracts. This contraction is anisotropic since $\Delta\varepsilon_{\perp}(U) > \Delta\varepsilon_{\parallel}(U)$ (see **Appendix A3.3**). The potential induced reversible decrease of Δd_{\perp} and Δd_{\parallel} indicate that a $\sim 0.5 \text{ nm}$ thick surface region of the crystalline Co_3O_4 crystallites is transformed into a structurally disordered phase. This near surface region is called skin layer in the following. The structural transformation of Co_3O_4 begins at a potential that is close to the

standard potential of reaction (3.1) [28]. The fact that these changes are occurring before the OER imply that the OER active surface on Co_3O_4 (111) is not a (111) plane but a structurally disordered skin layer. In addition, the coupling between the skin layer formation and the unit cell volume contraction suggests that the internal strains are induced by the skin layer. The structural changes are perfectly reversible as long as the potential remains in the range [0.97 V – 1.67 V]. Irreversible changes are observed at more negative potentials. For Co_3O_4 , it has been shown previously that the oxide starts to be reduced into $\text{Co}(\text{OH})_2$ below $1V_{\text{RHE}}$. The phenomenon is yet reversible. However, below 0.8V, irreversible structural changes start to appear, especially a roughening of the film (see **Appendix A3.4** and [14]).

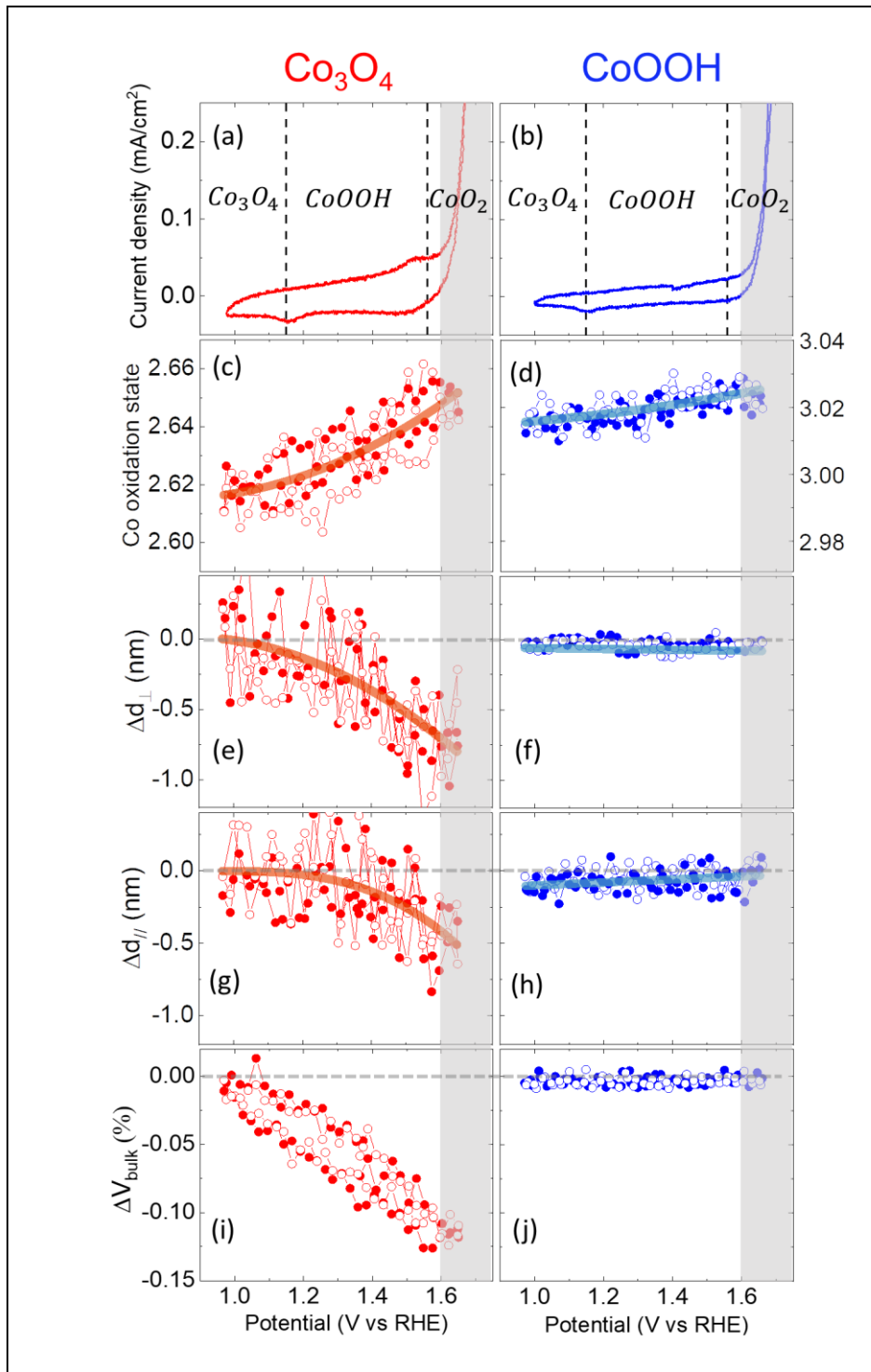
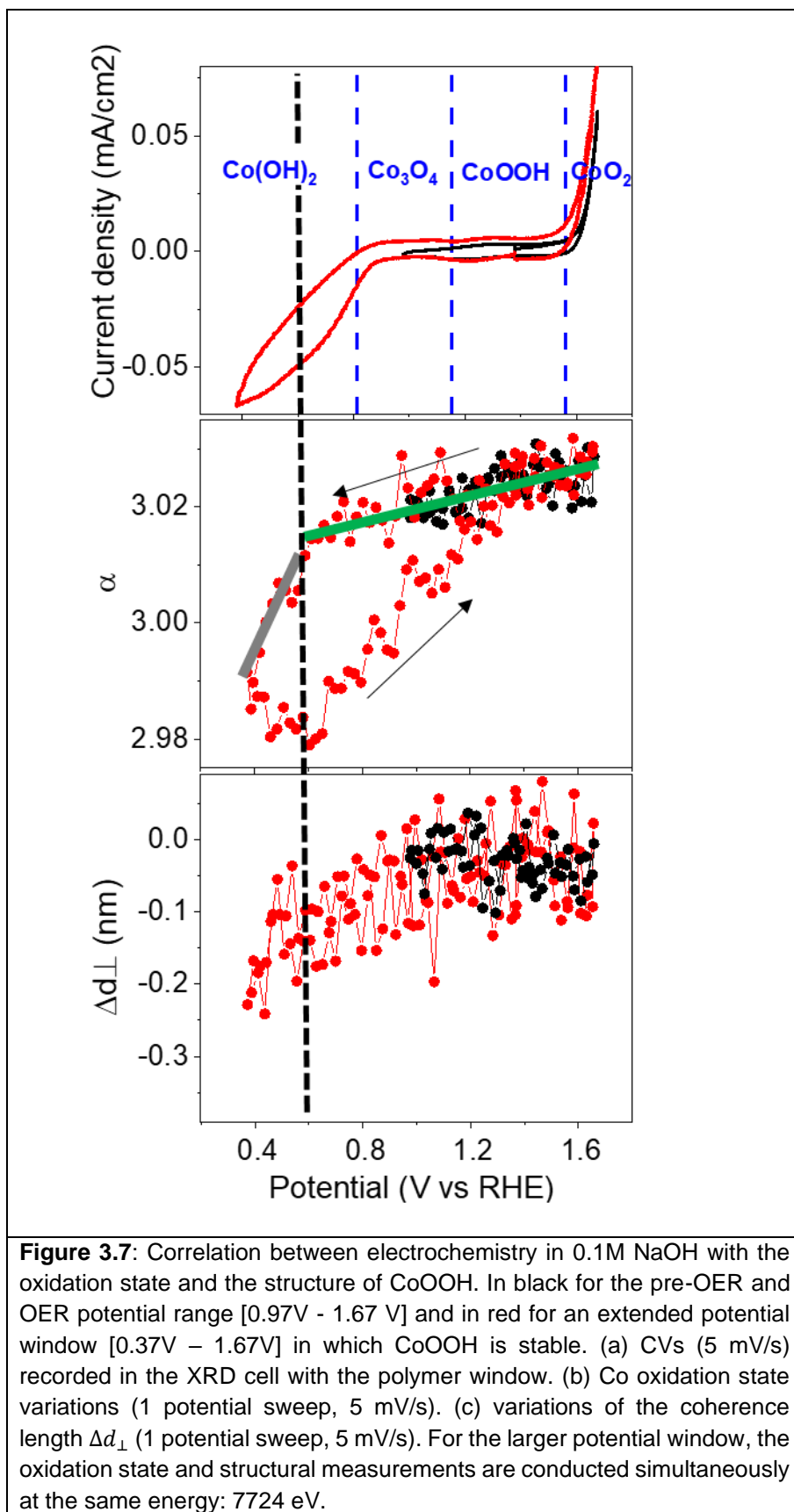


Figure 3.6: Correlation between electrochemistry in 0.1M NaOH with the oxidation state and the structure of Co_3O_4 (red, $\text{Co}_3\text{O}_4\text{-1}$) and CoOOH (blue, CoOOH-2) deposits. (a-b): CVs (5 mV/s) recorded in 0.1M NaOH in the electrochemical cell with the deflated polymer window. The grey shaded region highlights the OER regime and the cobalt oxides thermodynamic domains are delimited by dashed lines. (c-d): Co oxidation state as a function of potential (2 potential sweeps, 5 mV/s). (e-f), (g-h), (i-j): variations of the coherence lengths Δd_{\perp} , Δd_{\parallel} and relative variations of the unit cell volume $\Delta V_{\text{bulk}}\%$ (2 potential sweeps, 5 mV/s). The first cycle is shown with filled symbols and the second with open symbols.

By comparison, the CoOOH(001) layer remains structurally unchanged in the above potential range [0.97 V – 1.67 V] since Δd_{\perp} , Δd_{\parallel} ΔV_{bulk} do not show variations with potential. The deposit remains also stable down to 0.37 V. **Figure 3.7** compares the potential induced Co oxidation state and structural variations of CoOOH(001) in [0.97 V – 1.67 V] (black, same data as **Fig.3.6**) and in [0.37 V – 1.67 V] (red) potential windows. It shows in (a) the CVs, in (b) $\alpha(U)$ and in (c) $\Delta d_{\perp}(U)$ during a potential sweep (5mV/s) from 1.4 V down to 0.97 V (black curves) or 0.37V (red curve), then back to 1.67V and down to 1.4V (see black arrows). All plots overlay well in the common potential range [0.97 V - 1.67 V]. In the CV, the decrease in current below 0.85V is assigned to oxygen electrochemical reduction (the polymer membrane is not gas tight), and the thermodynamic stability domains of Co(OH)₂, CoOOH, Co₃O₄ and CoO₂ are delimited by dashed blue lines.

In the forward potential sweep, the red curve in **Fig.3.7b** shows two regimes of variations for α . Between 1.67V and 0.6V, the variations are linear with a slope which is the same as that measured in the range [1.67V – 0.97V], illustrated by a thick green line. Negative of 0.6V, α decreases also linearly with the potential but with a slope that is roughly 3 times larger (thick grey line). The potential of 0.6 V approximately marks the limit of CoOOH surface stability domain. Below this potential the surface starts to be converted into Co(OH)₂, that is the thermodynamically stable phase at this potential. This goes together with a slight decrease Δd_{\perp} , however it is difficult to determine clearly the structural changes associated with the transformation of CoOOH to Co(OH)₂ because both CoOOH and Co(OH)₂ have hexagonal structures with similar lattice parameters ($a_{CoOOH} = 0.285 \text{ nm}$ and $a_{Co(OH)_2} = 0.317 \text{ nm}$, $c_{CoOOH} = 1.315 \text{ nm}$ and $3c_{Co(OH)_2} = 1.392 \text{ nm}$). The changes associated with the conversion of a small fraction (~0.2 nm) of CoOOH in Co(OH)₂ would be within the noise of the measurement. A slight surface roughening induced by this transformation may explain the hysteretic behaviour of α while sweeping the potential back towards more positive values as well as the shift of OER onset towards lower potential for the red curve in **Fig3.7a**. The changes are yet reversible since the initial values of α and Δd_{\perp} are recovered at the end of the potential sweep. As a consequence, CoOOH(001) remains stable down to 0.6V_{RHE} with no significant structural changes and a linear variation of $\alpha(U)$ before the reduction of the film surface into Co(OH)₂.



Catalytic activity of Co_3O_4 and CoOOH :

Figure 3.8 shows iR corrected Tafel plots for (Co_3O_4 -1, red) and CoOOH (CoOOH – 2, blue) samples corresponding to CVs recorded in 0.1M NaOH without the polymer membrane, with a thick electrolyte layer on top of the sample to minimize the ohmic drop and allow relatively large OER currents. The samples were deposited on the same Au(111) crystal, ensuring the same large scale roughness and therefore a reliable comparison of their electrochemical properties. In **Fig.3.8**, the current density is given with respect to the electrochemical surface area (ECSA). To this end, the measured current density versus the geometrical area of the substrate is multiplied by the oxide's roughness factor (RF), defined as the ratio of the ECSA and the sample geometrical area (see **Table 3.1**). The two plots overlay, meaning that both types of oxides present a similar OER activity. This result is in agreement with reference [29,35]. The overpotential at a current density of $0.2\text{mA}/\text{cm}^2$ is 0.44V for both oxides and the Tafel slopes are 61 and 58 mV/decade, respectively for Co_3O_4 and CoOOH . These electrochemical data are summarized in **Table 3.2** below.

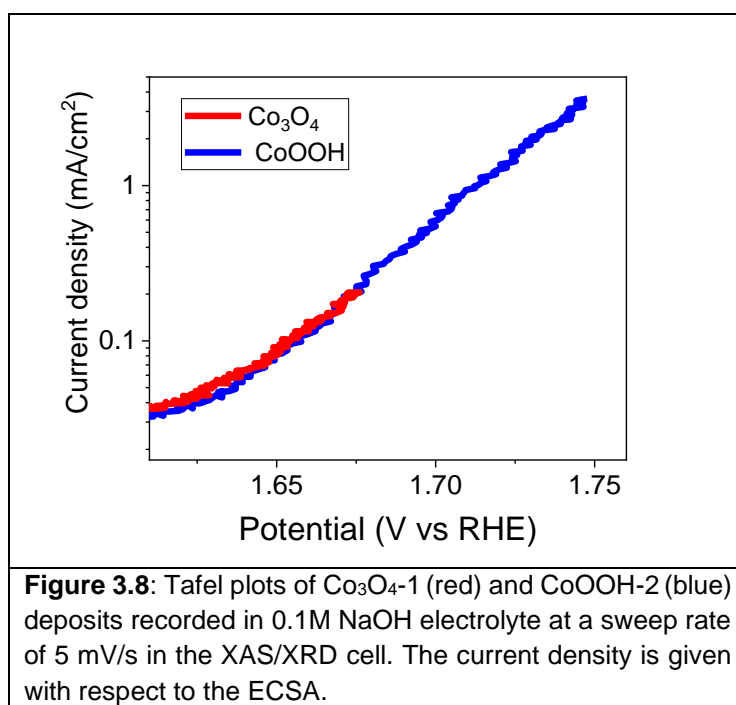


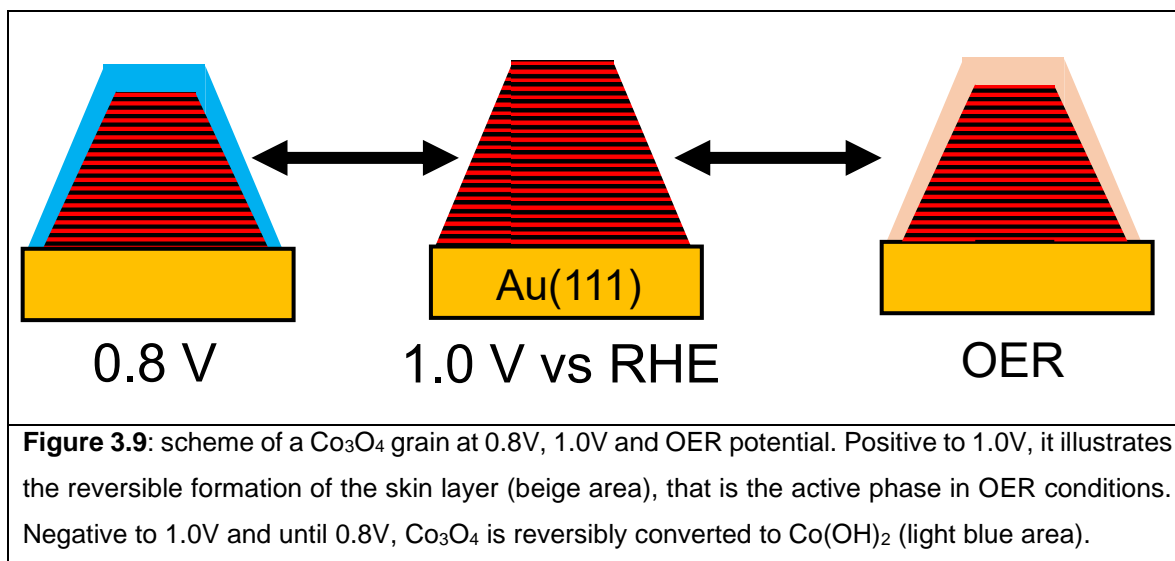
Table 3.2 Electrochemical properties of samples. RF is roughness factor, defined as the ratio of the ECSA and the geometrical surface of the electrode. b is the Tafel slope, η_{geo} and η_{ECSA} the overpotentials necessary to reach a current density of $0.2\text{mA}/\text{cm}^2$ and $0.2\text{mA}/\text{cm}^2_{\text{ECSA}}$ respectively.

Sample	RF	b (mV/dec)	η_{geo} (V)	η_{ECSA} (V)
Co_3O_4 - 1	1.75	61	0.425	0.44
CoOOH - 2	1	58	0.44	0.44

3.4 Discussion

Oxidation of $\text{Co}_3\text{O}_4(111)$: a skin effect

$\text{Co}_3\text{O}_4(111)$ thin films are composed of islands (see AFM image in **Fig.3.4**), which lateral dimension is larger than d_{\parallel} derived from XRD. This indicates that islands are composed of several crystallites although no grain boundary is resolved by AFM. **Figure 3.9** shows cartoons of one Co_3O_4 island at different potentials. According to **Fig. 3.6** and **Appendix A3.4**, the $\text{Co}_3\text{O}_4(111)$ islands undergo reversible variations of their dimensions in the potential range [0.8 V – 1.65 V]. Specifically, below 1 V, the island surface (top and side walls) is converted into $\text{Co}(\text{OH})_2$ over a sub-nm thickness (blue layer in the scheme on left). However, this layer is converted into crystalline Co_3O_4 by returning to 1V. Above 1.15 V, the top and side walls of Co_3O_4 islands start to be transformed into an X-ray amorphous phase (beige in the right scheme), the skin layer, which may be reduced back into crystalline Co_3O_4 by reversing the potential. This amorphization, also reported by Bergmann et al. [11], indicates that the Co atoms, mainly responsible for X-ray scattering, must move upon application of the potential above 1.15 V, forming a disordered phase.



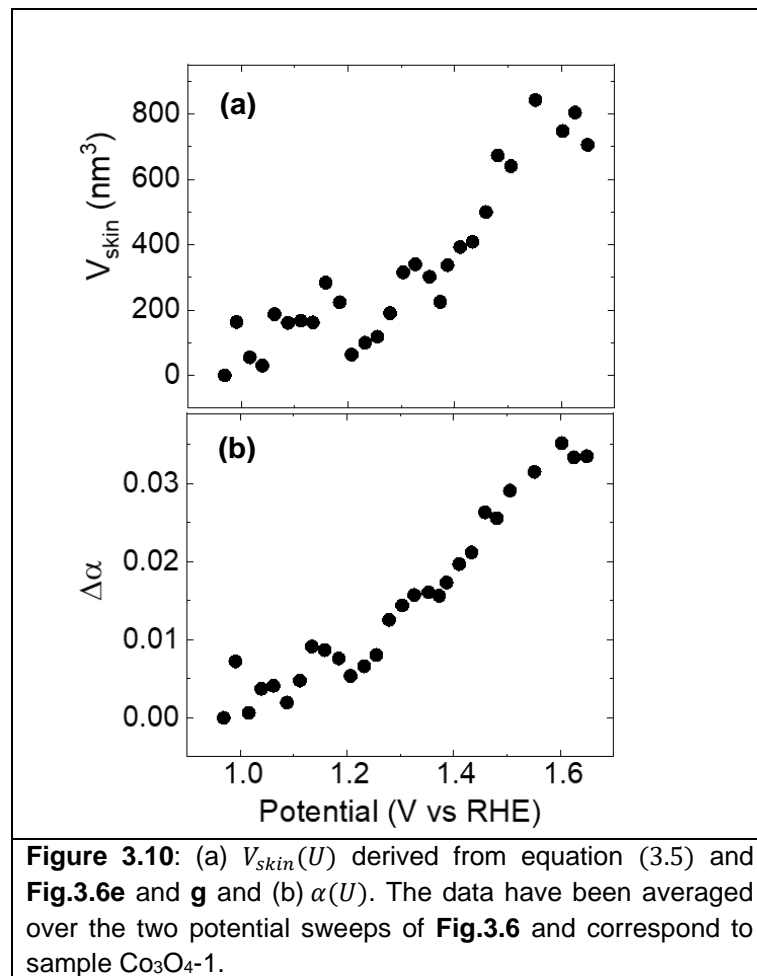
In this section, we will demonstrate that the oxidation state is close to +3 within the skin layer. To this end, we first address the one to one correlation between the variations of α , derived from XAS, and the volume of the skin layer, $V_{skin}(U)$, derived from SXRD. Using AFM images, $V_{skin}(U)$ may be estimated as explained in **Appendix A3.1** where the characteristic sizes of the prism (height and triangle side length) are the in plane and out of plane crystallite sizes d_{\parallel} and d_{\perp} (given in **Table 3.1**) The volume of one crystallite is given by equation (3.4).

$$V_{crystallite} = \frac{\sqrt{3}}{4} d_{\perp} d_{\parallel}^2 \quad (3.4)$$

Above 1.15 V, the crystallite has a core-shell structure (**Fig. 3.9**), the shell being the skin layer and the core is crystalline Co_3O_4 . The volume of the skin layer is the sum of a triangular prism of thickness Δd_{\perp} (on top) plus a volume corresponding to the difference between a prism of side length d_{\parallel} and one of side length $d_{\parallel} - \Delta d_{\parallel}$ (the sides). As a consequence, the skin volume $V_{skin}(U)$ can be written as:

$$V_{skin}(U) = \frac{\sqrt{3}}{4} \Delta d_{\perp}(U) \times d_{\parallel}^2 + \frac{\sqrt{3}}{2} \Delta d_{\parallel}(U) \times d_{\parallel} d_{\perp} \quad (3.5)$$

Figure 3.10 shows the variations of $V_{skin}(U)$ (a) and of the mean cobalt oxidation $\alpha(U)$ over the whole crystallite (b). To reduce the experimental noise, $\Delta\alpha(U)$ and $V_{skin}(U)$ have been averaged over the two potential cycles of **Fig.3.6c**. The interesting observation is that the variations of $\alpha(U)$ and $V_{skin}(U)$ follow similar potential induced trends with a low increase below 1.1-1.2V and a steeper evolution at more positive potentials. These findings suggest that the variations of $\alpha(U)$ most probably result from the change of the Co oxidation state in the skin layer only. The oxidation state of the rest of the film (the core part of Co_3O_4 crystallite) would remain unchanged in agreement with the fact that its structure is unaltered except for the small strain changes.



We may now determine the cobalt oxidation state $\alpha_{skin}(U)$ of Co atoms within the skin layer. The mean Co oxidation state $\alpha(U)$ of one individual Co_3O_4 crystallite is the sum of two contributions: (i) the oxidation state of Co atoms in the bulk (α_{bulk}) measured at $U = 0.97$ V which we will consider independent of the potential, and (ii) that of the skin layer (α_{skin}). These contributions are weighted by their respective volume, $V_{grain} - V_{skin}$ and V_{skin} . α can thus be written as follows:

$$\alpha(U) = \alpha_{skin}(U) \times \frac{V_{skin}(U)}{V_{grain}} + \alpha_{bulk} \times \frac{V_{grain} - V_{skin}(U)}{V_{grain}} \quad (3.6)$$

The variations of α as a function of potential can thus be written:

$$\Delta\alpha(U) = \frac{V_{skin}(U)}{V_{grain}} \times [\alpha_{skin}(U) - \alpha_{bulk}] \quad (3.7)$$

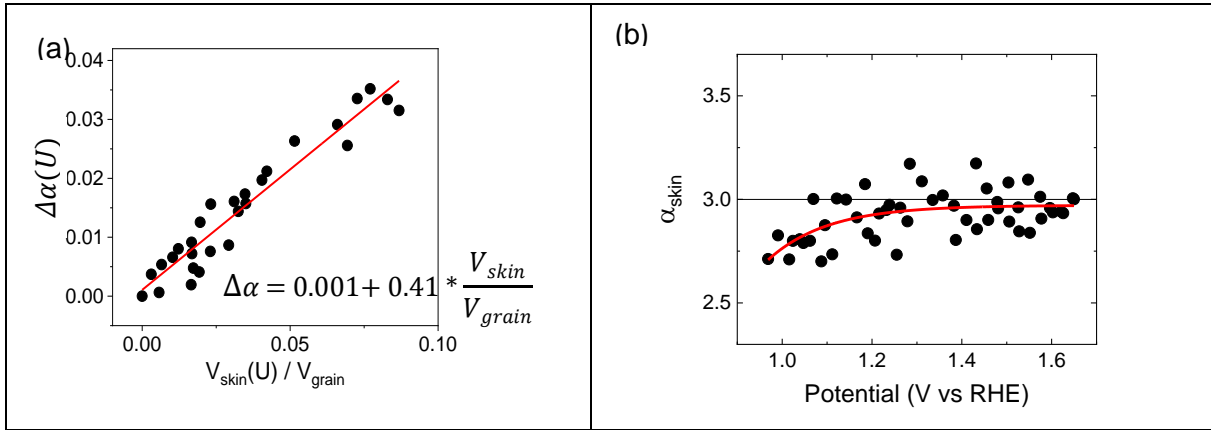


Figure 3.11: (a) Experimental variations in $[0.97 - 1.67 \text{ V}_{\text{RHE}}]$ of the relative oxidation state change $\Delta\alpha$ as a function of the ratio of skin and grain volume of Co_3O_4 . $\Delta\alpha$ and V_{skin}/V_{grain} potential dependence over the four sweeps 0.97 V to 1.67 V of the two potential cycles shown in **Figure 3.6** have been averaged. The red line is the linear fit which yields $\Delta\alpha = 0.001 + 0.41 * V_{skin}/V_{grain}$. (b) Skin layer oxidation state as a function of potential: $\alpha_{skin} = f(U)$ according to (3.8). The red line is an exponential fit of the experimental data and the black curve shows $\alpha_{skin} = 3$.

Figure 3.11 shows the variations of $\Delta\alpha(U)$ as a function of $\frac{V_{skin}(U)}{V_{grain}}$ for sample $\text{Co}_3\text{O}_4 - 1$ using the plots of **Fig.3.10**. This plot shows that $\Delta\alpha(U)$ may be fitted by a line with nearly zero-intercept (red line). The same data analysis has been performed on sample $\text{Co}_3\text{O}_4 - 2$ (shown in **Appendix A3.3**), and also results in a linear dependence. This yields an important conclusion: $\alpha_{skin}(U)$ is, in a first approximation, independent of the potential, meaning that the skin layer has a fixed oxidation state and the variations of α are essentially due to the change of the skin layer thickness. The slope of the linear fit in **Fig. 3.11** equals $\alpha_{skin}(U) - \alpha_{bulk} = 0.41$ yielding $\alpha_{skin}(U) = 3.03$ (**Table 3.3**). The analysis for sample $\text{Co}_3\text{O}_4 - 2$ yields a very similar value for $\alpha_{skin}(U)$ of 3.05 even though the two samples have different grain sizes and V_{skin} (see **Table 3.3** and **Appendix A3.3**). **Table 3.3** summarizes the parameters retrieved

and used for this analysis. To get more insight into the potential dependence of $\alpha_{skin}(U)$, we also plot $\alpha_{skin} = f(U)$ using equation (3.8), as shown in **Fig.3.11b**.

$$\alpha_{skin}(U) = \frac{V_{grain}}{V_{skin}(U)} \times \Delta\alpha(U) + \alpha_{bulk} \quad (3.8)$$

In spite of the scatter of the data points, we observe that $\alpha_{skin}(U)$ is around 2.7 at 1 V, increases to reach ~ 3 at 1.2 V and remains constant at this value until 1.7 V. In **Fig.3.11b**, the red curve is an exponential fit of the experimental data and the value of $\alpha_{skin} = 3$ is shown with a horizontal black line. This value as well as the shape of the curve are in agreement with the previous analysis stating that the skin layer, which is formed above 1.1-1.2V, has a fixed oxidation state. Since the skin layer formation is not measurable below 1.1-1.2V, the initial increase of $\alpha_{skin}(U)$ from 1.0V up to 1.2V may correspond to a transitional regime where surface Co atoms are slowly oxidized with increasing potential, via surface deprotonation for example. $\alpha_{skin}(1.0V)$ is slightly higher than α_{bulk} , which suggests that surface Co atoms may be a bit more oxidized than bulk Co at 1.0V.

Table 3.3: Selected parameters of Co_3O_4 samples. α_{bulk} is the Co mean oxidation state of the oxide at $U=0.97V$, the third column is the slope of the plot $\Delta\alpha(U)$ as a function of $V_{skin}(U)/V_{grain}$. α_{skin} is the oxidation state of the skin layer at 1.67 V, determined with equation (3.7), and the crystallite out of plane d_{\perp} size is taken as a measure of the average grain thickness.

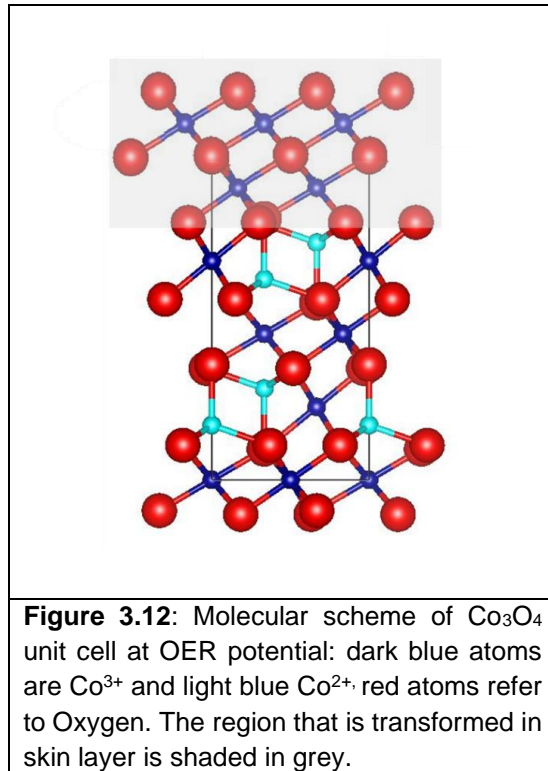
sample	α_{bulk}	Slope	α_{skin}	d_{\perp} (nm)
Co₃O₄ - 1	2.62 ± 0.03	0.41	3.03 ± 0.03	22
Co₃O₄ - 2	2.58 ± 0.03	0.47	3.05 ± 0.03	29

Consequently, the skin layer is exclusively containing Co^{3+} atoms at 1.6 V, which is the onset of OER. Co^{2+} atoms, which occupy tetrahedral sites, are oxidized and become unstable, which promotes atomic rearrangements to create a favourable local environment, close to the octahedral one in which Co^{3+} are stable. Not only Co atoms must move but also oxygen atoms must be inserted, which generates strains. The process is restricted to the first 2 Co^{2+} topmost atomic planes (**Fig. 3.2**) which contributes to make it reversible. A molecular scheme of this plausible atomic arrangement in one Co_3O_4 unit cell is shown in **Fig. 3.12**, with the skin layer highlighted in grey. In this scheme Co^{3+} atoms in the skin layer are in an octahedral environment, however in reality their environment might be more disordered. Our results therefore support the formation of a $\text{CoO}_x(\text{OH})_y$ phase that is often inferred in literature either from XAS [11,12], Raman Spectroscopy [31] or XPS [30]. Moreover, our results demonstrate that the skin is the result of the thermodynamics phase transition $\text{Co}_3\text{O}_4/\text{CoOOH}$. It must be emphasized that it is not promoted by OER. Even in the OER regime, this disordered near

surface region does not grow. This is the OER active phase on Co_3O_4 and it only contains Co^{3+} since the deviation of α_{skin} from 3 is practically within the error bar and would correspond to a proportion of Co^{4+} of less than 1.5%. There is therefore no indication of Co^{4+} within the accuracy of the measurements. However, the pre-OER region of Co_3O_4 CV (**Fig. 3.6**) exhibits a peak at 1.55V, which is often attributed to $\text{Co}^{3+} \rightarrow \text{Co}^{4+}$ transition [11,27,29]. In **Fig 3.6a** for Co_3O_4 -1, the charge under this peak is 0.06 mC/cm^2 which represents $3.8 \cdot 10^{14} \text{Co}^{4+}/\text{cm}^2$ considering that the peak corresponds to $\text{Co}^{3+} \rightarrow \text{Co}^{4+}$. As a comparison, one can estimate the concentration of Co atoms contained in Co_3O_4 skin layer. The latter will be called N_{skin}^{Co} and can be estimated with the following equation:

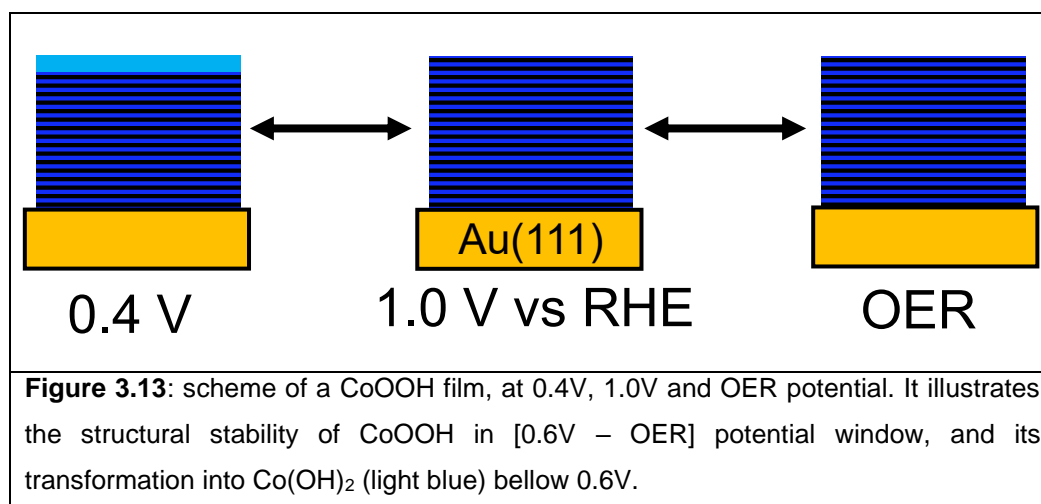
$$N_{skin}^{Co} = V_{skin}(1.67V) \times \rho_{Co_3O_4} \times N_{grain} \quad (3.9)$$

where $\rho_{Co_3O_4}$ is the Co density per nm^3 in Co_3O_4 and N_{grain} the number of Co_3O_4 grains per cm^2 of electrode. For Co_3O_4 -1, we find $N_{skin}^{Co} = 8.75 \cdot 10^{15} \text{Co}/\text{cm}^2$. Therefore, the number of Co^{4+} estimated from the area under the peak at 1.55V in the pre-OER regime of the CV would represent approximately 4% of all Co atoms within the skin layer. This is higher than 1.5% of Co^{4+} estimated from XAS measurements but still remains reasonably close to this value. In addition, the calculation above should be considered with precaution since it approximates Co density in the skin layer by that of Co_3O_4 which might not be the case. Overall, the presence and shape of this CV peak suggests that the skin layer mainly consists of Co^{3+} with probably a low amount of Co^{4+} .



Oxidation of CoOOH(001): a deprotonation effect

CoOOH(001) films are structurally stable in a wider potential window than Co₃O₄. As the films are very flat and smooth (see AFM image in **Fig.3.4**), they can be pictured as a 2D films, as illustrated in **Figure 3.13** CoOOH is stable below 1.15 V, where Co₃O₄ should form (reaction 3.2). The absence of any sizable phase transformation CoOOH → Co₃O₄ may be explained by two facts: (i) It requires complex atomic rearrangements since the bulk structure of Co₃O₄ is rather different from the layered structure of CoOOH (see **section 3.2**); (ii) To proceed, the reaction needs surface defects which are in low density. In fact, the CoOOH (001) surface is atomically smooth and atomic steps, from where the reaction should start, represent only a few % of surface atoms. Both factors contribute to hinder the reaction CoOOH → Co₃O₄. The transformation CoOOH → Co(OH)₂ should be easier because both phases present a layered structure with similar lattice parameters (see above), the main difference being an additional hydrogen per Co atom. It is inferred that the transformation is hindered for kinetic reasons (low density of surface defects), it therefore takes places at potential negative to 0.6V. At the reference potential of 1.0V, CoOOH is therefore kinetically stable.



The fact that structure of CoOOH deposits remains unchanged in the pre-OER and OER regimes and that the variations of $\alpha(U)$ are linear and 5 times smaller than for Co₃O₄ suggest that the latter stems from Co atoms at the CoOOH surface exclusively. As detailed in section 3.2 (**Fig.3.2**), the oxidation state of the Co surface atoms is related to the hydrogen surface coverage (hereafter called θ). Indeed, the charge balance of Co and O atoms at the surface differs from that of the bulk CoOOH. Bulk Co atoms are six-fold coordinated with OH_{0.5} groups, themselves shared by three Co atoms, therefore, the mean cobalt oxidation state in the bulk is : $\alpha_{bulk} = 3$. At the surface, Co atoms of the top Co plane have a mean oxidation state α_{surf} which depends on the protonation state of the oxygen groups (O or OH) in the topmost O-

plane. For example, $\alpha_{surf} = 3$ for a half-protonated surface ($\theta = 50\%$). The relationship between θ and α_{surf} may be written as:

$$\alpha_{surf} = 2.5 \times \theta + 3.5 \times (1 - \theta) \quad (3.10)$$

If θ varies with potential, so will α_{surf} and α , but not the structure of CoOOH, which makes it a plausible interpretation of the operando SXRD and XAS data.

The H coverage of the CoOOH(001) surface has already been addressed in literature using ab initio calculations. Chen et al. performed DFT calculations for 3 different θ values 0%, 50% and 100%, and showed that $\theta = 50\%$ in a 1.4V large potential window but they did not determine a fine dependence of θ in this large potential range [23]. More recent DTF calculations combined with molecular dynamics (DFT-MD) [34], which explicitly include the liquid water dynamics, examined the dependence over time of θ for different initial θ value. Results showed that a CoOOH surface in contact with water and with an initial θ value of 50% is stable with time. In all other cases, θ varies with time, indicating that the surfaces undergo interface reactions with water which modify their initial hydrogen coverage.

In the following, we will use the experimental $\alpha(U)$ to estimate θ as a function of potential. Since α is the mean Co oxidation state of a very flat CoOOH sample composed of n Co planes, α and α_{surf} are related by equation (3.11):

$$\alpha = \frac{n-1}{n} \times \alpha_{bulk} + \frac{1}{n} \times \alpha_{surf} \quad (3.11)$$

Where $\alpha_{bulk} = 3$ and $n = \frac{d_{\perp}(nm)}{0.438}$ because the distance between two Co planes in CoOOH is 0.438 nm (see **Fig.3.2a**). Using (3.10) and (3.11), we can express θ as a function of α :

$$\theta = 0.5 - n \times (\alpha - 3) \quad (3.12)$$

Since $\alpha(U)$ is linear in **Fig.3.6d**, equation (3.12) shows that θ also varies linearly with potential.

Let us first estimate the variations of θ : $\frac{\Delta\theta(U)}{\Delta U}$ which can be written:

$$\frac{\Delta\theta(U)}{\Delta U} = -n \times \frac{\Delta\alpha(U)}{\Delta U} \quad (3.13)$$

Equation (3.13) yields $\frac{\Delta\theta(U)}{\Delta U}$ with a very good accuracy since the estimation of $\frac{\Delta\alpha(U)}{\Delta U}$ from the linear fit of **Fig.3.6d** and that of n from the width of the diffraction peak are very precise ($\frac{\Delta\theta(U)}{\Delta U} \pm 2.5 * 10^{-3}$). However, the precision on the absolute value of θ is limited by the uncertainty of determining α from the XAS spectrum which is ± 0.03 . Indeed, a variation of θ by 1 (fully protonated to fully deprotonated) results in an α variation of $\frac{1}{n}$, in the range $\sim 0.025 - 0.03$ for

our samples. Therefore, to estimate the value of $\theta(U)$, one needs to make an assumption on the value of θ at a specific potential. As shown in **Fig.3.7**, the potential of $0.6V_{\text{RHE}}$ marks the beginning of the reduction of CoOOH into $\text{Co}(\text{OH})_2$ i.e. of Co^{3+} into Co^{2+} . This suggests that $\theta = 100\%$ at 0.6 V . We can thus estimate θ as a function of potential U with (3.14):

$$\theta(U) = 1 - n \frac{\Delta\alpha(U)}{\Delta U} (U - 0.6) \quad (3.14)$$

Table 3.4 gives the experimental parameters ($\frac{\Delta\alpha}{\Delta U}$, n) of the two CoOOH deposits mandatory to determine $\theta(U)$ and $\alpha(U)$.

The calculation yields the H-coverages in the pre-OER regime of **Fig.3.6** $\theta(U = 0.97\text{ V})$ and $\theta(U = 1.67\text{ V})$. The surface H-coverage varies from $\sim 80\%$ at 0.97 V to $\sim 55\%$ at the onset of OER conditions (1.67 V). These fine variations could not be observed in other reports. $\theta(1.67\text{ V})$ is 60% for CoOOH-1 and 51% for CoOOH-2 sample. They are in reasonable agreement the one with the other and indicate that the majority of Co surface atoms are Co^{3+} , meaning that according to our assumptions, the amount of Co^{4+} is below the detection limit at OER potential at the surface of CoOOH . The atomic arrangement of CoOOH at OER potential is pictured in **Fig.3.14** with the surface where OER takes place shaded in grey.

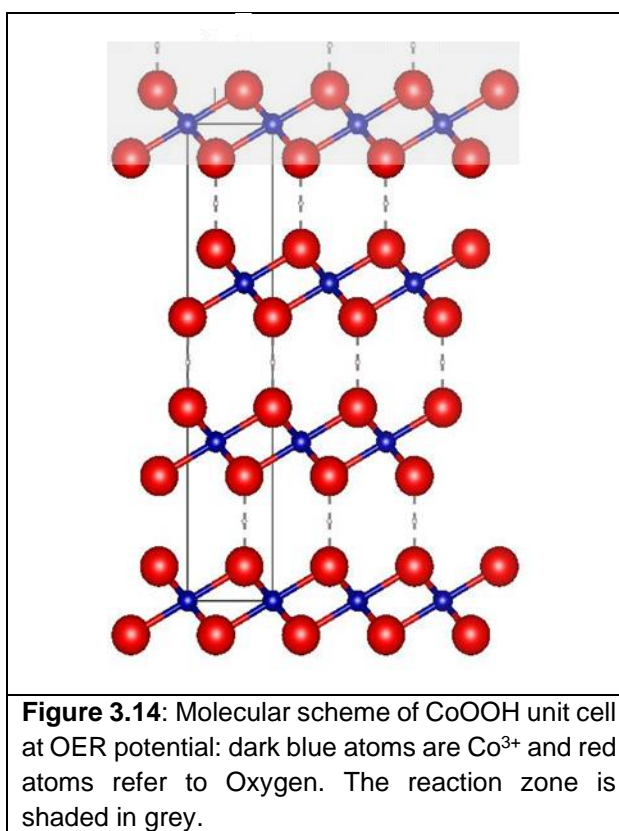


Table 3.4: Selected parameters of CoOOH samples. n is the number of layers in the CoOOH deposit considered and $\Delta\alpha/\Delta U$ is the experimental amplitude of variations of the cobalt oxidation state per Volt. θ is the calculated surface coverage of OH groups at a potential U (Eq. (3.14)) and α_{surf} is the corresponding oxidation state of surface cobalt.

Sample	n	$\Delta\alpha/\Delta U$ (V^{-1})	$\theta(0.97 V)$	$\theta(1.67 V)$	$\alpha_{surf}(1.67 V)$
CoOOH - 1	34.2	0.011	85 %	60 %	2.90
CoOOH - 2	38.8	0.012	81 %	51 %	2.99

Co oxides surface oxidation state and OER activity

One important consequence of the above analysis is the negligible amount of Co^{4+} sites detected within the skin on Co_3O_4 and at the surface of CoOOH: their quantity remains $\leq 5\%$ of surface sites even at the OER onset. This contrasts with previous studies where a significant fraction ($\sim 20\%$) of Co^{4+} was found [8,12,32,36,37].

This difference (between XAS measurements) could first result from different Co oxidation state calibration. For example, Dau et al. [8] measured that Co oxidation state increase from +2 to +3 corresponds to a shift of 2.3 eV of the main absorption edge while we measured a shift of 3.4 eV. Using their calibration, our variations of $\Delta\alpha(U)$ would be ~ 1.5 times larger and result to a higher amount of Co^{4+} at OER onset. However, the references used for calibration have been measured several times and reproducibly give the calibration shown in **section 2.3**.

The absence of a sizeable amount of Co^{4+} sites might be also due to their lifetime. According to the OER mechanism shown in **Fig.3.1**, the formation of Co^{4+} at the active sites is expected during the OER catalytic process. The mechanism corresponds to a constant equilibrium of oxidation/reduction in which Co^{3+} and Co^{4+} co-exist. Each reaction intermediate has a finite lifetime, which differ the one from the others according to the rate of each step, and the intermediates with the highest lifetime are those involved in the rate determining step. The steady state density of Co^{4+} can be estimated as the product of their lifetime during the OER catalytic cycle and the density of surface sites involved in OER mechanism (active sites). The density of Co^{4+} sites therefore increases with the number of active sites and/or their lifetime during the catalytic cycle. The higher amount of Co^{4+} found in other works might therefore be explained by two facts: (i) the density of active sites on the surface of these materials is higher than for our samples and/or (ii) the rate determining step of OER is different for these materials to promote a longer lifetime of Co^{4+} species. Compared to other catalysts such as CoCat for which a significant amount of Co^{4+} was measured, the density of active sites may be substantially lower on $Co_3O_4(111)$ and $CoOOH(001)$ surfaces. Dau et al. [8] indeed suggested that Co ions at the margin of CoCat motif are oxidized with increasing potential and participate to OER reaction. In our case, the proportion of Co atoms at step edges is of the order of $\sim 2\%$

for CoOOH. It is expected to be larger for Co₃O₄ but it is difficult to estimate precisely because of the rather vertical island facets, the difficulty to image atomic steps on such island morphology and the unknown morphology and atomic environment in the skin layer.

We have also seen that the catalytic activity of Co₃O₄ and CoOOH are very similar when the ECSA is taken into account (**Fig. 3.8**), which is consistent with their similar Co³⁺ content at OER potential. Since the skin layer of Co₃O₄ is supposed to be disordered, this also suggests that either the proportion of the Co atoms at defects sites (μ_2 -O sites) is the same for the two materials after surface normalization, or the μ_2 -O sites and μ_3 -O sites are as OER active. The first scenario does not seem credible given the disordered structure of the skin layer, which makes the second one plausible.

3.4 Conclusions

In this chapter we have described operando SXRDXAS measurements performed on cobalt oxide layers in epitaxy with Au(111). For both of them, operando XAS evidenced a progressive and small increase of the average Co oxidation state starting in pre-OER regime. The use of well-defined films and simultaneous operando SXRDXAS characterizations enabled a quantitative interpretation of XAS data. For Co₃O₄, a skin layer is forming due to the oxidation of Co²⁺ into Co³⁺ near the surface. The process is restricted to the first 2-3 atomic planes and all Co centers in this region are +3. In the case of CoOOH, which is structurally stable, XAS data indicate a progressive deprotonation of the surface, which is about 50% protonated in OER conditions. For both oxides, the amount of Co⁴⁺ remains marginal, which may be attributed to their low density of step edges sites where Co⁴⁺ would be formed.

3.5 Bibliography

- [1] Song, F.; Bai, L.; Moysiadou, A.; Lee, S.; Hu, C.; Liardet, L.; Hu, X. Transition Metal Oxides as Electrocatalysts for the Oxygen Evolution Reaction in Alkaline Solutions: An Application-Inspired Renaissance. *J. Am. Chem. Soc.* **2018**, *140* (25), 7748–7759. <https://doi.org/10.1021/jacs.8b04546>.
- [2] Doyle, R. L.; Godwin, I. J.; Brandon, M. P.; Lyons, M. E. G. Redox and electrochemical water splitting catalytic properties of hydrated metal oxide modified electrodes. *Phys. Chem. Chem. Phys.* **2013**, *15* (33), 13737–13783. <https://doi.org/10.1039/c3cp51213d>.
- [3] Gerken, J. B.; McAlpin, J. G.; Chen, J. Y. C.; Rigsby, M. L.; Casey, W. H.; Britt, R. D.; Stahl, S. S. Electrochemical water oxidation with cobalt-based electrocatalysts from pH 0-14: The thermodynamic basis for catalyst structure, stability, and activity. *J. Am. Chem. Soc.* **2011**, *133* (36), 14431–14442. <https://doi.org/10.1021/ja205647m>.

- [4] Surendranath, Y.; Kanan, M. W.; Nocera, D. G. Mechanistic studies of the oxygen evolution reaction by a cobalt-phosphate catalyst at neutral pH. *J. Am. Chem. Soc.* **2010**, *132* (46), 16501–16509. <https://doi.org/10.1021/ja106102b>.
- [5] Zhang, M.; De Respini, M.; Frei, H. Time-resolved observations of water oxidation intermediates on a cobalt oxide nanoparticle catalyst. *Nat. Chem.* **2014**, *6* (4), 362–367. <https://doi.org/10.1038/nchem.1874>.
- [6] Van Oversteeg, C. H. M.; Doan, H. Q.; De Groot, F. M. F.; Cuk, T. In situ X-ray absorption spectroscopy of transition metal based water oxidation catalysts. *Chem. Soc. Rev.* **2017**, *46* (1), 102–125. <https://doi.org/10.1039/c6cs00230g>.
- [7] Chang, C. J.; Zhu, Y.; Wang, J.; Chen, H. C.; Tung, C. W.; Chu, Y. C.; Chen, H. M. In situ X-ray diffraction and X-ray absorption spectroscopy of electrocatalysts for energy conversion reactions. *J. Mater. Chem. A* **2020**, *8* (37), 19079–19112. <https://doi.org/10.1039/d0ta06656g>.
- [8] Risch, M.; Ringleb, F.; Kohlhoff, M.; Bogdanoff, P.; Chernev, P.; Zaharieva, I.; Dau, H. Water oxidation by amorphous cobalt-based oxides: In situ tracking of redox transitions and mode of catalysis. *Energy Environ. Sci.* **2015**, *8* (2), 661–674. <https://doi.org/10.1039/c4ee03004d>.
- [9] Ullman, A. M.; Brodsky, C. N.; Li, N.; Zheng, S. L.; Nocera, D. G. Probing Edge Site Reactivity of Oxidic Cobalt Water Oxidation Catalysts. *J. Am. Chem. Soc.* **2016**, *138* (12), 4229–4236. <https://doi.org/10.1021/jacs.6b00762>.
- [10] Pasquini, C.; D'Amario, L.; Zaharieva, I.; Dau, H. Operando Raman spectroscopy tracks oxidation-state changes in an amorphous Co oxide material for electrocatalysis of the oxygen evolution reaction. *J. Chem. Phys.* **2020**, *152* (19), 194202. <https://doi.org/10.1063/5.0006306>.
- [11] Bergmann, A.; Martinez-Moreno, E.; Teschner, D.; Chernev, P.; Gliech, M.; De Araújo, J. F.; Reier, T.; Dau, H.; Strasser, P. Reversible amorphization and the catalytically active state of crystalline Co₃O₄ during oxygen evolution. *Nat. Commun.* **2015**, *6*. <https://doi.org/10.1038/ncomms9625>.
- [12] Bergmann, A.; Jones, T. E.; Martinez Moreno, E.; Teschner, D.; Chernev, P.; Gliech, M.; Reier, T.; Dau, H.; Strasser, P. Unified structural motifs of the catalytically active state of Co(oxyhydr)oxides during the electrochemical oxygen evolution reaction. *Nat. Catal.* **2018**, *1* (9), 711–719. <https://doi.org/10.1038/s41929-018-0141-2>.
- [13] Friebel, D.; Bajdich, M.; Yeo, B. S.; Louie, M. W.; Miller, D. J.; Sanchez Casalongue, H.; Mbuga, F.; Weng, T. C.; Nordlund, D.; Sokaras, D.; Alonso-Mori, R.; Bell, A. T.; Nilsson, A. On the chemical state of Co oxide electrocatalysts during alkaline water splitting. *Phys. Chem. Chem. Phys.* **2013**, *15* (40), 17460–17467. <https://doi.org/10.1039/c3cp52981a>.
- [14] Reikowski, F.; Maroun, F.; Pacheco, I.; Wiegmann, T.; Allongue, P.; Stettner, J.; Magnussen, O. M. Operando Surface X-ray Diffraction Studies of Structurally Defined Co₃O₄ and CoOOH Thin Films during Oxygen Evolution. *ACS Catal.* **2019**, *9* (5), 3811–3821. <https://doi.org/10.1021/acscatal.8b04823>.

- [15] Wang, H. Y.; Hung, S. F.; Chen, H. Y.; Chan, T. S.; Chen, H. M.; Liu, B. In Operando Identification of Geometrical-Site-Dependent Water Oxidation Activity of Spinel Co₃O₄. *J. Am. Chem. Soc.* **2016**, *138* (1), 36–39. <https://doi.org/10.1021/jacs.5b10525>.
- [16] Xiao, Z.; Huang, Y. C.; Dong, C. L.; Xie, C.; Liu, Z.; Du, S.; Chen, W.; Yan, D.; Tao, L.; Shu, Z.; Zhang, G.; Duan, H.; Wang, Y.; Zou, Y.; Chen, R.; Wang, S. Operando Identification of the Dynamic Behavior of Oxygen Vacancy-Rich Co₃O₄ for Oxygen Evolution Reaction. *J. Am. Chem. Soc.* **2020**, *142* (28), 12087–12095. <https://doi.org/10.1021/jacs.0c00257>.
- [17] Ortiz Peña, N.; Ihiwakrim, D.; Han, M.; Lassalle-Kaiser, B.; Carencio, S.; Sanchez, C.; Laberty-Robert, C.; Portehault, D.; Ersen, O. Morphological and Structural Evolution of Co₃O₄ Nanoparticles Revealed by in Situ Electrochemical Transmission Electron Microscopy during Electrocatalytic Water Oxidation. *ACS Nano* **2019**, *13* (10), 11372–11381. <https://doi.org/10.1021/acsnano.9b04745>.
- [18] Seo, B.; Sa, Y. J.; Woo, J.; Kwon, K.; Park, J.; Shin, T. J.; Jeong, H. Y.; Joo, S. H. Size-Dependent Activity Trends Combined with in Situ X-ray Absorption Spectroscopy Reveal Insights into Cobalt Oxide/Carbon Nanotube-Catalyzed Bifunctional Oxygen Electrocatalysis. *ACS Catal.* **2016**, *6* (7), 4347–4355. <https://doi.org/10.1021/acscatal.6b00553>.
- [19] Zhou, J.; Wang, Y.; Su, X.; Gu, S.; Liu, R.; Huang, Y.; Yan, S.; Li, J.; Zhang, S. Electrochemically accessing ultrathin Co (oxy)-hydroxide nanosheets and: Operando identifying their active phase for the oxygen evolution reaction. *Energy Environ. Sci.* **2019**, *12* (2), 739–746. <https://doi.org/10.1039/c8ee03208d>.
- [20] Huang, J.; Chen, J.; Yao, T.; He, J.; Jiang, S.; Sun, Z.; Liu, Q.; Cheng, W.; Hu, F.; Jiang, Y.; Pan, Z.; Wei, S. CoOOH Nanosheets with High Mass Activity for Water Oxidation. *Angew. Chemie - Int. Ed.* **2015**, *54* (30), 8722–8727. <https://doi.org/10.1002/anie.201502836>.
- [21] Bajdich, M.; García-Mota, M.; Vojvodic, A.; Nørskov, J. K.; Bell, A. T. Theoretical investigation of the activity of cobalt oxides for the electrochemical oxidation of water. *J. Am. Chem. Soc.* **2013**, *135* (36), 13521–13530. <https://doi.org/10.1021/ja405997s>.
- [22] Mattioli, G.; Risch, M.; Amore Bonapasta, A.; Dau, H.; Guidoni, L. Protonation states in a cobalt-oxide catalyst for water oxidation: Fine comparison of ab initio molecular dynamics and X-ray absorption spectroscopy results. *Phys. Chem. Chem. Phys.* **2011**, *13* (34), 15437–15441. <https://doi.org/10.1039/c1cp21776c>.
- [23] Chen, J.; Selloni, A. First principles study of cobalt (Hydr)oxides under electrochemical conditions. *J. Phys. Chem. C* **2013**, *117* (39), 20002–20006. <https://doi.org/10.1021/jp406331h>.
- [24] Pham, H. H.; Cheng, M. J.; Frei, H.; Wang, L. W. Surface Proton Hopping and Fast-Kinetics Pathway of Water Oxidation on Co₃O₄ (001) Surface. *ACS Catal.* **2016**, *6* (8), 5610–5617. <https://doi.org/10.1021/acscatal.6b00713>.

- [25] Kanan, M. W.; Nocera, D. G. In situ formation of an oxygen-evolving catalyst in neutral water containing phosphate and Co^{2+} . *Science* (80-.). **2008**, *321* (5892), 1072–1075. <https://doi.org/10.1126/science.1162018>.
- [26] Risch, M.; Klingan, K.; Ringleb, F.; Chernev, P.; Zaharieva, I.; Fischer, A.; Dau, H. Water oxidation by electrodeposited cobalt oxides-role of anions and redox-inert cations in structure and function of the amorphous catalyst. *ChemSusChem* **2012**, *5* (3), 542–549. <https://doi.org/10.1002/cssc.201100574>.
- [27] Faisal, F.; Bertram, M.; Stumm, C.; Cherevko, S.; Geiger, S.; Kasian, O.; Lykhach, Y.; Lytken, O.; Mayrhofer, K. J. J.; Brummel, O.; Libuda, J. Atomically Defined $\text{Co}_3\text{O}_4(111)$ Thin Films Prepared in Ultrahigh Vacuum: Stability under Electrochemical Conditions. *J. Phys. Chem. C* **2018**, *122* (13), 7236–7248. <https://doi.org/10.1021/acs.jpcc.8b00558>.
- [28] Behl, W. K.; Toni, J. E. Anodic oxidation of cobalt in potassium hydroxide electrolytes. *J. Electroanal. Chem.* **1971**, *31* (1), 63–75. [https://doi.org/10.1016/S0022-0728\(71\)80043-8](https://doi.org/10.1016/S0022-0728(71)80043-8).
- [29] Koza, J. A.; He, Z.; Miller, A. S.; Switzer, J. A. Electrodeposition of crystalline Co_3O_4 -A catalyst for the oxygen evolution reaction. *Chem. Mater.* **2012**, *24* (18), 3567–3573. <https://doi.org/10.1021/cm3012205>.
- [30] Favaro, M.; Yang, J.; Nappini, S.; Magnano, E.; Toma, F. M.; Crumlin, E. J.; Yano, J.; Sharp, I. D. Understanding the Oxygen Evolution Reaction Mechanism on CoO_x using Operando Ambient-Pressure X-ray Photoelectron Spectroscopy. *J. Am. Chem. Soc.* **2017**, *139* (26), 8960–8970. <https://doi.org/10.1021/jacs.7b03211>.
- [31] Yeo, B. S.; Bell, A. T. Enhanced activity of gold-supported cobalt oxide for the electrochemical evolution of oxygen. *J. Am. Chem. Soc.* **2011**, *133* (14), 5587–5593. <https://doi.org/10.1021/ja200559j>.
- [32] Moysiadou, A.; Lee, S.; Hsu, C. S.; Chen, H. M.; Hu, X. Mechanism of Oxygen Evolution Catalyzed by Cobalt Oxyhydroxide: Cobalt Superoxide Species as a Key Intermediate and Dioxygen Release as a Rate-Determining Step. *J. Am. Chem. Soc.* **2020**, *142* (27), 11901–11914. <https://doi.org/10.1021/jacs.0c04867>.
- [33] Risch, M.; Khare, V.; Zaharieva, I.; Gerencser, L.; Chernev, P.; Dau, H. Cobalt-oxo core of a water-oxidizing catalyst film. *J. Am. Chem. Soc.* **2009**, *131* (20), 6936–6937. <https://doi.org/10.1021/ja902121f>.
- [34] Creazzo, F.; Oxygen evolution reaction at cobalt oxides/water interfaces: heterogeneous electrocatalysis by DFT-MD simulations & metadynamics. Other. Université Paris-Saclay, **2020**
- [35] Liu, Y. C.; Koza, J. A.; Switzer, J. A. Conversion of electrodeposited $\text{Co}(\text{OH})_2$ to CoOOH and Co_3O_4 , and comparison of their catalytic activity for the oxygen evolution reaction. *Electrochim. Acta* **2014**, *140*, 359–365. <https://doi.org/10.1016/j.electacta.2014.04.036>.

Chapter 3

[36] Kutin, Y., Cox, N., Lubitz, W., Schnegg, A., Rüdiger, O. In situ EPR characterization of a cobalt oxide water oxidation catalyst at neutral pH. *Catalysts*, **2019**, 9, 11. <https://www.mdpi.com/2073-4344/9/11/926>

[37] McAlpin, J. G., Surendranath, Y., Dincă, M., Stich, T. A., Stoian, S. A., Casey, W. H., Nocera, D. G., & Britt, R. D. EPR evidence for Co(IV) species produced during water oxidation at neutral pH. *Journal of the American Chemical Society*, **2010**, 132, 6882–6883. <https://pubs.acs.org/doi/10.1021/ja1013344>

3.6 Appendix

A3.1: Geometrical model for Co_3O_4 (111) crystallites

According to AFM observations, Co_3O_4 (111) crystallites are 3D triangular islands. Vertical AFM profile (**Fig. 3.3b**) shows that the crystallites have a rather flat top and quite sharp edges. This is consistent with the fact that the angle between (111) and $(11\bar{1})$ planes is equal to 70.53° . As shown in **Figure A3.1**, Co_3O_4 crystallites are consequently modelled as triangular prisms of height d_\perp . The prism base and top are equilateral triangles which side length is called b .

The external area of the prism A_{prism} (the facets of the crystallites exposed to the electrolyte solution) is computed as follows:

$$A_{prism} = A_{top} + 3 A_{sides} \quad (3.15)$$

$$A_{prism} = \frac{\sqrt{3}}{4} b^2 + 3d_\perp b \quad (3.16)$$

The volume of the crystallite is expressed as:

$$V_{grain} = \frac{\sqrt{3}}{4} d_\perp b^2 \quad (3.17)$$

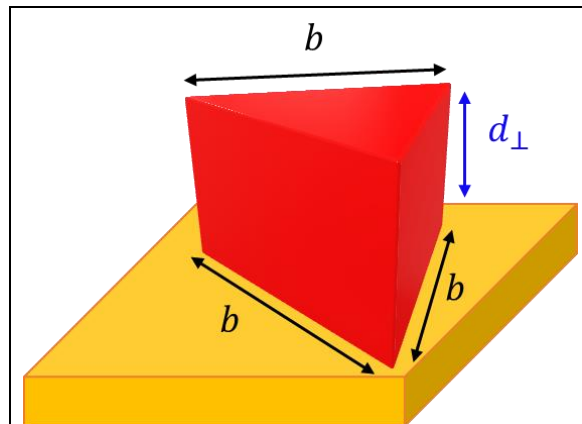
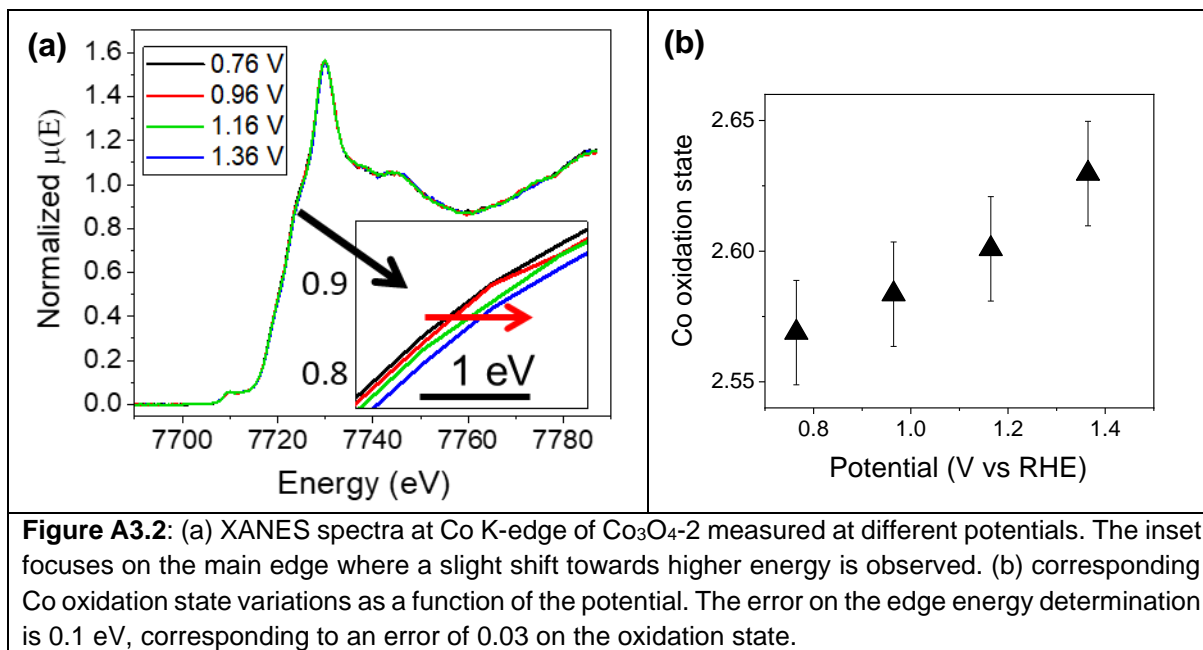


Figure A3.1 schematic representation of $\text{Co}_3\text{O}_4(111)$ crystallite on $\text{Au}(111)$ substrate. It is modeled as a triangular prism of height d_\perp and which base is an equilateral triangle of side length b .

The ECSA of a $\text{Co}_3\text{O}_4(111)$ sample can be estimated with this model and AFM images since the islands density and sizes are homogeneous on the whole sample. For sample Co_3O_4-1 imaged on **Fig. 3.4b**, there are around 400 triangular islands of averaged side length 50 nm and averaged height d_\perp (22 nm for this sample deduced from XRD). Using the triangular prism model of the islands detailed above and Eq. (3.14) results in a total surface area exposed to the electrolyte 1.75 times larger than the geometrical area of the electrode

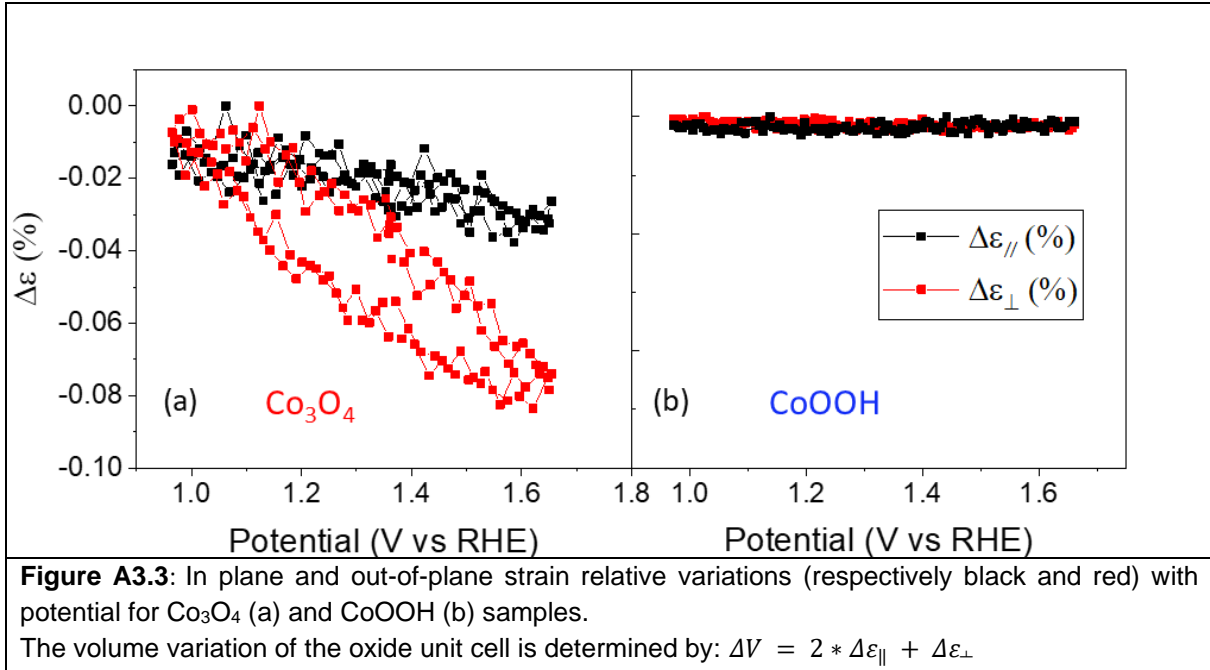
A3.2: XANES spectra of Co_3O_4 -2 recorded at different potentials

Fig.A3.2a shows XANES spectra of Co_3O_4 -2 measured at Co K-edge in 0.1M NaOH at four different potentials. The inset highlights a slight shift towards higher energies of the main edge energy with increasing potential. This shift is quantified into mean Co oxidation state increase with potential (**Fig.A3.2b**).



A3.3: Additional structural data in [0.97 – 1.67V]

Fig.A3.3 gives the relative changes in $\Delta\varepsilon_{\perp}$, $\Delta\varepsilon_{\parallel}$ that are used to plot the relative unit cell volume variations $\Delta V_{bulk} = \Delta\varepsilon_{\perp} + 2 \Delta\varepsilon_{\parallel}$ in **Fig.3.6 i** and **j**. $\Delta V_{bulk} < 0$ indicates a contraction of the unit cell of the oxide toward positive potentials since $\Delta\varepsilon_{\perp}$ and $\Delta\varepsilon_{\parallel}$ are both < 0 for the spinel phase (see **Fig.A3.3a**). By contrast no strain is induced in CoOOH (**Fig.A3.3b**).



A3.4: Operando structural characterization during potential sweeps negative to pre-OER regime

Figure A3.4a-c show operando structural variations of $\text{Co}_3\text{O}_4(111)$ recorded during a CV (a) between $0.8V_{\text{RHE}}$ and $1.77V_{\text{RHE}}$ at 10 mV/s in 0.1M NaOH in the SXR cell. The relative in-plane and out-of-plane crystallite size changes Δd_{\parallel} and Δd_{\perp} are shown in (b) and (c). Compared to **Fig.3.6**, the potential window is 0.2V more negative and both Δd_{\parallel} and Δd_{\perp} decrease in the range $[0.8 - 1.0] V_{\text{RHE}}$. This is attributed to the beginning of the reduction of Co_3O_4 into $\text{Co}(\text{OH})_2$ which standard potential is $0.81 V_{\text{RHE}}$ [28]. In this potential window, the crystallite size changes remain reversible. However, scanning more negative until 0.4V does not restore properly the crystallite size and results in roughening of the film, as shown in **Fig.A3.4d** for Δd_{\perp} (red). In the case of CoOOH (blue), irreversible changes occur when it is submitted to a potential of 0V.

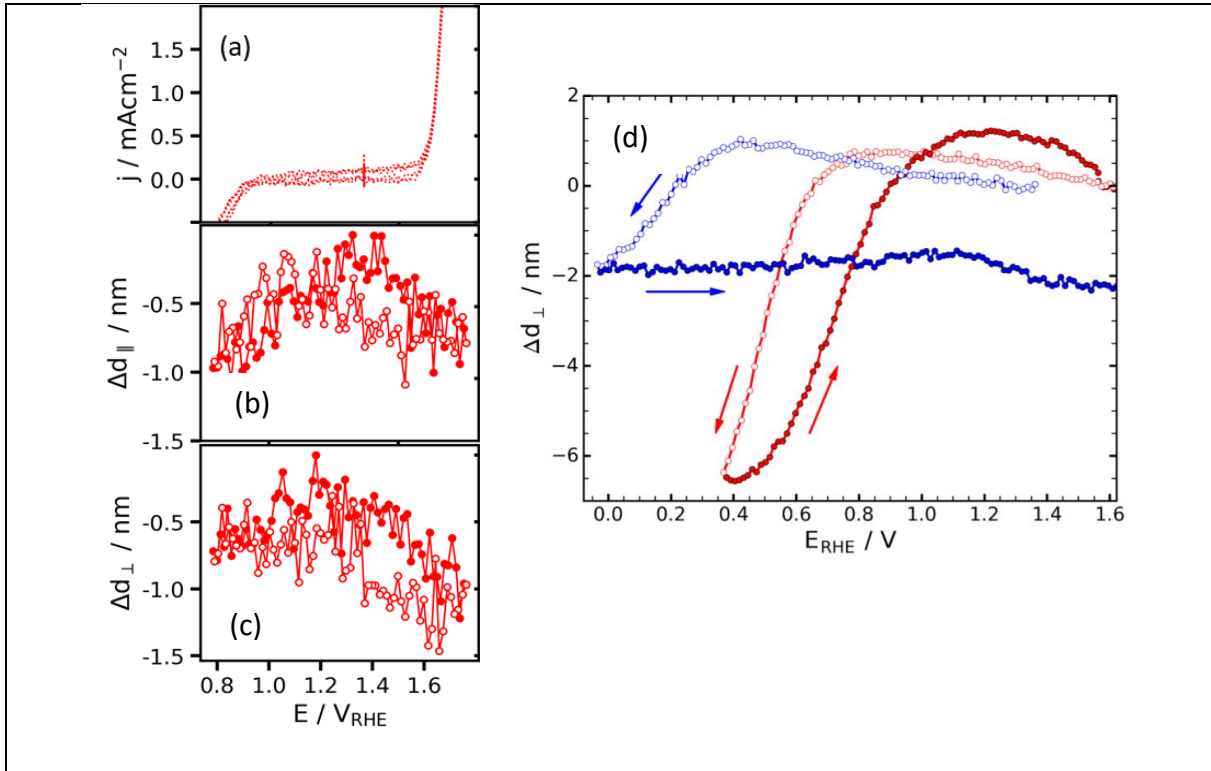


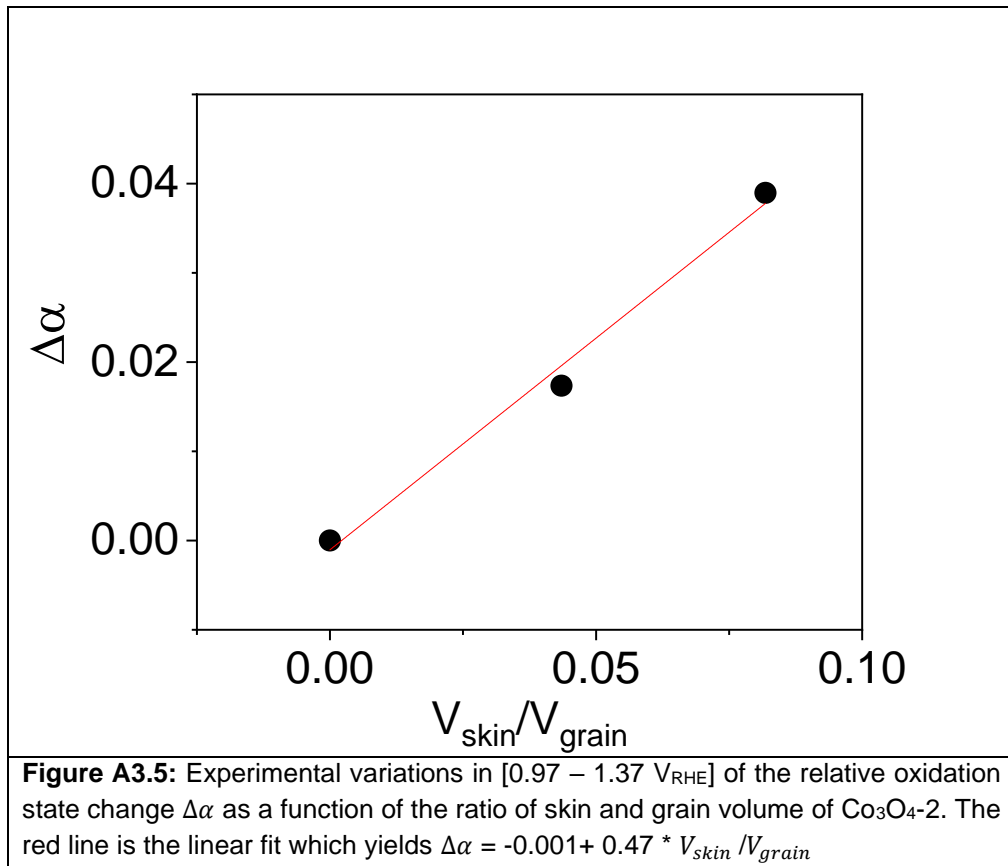
Figure A3.4: Structural variations of $\text{Co}_3\text{O}_4(111)$ recorded during a CV at 10 mV/s in 0.1M NaOH electrolyte in [0.8-1.77V_{RHE}] potential window (a). The in- plane and out-of-plane crystallite size changes, $\Delta d_{||}$, Δd_{\perp} with potential are respectively shown in (b) and (c).

(d) Changes in out-of-plane crystallite size Δd_{\perp} for Co_3O_4 (red) and CoOOH (blue) films during a potential sweep at 10 mV/s in 0.1M NaOH in the range [0 - 1.6V] (CoOOH) and [0.4 - 1.6V] (Co_3O_4).

A3.5: Analysis of combined XAS and XRD data of Co_3O_4 -2

In 3.3, the experimental variations with potential of Co mean oxidation state $\Delta\alpha(U)$ in Co_3O_4 are plotted versus $\frac{V_{skin}(U)}{V_{grain}}$ (see Eq. 3.7) for Co_3O_4 -1 sample. **Figure A3.5** shows the same plot for sample Co_3O_4 -2, measured in [0.97 – 1.37 V_{RHE}] potential window.

For this sample, the oxidation state and crystallite sizes changes with potential were not investigated during a potential sweep but for potential steps. This means that XANES spectra were recorded at selected potentials (every 0.2V) forward and backward and Co oxidation state was determined from them (see 2.3 for more details). 2D detector images of Co_3O_4 (113) Bragg peak were also recorded every 0.1V. The data shown in **Fig.A3.5** are averaged over the two data points of the backward and forward potential steps measured. As mentioned in 3.3, a linear dependence is also found between the x and y axis of the plot, which fit yields $\Delta\alpha = -0.001 + 0.47 * V_{skin} / V_{grain}$.



For comparison of the two Co_3O_4 samples, $V_{skin}(U = 1.37 V)$ together with V_{grain} and the amplitude of Δd_{\perp} and Δd_{\parallel} are given in **Table A3.1** for both Co_3O_4 samples.

Table A3.1: Selected structural parameters of Co_3O_4 films. V_{grain} is the average volume of Co_3O_4 crystallites, Δd_{\perp} and Δd_{\parallel} are the amplitudes of the crystallites height and width variations measured during a potential sweep at $U = 1.37V/RHE$. V_{skin} is the volume of the skin layer at $U = 1.37V_{RHE}$ determined with (3.5).

Sample	V_{grain} (nm ³)	Δd_{\perp} (nm)	Δd_{\parallel} (nm)	V_{skin} (nm ³)
Co_3O_4 - 1	4201	0.4	0.3	~200
Co_3O_4 - 2	5538	0.6	0.8	~500

Chapter 4: Fe doped Co oxide thin films

4.1 Introduction

The introduction of Fe in Co and Ni oxides is known to enhance their catalytic activity [1-4]. For example, Burke et al. [3] established the following activity trend for Fe group metal oxyhydroxides: $\text{NiFeO}_x\text{H}_y > \text{CoFeO}_x\text{H}_y > \text{FeO}_x\text{H}_y > \text{CoO}_x\text{H}_y > \text{NiO}_x\text{H}_y$. The catalytic activity of CoFeO_y catalysts may also depend on the Co/Fe ratio in the catalyst. For example, Burke et al. [5] found the highest activity for an iron content of ~ 50% in Co-Fe hydroxides, and so did Smith et al. [22] for amorphous films obtained by photochemical metal organic deposition (PMOD). Smith et al. [11] showed that an iron content of 25% corresponds to the best activity in photochemically deposited Fe–Co oxide amorphous films, and Co_2FeO_4 is reported as the best catalysts amongst typical $\text{Co}_{3-x}\text{Fe}_x\text{O}_4$ spinels with x integer in [0;3] [19,23,24].

Many studies have focused on understanding how Fe acts to improve the catalytic properties of these materials [3-13]. Different roles for iron have been proposed, among them:

(i) Fe is the active site and Ni/Co oxides/oxyhydroxides provide a conductive support and serve as chemically stable host for Fe catalysis [3,5-8]. This hypothesis is especially supported by Mossbauer experiments that support the presence of Fe^{4+} species in OER conditions [4,9].

(ii) Ni or Co are the active sites and Fe^{3+} helps to activate these sites to accelerate OER [10-13]. This can involve promoting the formation of high valence cations like Ni^{4+} [10], decreasing the energetic barrier for the formation of reactive intermediates [11] or facilitating the surface reconstruction to form oxyhydroxide-like layers [12].

(iii) Ni/Co work together with Fe to enhance OER activity, for example by forming new active sites made of dimetal oxo bridges [11]. In situ and operando techniques particularly have been used to elucidate the behaviour of the different cations during OER, especially X-ray Absorption Spectroscopy to probe the oxidation state and local environment.

The beneficial role of iron is somewhat surprising because iron oxides are not considered as good OER catalysts compared to cobalt and nickel oxides [1,14,15], even though Burke et al. [3] claim that FeO_xH_y is a better catalyst than CoO_xH_y and NiO_xH_y when the effective TOF is taken as mean to evaluate OER activity. Crystalline and oriented Fe_3O_4 films have been studied as a model catalyst [12,16-19]. They have shown that Fe_3O_4 is covered by a Fe^{3+} rich surface layer, sometimes assigned to a kind of Fe_2O_3 layer [18,19], instead of FeOOH , because the latter presents a structure that is very different from that of Fe_3O_4 [12,19]. This may be linked to the high stability reported for $\text{Fe}_3\text{O}_4(110)$ and (001) in alkaline medium [16,17] and the absence of structural modifications upon increasing potential until OER regime [12,16].

In the case of CoFe oxides, different behaviours in terms of potential induced oxidation states changes are reported depending on the material phase and initial oxidation state of Fe and Co. In [11], the authors showed with operando XAS measurements that in amorphous CoFeO_x oxides containing Fe^{3+} , iron is not oxidized while increasing potential until OER regime. Instead, Co^{2+} are oxidized into Co^{3+} . The oxidation of Co^{2+} into Co^{3+} is also reported in Co_2FeO_4 , CoFe_2O_4 and $\text{Co}_{0.6}\text{Fe}_{2.4}\text{O}_4$ spinel, together with the oxidation of Fe^{2+} into Fe^{3+} [19]. No oxidation of Co was detected in $\text{Co}_{0.8}\text{Fe}_{0.2}\text{O}_x\text{H}_y$ and $\text{Co}_{0.6}\text{Fe}_{0.4}\text{O}_x\text{H}_y$ oxyhydroxides made of Co^{3+} and Fe^{3+} but a partial Fe oxidation to $\text{Fe}^{>3+}$ was reported [6]. This diversity of results obtained for different types of CoFe oxide materials tells the need for using well defined and characterized materials, that should be compared the one with the other if one wants to reliably study the transformations of the materials during the catalytic reaction.

With crystalline $\text{Co}_{3-x}\text{Fe}_x\text{O}_4$ spinel, such studies are possibly facilitated by a good knowledge of the structure and the atomic arrangement. Regarding the latter, the environment of Co atoms has been identified has a key parameter in understanding the catalytic activity of Co based spinel oxides [13,19,24-26]. For instance, in the case of CoFe_2O_4 and Co_2FeO_4 , the Co oxidation state change with potential measured by XAS was attributed to the oxidation of tetrahedrally coordinated Co^{2+} since it was smaller in CoFe_2O_4 than in Co_2FeO_4 , richer in $\text{Co}^{2+}_{\text{Th}}$. [19]. In addition, studying crystalline samples opens the possibility to investigate how the structure behaves upon increasing potential to OER, which is not often considered in operando studies of these materials. Hsu et al. [12] used operando SXRD to study CoFe_2O_4 crystalline nanocubes in which Co^{2+} are in octahedral sites. They determined the formation of a new phase at potentials higher than OER onset, identified as $\beta\text{-COOOH}$, and accompanied by a redox wave around 1.5V. Post OER TEM shows the existence of an amorphous layer. This was also observed by Calvillo et al. [19] for Co_2FeO_4 and CoFe_2O_4 , and the authors concluded that this amorphization is irreversible. These measurements also evidence a phase transformation into an active OER phase, as described for Co_3O_4 in previous works [21,30] and in **chapter 3**.

In this chapter, crystalline and epitaxial $\text{Co}_{1-x}\text{Fe}_x\text{O}_y$ oxides with x in [0.2-0.5] are synthesized and characterized by SXRD, AFM and XAS in order to give a precise determination of the structure, atoms oxidation states and active surface area of the samples. After characterization of their structure and redox states, they are compared to Co_3O_4 and Fe_3O_4 , in terms of OER activity, potential dependant structural behaviour and oxidation state changes in operando conditions. A common behaviour trend is found for all samples: the reversible transformation, before OER potential, of a surface layer into a disordered species. We show that this transformation is correlated to the oxidation of cations in the near surface region of the

crystallites, and discuss the amplitude of structural changes of $\text{Co}_{1-x}\text{Fe}_x\text{O}_y$ in regards of their structure and catalytic activity.

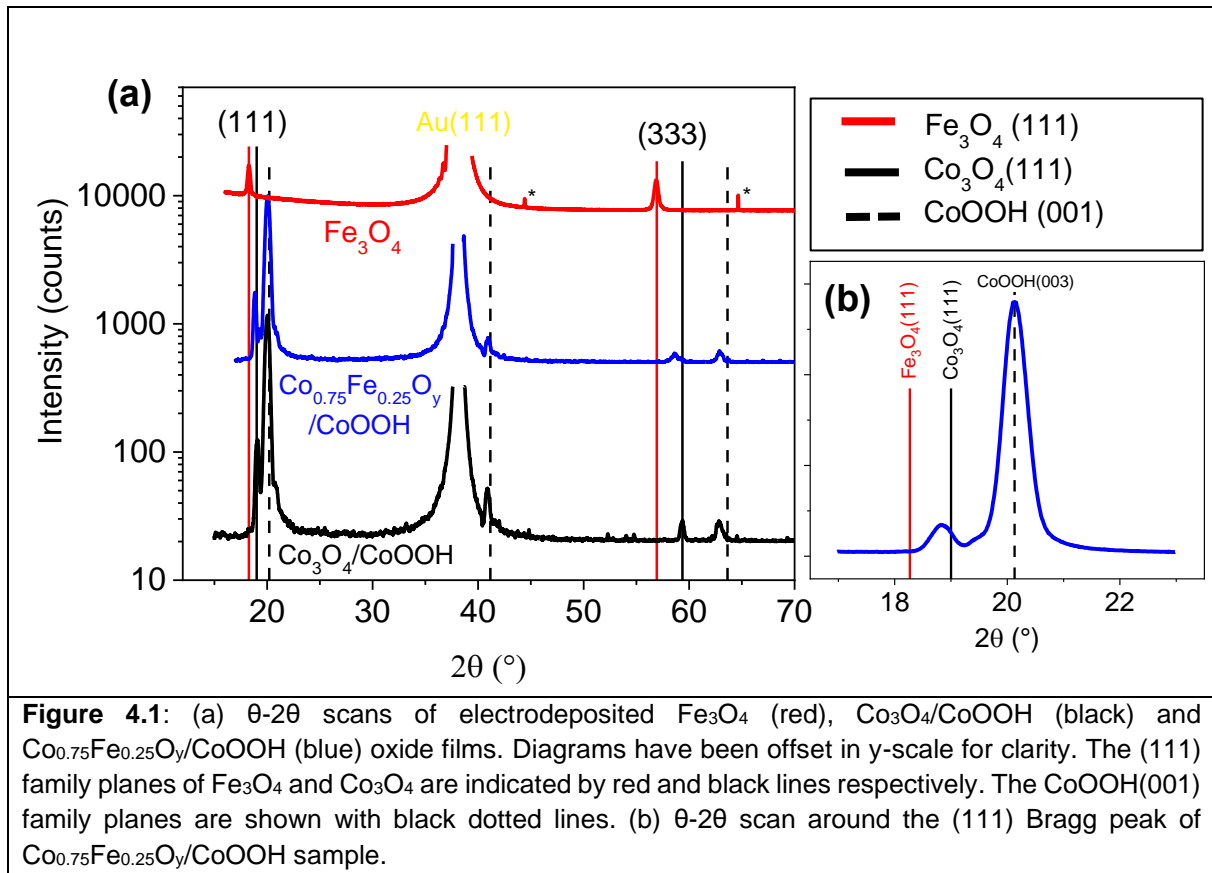
4.2 Characterizations of as prepared samples up to immersion

The $\text{Co}_{1-x}\text{Fe}_x\text{O}_y$ and Co_3O_4 layers are electrodeposited on a CoOOH buffer layer. Fe_3O_4 layers are deposited on Au(111), because it is a cathodic reaction that is not compatible with deposition CoOOH (the Co oxide is reduced). The synthesis of samples is explained in **Chapter 2** and the determination of the Co/Fe composition of $\text{Co}_{1-x}\text{Fe}_x\text{O}_y$ layers is exposed in **Appendix 4.1**. For the sake of simplicity samples are named by the top layer without mention of the substrate, unless there is ambiguity.

Structure of $\text{Co}_{1-x}\text{Fe}_x\text{O}_y$ layers

Figure 4.1a shows XRD θ - 2θ scans of $\text{Fe}_3\text{O}_4/\text{Au}(111)$ (red), $\text{Co}_3\text{O}_4/$ (black) and $\text{Co}_{0.75}\text{Fe}_{0.25}\text{O}_y$ (blue) electrodeposited oxides in a wide angular range (2θ between 17° and 70°). In all diagrams the most intense peak at 38° is that of the Au(111) substrate, and other Au peaks marked with a star* can also be seen on some scans. The (003), (006) and (009) Bragg peaks of the CoOOH buffer layer (at 20° , 40.9° and 62.9°) are marked with vertical dotted lines. Their presence on the XRD pattern of $\text{Co}_3\text{O}_4/$ and $\text{Co}_{0.75}\text{Fe}_{0.25}\text{O}_y$ shows that CoOOH layer is not dissolved after the second oxide electrodeposition. Fe_3O_4 diffractogram exhibits two peaks at: 18.3° and 56.9° , respectively assigned to $\text{Fe}_3\text{O}_4(111)$ and (333). For Co_3O_4 , $\text{Co}_3\text{O}_4(111)$ and (333) peaks at 19° and 59.4° are at the same positions as for Co_3O_4 thin film in **Chapter 3**. $\text{Co}_{0.75}\text{Fe}_{0.25}\text{O}_y$ exhibits peaks at 18.85° and 58.7° , resulting from a shift of $\text{Co}_3\text{O}_4(111)$ and (333) peaks toward lower angles due to Fe incorporation. These observations indicate that electrodepositing Co_3O_4 , Fe_3O_4 and $\text{Co}_{1-x}\text{Fe}_x\text{O}_y$ yields epitaxial films with a (111) orientation.

Fig.4.1b shows $\text{Co}_{0.75}\text{Fe}_{0.25}\text{O}_y$ diffractogram in a narrower θ - 2θ range to illustrate that $\text{Co}_{0.75}\text{Fe}_{0.25}\text{O}_y$ peak is located in between $\text{Co}_3\text{O}_4(111)$ and $\text{Fe}_3\text{O}_4(111)$ (indicated by black and red lines). The $\text{Co}_{1-x}\text{Fe}_x\text{O}_y$ peak position depends on x . As shown in **Appendix 4.2**, the out-of-plane unit cell parameter c , retrieved from the $\text{Co}_{1-x}\text{Fe}_x\text{O}_y$ (111) peak position, remains in between $c_{\text{Co}_3\text{O}_4}$ and $c_{\text{Fe}_3\text{O}_4}$ and decreases with increasing Fe content. The (111) peak FWHM is used to determine the average height of the oxides' crystallites. For instance, $\text{Co}_{0.75}\text{Fe}_{0.25}\text{O}_y$ layer in **Fig. 4. 1b** is 19.6 nm thick and the CoOOH layer is 17.9 nm.



Further structural characterizations using SXRD confirm the epitaxial orientation of the electrodeposited films. **Figure 4.2** shows scans along Au(01L) rod for Fe_3O_4 (red) $\text{Co}_{0.75}\text{Fe}_{0.25}\text{O}_y/$ (blue) and $\text{Co}_3\text{O}_4/$ (black) samples. In the $[0 - 5.5]$ L range, 2 Au peaks at $L=2$ and $L=5$ are visible for all samples. Four oxide peaks are found (marked by vertical solid lines), identified as $(1\bar{1}3)$, $(2\bar{2}2)$, (115) and (404) of $\text{Fe}_3\text{O}_4(111)$ (red) and $\text{Co}_3\text{O}_4(111)$ (black). Peaks of the $\text{CoOOH}(001)$ buffer layer are also found for $\text{Co}_{0.75}\text{Fe}_{0.25}\text{O}_y/$ and $\text{Co}_3\text{O}_4/$ and marked with dashed lines. **Fig.4.2b** shows the L-region $[3.25 - 4.2]$ where (115) and (404) of Co_3O_4 and Fe_3O_4 are located (highlighted in green in **Fig.4.2a**). For Co_3O_4 and Fe_3O_4 , (115) and (404) peaks are close to the expected position, indicating that the deposits are almost strain free. $\text{Co}_{0.75}\text{Fe}_{0.25}\text{O}_y$ (115) and (404) peaks appear in between those of Fe_3O_4 and Co_3O_4 . As for the (111) peak position, the peak positions measured in L-scans show a dependence on the Fe content x measured by EDX. An example of this dependence for the (115) peak position of various $\text{Co}_{1-x}\text{Fe}_x\text{O}_y/$ samples is shown in **Appendix 4.2**. As the same peaks are found for the mixed and pure oxides, the synthesized $\text{Co}_{1-x}\text{Fe}_x\text{O}_y$ oxides preserve the spinel structure of Co_3O_4 and Fe_3O_4 , together with their (111) orientation. The (111) epitaxial growth of Co_3O_4 and $\text{Co}_{1-x}\text{Fe}_x\text{O}_y$ on CoOOH is probably facilitated by the similarity of the in-plane lattice constants of $\text{CoOOH}(001)$ ($a_{\text{CoOOH}} = 0.285 \text{ nm}$), $\text{Co}_3\text{O}_4(111)$ hexa $a_{\text{Co}_3\text{O}_4} = 0.572 \text{ nm} = 2 * 0.286 \text{ nm}$) and $\text{Co}_{1-x}\text{Fe}_x\text{O}_y(111)$ hexa ($a_{\text{Co}_3\text{O}_4} = 0.572 \text{ nm} = 2 * 0.286 \text{ nm} < a_{\text{Co}_{1-x}\text{Fe}_x\text{O}_y} <$

$a_{Fe_3O_4} = 0.594 \text{ nm} = 2 * 0.297 \text{ nm}$) leading to a small in-plane lattice mismatch between substrate and deposit.

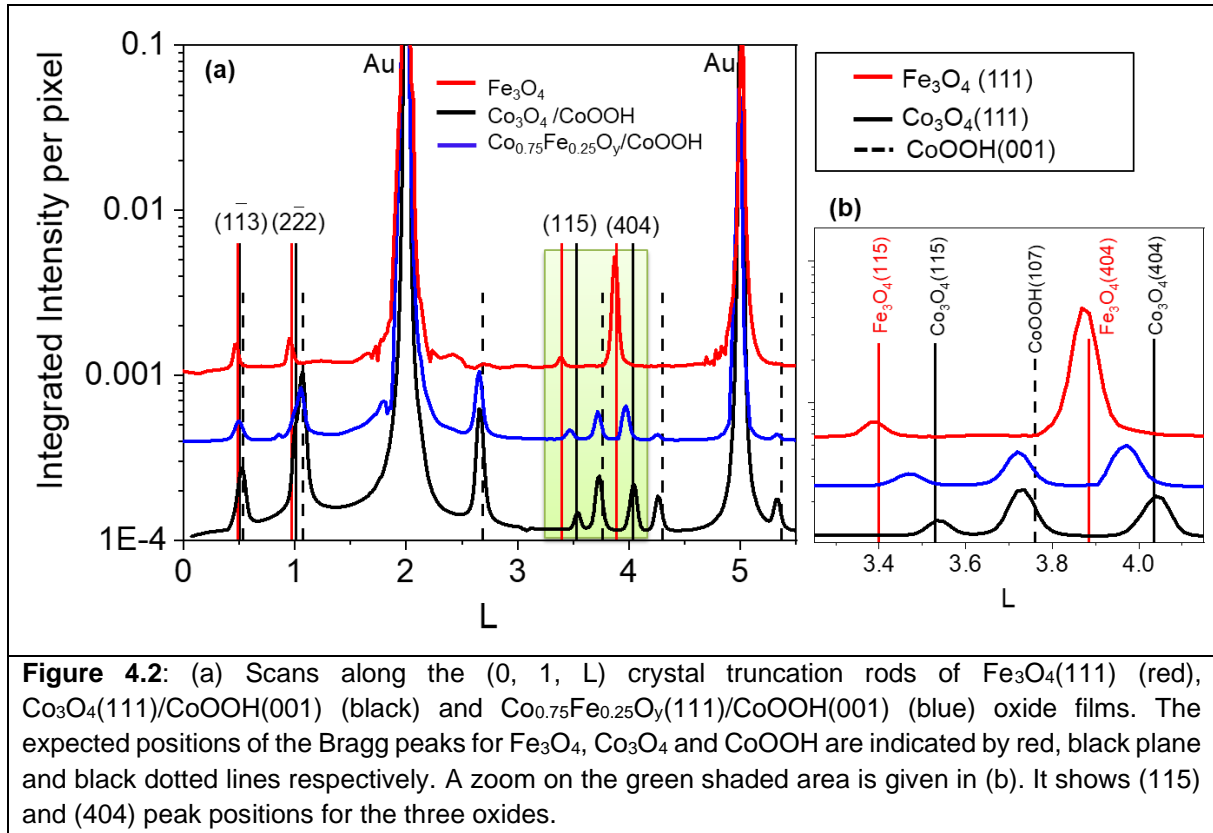


Figure 4.2: (a) Scans along the (0, 1, L) crystal truncation rods of $Fe_3O_4(111)$ (red), $Co_3O_4(111)/CoOOH(001)$ (black) and $Co_{0.75}Fe_{0.25}O_y(111)/CoOOH(001)$ (blue) oxide films. The expected positions of the Bragg peaks for Fe_3O_4 , Co_3O_4 and $CoOOH$ are indicated by red, black plane and black dotted lines respectively. A zoom on the green shaded area is given in (b). It shows (115) and (404) peak positions for the three oxides.

The above results demonstrate that electrodeposition yields *single phase* $Co_{1-x}Fe_xO_y$ oxide films. Over several samples' preparations, $Co_{1-x}Fe_xO_y$ samples with x varying in [0.18 – 0.5] were obtained. All layers present a spinel structure and the pending question is the exact distribution of Co and Fe cations in tetrahedral (Th) and Octahedral (Oh) sites. It is well-known that Co_3O_4 and Fe_3O_4 present respectively a normal and inverse spinel. In Co_3O_4 , Co^{3+} occupy octahedral (Oh) sites and Co^{2+} tetrahedral (Th) sites and its formula may be written as $((Co^{2+})_1)_{Th}((Co^{3+})_2)_{Oh}(O_4)$. In Fe_3O_4 , Fe^{2+} are in Oh sites and Fe^{3+} are half in Oh half in Th sites, which gives the formula $((Fe^{3+})_1)_{Th}((Fe^{3+})_1(Fe^{2+})_1)_{Oh}(O_4)$. This means that Fe^{3+} ions are stable in both Th and Oh environments. Mixed $Co_{3-3x}Fe_{3x}O_4$ spinel oxides might have a normal or inverse structure depending on the cation's distributions in the octahedral and tetrahedral sites. The defined compounds Co_2FeO_4 and $CoFe_2O_4$ are inverse spinel, respectively with the formula $(Co^{2+}_{0.45}Fe^{3+}_{0.55})_{Tetra}(Co^{2+}_{0.55}Co^{3+}_1Fe^{3+}_{0.45})_{Octa}(O_4)$ and $(Co^{2+}_{0.25}Fe^{3+}_{0.75})_{Tetra}(Co^{2+}_{0.75}Fe^{3+}_{1.25})_{Octa}(O_4)$ [19,27,28]. The lattice parameter a of these defined compounds is larger than the one expected from Vegard's law assuming a linear increase of the lattice parameter with the iron content x in between $a_{Co_3O_4}$ and $a_{Fe_3O_4}$ [35]. In the case of our electrodeposited $Co_{1-x}Fe_xO_y$ oxide films, their lattice parameter is generally along or below Vegard's law (see **Appendix A4.3**). This analysis is further developed in Ivan Pacheco-Bubi PhD thesis [36], where it is

shown that the lattice parameter of our mixed $\text{Co}_{1-x}\text{Fe}_x\text{O}_y$ spinel oxides indicates a normal spinel structure with Co^{2+} in octahedral sites.

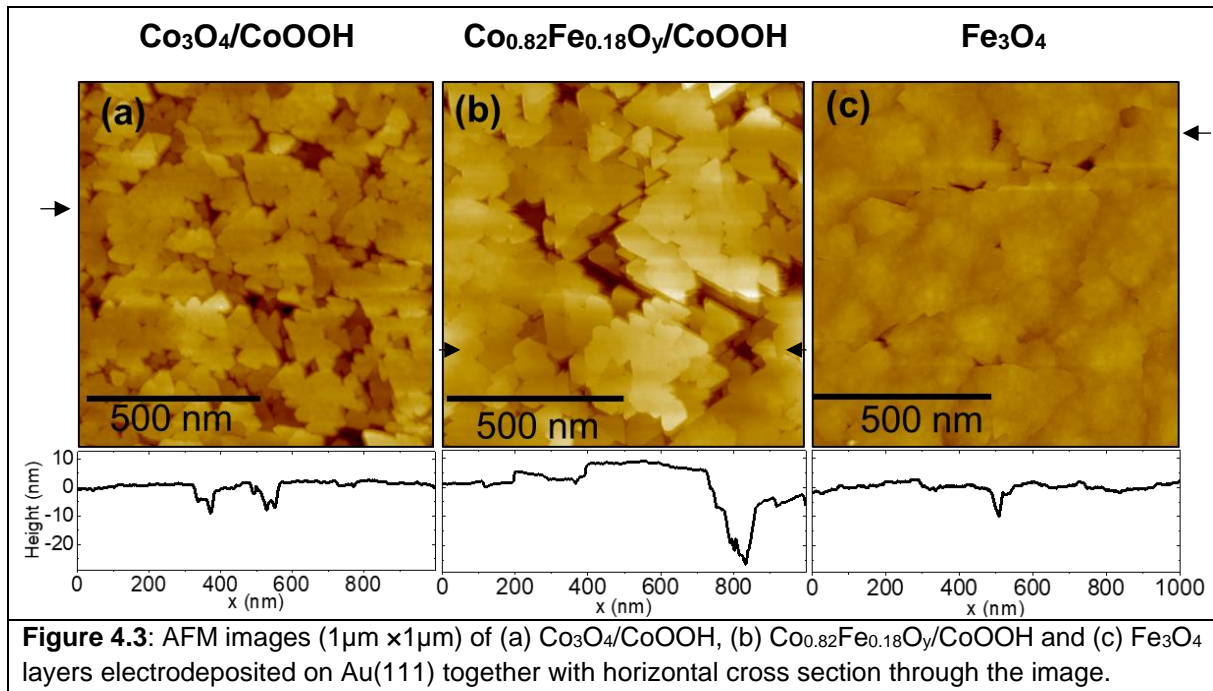
Since the beginning of the chapter, the mixed CoFe oxides are referred as $\text{Co}_{1-x}\text{Fe}_x\text{O}_y$ which especially indicates the percentage of each metal in the film. Since we have just seen that these oxides have a spinel structure, a more adequate notation taking x as the iron content in [0;1] would be: $\text{Co}_{3-3x}\text{Fe}_{3x}\text{O}_4$. For simplicity and convenience to read the oxide composition, the notation $\text{Co}_{1-x}\text{Fe}_x\text{O}_y$ will however be kept in the following.

Morphology of $\text{Co}_{1-x}\text{Fe}_x\text{O}_y$ layers

Figure 4.3 displays typical AFM images of (a) $\text{Co}_3\text{O}_4/\text{CoOOH}$ (Co_3O_4 and CoOOH XRD crystallite heights are respectively $d_{\perp} = 28$ nm and $d_{\perp} = 22$ nm), (b) $\text{Co}_{1-x}\text{Fe}_x\text{O}_y/\text{CoOOH}$ ($\text{Co}_{1-x}\text{Fe}_x\text{O}_y$ and CoOOH XRD crystallite heights are respectively $d_{\perp} = 27$ nm and $d_{\perp} = 17$ nm) and (c) Fe_3O_4 ($d_{\perp} = 27$ nm) samples.

All films are composed of densely packed islands fully covering the substrate surface. $\text{Co}_{1-x}\text{Fe}_x\text{O}_y/\text{CoOOH}$ and $\text{Co}_3\text{O}_4/\text{CoOOH}$ bilayers have a very similar morphology: they present tightly packed triangular islands adopting two main orientations separated by 180° . The compactness of the top layer ensures that the CoOOH underlayer is negligibly exposed to the electrolyte. In fact, in **Fig.4.3b**, the hole present in the cross section is approximately as deep as $t_{\text{Co}_{1-x}\text{Fe}_x\text{O}_y}$, meaning that the AFM tip likely hits the CoOOH beneath layer at this location, while elsewhere, the $\text{Co}_{1-x}\text{Fe}_x\text{O}_y$ film is dense. This guarantees that the electrochemical response of the sample is coming from the top oxide layer.

Compared to Co_3O_4 , the $\text{Co}_3\text{O}_4/\text{CoOOH}$ bilayer is slightly more densely packed: the triangular islands are less discernible as they seem more interconnected. For instance, flat terraces 150 to 200 nm wide probably composed of several Co_3O_4 grains can be observed in (a). The compactness of $\text{Co}_{1-x}\text{Fe}_x\text{O}_y/\text{CoOOH}$ layer may vary from one sample to another with no dependence on the Fe content. The roughness is never greater than that of than $\text{Co}_3\text{O}_4/\text{Au}(111)$ and some samples may be very flat. The morphology of Fe_3O_4 differs from that of Co_3O_4 and $\text{Co}_{1-x}\text{Fe}_x\text{O}_y$ in the islands shape that is more spherical-like than triangular. The large islands (~ 150 - 250 nm wide) seem to contain several smaller islands (~ 30 nm wide) merged together. However, the resulting deposit is continuous and notably flat.



Cobalt and iron oxidation state in $\text{Co}_{1-x}\text{Fe}_x\text{O}_y$ oxide films

The oxidation state of both iron and cobalt in the materials have been investigated using X-ray Absorption Spectroscopy. **Fig.4.4a** compares XAS spectra of $\text{Co}_{0.82}\text{Fe}_{0.18}\text{O}_y/\text{CoOOH}$ (green), $\text{Co}_{0.75}\text{Fe}_{0.25}\text{O}_y/\text{CoOOH}$ (red) and Co_3O_4 (black, same as in **Fig.3.4**) at Co K-edge. In the case of $\text{Co}_{1-x}\text{Fe}_x\text{O}_y$, the XAS spectrum results from the contribution of Co atoms in both CoOOH and $\text{Co}_{1-x}\text{Fe}_x\text{O}_y$ layers. The XANES spectra of Co_3O_4 and $\text{Co}_{1-x}\text{Fe}_x\text{O}_y/\text{CoOOH}$ are very similar, suggesting similarity in Co atomic arrangements. **Table 4.1** gives the edge energy E_{edge} calculated with $\text{Co}_{0.82}\text{Fe}_{0.18}\text{O}_y/\text{CoOOH}$ and $\text{Co}_{0.75}\text{Fe}_{0.25}\text{O}_y/\text{CoOOH}$ XAS spectra and the corresponding mean Co oxidation state in the bilayer $\alpha\text{Co}_{bilayer}$. For $\text{Co}_{0.82}\text{Fe}_{0.18}\text{O}_y/\text{CoOOH}$, $\alpha\text{Co}_{bilayer}$ is 2.46 in air and increases to 2.58 at 0.97V in 0.1M NaOH. **Fig.4.4b** shows XAS spectra at Fe K-edge of $\text{Co}_{0.82}\text{Fe}_{0.18}\text{O}_y/\text{CoOOH}$ (green), $\text{Co}_{0.75}\text{Fe}_{0.25}\text{O}_y/\text{CoOOH}$ (red), electrodeposited Fe_3O_4 (black) and Fe_2O_3 reference pellet (black). While the edge region of $\text{Co}_{1-x}\text{Fe}_x\text{O}_y/\text{CoOOH}$ and Fe_2O_3 are very alike, the edge energy of Fe_3O_4 is shifted towards lower energies. Fe_3O_4 edge energy corresponds to a Fe oxidation state αFe of 2.61 in air and 2.66 at 0.97V in 0.1M NaOH (see **Table 4.1**), in very good agreement with the value of 2.66 expected for this oxide. $\alpha(\text{Fe})$ is slightly higher than 3 for $\text{Co}_{0.82}\text{Fe}_{0.18}\text{O}_y/\text{CoOOH}$, matching the spectral similarity with Fe_2O_3 . In $\text{Co}_{0.75}\text{Fe}_{0.25}\text{O}_y/\text{CoOOH}$ bilayer, αFe was also found to be 3, and αCo is 2.63 in air (see **Table 4.1**).

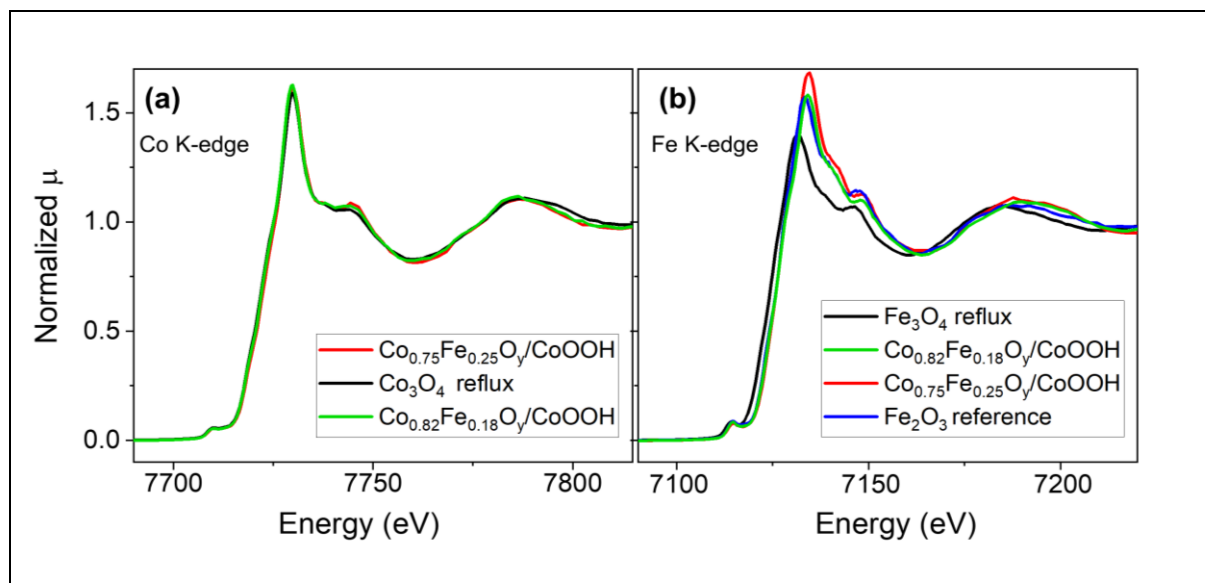


Figure 4.4: (a) normalized XANES spectra recorded at Co K-edge in air of electrodeposited $\text{Co}_{0.75}\text{Fe}_{0.25}\text{O}_y/\text{CoOOH}$ (green) and Co_3O_4 (black). (b) normalized XANES spectra recorded at Fe K-edge in air of electrodeposited $\text{Co}_{0.82}\text{Fe}_{0.18}\text{O}_y/\text{CoOOH}$ (green) and Fe_3O_4 (red). XANES spectra of Fe_2O_3 (reference compound) is also shown (black).

Table 4.1: Spectroscopic parameters of as prepared Fe_3O_4 , Co_3O_4 and $\text{Co}_{0.82}\text{Fe}_{0.18}\text{O}_y/\text{CoOOH}$ and $\text{Co}_{0.75}\text{Fe}_{0.25}\text{O}_y/\text{CoOOH}$ bilayers samples in air and in parenthesis in 0.1M NaOH at 0.97V: the first 2 columns give the spectroscopic parameters (E_{edge} and α) measured at Fe K-edge and the next columns the ones measured at Co K-edge. E_{edge} is determined with a precision of ± 0.1 eV and $\alpha \pm 0.03$.

Sample	E_{edge} (eV) at Fe K-edge	α_{Fe}	E_{edge} (eV) at Co K-edge	$\alpha_{Co_{bilayer}}$
Fe_3O_4	7123.31 (7123.49)	2.61 (2.66)	-	-
$\text{Co}_{0.82}\text{Fe}_{0.18}\text{O}_y/\text{CoOOH}$	7124.87 (7125.09)	3.01 (3.06)	7720.40 (7720.81)	2.46 (2.58)
$\text{Co}_{0.75}\text{Fe}_{0.25}\text{O}_y/\text{CoOOH}$	7124.93 (7124.88)	3.02 (3.01)	7721.0 (7721.24)	2.63 (2.69)
Co_3O_4	-	-	7720.69 (7720.95)	-

The fact that Fe is introduced as Fe^{3+} in $\text{Co}_{1-x}\text{Fe}_x\text{O}_y$ layers is consistent with the synthesis method. The Fe precursor is indeed a Fe^{3+} complex, which is not oxidized at the deposition potential. It is probably adsorbing on the surface of the growing oxide and gets incorporated in the spinel structure as Fe^{3+} .

For Co, XAS gives an oxidation state $\alpha_{Co_{bilayer}}$ that is averaged over all cobalt atoms present in the $\text{Co}_{1-x}\text{Fe}_x\text{O}_y$ and in the CoOOH layer. The contribution of the buffer layer needs to be accounted for to determine the cobalt oxidation state in the $\text{Co}_{1-x}\text{Fe}_x\text{O}_y$ layer only, that will be

called $\alpha Co_{Co_{1-x}Fe_xO_y}$. Let us consider the $Co_{1-x}Fe_xO_y/CoOOH$ sample as a bilayer. The mean Co oxidation state $\alpha Co_{bilayer}$ may be written:

$$\alpha Co_{bilayer} = \frac{\alpha Co_{Co_{1-x}Fe_xO_y} * N_{Co_{1-x}Fe_xO_y} + \alpha Co_{CoOOH} * N_{CoOOH}}{N_{tot}} \quad (4.1)$$

Where N' s are the number of Co atoms per nm^3 of the respective layers designated by the subscript. N_{CoOOH} is the number of Co atoms in the CoOOH film that is considered as a layer of thickness $d_{\perp,CoOOH}$. The volume density of Co atoms in bulk CoOOH being $\rho_{CoOOH} = 32.4 \text{ nm}^{-3}$ (see **Chapter 3**), one may write:

$$N_{CoOOH} = d_{\perp,CoOOH} * \rho_{CoOOH} \quad (4.2)$$

The volume density of Co atoms in Co_3O_4 is $\rho_{Co_3O_4} = 45.4 \text{ nm}^{-3}$ (see **Chapter 3**) therefore we approximate the volume density of Co atoms in $Co_{1-x}Fe_xO_y$ is: $\rho_{Co_{1-x}Fe_xO_y} = 45.4 * (1 - x) \text{ nm}^{-3}$ because the lattice parameter of $Co_{1-x}Fe_xO_y$ layers remains very close to that of Co_3O_4 . This yields:

$$N_{Co_{1-x}Fe_xO_y} = d_{\perp,Co_{1-x}Fe_xO_y} * \rho_{Co_{1-x}Fe_xO_y} \quad (4.3)$$

Finally, N_{tot} is the total number of Co atoms per nm^3 in the bilayer: $N_{tot} = N_{CoOOH} + N_{Co_{1-x}Fe_xO_y}$.

Using $\alpha Co_{CoOOH} = 3$ in Eq. (4.1) (see **Chapter 3**) $\alpha Co_{Co_{1-x}Fe_xO_y}$ may be computed. Its value for the as-prepared samples and at 1.0V in 0.1M NaOH are given in **Table 4.2** for the two samples studied by both XAS and SXRD. The corresponding $d_{\perp,CoOOH}$, $d_{\perp,Co_{1-x}Fe_xO_y}$ and $\alpha Co_{bilayer}$ are also given. For both $Co_{1-x}Fe_xO_y$ oxides, Co oxidation state in air is close to 2.4, and slightly increases to ~2.5 after immersion at 1.0V in 0.1M NaOH. One may also calculate $\alpha Co_{Co_{1-x}Fe_xO_y}$ from the spinel oxide's stoichiometry, considering only Fe^{3+} and no oxygen vacancies. In this type of spinel, the mean oxidation state of the cations is 2.66, which leads to the following expression:

$$\alpha Co_{Co_{1-x}Fe_xO_y}^{Stochiom} = \frac{2.66 - 3 * x}{(1 - x)} \quad (4.4)$$

The corresponding values of $\alpha Co_{Co_{1-x}Fe_xO_y}^{Stochiom}$ in the two samples are given in **Table 4.2** (last column). The data show that as prepared $Co_{1-x}Fe_xO_y$ layers, in which Fe^{3+} have substituted in part the Co^{3+} , present a smaller average Co oxidation state than in Co_3O_4 . Moreover, the difference between $\alpha Co_{Co_{1-x}Fe_xO_y}$ and $\alpha Co_{Co_{1-x}Fe_xO_y}^{Stochiom}$ suggests the presence of Oxygen vacancies. After immersion of the sample this difference is reduced, suggesting that part of the O-vacancies have been filled.

Table 4.2: $\alpha Co_{Co1-xFexOy}$ the Co mean oxidation state in as prepared $Co_{1-x}Fe_xO_y$ layers together with measured the structural and spectroscopic parameters needed to compute its value: $d_{\perp,CoOOH}$, $d_{\perp,Co1-xFexOy}$ and $\alpha Co_{bilayer}$. The α values at 1.0V in 0.1M NaOH are given in parenthesis. The mean oxidation state measured in Co_3O_4 deposit (**chapter 3**) is given for comparison. All oxidation states are given ± 0.03 . The last column gives the $\alpha Co_{Co1-xFexOy}^{Stochiom}$ derived from stoichiometry and accounting that Fe is present as Fe^{3+} only.

Sample	$d_{\perp,Co1-xFexOy}$	$d_{\perp,CoOOH}$	$\alpha Co_{bilayer}$ (as measured)	$\alpha Co_{Co1-xFexOy}$ (calculated from XAS)	$\alpha Co_{Co1-xFexOy}^{Stochiom}$ (calculated from stoichiometry)
$Co_{0.82}Fe_{0.18}O_y$	37 nm	7 nm	2.46 (2.58)	2.37 (2.51)	2.59
$Co_{0.75}Fe_{0.25}O_y$	26 nm	7 nm	2.63 (2.69)	2.40 (2.50)	2.55
Co_3O_4				2.54 (2.62)	2.66

4.3 Operando characterizations

Potential induced structural changes

Table 4.3 lists all the samples that have been characterized by operando SXRD during cyclic voltammograms in 0.1M NaOH (same principle as what was described in **chapter 3** for Co_3O_4 and $CoOOH$). We are especially interested in the variations with potential of four parameters: the relative in-plane and out-of-plane unit cell strain variations $\Delta\varepsilon_{\parallel}(U)$ and $\Delta\varepsilon_{\perp}(U)$ and the relative in-plane and out-of-plane crystallite sizes variations $\Delta d_{\parallel}(U)$ and $\Delta d_{\perp}(U)$.

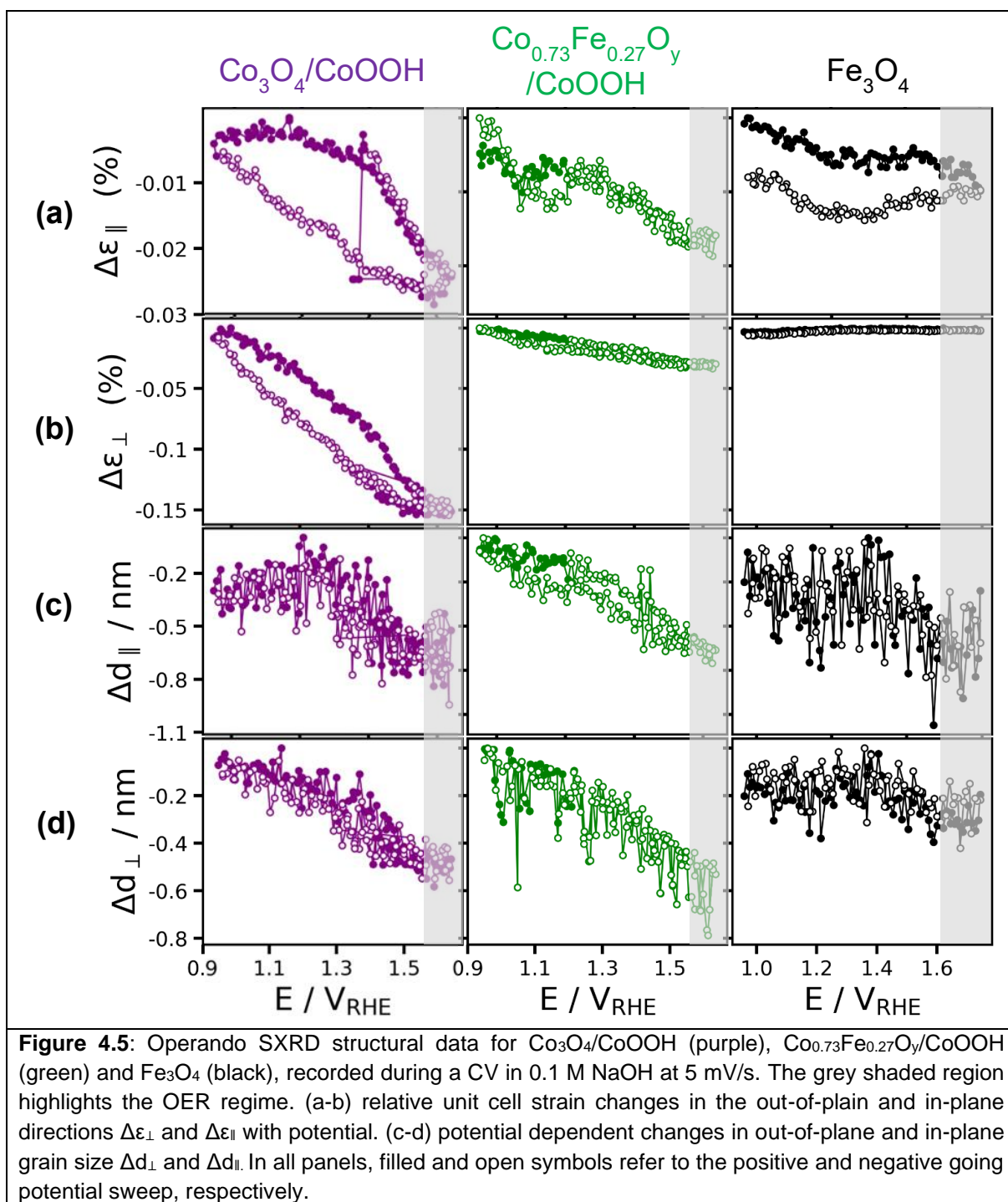
Figure 4.5 compares the potential induced variations of $\Delta\varepsilon_{\parallel}(U)$ (a), $\Delta\varepsilon_{\perp}(U)$ (b), $\Delta d_{\parallel}(U)$ (c) and $\Delta d_{\perp}(U)$ (d) for Co_3O_4 -2 (pink, left panel), $Co_{0.73}Fe_{0.27}O_y$ (green, middle panel) and Fe_3O_4 (black, right panel). For all samples, the relative strain variations $\Delta\varepsilon_{\parallel}$ and $\Delta\varepsilon_{\perp}$ both decrease with potential and recover their initial value after a potential cycle, indicating that the unit cell volume of the oxides is reversibly compressed upon increasing potential. $\Delta\varepsilon_{\parallel}(U)$ is slightly smaller (~ 1.5 - 2 times) for $Co_{0.73}Fe_{0.27}O_y$ and Fe_3O_4 than for Co_3O_4 -2. In the case of $\Delta\varepsilon_{\perp}(U)$, the variations are clearly reduced (approximately by 5) for $Co_{0.73}Fe_{0.27}O_y$ compared to Co_3O_4 -2, and are almost non-existent for Fe_3O_4 .

In all cases, the in plane and out-of-plane crystallite sizes changes $\Delta d_{\parallel}(U)$ and $\Delta d_{\perp}(U)$ also reversibly decrease with potential. For the cobalt-based oxides, the decrease begins around ~ 1.0 -1.2 V and implies the reversible formation of a 0.5 to 1 nm thick layer at the surface of the oxides' crystallites. In the case of Fe_3O_4 , the decrease occurs later, around 1.4V_{RHE} and involves the transformation of a thinner surface layer of approximately 0.2 nm. A few hundreds of mV before OER, a sub nm thick surface layer starts transforming into an X-ray amorphous phase, the skin layer, that is the active phase for OER. A skin layer also forms at the surface of $Co_{0.73}Fe_{0.27}O_y(111)$ and $Fe_3O_4(111)$, before OER onset potential. This is accompanied by a

compression of the unit cell lattice, that is significantly reduced in the out-of-plane direction when Fe is present in the oxide.

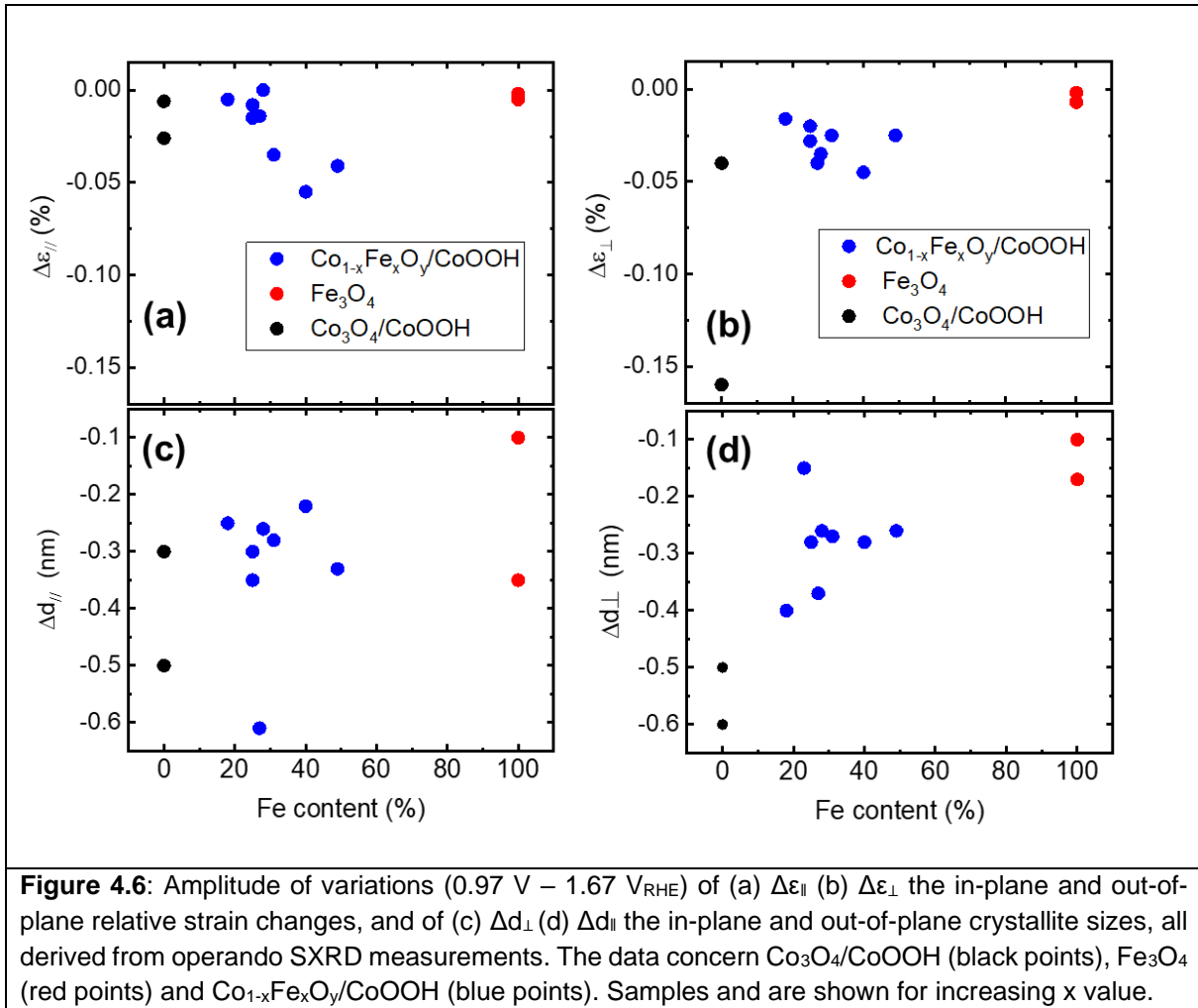
Table 4.3: structural parameters of $\text{Co}_{1-x}\text{Fe}_x\text{O}_y/\text{CoOOH}$, $\text{Co}_3\text{O}_4/\text{CoOOH}$ and Fe_3O_4 samples included in this study. d_{\perp} and d_{\parallel} are the out-of-plane and in-plane crystallite sizes determined from SXRD measurements and a is the lattice parameter determined from XRD measurements.

Sample	Substrate	d_{\perp} (nm)	d_{\parallel} (nm)	a (Å)
Co_3O_4 -1	CoOOH	24	24	8.091
Co_3O_4 -2	CoOOH	19	14	8.062
$\text{Co}_{0.82}\text{Fe}_{0.18}\text{O}_y$	CoOOH	37	23	8.177
$\text{Co}_{0.75}\text{Fe}_{0.25}\text{O}_y$ -1	CoOOH	26	25	8.217
$\text{Co}_{0.75}\text{Fe}_{0.25}\text{O}_y$ -2	CoOOH	17	27	-
$\text{Co}_{0.73}\text{Fe}_{0.27}\text{O}_y$	CoOOH	18	28	8.176
$\text{Co}_{0.72}\text{Fe}_{0.28}\text{O}_y$	CoOOH	15	14	8.185
$\text{Co}_{0.69}\text{Fe}_{0.31}\text{O}_y$	CoOOH	15	22	8.194
$\text{Co}_{0.60}\text{Fe}_{0.40}\text{O}_y$	CoOOH	15	16	8.189
$\text{Co}_{0.51}\text{Fe}_{0.49}\text{O}_y$	CoOOH	15	23	8.202
Fe_3O_4 -1	Au(111)	15	23	8.465
Fe_3O_4 -2	Au(111)	28	26	8.433



Similar variations have been measured for all the samples listed in **Table 4.3**. **Fig.4.6 a** and **b** show the in-plane and out-of-plane relative strain changes $\Delta\varepsilon_{\perp}(1.67V)$ and $\Delta\varepsilon_{\parallel}(1.67V)$ as a function of the iron content x . The volume of Fe_3O_4 unit cell is almost unchanged in the studied potential window since both $\Delta\varepsilon_{\parallel}(1.67V)$ and $\Delta\varepsilon_{\perp}(1.67V)$ are almost 0%, while that of Co_3O_4 is compressed preferentially in out-of-plane direction. Small $\Delta\varepsilon_{\perp}(1.67V)$ ($<0.05\%$) are measured for $\text{Co}_{1-x}\text{Fe}_x\text{O}_y$. $\Delta\varepsilon_{\parallel}(1.67V)$ is also small for oxide with low Fe content and is larger for oxides with $x > \sim 0.3$.

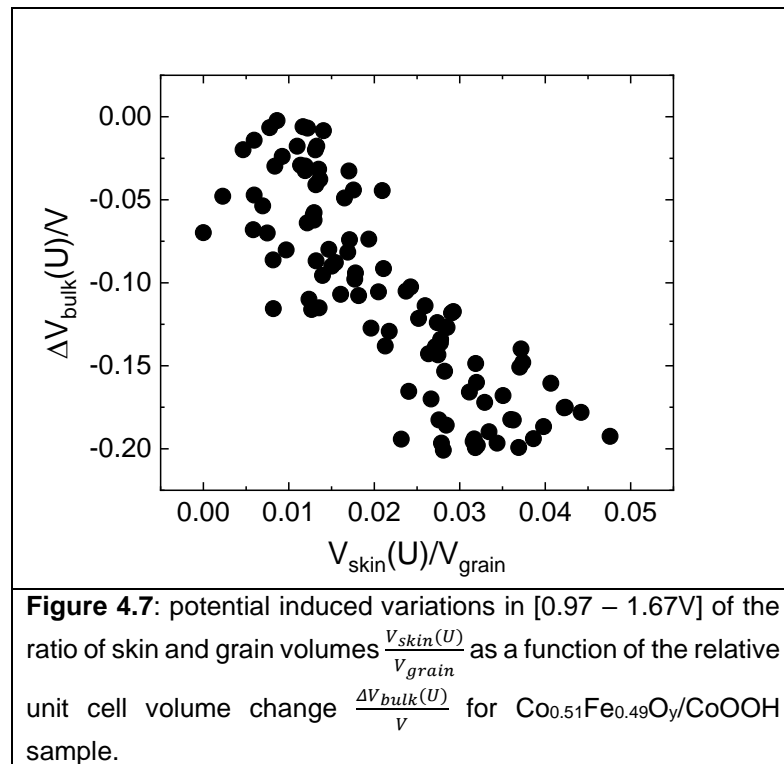
Figure 4.6 c and d show $\Delta d_{\parallel}(1.67V)$ and $\Delta d_{\perp}(1.67V)$ as a function of x . In spite of some scatter, the plot of $\Delta d_{\perp}(1.67V)$ shows an increase with increasing x , which means a decrease in the absolute skin layer thickness $|\Delta d_{\perp}(1.67V)|$ upon increasing Fe content in $\text{Co}_{1-x}\text{Fe}_x\text{O}_y$. Both $\text{Co}_3\text{O}_4/\text{CoOOH}$ samples present a $|\Delta d_{\perp}(1.67V)|$ of $\sim 0.5 - 0.6$ nm, similar to that of Co_3O_4 shown in chapter 3 while for Fe_3O_4 $|\Delta d_{\perp}(1.67V)|$ is ~ 0.2 nm. On the contrary, $\Delta d_{\parallel}(1.67V)$ does not show significant trend with x .



The general tendency from **Figure 4.6** is that the amplitudes of potential induced changes $\Delta d_{\perp,\parallel}(1.67V)$ and $\Delta \epsilon_{\perp,\parallel}(1.67V)$ follow the same trend and that they are lower for Fe_3O_4 than for $\text{Co}_{1-x}\text{Fe}_x\text{O}_y$, themselves lower than for Co_3O_4 . This suggests that the thickness (in both in plane and out-of-plane directions) of the skin layer formed just before OER is correlated to the strain changes, i.e. a thicker skin induces larger strain changes. To investigate this point, we chose two parameters representing the skin layer and the strain changes: (i) the skin volume fraction:

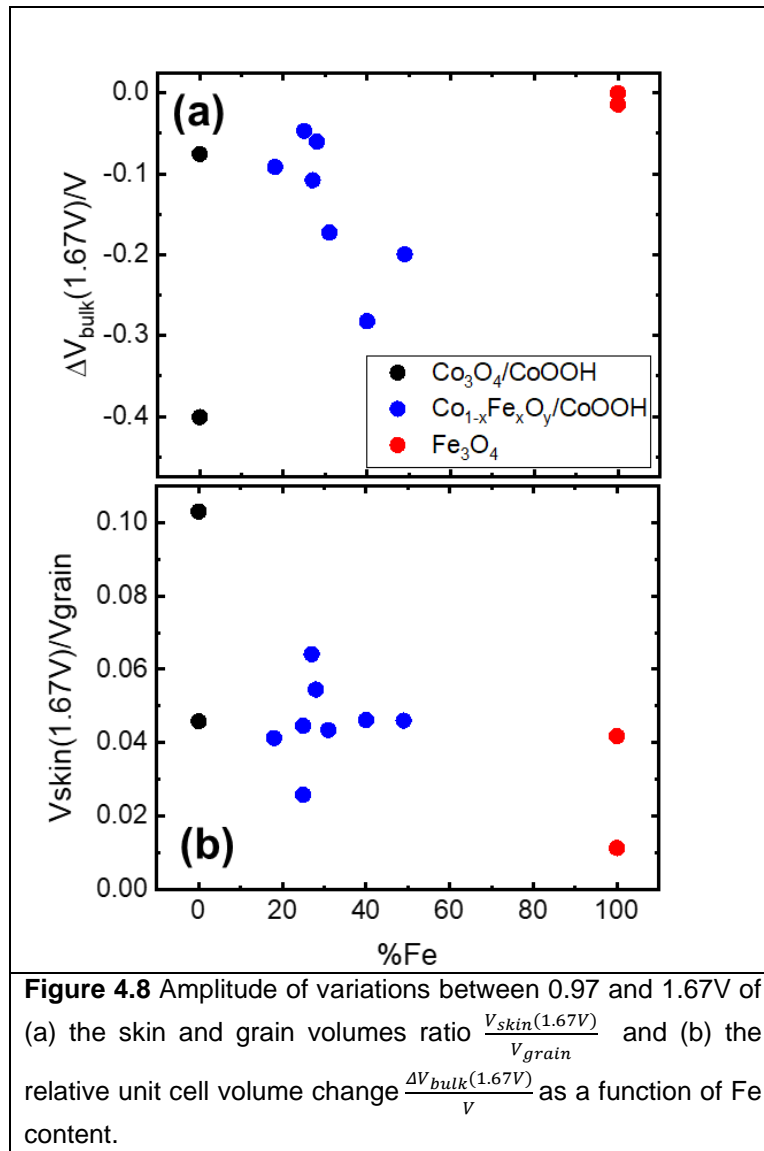
$\frac{V_{\text{skin}}}{V_{\text{grain}}}$ and (ii) the relative unit cell volume change $\frac{\Delta V_{\text{bulk}}}{V}$ (see **Chapter 3** for more details about their analytic expression). A correlation between these two parameters might be found by

looking at the potential dependency of the one versus the other. In the following, we show this dependency for one typical sample that stands for all samples included in this study since similar variations are obtained for them. **Figure 4.7** shows the potential induced variations in [0.97-1.67V] of the skin volume fraction $\frac{V_{skin}(U)}{V_{grain}}$ as a function of the relative unit cell volume change $\frac{\Delta V_{bulk}(U)}{V}$ for $Co_{0.51}Fe_{0.49}O_y/CoOOH$ sample. In spite of some scatter, there is a linear relationship between $\frac{\Delta V_{bulk}(U)}{V}$ and $\frac{V_{skin}(U)}{V_{grain}}$. This indicates that the compression of the oxide unit cell is at least partly induced by the formation of the skin layer. Indeed, in the skin layer, Co atoms are disordered compared to the spinel arrangement. XAS measurements on Co oxides by Bergmann et al. [20] have shown a contraction of Co-O bond length upon increasing potential. This contraction is associated to a partial change in Co environment from tetrahedral to octahedral upon Co^{2+} oxidation in the near surface planes, corresponding to the formation of the skin layer. This is accompanied by a slight rearrangement of oxygen atoms, and results in a strain that is transmitted to the bulk lattice, which shrinks. It is therefore logical that the increase of the skin layer thickness, i.e. the increase of the volume containing disordered atoms would also increase the strain that is transmitted to the bulk, implying larger compression of the unit cell volume.



We have shown that the unit cell volume changes are related to the formation of the skin layer, which may explain the differences of amplitude in $\Delta d_{\perp,\parallel}(1.67V)$ and $\Delta \varepsilon_{\perp,\parallel}(1.67V)$ in between Fe_3O_4 , $Co_{1-x}Fe_xO_y$ and Co_3O_4 . **Figure 4.8** shows the amplitude at OER potential of the two

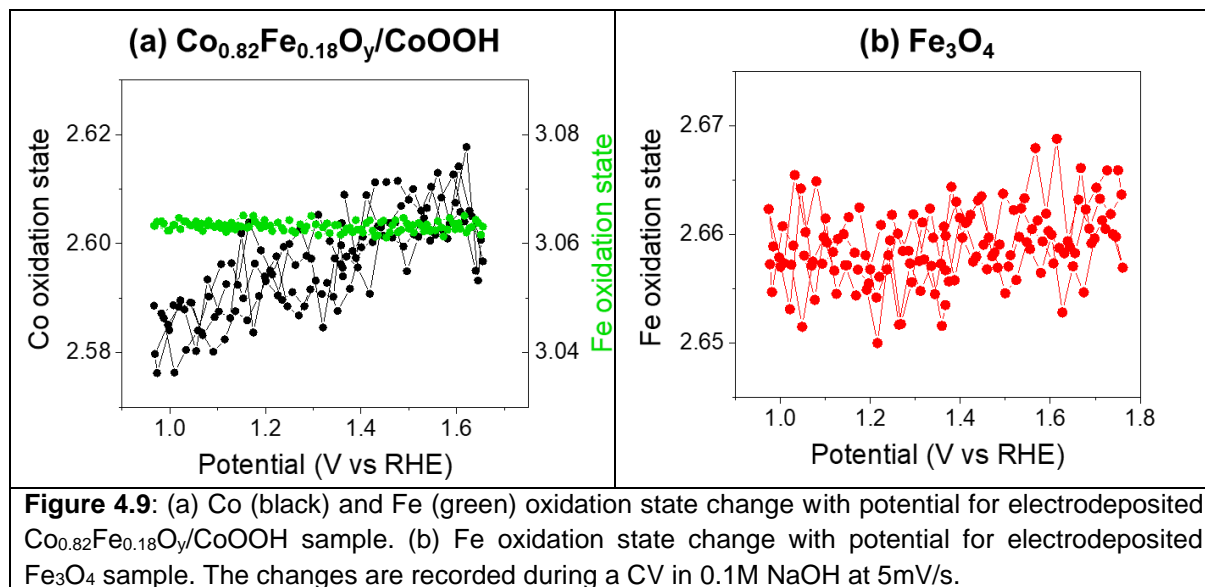
parameters we have stated before (a) $\frac{V_{skin(1.67V)}}{V_{grain}}$ and (b) $\frac{\Delta V_{bulk(1.67V)}}{V}$ as a function of the iron content x . The skin volume fraction $\frac{V_{skin(1.67V)}}{V_{grain}}$ roughly decreases with increasing iron content. For $\frac{\Delta V_{bulk(1.67V)}}{V}$ (**Fig.4.8b**), we indeed observe that the relative unit cell compression is larger for Co_3O_4 than for Fe_3O_4 , which agrees with the small skin layer volume measured for Fe_3O_4 samples. The tendency among $Co_{1-x}Fe_xO_y$ is less easy to determine: $\frac{\Delta V_{bulk(1.67V)}}{V}$ may seem to increase with increasing iron content, which goes in the opposite direction of what is observed for $\frac{V_{skin(1.67V)}}{V_{grain}}$. Samples with an iron content around 20-30% have similar $\frac{\Delta V_{bulk(1.67V)}}{V}$ values while another group with higher Fe content shows higher $\frac{\Delta V_{bulk(1.67V)}}{V}$. The behaviour of these Fe richer oxides is in fact mainly dictated by $\Delta\varepsilon_{||}(1.67V)$, that is significantly larger than for the other mixed oxides (see **Fig.4.6**). This may be linked to the more granular morphology of these deposits which could allow larger in plane strains because the grains are less packed.



Co and Fe oxidation state changes with potential

The variations of Co and Fe oxidation state with potential $\alpha_{\text{Co}_{\text{bilayer}}}(U)$ and $\alpha_{\text{Fe}}(U)$ are presented in **Figure 4.9a** for $\text{Co}_{0.82}\text{Fe}_{0.18}\text{O}_y/\text{CoOOH}$ and in **Figure 4.9b** for Fe_3O_4 . They were recorded during CVs at 5mV/s in 0.1M NaOH electrolyte using the method described in **section 2.3**. In the potential window [0.97 – 1.67 V_{RHE}] in $\text{Co}_{0.82}\text{Fe}_{0.18}\text{O}_y/\text{CoOOH}$ film, $\alpha_{\text{Fe}}(U)$ (green plot) remains unchanged, while $\alpha_{\text{Co}}(U)$ (black plot) increases reversibly and significantly with potential ($\frac{\Delta\alpha_{\text{Co}}}{\alpha_{\text{Co}}} \approx 1.1\%$, comparable to $\frac{\Delta\alpha_{\text{Co}}}{\alpha_{\text{Co}}}$ of 1.5% measured for Co_3O_4 in **chapter 3**). Simultaneously, the potential dependence of the film structure was probed and showed a similar behaviour as described in **Fig.4.5**. These observations indicate that iron, present as Fe^{3+} in $\text{Co}_{1-x}\text{Fe}_x\text{O}_y$, is not oxidized during the pre-OER and OER process, while Co cations, present as both Co^{2+} and Co^{3+} get oxidized, as a skin layer is formed. This is similar to what was measured for Co_3O_4 . Since $\alpha_{\text{Fe}}(U)$ is constant in the studied potential window,

the skin layer formation on these oxides is probably linked to the oxidation of Co atoms only. This is in agreement with other operando XAS studied on CoFeOx oxides: when iron is present as Fe³⁺ in the oxide, it remains Fe(III) in OER conditions while Co oxidation state increases [7,11].



In the case of Fe₃O₄ (**Fig.4.9b**) $\alpha Fe(U)$ remains constant between 1.0 V and 1.4V, and a slight increase of Fe oxidation state ($\frac{\Delta\alpha Fe}{\alpha Fe} \approx 0.2\%$) is measured at potentials $> 1.4V_{RHE}$. A reversible decrease of Fe₃O₄ crystallite size was also measured starting 1.4V_{RHE} (see **Figure 4.5**). As for Co₃O₄, Fe²⁺ at the surface might be oxidized at $U > 1.4V$ to form another Fe oxide phase. We attempted to derive a quantitative correlation between structural and oxidation state changes measured for Fe₃O₄, as done for Co₃O₄ in **chapter 3**. However, the results were not conclusive so as to determine the oxidation state of Fe atoms within Fe₃O₄ skin layer with enough precision. This is especially due to the significant scatter in the data caused by the very little potential induced variations in oxidation state and skin volume shown by this sample, especially at low potentials. Since Fe₃O₄ shows almost no oxidation state changes with potential, its skin layer likely contains both Fe²⁺ and Fe³⁺ ions. Different works about crystalline Fe₃O₄ oxidation in alkaline media suggest that Fe₃O₄ surface is passivated by a Fe³⁺ based oxide layer of a few Fe planes at OER potentials [17,18,19]. In our case for electrodeposited Fe₃O₄(111), if this phase transformation occurs, it would be limited to the very top surface and begin around 1.4V. This is largely more positive than the standard potential of the Fe₃O₄/Fe₂O₃ transition (around 0.15 V_{RHE} [34]). Only ~ 1 Fe plane would be oxidized at OER onset and this plane may act as a passivation layer that prevents further oxidation of the film, as evoked in [17], which may explain the small skin layer thickness we measure.

Let us now consider the $\text{Co}_{1-x}\text{Fe}_x\text{O}_y/\text{CoOOH}$ bilayers in order to determine the mean oxidation state of Co atoms within $\text{Co}_{1-x}\text{Fe}_x\text{O}_y$ skin layer, using a similar methodology as described for Co_3O_4 in **chapter 3**. To simplify the notations, let us call B the following quantity:

$$B = \frac{N_{\text{Co}_{1-x}\text{Fe}_x\text{O}_y}}{N_{\text{tot}}} \quad (4.6)$$

$\alpha\text{Co}_{\text{bilayer}}(U)$ (Eq. (4.1)) is therefore written as:

$$\alpha\text{Co}_{\text{bilayer}}(U) = \alpha\text{Co}_{\text{Co}_{1-x}\text{Fe}_x\text{O}_y}(U) * B + \alpha\text{Co}_{\text{CoOOH}} * (1 - B) \quad (4.7)$$

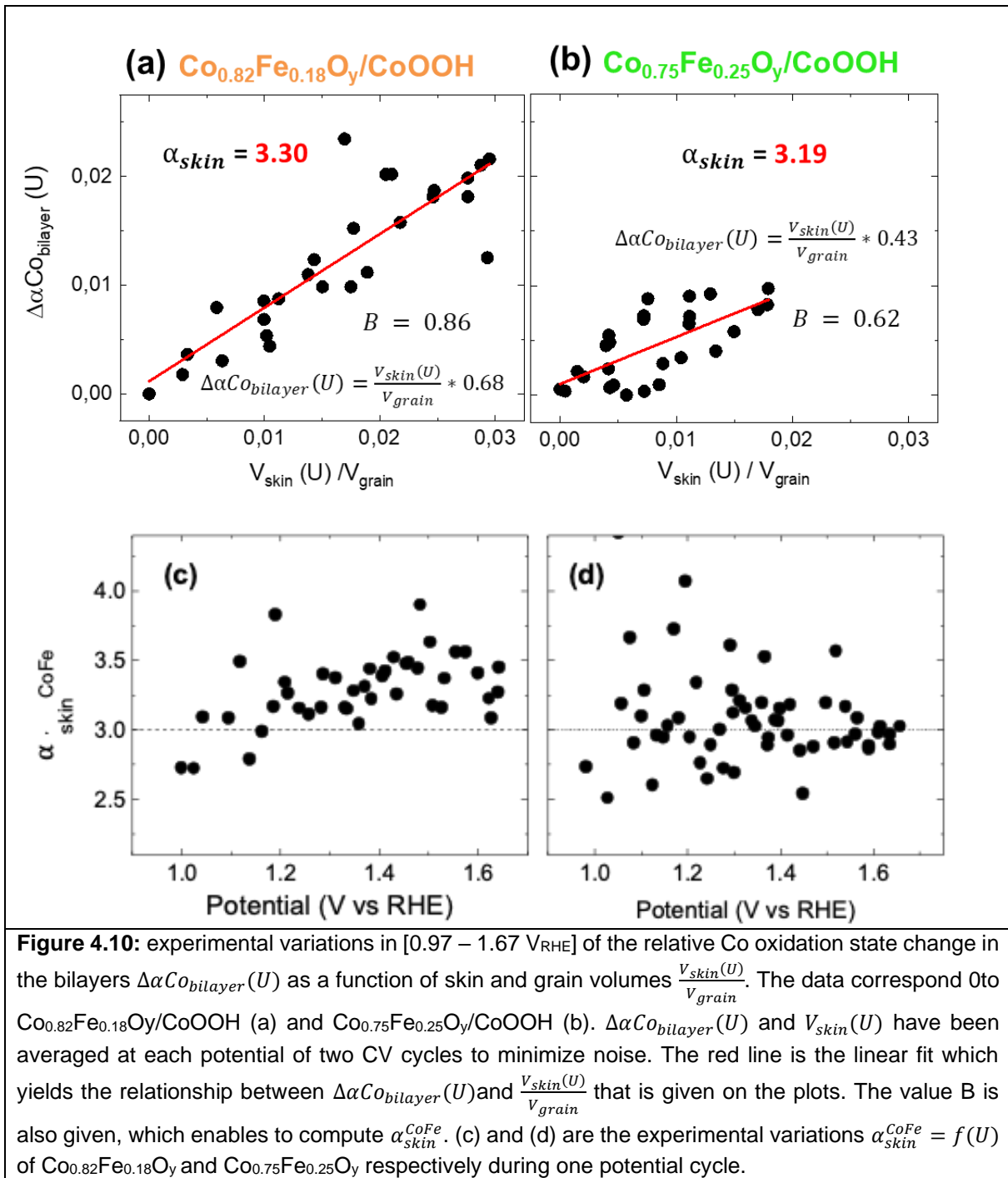
Where $\alpha\text{Co}_{\text{CoOOH}}$ is independent of U since the CoOOH layer is buried underneath $\text{Co}_{1-x}\text{Fe}_x\text{O}_y$ and not exposed to the electrolyte. As a consequence, the potential induced variations of $\Delta\alpha\text{Co}_{\text{bilayer}}$ are only related to $\Delta\alpha\text{Co}_{\text{Co}_{1-x}\text{Fe}_x\text{O}_y}$ the Co oxidation state variations in $\text{Co}_{1-x}\text{Fe}_x\text{O}_y$ layer. The latter is expressed like in Eq. (4.5). This gives:

$$\Delta\alpha\text{Co}_{\text{bilayer}}(U) = \frac{V_{\text{skin}}(U)}{V_{\text{grain}}} * B * [\alpha_{\text{skin}}^{\text{CoFe}}(U) - \alpha_{\text{bulk}}^{\text{CoFe}}] \quad (4.8)$$

Where $\alpha_{\text{bulk}}^{\text{CoFe}}$ refers to $\alpha\text{Co}_{\text{Co}_{1-x}\text{Fe}_x\text{O}_y}(0.97\text{V})$, the Co oxidation in $\text{Co}_{1-x}\text{Fe}_x\text{O}_y$ layer at 0.97V (see **Table 4.1**) and $\alpha_{\text{skin}}^{\text{CoFe}}(U)$ the Co mean oxidation state in the skin layer of volume $V_{\text{skin}}(U)$.

Figure 4.10 shows the variations of $\Delta\alpha\text{Co}_{\text{bilayer}}(U)$ as a function of $\frac{V_{\text{skin}}(U)}{V_{\text{grain}}}$, for (a) $\text{Co}_{0.82}\text{Fe}_{0.18}\text{O}_y$ and (b) $\text{Co}_{0.75}\text{Fe}_{0.25}\text{O}_y$. The data are averaged over two potential sweeps in order to minimize noise. The red lines are linear fits of the data, which equation is given on the top of each figure. It clearly shows a linear dependence between $\Delta\alpha\text{Co}_{\text{bilayer}}(U)$ and $\frac{V_{\text{skin}}(U)}{V_{\text{grain}}}$ since both fits have a nearly 0 intercept ($\sim 10^{-3}$). This shows that $\alpha_{\text{skin}}^{\text{CoFe}}(U)$ is, in a first approximation, independent of the potential: the skin layer oxidation state retrieved from the slope of the linear fits is: $\alpha_{\text{skin}}^{\text{CoFe}} = \frac{\text{slope}}{B} + \alpha_{\text{bulk}}^{\text{CoFe}}$. The B value is given for each sample on the corresponding plot, together with $\alpha_{\text{skin}}^{\text{CoFe}}$. The analysis yields $\alpha_{\text{skin}}^{\text{CoFe}} = 3.30 \pm 0.03$ for $\text{Co}_{0.82}\text{Fe}_{0.18}\text{O}_y$ and $\alpha_{\text{skin}}^{\text{CoFe}} = 3.19 \pm 0.03$ for $\text{Co}_{0.75}\text{Fe}_{0.25}\text{O}_y$. This means that $\alpha\text{Co}_{\text{bilayer}}(U)$ increase results from the oxidation of $\text{Co}^{2+/3+}$ atoms within the skin layer to $\text{Co}^{3+/4+}$. Unlike for Co_3O_4 , $\alpha_{\text{skin}}^{\text{CoFe}}$ is significantly higher than 3, which evidences the formation of 20-30% Co^{4+} at the mixed oxides surfaces. Based on the example of these two samples, the Co^{4+} concentration of the skin layer may vary with the sample (surface) iron content. In **Figure 4.10** (c) and (d) are respectively shown the evolution of $\alpha_{\text{skin}}^{\text{CoFe}} = f(U)$ for one potential cycle of $\text{Co}_{0.82}\text{Fe}_{0.18}\text{O}_y$ and $\text{Co}_{0.75}\text{Fe}_{0.25}\text{O}_y$. $\alpha_{\text{skin}}^{\text{CoFe}} = 3$ is shown with a dotted horizontal line. In both cases, $\alpha_{\text{skin}}^{\text{CoFe}}$ increases between 1.0V and 1.1-1.2V and then remains approximately constant at a value > 3 . As expected from the analysis of **Fig.4.10** (a) and (b), $\alpha_{\text{skin}}^{\text{CoFe}}$ is higher for $\text{Co}_{0.82}\text{Fe}_{0.18}\text{O}_y$ than $\text{Co}_{0.75}\text{Fe}_{0.25}\text{O}_y$.

Compared to Co_3O_4 , the formation of Co^{4+} species could be facilitated in the mixed oxides by the presence of Fe^{3+} , as suggested for NiFe and CoFe oxides [10,38]. In the case of NiFe oxides, Fe^{3+} were thought to act as Lewis acid and promote the formation of Ni^{4+} [10]. However in our case, operando XAS measurements show that Fe oxidation state does not change with potential, making unlikely an electron transfer between Fe^{3+} and Co^{2+} . In the case of CoFe oxides, the authors suggested that the presence of Fe^{3+} adjacent to surface Co atoms (Co-O-Fe groups) may facilitate the deprotonation of Co^{3+} -OH groups to form $\text{Co}^{4+}=\text{O}$ [38], compared to Co-O-Co groups present in pure Co oxides. This mechanism involving Fe^{3+} would be in line with the skin layer oxidation state values determined for both pure Co oxides (chapter 3) and mixed CoFe oxides. In addition, if the formation of Co^{4+} results from the kinetic deprotonation of surface Co^{3+} , this may explain why Co^{3+} can be oxidized at 1.2V while Co^{4+} species are thermodynamically stable above 1.5V. Since there might be a substantial amount of oxygen vacancies in $\text{Co}_{1-x}\text{Fe}_x\text{O}_y$ oxide films (see section 4.2), another possibility would be that their presence may facilitate the formation of Co^{4+} and oxygen insertion in the lattice.



4.4 Composition dependence of catalytic properties

Catalytic activity of Fe-doped Co_3O_4 :

The catalytic activity of the different $\text{Co}_{1-x}\text{Fe}_x\text{O}_y/\text{CoOOH}$ samples listed in **Table 4.3** has been investigated in 0.1M NaOH electrolyte, and compared to that of $\text{Co}_3\text{O}_4/\text{CoOOH}$ and Fe_3O_4 . Their catalytic parameters are given in **Table 4.4**. It includes the Tafel slope b, the current density measured at $1.65V_{RHE}$ and the overpotential at a current density of $1\text{mA}/\text{cm}^2$ both measured versus the geometrical surface area of the substrate. For each sample, cyclic

voltammograms in pre-OER and OER regimes are recorded before any operando X-ray based measurement and the catalytic parameters of the oxides are derived from these CVs. **Figure 4.11** shows an example of this procedure. In (a) it compares CVs at 5mV/s of Co_3O_4 -1 (black), $\text{Co}_{0.51}\text{Fe}_{0.49}\text{O}_y$ (green) and Fe_3O_4 -1 (red) samples all electrodeposited on the same Au(111) substrate. The OER onset potential is smaller for $\text{Co}_{0.51}\text{Fe}_{0.49}\text{O}_y$, as well as the current density at $1.65V_{\text{RHE}}$ (+410 mV at $1\text{mA}/\text{cm}^2$ and $1.65\text{ mA}/\text{cm}^2$) than for $\text{Co}_3\text{O}_4/\text{CoOOH}$ (+452 mV and $0.29\text{ mA}/\text{cm}^2$) and Fe_3O_4 (+480 mV and $0.09\text{ mA}/\text{cm}^2$). Corresponding Tafel plots in OER regime are shown in **Fig.4.11b**, illustrating that $\text{Co}_{0.51}\text{Fe}_{0.49}\text{O}_y/\text{CoOOH}$ Tafel slope (46 mV/decade) is smaller than that of $\text{Co}_3\text{O}_4/$ (58 mV/decade), itself smaller than the one of Fe_3O_4 (71 mV/decade). These measurements evidence the role of Fe addition to Co_3O_4 in improving its catalytic activity towards OER. They are also consistent with the reported higher OER activity of Co oxide compared to Fe oxides [1,4,11,14,15,19]. The pre-OER regime of the CVs [0.97-1.57 V] is presented in **Appendix 4.3**.

Table 4.4: Electrochemical and structural properties of $\text{Co}_{1-x}\text{Fe}_x\text{O}_y/\text{CoOOH}$, $\text{Co}_3\text{O}_4/\text{CoOOH}$ and Fe_3O_4 samples. j at $1.65V_{\text{RHE}}$ is the current density per cm^2_{geo} at 1.65V, b is the Tafel slope, η_{geo} is the overpotential necessary to reach a current density of $1\text{ mA}/\text{cm}^2_{\text{geo}}$. d_{\perp} and d_{\parallel} are the out-of-plane and in-plane crystallite sizes determined from SXRD measurements. RF max is the maximal roughness factor of the films (for disconnected islands of sizes d_{\perp} and d_{\parallel}).

Sample	Substrate	j at $1.65V_{\text{RHE}}$ ($\text{mA}/\text{cm}^2_{\text{geo}}$)	b (mV/dec)	η_{geo} (mV)	d_{\perp} (nm)	d_{\parallel} (nm)	RF max
Co_3O_4 -1	CoOOH	0.29	58	452	24	24	4.0
Co_3O_4 -2	CoOOH	2.03	53	402	19	14	5.1
$\text{Co}_{0.82}\text{Fe}_{0.18}\text{O}_y$	CoOOH	2.24	47	403	37	23	5.8
$\text{Co}_{0.75}\text{Fe}_{0.25}\text{O}_y$ -1	CoOOH	0.16	49	>460	26	25	4.1
$\text{Co}_{0.75}\text{Fe}_{0.25}\text{O}_y$ -2	CoOOH	3.33	47	387	17	27	2.9
$\text{Co}_{0.73}\text{Fe}_{0.27}\text{O}_y$	CoOOH	0.89	53	415	18	28	2.9
$\text{Co}_{0.72}\text{Fe}_{0.28}\text{O}_y$	CoOOH	0.52	51	433	15	14	4.2
$\text{Co}_{0.69}\text{Fe}_{0.31}\text{O}_y$	CoOOH	0.49	52	434	15	22	3.0
$\text{Co}_{0.60}\text{Fe}_{0.40}\text{O}_y$	CoOOH	0.30	59	452	15	16	3.8
$\text{Co}_{0.51}\text{Fe}_{0.49}\text{O}_y$	CoOOH	1.35	46	410	15	23	3.0
Fe_3O_4 -1	Au(111)	0.09	71	480	15	23	3.0
Fe_3O_4 -2	Au(111)	0.05	62	527	28	26	4.2

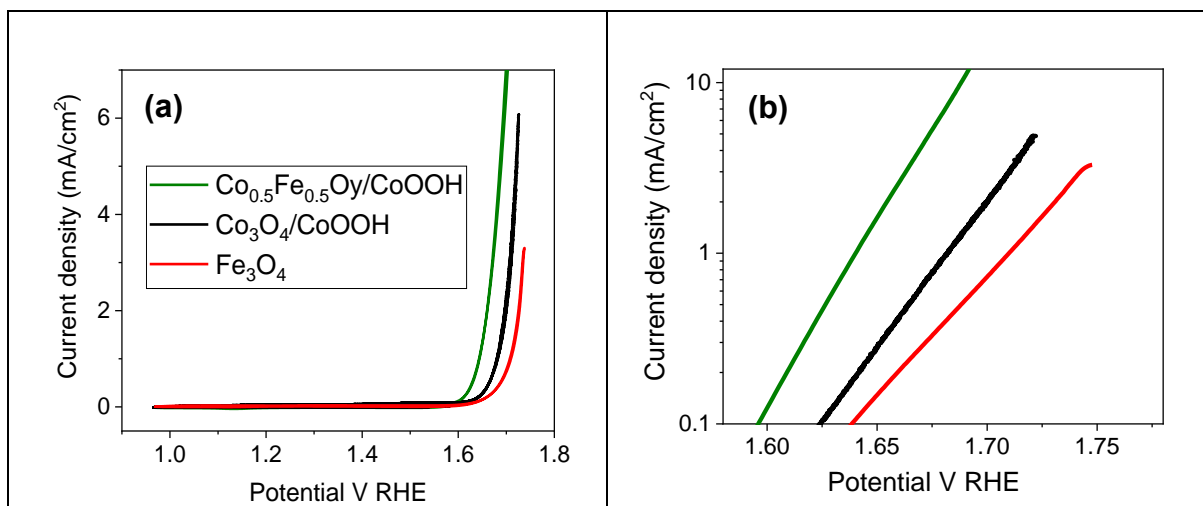


Figure 4.11: (a) Cyclic voltammograms (5 mV/s) recorded in 0.1M NaOH electrolyte of electrodeposited Co_{0.5}Fe_{0.5}O_y/CoOOH (green), Co₃O₄/CoOOH (black) and Fe₃O₄ (red) and corresponding Tafel plots in (b). The current density is given with respect to the geometrical surface area of the substrate which is the same Au(111) crystal.

Figure 4.12a shows the Tafel slopes of all samples included in **Table 4.4** as a function of the iron content, with Fe₃O₄ in red, Co_{1-x}Fe_xO_y in blue and Co₃O₄ in black. The Tafel slopes are lower for Co_{1-x}Fe_xO_y than for both Co₃O₄ and Fe₃O₄. Fe₃O₄ exhibit the higher Tafel slopes, approximately 10 mV/decade higher than the one of Co₃O₄. This could suggest that the OER mechanism, for example the rate determining step, may differ for the three oxide species presented here.

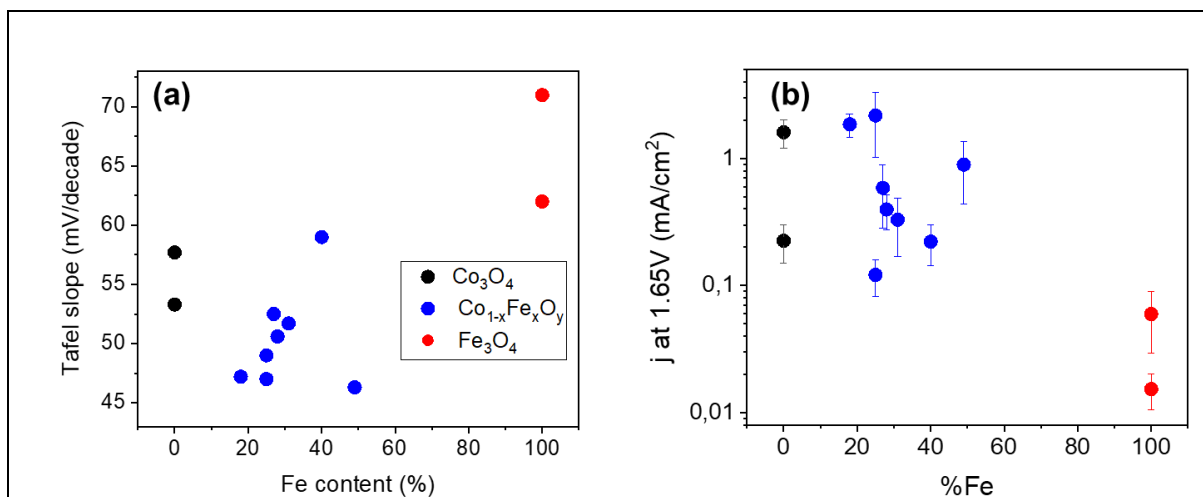


Figure 4.12: (a) Tafel slopes and (b) current density at 1.65V_{RHE} of Co₃O₄/CoOOH (black points), Fe₃O₄ (red points) and Co_{1-x}Fe_xO_y/CoOOH (blue points) samples as a function of the Fe content *x*. The lower end of the error bar on the current density corresponds to the current density normalized with respect to geometrical area of the sample and the upper end with respect to the maximum roughness factor of the sample (derived from the grain sizes measured in XRD, see **Table 4.4**).

The XRD crystallite sizes in plane (d_{\parallel}) and out-of-plane (d_{\perp}) determined by Co₃O₄ or Fe₃O₄ (113) or (404) Bragg peak analysis using SXRD are also given in **Table 4.4**. These parameters

can serve as computing a maximal roughness factor (RF) for each sample. Following the crystallite model given in **Chapter 3 (Appendix A3.1)**, we can determine from d_{\perp} and d_{\parallel} the external surface area of one crystallite assuming that the crystallites are disconnected. The maximal RF is the ratio of this surface and the top surface of a crystallite (fully packed film). For each sample of **Table 4.4**, a maximum value for η and a minimum value for j are obtained from the maximal RF, while η_{geo} and j per mA/cm²_{geo} (**Table 4.4**) are respectively the minimum and maximum value for these parameters. **Fig.4.12b** shows j as a function of the Fe content x . The data points in these graphs are the average of the two maximum and minimum values and the error bar joins these two extreme values. The data confirm that Fe₃O₄ is not a good catalyst compared to Co₃O₄. They also suggest that Co_{1-x}Fe_xO_y oxide layers present an intermediate OER activity. It is however difficult to establish a clear trend as a function of Fe content. We will see in next sub-section that a refined analysis is necessary.

OER activity and skin layer

Results obtained in our group indicate that the OER activity of epitaxial electrodeposited Co₃O₄ (111) layers increases with the skin volume [37]. We tentatively used this approach here. Namely, we checked the correlation between the OER activity with the “average skin layer thickness”. This corresponds to the parameter $\langle d_{skin} \rangle$ which is defined as the skin layer volume of one crystallite at 1.67V, $V_{skin}(1.65V)$, divided by its surface area (referred as A_{top} in **Appendix A3.1** of chapter 3 where its analytical expression is given):

$$\langle d_{skin} \rangle = \Delta d_{\perp}(1.65V) + 2 \cdot \frac{d_{\perp}}{d_{\parallel}} \cdot \Delta d_{\parallel}(1.65V) \quad (4.9)$$

$\langle d_{skin} \rangle$ has a unit of a length (nm). **Figure 4.13a** shows $\langle d_{skin} \rangle$ as a function of the iron content for Co₃O₄/CoOOH Co_{1-x}Fe_xO_y/CoOOH and Fe₃O₄ samples shown in **Table 4.4**. Additional Co₃O₄ samples measured during similar experiments have been added to the graph in order to increase statistics. The figure shows that $\langle d_{skin} \rangle$ follows the tendency: Fe₃O₄ < Co_{1-x}Fe_xO_y < Co₃O₄ and in Co_{1-x}Fe_xO_y it decreases with increasing iron content. This is consistent with the rough decrease of $\frac{V_{skin}(1.67V)}{V_{grain}}$ with increasing Fe content (**Figure 4.8**). However, the trend is clearer when plotting $\langle d_{skin} \rangle$. Within Co₃O₄ samples, a variability of $\langle d_{skin} \rangle$ can be observed, probably because of the Δd_{\parallel} value that likely varies with the oxide morphology. Therefore, pure cobalt oxides Co₃O₄ roughly have the highest “average skin layer thickness”, which then decreases gradually when adding Fe to the film until becoming very thin for pure Fe oxides Fe₃O₄.

Figure 4.13b shows the current density measured at 1.65V_{RHE} versus the geometric surface area as a function of $\langle d_{skin} \rangle$ for Co₃O₄ and Fe₃O₄ samples, both shown on logarithmic scale.

Previously [37], our group evidenced a correlation trend between $\langle d_{skin} \rangle$ and the current density j obtained for different $\text{Co}_3\text{O}_4(111)$ samples prepared in different conditions, as illustrated by the dashed line. Because the OER activity increases with the skin layer thickness, it is therefore related to the amount of Co sites in the skin. This correlation implies that all atoms within the skin layer are active sites for OER. In comparison, Fe_3O_4 samples which $\langle d_{skin} \rangle$ is smaller than that of Co_3O_4 samples, present a smaller OER activity. Following the statement that all Co/Fe atoms in the skin layer are active sites, and since the volume density of Fe and Co in Co_3O_4 and Fe_3O_4 are approximately similar, the tendency of **Fig 4.13b** would suggest that, compared to Co_3O_4 , fewer active sites are involved in OER at Fe_3O_4 surface, leading to smaller OER current at a same potential. This might therefore indicate that the low OER activity of Fe_3O_4 is due to the small skin layer formed at their surface. However, more data would be required to confirm this statement.

Figure 4.13c now compares $\langle d_{skin} \rangle$ as function of the current density at 1.65V for both Co_3O_4 and $\text{Co}_{1-x}\text{Fe}_x\text{O}_y$. We observe that $\text{Co}_{1-x}\text{Fe}_x\text{O}_y$ oxides also follow a $\langle d_{skin} \rangle - j$ trend, as illustrated with the green dashed line (linear fit of the data). This trend is placed slightly above the data points of pure Co_3O_4 oxides (in black). This means that a skin layer containing less active sites is required for $\text{Co}_{1-x}\text{Fe}_x\text{O}_y$ to achieve the same OER activity as Co_3O_4 . As a consequence, the intrinsic activity of $\text{Co}_{1-x}\text{Fe}_x\text{O}_y$ oxides, i.e. the activity per active site, is slightly higher than that of Co_3O_4 . Since both Co and Fe atoms are present in the skin layer of $\text{Co}_{1-x}\text{Fe}_x\text{O}_y$, this further suggests that both Co and Fe atoms participate in the OER reaction in the mixed oxides.

In $\text{Co}_{1-x}\text{Fe}_x\text{O}_y$ spinel oxides, we expect the presence of both Co-O-Fe and Co-O-Co bridges, and this should also be the case in their skin layer, while only Co-O-Co bridges are present in the skin layer of Co_3O_4 according the works of Dau et al. [21]. Therefore, both Co-O-Fe and Co-O-Co bridges could be catalytic sites in the mixed oxides. The existence of another catalytic site where neighbouring Fe^{3+} play a role may stand for variations observed between $\text{Co}_{1-x}\text{Fe}_x\text{O}_y$ and Co_3O_4 catalytic behaviours. First, the OER mechanism and especially the rate determining step could not be the same at each of the catalytic sites, as suggested by Smith et al. [11] and Dionigi et al. [39]. This would be in line with the lower Tafel slopes measured for $\text{Co}_{1-x}\text{Fe}_x\text{O}_y$: $\sim 45\text{-}50$ mV/decade against $55\text{-}60$ mV/decade for Co_3O_4 . Second, the presence of neighbouring Fe^{3+} seems to increase the mean Co oxidation state in the skin layer, as described in **section 4.3**. The higher intrinsic OER activity of $\text{Co}_{1-x}\text{Fe}_x\text{O}_y$ compared to Co_3O_4 could therefore be associated to a higher amount of Co^{4+} present in their skin layer. To check this possibility, we plotted in **Figure 4.13d** the ratio $j(1.65V) / \langle d_{skin} \rangle$ that represents the current density per atom in the skin layer, as a function of Co mean oxidation state in the skin layer. The graph compares Co_3O_4 -1 sample from **chapter 3** in black, $\text{Co}_{0.82}\text{Fe}_{0.18}\text{O}_y$ and $\text{Co}_{0.75}\text{Fe}_{0.25}\text{O}_y$ -1 samples (**Fig 4.10**) in green (these are the two samples for which operando

XAS is available). This plot shows that the catalytic activity per atom within the skin layer is increasing with the average oxidation state of Co atoms in the skin. Based on the results of these three samples, the presence of Co^{4+} in the skin layer therefore improves the OER catalytic activity of Co based oxides. More data would however be needed to establish a stronger trend between catalytic activity per active site and Co oxidation state.

Overall, these data rationalize the OER activity measured for Co_3O_4 and $\text{Co}_{1-x}\text{Fe}_x\text{O}_y$ oxides and show that the number of active sites within the skin layer is a good descriptor for OER activity. In addition, for Co containing oxides, a higher OER activity per active site is associated to higher Co oxidation state.

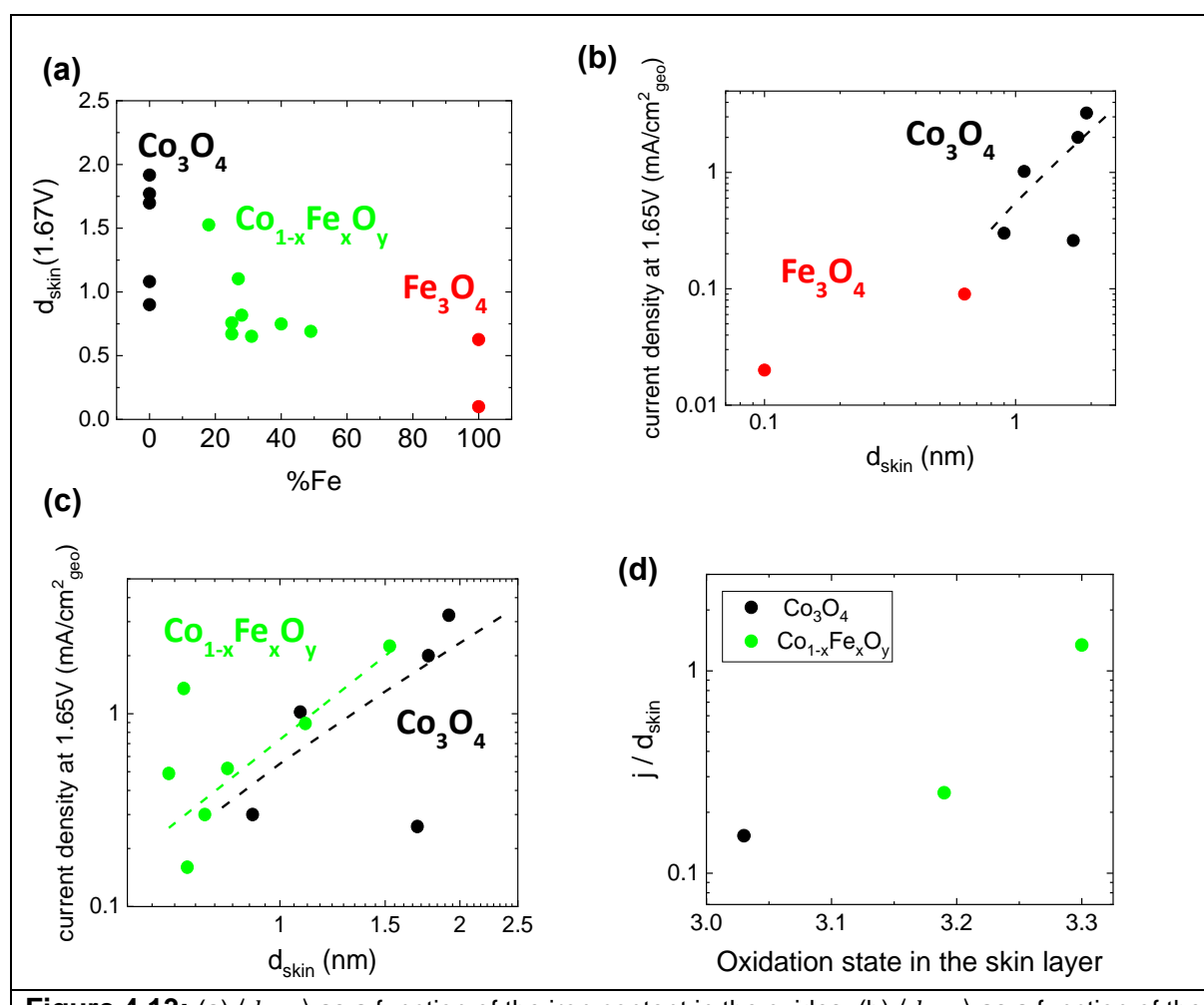


Figure 4.13: (a) $\langle d_{skin} \rangle$ as a function of the iron content in the oxides. (b) $\langle d_{skin} \rangle$ as a function of the current density measured at a potential of 1.65V for Co_3O_4 and Fe_3O_4 oxides. The dashed line shows the correlation between j and $\langle d_{skin} \rangle$ obtained for Co_3O_4 samples shown here. (c) $\langle d_{skin} \rangle$ as a function of the current density measured at a potential of 1.65V for Co_3O_4 and $\text{Co}_{1-x}\text{Fe}_x\text{O}_y$ oxides. The correlations between j and $\langle d_{skin} \rangle$ are shown with green and black dashed lines for $\text{Co}_{1-x}\text{Fe}_x\text{O}_y$ and Co_3O_4 respectively. (d) Current density per atom in the skin determined as the ratio $j / \langle d_{skin} \rangle$ as a function of Co mean oxidation state in the skin layer (obtained by operando XAS measurements).

4.5 Conclusion

In this chapter we have shown that electrodeposited Fe_3O_4 and $\text{Co}_{1-x}\text{Fe}_x\text{O}_y$ grow on Au(111) and CoOOH/Au(111) substrate as spinel oxides with a (111) orientation. Their morphology is similar to that of Co_3O_4 , resulting in well-defined thin films. Spectroscopic characterizations using XAS show that they contain Fe^{3+} , Co^{2+} and Co^{3+} cations. Upon increasing potential until OER onset, all oxides suffer reversible structural changes, sign of a surface transformation into the OER active phase. The formation of the skin layer generates compressive strains in the oxides' unit cell, which are proportional to its volume. Using operando XAS we have shown that this surface transformation results from the oxidation of Co^{2+} into $\text{Co}^{3/4+}$ in the case of $\text{Co}_{1-x}\text{Fe}_x\text{O}_y$ and from the oxidation of Fe^{2+} in Fe^{3+} for Fe_3O_4 . In $\text{Co}_{1-x}\text{Fe}_x\text{O}_y$, Fe remains at the oxidation state +3 and its presence may promote the formation of Co^{4+} in the mixed oxides. We have shown that the OER activity of the oxides, measured as the current density at 1.65V, is linked to the equivalent thickness of their skin layer. The latter decreases with increasing Fe content. However, $\text{Co}_{1-x}\text{Fe}_x\text{O}_y$ oxides show slightly higher intrinsic activity compared to Co_3O_4 : even though $\text{Co}_{1-x}\text{Fe}_x\text{O}_y$ form thinner skin layer compared to Co_3O_4 , their skin layer contains more Co^{4+} atoms, and we show that their amount is associated to high OER activity. Fe_3O_4 show the lowest catalytic activity, which may be rationalized by the very small skin layer formed at their surface.

4.6 Bibliography

- [1] McCrory, C. C. L.; Jung, S.; Ferrer, I. M.; Chatman, S. M.; Peters, J. C.; Jaramillo, T. F. Benchmarking Hydrogen Evolving Reaction and Oxygen Evolving Reaction Electrocatalysts for Solar Water Splitting Devices. *J. Am. Chem. Soc.* **2015**, *137* (13), 4347–4357. <https://doi.org/10.1021/ja510442p>.
- [2] Morales-Guio, C. G.; Liardet, L.; Hu, X. Oxidatively Electrodeposited Thin-Film Transition Metal (Oxy)hydroxides as Oxygen Evolution Catalysts. *J. Am. Chem. Soc.* **2016**, *138* (28), 8946–8957. <https://doi.org/10.1021/jacs.6b05196>.
- [3] Burke, M. S.; Zou, S.; Enman, L. J.; Kellon, J. E.; Gabor, C. A.; Pledger, E.; Boettcher, S. W. Revised Oxygen Evolution Reaction Activity Trends for First-Row Transition-Metal (Oxy)hydroxides in Alkaline Media. *J. Phys. Chem. Lett.* **2015**, *6* (18), 3737–3742. <https://doi.org/10.1021/acs.jpcclett.5b01650>.
- [4] Feng, C.; Faheem, M. B.; Fu, J.; Xiao, Y.; Li, C.; Li, Y. Fe-Based Electrocatalysts for Oxygen Evolution Reaction: Progress and Perspectives. *ACS Catal.* **2020**, *10* (7), 4019–4047. <https://doi.org/10.1021/acscatal.9b05445>.
- [5] Burke, M. S.; Kast, M. G.; Trotochaud, L.; Smith, A. M.; Boettcher, S. W. Cobalt-Iron (Oxy)hydroxide Oxygen Evolution Electrocatalysts: The Role of Structure and Composition on Activity, Stability, and Mechanism. *J. Am. Chem. Soc.* **2015**, *137* (10), 3638–3648. <https://doi.org/10.1021/jacs.5b00281>.

- [6] Enman, L. J.; Stevens, M. B.; Dahan, M. H.; Nellist, M. R.; Toroker, M. C.; Boettcher, S. W. Operando X-Ray Absorption Spectroscopy Shows Iron Oxidation Is Concurrent with Oxygen Evolution in Cobalt–Iron (Oxy)hydroxide Electrocatalysts. *Angew. Chemie - Int. Ed.* **2018**, *57* (39), 12840–12844. <https://doi.org/10.1002/anie.201808818>.
- [7] Gong, L.; Chng, X. Y. E.; Du, Y.; Xi, S.; Yeo, B. S. Enhanced Catalysis of the Electrochemical Oxygen Evolution Reaction by Iron(III) Ions Adsorbed on Amorphous Cobalt Oxide. *ACS Catal.* **2018**, *8* (2), 807–814. <https://doi.org/10.1021/acscatal.7b03509>.
- [8] Song, F.; Bai, L.; Moysiadou, A.; Lee, S.; Hu, C.; Liardet, L.; Hu, X. Transition Metal Oxides as Electrocatalysts for the Oxygen Evolution Reaction in Alkaline Solutions: An Application-Inspired Renaissance. *J. Am. Chem. Soc.* **2018**, *140* (25), 7748–7759. <https://doi.org/10.1021/jacs.8b04546>.
- [9] Chen, J. Y. C.; Dang, L.; Liang, H.; Bi, W.; Gerken, J. B.; Jin, S.; Alp, E. E.; Stahl, S. S. Operando Analysis of NiFe and Fe Oxyhydroxide Electrocatalysts for Water Oxidation: Detection of Fe⁴⁺ by Mössbauer Spectroscopy. *J. Am. Chem. Soc.* **2015**, *137* (48), 15090–15093. <https://doi.org/10.1021/jacs.5b10699>.
- [10] Li, N.; Bediako, D. K.; Hadt, R. G.; Hayes, D.; Kempa, T. J.; Von Cube, F.; Bell, D. C.; Chen, L. X.; Nocera, D. G. Influence of iron doping on tetravalent nickel content in catalytic oxygen evolving films. *Proc. Natl. Acad. Sci. U. S. A.* **2017**, *114* (7), 1486–1491. <https://doi.org/10.1073/pnas.1620787114>.
- [11] Smith, R. D. L.; Pasquini, C.; Loos, S.; Chernev, P.; Klingan, K.; Kubella, P.; Mohammadi, M. R.; Gonzalez-Flores, D.; Dau, H. Spectroscopic Identification of Active Sites for the Oxygen Evolution Reaction on Iron-Cobalt Oxides. *Nat. Commun.* **2017**, *8* (1). <https://doi.org/10.1038/s41467-017-01949-8>.
- [12] Hsu, C. S.; Suen, N. T.; Hsu, Y. Y.; Lin, H. Y.; Tung, C. W.; Liao, Y. F.; Chan, T. S.; Sheu, H. S.; Chen, S. Y.; Chen, H. M. Valence- and element-dependent water oxidation behaviors: In situ X-ray diffraction, absorption and electrochemical impedance spectroscopies. *Phys. Chem. Chem. Phys.* **2017**, *19* (13), 8681–8693. <https://doi.org/10.1039/c6cp07630k>.
- [13] Hung, S. F.; Hsu, Y. Y.; Chang, C. J.; Hsu, C. S.; Suen, N. T.; Chan, T. S.; Chen, H. M. Unraveling Geometrical Site Confinement in Highly Efficient Iron-Doped Electrocatalysts toward Oxygen Evolution Reaction. *Adv. Energy Mater.* **2018**, *8* (7), 1–11. <https://doi.org/10.1002/aenm.201701686>.
- [14] Subbaraman, R.; Tripkovic, D.; Chang, K. C.; Strmcnik, D.; Paulikas, A. P.; Hirunsit, P.; Chan, M.; Greeley, J.; Stamenkovic, V.; Markovic, N. M. Trends in activity for the water electrolyser reactions on 3d M(Ni,Co,Fe,Mn) hydr(oxy)oxide catalysts. *Nat. Mater.* **2012**, *11* (6), 550–557. <https://doi.org/10.1038/nmat3313>.
- [15] Lyons, M. E. G.; Brandon, M. P. A comparative study of the oxygen evolution reaction on oxidised nickel, cobalt and iron electrodes in base. *J. Electroanal. Chem.* **2010**, *641* (1–2), 119–130. <https://doi.org/10.1016/j.jelechem.2009.11.024>.
- [16] Müllner, M.; Riva, M.; Kraushofer, F.; Schmid, M.; Parkinson, G. S.; Mertens, S. F. L.; Diebold, U. Stability and Catalytic Performance of Reconstructed Fe₃O₄ (001) and Fe₃O₄ (110) Surfaces during Oxygen Evolution Reaction. *J. Phys. Chem. C* **2019**, *123* (13), 8304–8311. <https://doi.org/10.1021/acs.jpcc.8b08733>.
- [17] Grumelli, D.; Wiegmann, T.; Barja, S.; Reikowski, F.; Maroun, F.; Allongue, P.; Balajka, J.; Parkinson, G. S.; Diebold, U.; Kern, K.; Magnussen, O. M. Electrochemical Stability of the

Reconstructed Fe₃O₄ (001) Surface. *Angew. Chemie* **2020**, 132 (49), 22088–22092. <https://doi.org/10.1002/ange.202008785>.

[18] Toney, M. F.; Davenport, A. J.; Oblonsky, L. J.; Ryan, M. P.; Vitus, C. M. Atomic structure of the passive oxide film formed on iron. *Phys. Rev. Lett.* **1997**, 79 (21), 4282–4285. <https://doi.org/10.1103/PhysRevLett.79.4282>.

[19] Calvillo, L.; Carraro, F.; Vozniuk, O.; Celorrio, V.; Nodari, L.; Russell, A. E.; Debellis, D.; Fermin, D.; Cavani, F.; Agnoli, S.; Granozzi, G. Insights into the durability of Co-Fe spinel oxygen evolution electrocatalysts: Via operando studies of the catalyst structure. *J. Mater. Chem. A* **2018**, 6 (16), 7034–7041. <https://doi.org/10.1039/c7ta10892c>.

[20] Bergmann, A.; Jones, T. E.; Martinez Moreno, E.; Teschner, D.; Chernev, P.; Gliech, M.; Reier, T.; Dau, H.; Strasser, P. Unified Structural Motifs of the Catalytically Active State of Co(Oxyhydr)Oxides during the Electrochemical Oxygen Evolution Reaction. *Nat. Catal.* **2018**, 1 (9), 711–719. <https://doi.org/10.1038/s41929-018-0141-2>.

[21] Bergmann, A.; Martinez-Moreno, E.; Teschner, D.; Chernev, P.; Gliech, M.; De Araújo, J. F.; Reier, T.; Dau, H.; Strasser, P. Reversible Amorphization and the Catalytically Active State of Crystalline Co₃O₄ during Oxygen Evolution. *Nat. Commun.* **2015**, 6. <https://doi.org/10.1038/ncomms9625>.

[22] Smith, R. D. L.; Prévot, M. S.; Fagan, R. D.; Trudel, S.; Berlinguette, C. P. Water oxidation catalysis: Electrocatalytic response to metal stoichiometry in amorphous metal oxide films containing iron, cobalt, and nickel. *J. Am. Chem. Soc.* **2013**, 135 (31), 11580–11586. <https://doi.org/10.1021/ja403102j>.

[23] Laouini, E.; Berghoute, Y.; Douch, J.; Mendonça, M. H.; Hamdani, M.; Pereira, M. I. S. Electrochemical behaviour of Fe_xCo_{3-x}O₄ with (x = 0, 1, 2 and 3) oxides thin film electrodes in alkaline medium. *J. Appl. Electrochem.* **2009**, 39 (12), 2469–2479. <https://doi.org/10.1007/s10800-009-9944-9>.

[24] Wang, X. T.; Ouyang, T.; Wang, L.; Zhong, J. H.; Ma, T.; Liu, Z. Q. Redox-Inert Fe³⁺ Ions in Octahedral Sites of Co-Fe Spinel Oxides with Enhanced Oxygen Catalytic Activity for Rechargeable Zinc–Air Batteries. *Angew. Chemie - Int. Ed.* **2019**, 58 (38), 13291–13296. <https://doi.org/10.1002/anie.201907595>.

[25] Wang, H. Y.; Hung, S. F.; Chen, H. Y.; Chan, T. S.; Chen, H. M.; Liu, B. In Operando Identification of Geometrical-Site-Dependent Water Oxidation Activity of Spinel Co₃O₄. *J. Am. Chem. Soc.* **2016**, 138 (1), 36–39. <https://doi.org/10.1021/jacs.5b10525>.

[26] Wang, X.; Liu, Y.; Zhang, T.; Luo, Y.; Lan, Z.; Zhang, K.; Zuo, J.; Jiang, L.; Wang, R. Geometrical-Site-Dependent Catalytic Activity of Ordered Mesoporous Co-Based Spinel for Benzene Oxidation: In Situ DRIFTS Study Coupled with Raman and XAFS Spectroscopy. *ACS Catal.* **2017**, 7 (3), 1626–1636. <https://doi.org/10.1021/acscatal.6b03547>.

[27] Ferreira, T. A. S.; Waerenborgh, J. C.; Mendonça, M. H. R. M.; Nunes, M. R.; Costa, F. M. Structural and morphological characterization of FeCo₂O₄ and CoFe₂O₄ spinels prepared by a coprecipitation method. *Solid State Sci.* **2003**, 5 (2), 383–392. [https://doi.org/10.1016/S1293-2558\(03\)00011-6](https://doi.org/10.1016/S1293-2558(03)00011-6).

[28] Carraro, F.; Vozniuk, O.; Calvillo, L.; Nodari, L.; La Fontaine, C.; Cavani, F.; Agnoli, S. In operando XAS investigation of reduction and oxidation processes in cobalt and iron mixed spinels during the chemical loop reforming of ethanol. *J. Mater. Chem. A* **2017**, 5 (39), 20808–20817. <https://doi.org/10.1039/c7ta06785b>.

- [29] Hung, S. F.; Chan, Y. Te; Chang, C. C.; Tsai, M. K.; Liao, Y. F.; Hiraoka, N.; Hsu, C. S.; Chen, H. M. Identification of Stabilizing High-Valent Active Sites by Operando High-Energy Resolution Fluorescence-Detected X-ray Absorption Spectroscopy for High-Efficiency Water Oxidation. *J. Am. Chem. Soc.* **2018**, *140* (49), 17263–17270. <https://doi.org/10.1021/jacs.8b10722>.
- [30] Reikowski, F.; Maroun, F.; Pacheco, I.; Wiegmann, T.; Allongue, P.; Stettner, J.; Magnussen, O. M. Operando Surface X-Ray Diffraction Studies of Structurally Defined Co₃O₄ and CoOOH Thin Films during Oxygen Evolution. *ACS Catal.* **2019**, *9* (5), 3811–3821. <https://doi.org/10.1021/acscatal.8b04823>
- [31] De Groot, F.; Vankó, G.; Glatzel, P. The 1s X-Ray Absorption Pre-Edge Structures in Transition Metal Oxides. *J. Phys. Condens. Matter* **2009**, *21* (10). <https://doi.org/10.1088/0953-8984/21/10/104207>.
- [32] Van Oversteeg, C. H. M.; Doan, H. Q.; De Groot, F. M. F.; Cuk, T. In Situ X-Ray Absorption Spectroscopy of Transition Metal Based Water Oxidation Catalysts. *Chem. Soc. Rev.* **2017**, *46* (1), 102–125. <https://doi.org/10.1039/c6cs00230g>.
- [33] Parkinson, G. S. Iron Oxide Surfaces. *Surf. Sci. Rep.* **2016**, *71* (1), 272–365. <https://doi.org/10.1016/j.surfrep.2016.02.001>.
- [34] Zeng, Z.; Chan, M. K. Y.; Zhao, Z. J.; Kubal, J.; Fan, D.; Greeley, J. Towards First Principles-Based Prediction of Highly Accurate Electrochemical Pourbaix Diagrams. *J. Phys. Chem. C* **2015**, *119* (32), 18177–18187. <https://doi.org/10.1021/acs.jpcc.5b03169>.
- [35] Kim, K. J.; Kim, H. K.; Park, Y. R.; Ahn, G. Y.; Kim, C. S.; Park, J. Y. Magnetic and optical properties of spinel Fe_xCo_{3-x}O₄ thin films. *J. Magn. Magn. Mater.* **2006**, *300* (2), 300–305. <https://doi.org/10.1016/j.jmmm.2005.05.013>.
- [36] Pacheco Bubi, I.; Transition metal oxide model catalysts for water splitting, **2021**, Institut Polytechnique de Paris.
- [37] Wiegmann, T. ; Pacheco, I. ; Reikowski, F.; Stettner, J.; Qiu, C.; Bouvier, M.; Bertram, M.; Faisal, F.; Brummel, O.; Libuda, J.; Drnec, J.; Allongue, P.; Maroun, F.; Magnussen, O. M. Operando Identification of the Reversible Skin Layer on Co₃O₄ as a Three-Dimensional Reaction Zone for Oxygen Evolution. *ACS Catalysis*, **2022**, 3256–3268. <https://pubs.acs.org/doi/pdf/10.1021/acscatal.1c05169>
- [38] Wu, T.; Sun, S.; Song, J.; Xi, S.; Du, Y.; Chen, B.; Sasangka, W. A.; Liao, H.; Gan, C. L.; Scherer, G. G.; Zeng, L.; Wang, H.; Li, H.; Grimaud, A.; Xu, Z. J. Iron-facilitated dynamic active-site generation on spinel CoAl₂O₄ with self-termination of surface reconstruction for water oxidation. *Nature Catalysis*, **2019**, *2*(9), 763–772. <https://www.nature.com/articles/s41929-019-0325-4>
- [39] Dionigi, F.; Zeng, Z.; Sinev, I.; Merzdorf, T.; Deshpande, S.; Lopez, M. B.; Kunze, S.; Zegkinoglou, I.; Sarodnik, H.; Fan, D.; Bergmann, A.; Drnec, J.; Araujo, J. F. de, Gliech, M.; Teschner, D.; Zhu, J.; Li, W. X.; Greeley, J.; Roldan Cuenya, B.; Strasser, P.; In-situ structure and catalytic mechanism of NiFe and CoFe layered double hydroxides during oxygen evolution. **2020**, *Nature Communications*, *11*(1)1–10. <https://www.nature.com/articles/s41467-020-16237-1>

4.7 Appendix

4.1 Example of Fe content determination in $\text{Co}_{1-x}\text{Fe}_x\text{O}_y/\text{CoOOH}$ bilayers using EDX

As mentioned in the beginning of 4.2, the iron content in $\text{Co}_{1-x}\text{Fe}_x\text{O}_y/\text{CoOOH}$ bilayers is determined with EDX. This section shows an example of the procedure used to calculate x in $\text{Co}_{0.51}\text{Fe}_{0.49}\text{O}_y/\text{CoOOH}$ sample. After CoOOH deposition on $\text{Au}(111)$, EDX spectra at different locations on the sample are measured. Fig.A4.1 shows an example of such EDX spectrum. It shows Co K lines and Au L-lines. The net counts represented by these lines are determined by EDX software (see Table **A4.1**), and averaged over the different locations probed on the sample in order to get an average Co counts in CoOOH layer.

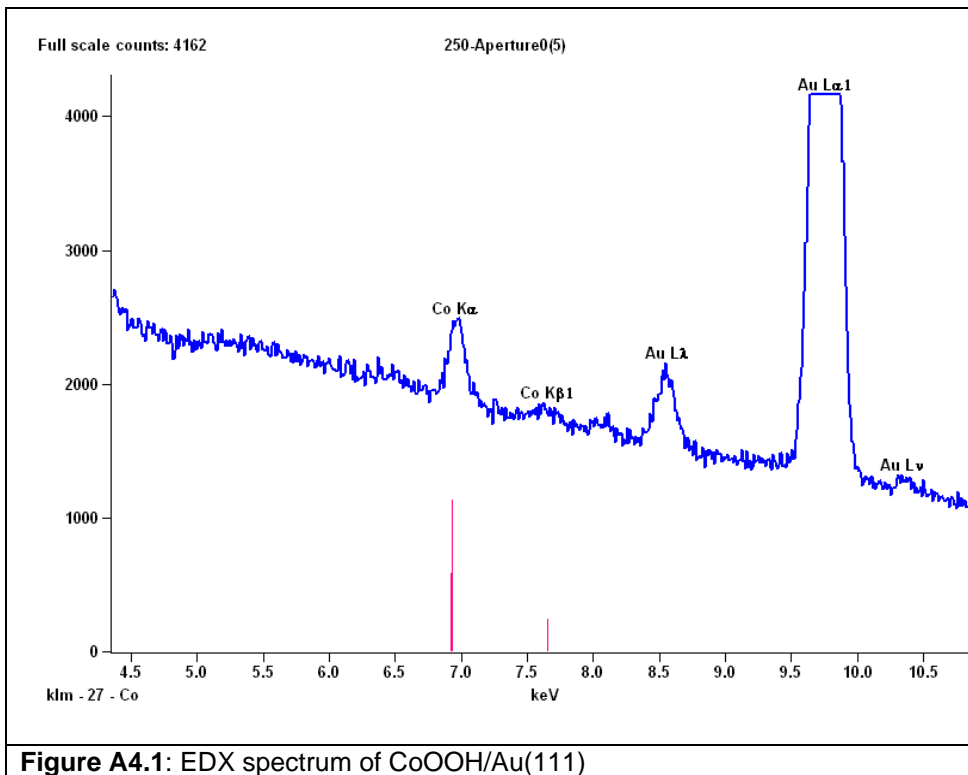


Figure A4.1: EDX spectrum of $\text{CoOOH}/\text{Au}(111)$

Table A4.1: Net counts of the fluorescence peaks detected by EDX software for the spectrum shown in **Fig.A4.1**.

Element Line	Net Counts
Co K	9922
Au L	296357

$\text{Co}_{1-x}\text{Fe}_x\text{O}_y$ is then electrodeposited on $\text{CoOOH}/\text{Au}(111)$ substrate, and EDX spectra are recorded again on several locations on the sample. **Fig.A4.2** shows an example of spectrum, where Fe K line is added to previous Co K and Au L lines. The net counts represented by these lines are determined by EDX software (see Table **A4.2**), and averaged over the different locations. The averaged Co counts in CoOOH layer is subtracted to the one obtained for Co_{1-}

$x\text{Fe}_x\text{O}_y/\text{CoOOH}$ to result in a net Co counts in $\text{Co}_{1-x}\text{Fe}_x\text{O}_y$, as shown in **Table A4.3**. The ratio between Fe counts in $\text{Co}_{1-x}\text{Fe}_x\text{O}_y/\text{CoOOH}$ and the total Co nets counts plus Fe counts yields the iron percentage in the layer : 49% in the case presented here.

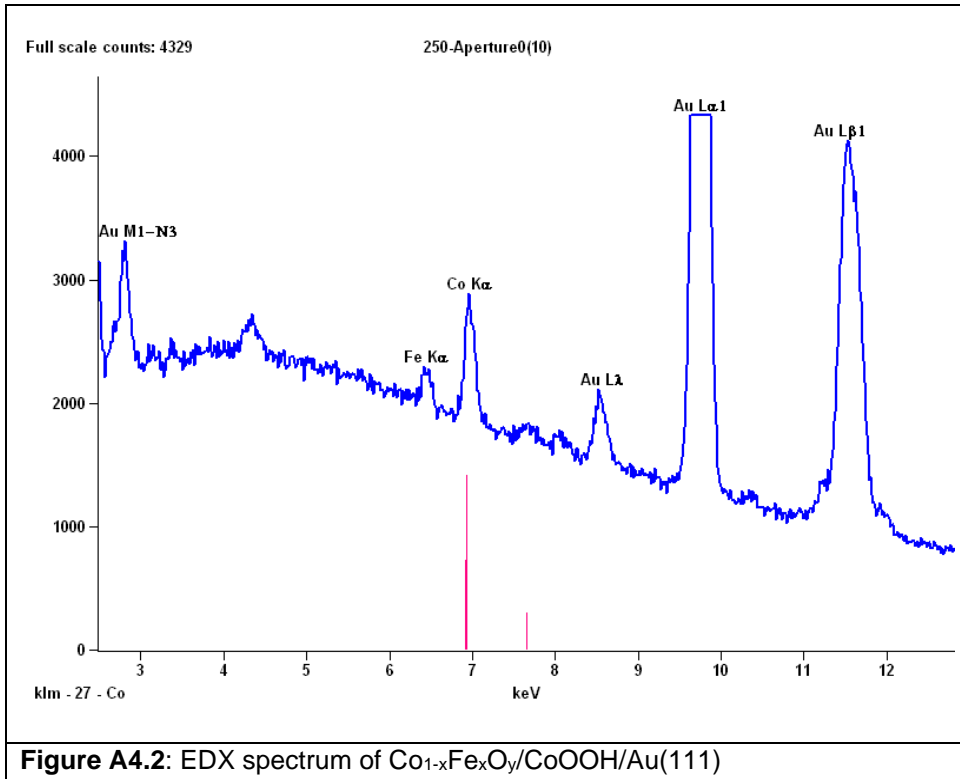


Table A4.2: Net counts of the fluorescence peaks detected by EDX software for the spectrum shown in **Fig.A4.2**.

Element Line	Net Counts
Fe K	5205
Co K	15423
Au L	286488

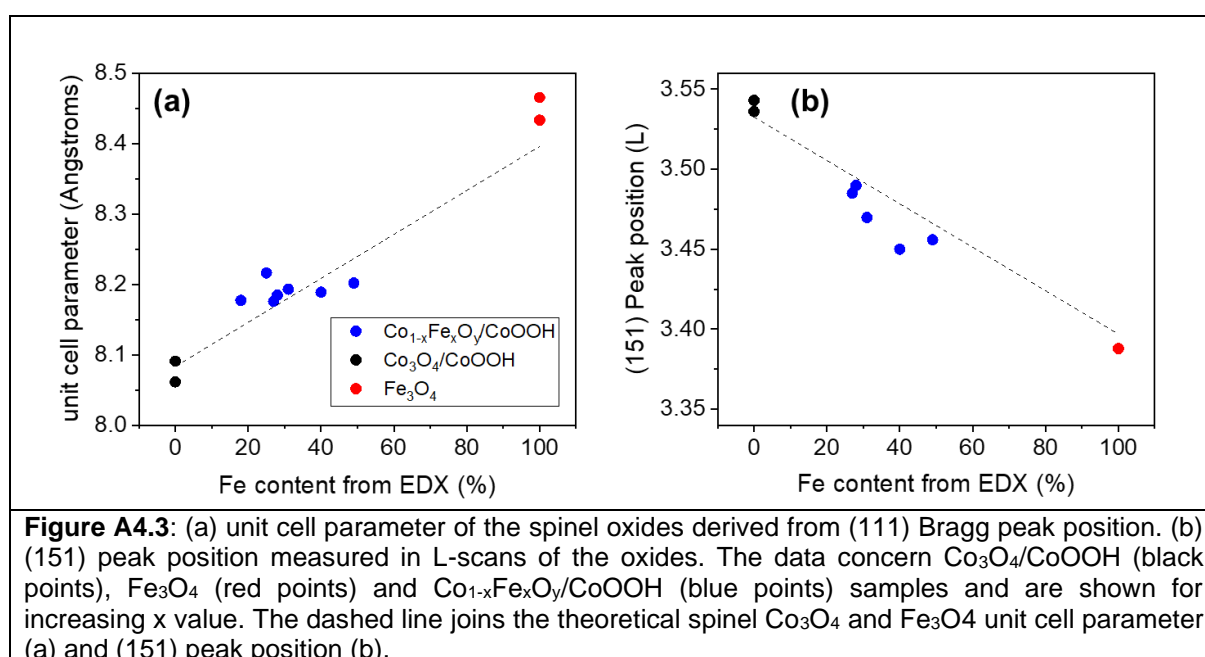
Table A4.3: Balance of Co counts in $\text{Co}_{1-x}\text{Fe}_x\text{O}_y$ from $\text{CoOOH}/\text{Au}(111)$ and $\text{Co}_{1-x}\text{Fe}_x\text{O}_y/\text{CoOOH}/\text{Au}(111)$ EDX counts, from which the iron percentage %Fe in $\text{Co}_{1-x}\text{Fe}_x\text{O}_y$ is determined.

CoOOH/Au(111)	$\text{Co}_{1-x}\text{Fe}_x\text{O}_y/\text{CoOOH}/\text{Au}(111)$			
Co counts	Co counts	Co net counts	Fe counts	Fe/(Fe+Co) %
9922	15423	5501	5205	49 %

4.2 Structure and Fe content x in $\text{Co}_{1-x}\text{Fe}_x\text{O}_y/\text{CoOOH}$ bilayers

From XRD $\text{Co}_{1-x}\text{Fe}_x\text{O}_y$ (111) peak position, $2\theta_{\text{Co}_{1-x}\text{Fe}_x\text{O}_y}$, the unit cell parameter $a_{\text{Co}_{1-x}\text{Fe}_x\text{O}_y}$ is computed determined as : $a_{\text{Co}_{1-x}\text{Fe}_x\text{O}_y} = \sqrt{3} * \frac{\lambda}{2\sin(\theta_{\text{Co}_{1-x}\text{Fe}_x\text{O}_y})}$. It is plotted in **figure A4.3a** as

a function of x the iron content determined with EDX, together with the unit cell parameter of $\text{Co}_3\text{O}_4/\text{CoOOH}$ (black) and Fe_3O_4 (red) samples. The dashed line connects the theoretical $a_{\text{Co}_3\text{O}_4}$ and $a_{\text{Fe}_3\text{O}_4}$ values. The same plot for (151) peak position measured in L-scans is shown in **figure A4.3b**. In **Fig. A4.3a** the data points roughly follow the trend of increasing unit cell parameter with increasing x that is expected from Vegard's law. However, the evolution of $a_{\text{Co}_{1-x}\text{Fe}_x\text{O}_y}$ with x is not linear especially for high iron content. Moreover, there is a non-negligible peak position difference between two $\text{Co}_3\text{O}_4/\text{CoOOH}$ or Fe_3O_4 samples, which suggests a non-negligible intrinsic error on the peak positions of $\text{Co}_{1-x}\text{Fe}_x\text{O}_y/\text{CoOOH}$. In the case of **Fig.A4.4**, the difference is smaller, and $\text{Co}_{1-x}\text{Fe}_x\text{O}_y$ (151) peak position decreases in L for increasing x , even though the data points are all below the theoretical line.

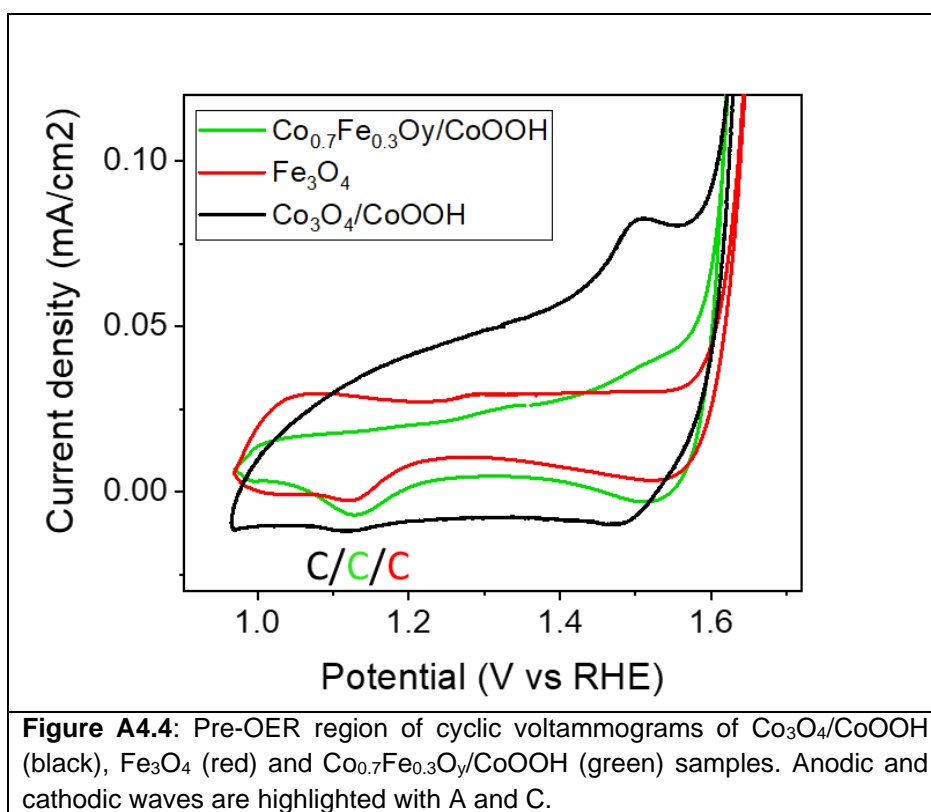


4.3 CVs in pre-OER regime

Figure A4.4 shows cyclic voltammograms of $\text{Co}_3\text{O}_4/\text{CoOOH}$ (black), $\text{Co}_{0.7}\text{Fe}_{0.3}\text{O}_y/\text{CoOOH}$ (green) and Fe_3O_4 (red), centred in the pre-OER regime [0.97-1.57 V]. It exhibits two anodic and cathodic waves. In the case of $\text{Co}_3\text{O}_4/\text{CoOOH}$, the waves appear at the same potentials as for Co_3O_4 : a pair of positive and negative waves at 1.52V and one negative wave around 1.15V. The latter is also present in the CVs of Fe_3O_4 and $\text{Co}_{1-x}\text{Fe}_x\text{O}_y/\text{CoOOH}$. A positive wave around 1.30-1.35V is found for Fe_3O_4 and some of $\text{Co}_{1-x}\text{Fe}_x\text{O}_y/\text{CoOOH}$ samples, while the pair of waves at 1.52V can be observed for some $\text{Co}_{1-x}\text{Fe}_x\text{O}_y/\text{CoOOH}$ samples but not all of them. The sample $\text{Co}_{0.7}\text{Fe}_{0.3}\text{O}_y/\text{CoOOH}$ shown here presents all the anodic and cathodic waves possibly observed for $\text{Co}_{1-x}\text{Fe}_x\text{O}_y/\text{CoOOH}$ samples.

The pair of anodic and cathodic waves at 1.5 V is often attributed to $\text{Co}^{3+} \rightarrow \text{Co}^{4+}$ and is observed in Co_3O_4 , Co_2FeO_4 and sometimes in CoFe_2O_4 [13, 23]. Regarding the oxidation of Co^{2+} into Co^{3+} , a pair of cathodic and anodic waves at $\sim 1.3 - 1.35\text{V}$ and $\sim 1.2 - 1.25\text{V}$ are measured by the authors [13, 23] and attributed to this redox transition. They also add that this wave shifts anodically when the iron content increases, which has also been mentioned for non-spinel CoFe systems [11]. Since this wave could not be observed for all samples, it is not possible to tell whether this is also the case for our samples. Laouini et al. [23] measured the apparition of this wave only after a negative sweep down to -0.2V , which may explain why it is not observed for some samples.

For Fe_3O_4 , no redox wave appears in this potential window according to [13,23]. Since XAS measurements evidence a slight oxidation of Fe_3O_4 after 1.4V_{RHE} , the wave around 1.3V may be attributed to $\text{Fe}^{2+} \rightarrow \text{Fe}^{3+}$.



Chapter 5: Anodic oxides

5.1 Introduction

In this chapter we focus on cobalt, iron and mixed cobalt-iron oxides prepared by anodic oxidation of metallic Co, Fe and CoFe epitaxial films electrodeposited on Au(111) substrate. The electrodeposition of ultrathin and crystalline Co and Fe metallic films on (111) oriented substrates has been previously demonstrated [1,2,21,22]. Both types of deposits are characterized by an homogeneous nucleation across the substrate surface, together with a lateral expansion of the islands until reaching a full coverage. The islands are mono (Fe) or bi atomic (Co) and the growth proceeds by mono/bi atomic layer by layer growth. The deposition method enables controlling the number of electrodeposited monolayers on the substrate so that deposits of well-known and ultrathin ($> 2\text{ML}$) thicknesses can be obtained [2,21,22]. According to their growth mode, these layers are also atomically flat, their active surface area is therefore the same of the one of the substrate. They are also crystalline: Co has an hexagonal structure and grows epitaxially with a (0001) orientation [1]. In the case of Fe deposits thicker than 3 ML are bcc-Fe(110) [2].

These ultrathin and smooth metallic deposits are prepared in acidic aqueous electrolytes. They can further be transferred in alkaline electrolyte where they may be oxidized in order to form oxide films. This approach for elaborating oxides gathers some advantages compared to crystalline oxides. The catalyst is prepared inside the electrochemical cell where it can be directly characterized in situ, avoiding possible external contaminations or surface modifications (see **chapter 2** for details about preparation method). Moreover, ultrathin metallic layers ($<1\text{nm}$) can be electrodeposited, which enables the total conversion of the metallic layer into an oxide. The as-formed metal oxide catalysts will also be ultrathin. This is especially interesting for operando XAS experiments. Indeed, XAS signal is sensitive to the total amount of Co/Fe atoms in the film, while redox processes might take place at the surface of the material only. The use of ultrathin sample is of great interest in this context compared to “bulk” samples since surface atoms represent a large part of the sample: measured oxidation state changes originate from a large part of the atoms contained in the film. This preparation method may also provide more flexibility in tuning the composition of mixed oxides. Using electrodeposition method, it is indeed possible to prepare bimetallic alloys in a continuous range of concentration. For example, Kakuno et al. [9] or Qiang et al. [10] reported the elaboration of $\text{Co}_x\text{Fe}_{1-x}$ alloys of several compositions by tuning the concentration of Fe and Co in the electrolyte bath. This may yield oxides with concentrations that cannot be easily obtained for crystalline oxides. Finally, compared to non-crystalline Co-Fe

oxides/oxyhydroxides obtained by direct electrodeposition [3-5] which have a poorly defined morphology, the anodic oxides have the advantages of presenting a morphology close to flat films because of their very low thickness and mode of growth, which is of high importance in order to determine and compare the OER activity of the oxides.

As a general trend, the growth of transition metal (M) oxide passive films is 3D at large overpotential and is self-limited [6]. In this chapter, we focus on passive oxides formed at high potentials compared to the metallic films equilibrium potentials, close to Co(II)/Co(III) or Fe(II)/Fe(III) potentials. The anodic oxidation in alkaline medium of Co and Fe metal films has been studied with several techniques such as X-ray Diffraction, AFM, STM, XPS or Raman spectroscopy [1,13,14,18-20,23,24]. In the case of Co, in situ XRD [1] and XPS [14] and STM [13] evidenced the formation of $\text{Co}(\text{OH})_2$ when Co is oxidized at 0.4 – 0.6V_{RHE}. The layer grows probably from grain boundaries and expands laterally, Based on XPS characterizations, the formation of a $\text{Co}(\text{OH})_2$ - CoOOH mixture was reported for further oxidation of Co at 1.4V_{RHE} [14]. Studies on metallic iron oxidation in alkaline medium based on in situ AFM and XPS [19,20] suggest the formation of a Fe^{2+} oxide - $\text{Fe}(\text{OH})_2$ or FeO - which outer layer is converted into a Fe^{3+} rich hydroxides at 1.2V. In pH 8 buffer electrolyte, the anodic passive film formed on iron was identified by XRD and Raman as an oxide with a spinel-like structure with both octahedral and tetrahedral vacancies, and octahedral interstitial sites [23, 24]. XRR studies [18] evidenced three growth stages: first the formation of a defective spinel, followed by defects filling to progressively form a species which electron density is close to that of magnetite. In the same electrolyte, according to XRD, the passive Fe oxide layer grows with an epitaxial relationship regarding the substrate and has a nanocrystalline microstructure.

In this chapter, planar, ultrathin and epitaxial Co, Fe metal films and CoFe bimetallic alloys of different composition are electrodeposited and characterized in situ using both SXRD and XAS. Their oxidation in alkaline electrolyte is monitored with these techniques, showing that oxides with different Co and Fe oxidation states are obtained. The evolution of both Fe and Co oxidation states during potential sweeps until OER regime is consequently measured and quantified in light of the structural characteristics determined for firstly electrodeposited metals and alloys films. The composition, operando behaviours and catalytic activity of crystalline Co and Fe oxides presented in chapters 3 and 4 are compared with those of anodic oxides, in order to investigate the similarities and differences on how OER proceeds on these two types of materials of similar composition.

5.2 Structure of Co and Fe metals

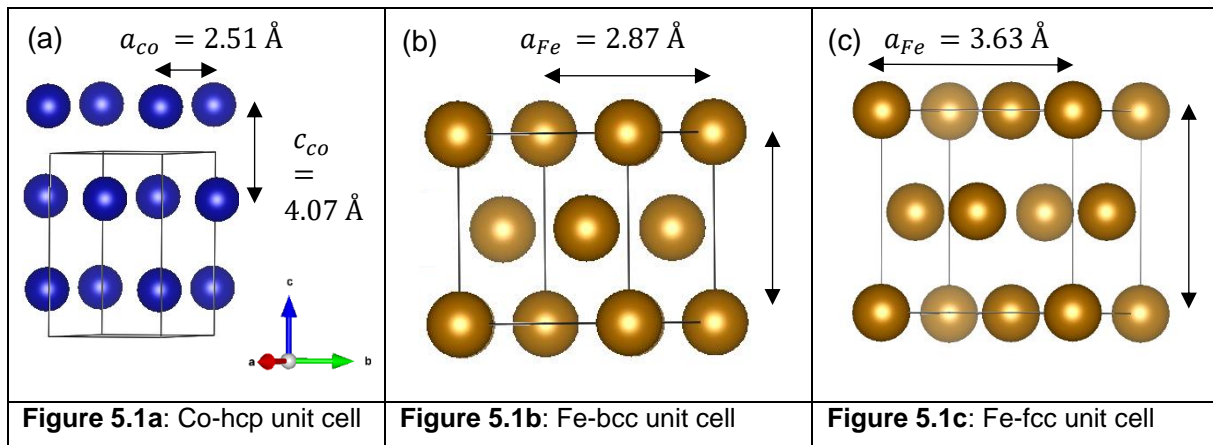
Cobalt under its metallic form has a hexagonal close packed (hcp) structure, made of alternating atom layers overlaying one another. **Fig.5.1a** shows a scheme of three alternating

Co planes along the c direction. The unit cell (shown in black) contains two Co atoms and the unit cell parameters are: $a_{Co} = 2.51 \text{ \AA}$ and $c_{Co} = 4.07 \text{ \AA}$.

Metallic iron can either have a body centred cubic (BCC) structure or a face centred cubic (FCC) structure. BCC iron unit cell is shown in **Fig.5.1b**. The lattice parameter is $a_{Fe} = 2.87 \text{ \AA}$ and the unit cell contains two Fe atoms. **Fig.5.1c** shows FCC iron unit cell with a lattice parameter $a_{Fe} = 3.63 \text{ \AA}$. In this case, there are four Fe atoms in the unit cell.

In the following, a Co or Fe monolayer (ML) corresponds to one single Co or Fe plane. Its thickness is defined as the distance between two adjacent Co or Fe layers. In the case of hcp-Co, it equals $\frac{c_{Co}}{2}$, and it is $\frac{a_{Fe}}{2}$ for both bcc-Fe and fcc-Fe. A “monolayer unit cell” can also be defined, which characteristics for each structure are:

- (i) hcp-Co: contains 1 Co atom, $c_{ML} = \frac{c_{Co}}{2} = 2.035 \text{ \AA}$, $a_{ML} = a_{Co}$. The Co density in one ML is: $\rho_{ML} = \frac{1}{a_{Co}^2} = 15.9 \text{ Co/nm}^2$.
- (ii) bcc-Fe: contains 1 Fe atom, $c_{ML} = \frac{a_{Fe}}{2} = 1.435 \text{ \AA}$, $a_{ML} = a_{Fe}$. The Fe density in one ML is: $\rho_{ML} = \frac{1}{a_{Fe}^2} = 12.1 \text{ Fe/nm}^2$.
- (iii) fcc-Fe: contains 2 Fe atoms, $c_{ML} = \frac{a_{Fe}}{2} = 1.815 \text{ \AA}$, $a_{ML} = a_{Fe}$. The Fe density in one ML is $\rho_{ML} = \frac{2}{a_{Fe}^2} = 15.2 \text{ Fe/nm}^2$



5.3 Results

Monitoring Co/Fe electrodeposition and anodic oxidation

The detailed electrodeposition procedure is given in **chapter 2**. Briefly, the process begins with the metal electrodeposition on Au(111) substrate from an adapted electrolyte which is acid (pH 3-4) and contains 1mM of Co or Fe salt. The electrodeposition consists in stepping the potential at a value negative to the redox wave of the metal formation. The potential is then kept constant for a given amount of time that determines the amount of metal layer electrodeposited. The

deposition is stopped by stepping the potential back to the equilibrium potential where no deposition nor dissolution take place. Then, the electrolyte is switched to an alkaline one (pH 13), under potential control. For Co [1] and Fe [2] films, it has been shown previously that the electrodeposition procedure yields crystalline, epitaxially grown, flat metal and continuous deposits. In order to check the characteristics of the electrodeposited layers, two measurements are performed. (i) we measure a XANES spectrum at the K-edge of the deposited metal. (ii) We look for XRD peak(s) of the metal at expected positions because the epitaxial growth of Co(001) and Fe(110) on Au(111) are known. If both measurements yield the desired output, anodic oxidation is performed by stepping the potential to $1.4V_{RHE}$ where the oxide is stable. The corresponding oxidation peak is recorded, and once the current is stabilized (a few seconds), the two previous characterizations are performed again. The shape and edge energy of the XANES spectrum is expected to change, and the XRD metal peak to disappear if the metal layer is completely oxidized.

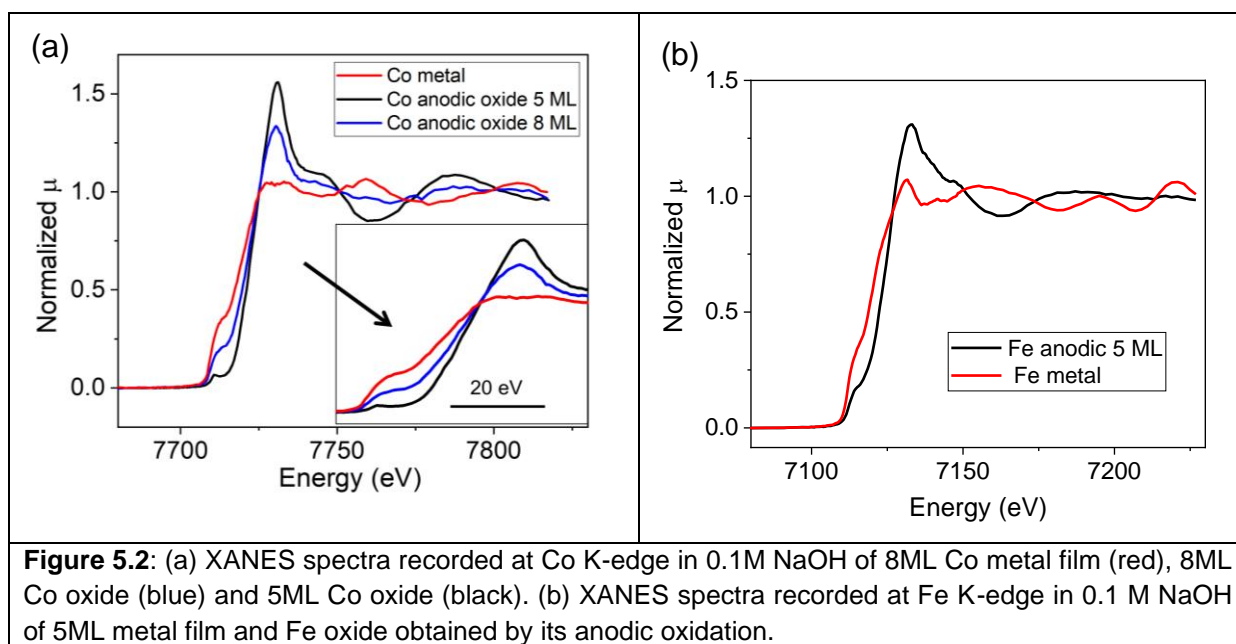
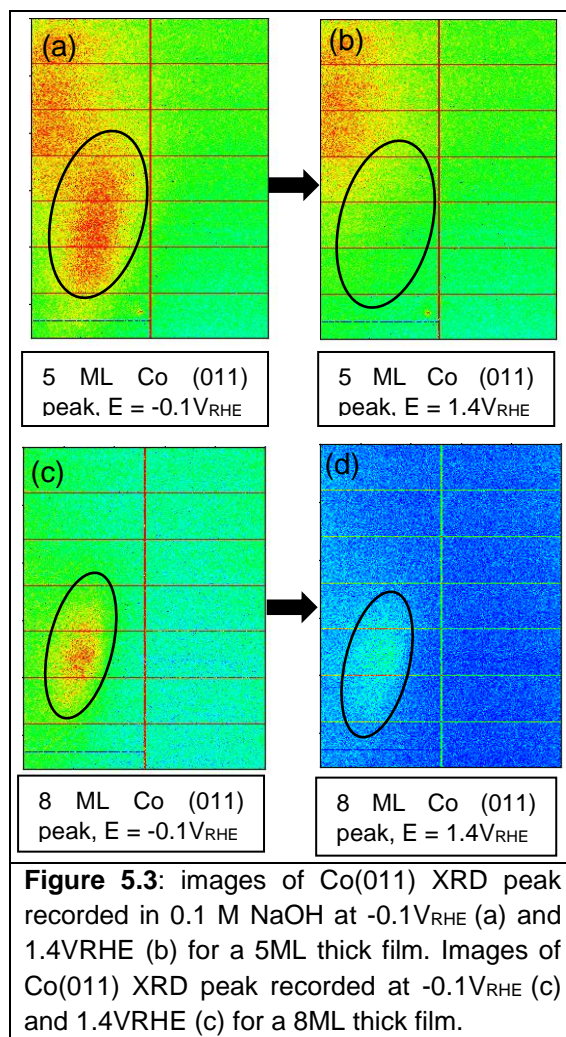


Figure 5.2a shows an example of XANES spectra recorded during the two steps of this procedure for two Co deposits of different thicknesses (5 and 8 ML (monolayers)). **Figure 5.2b** is the analogous for Fe deposit of 5ML. **Figure 5.3** shows the corresponding XRD peak images for the 5 ML Co/Au(111) film (panels a-b) and the 8ML film (panels c-d). In **Fig. 5.2**, the red spectrum is that of Co metal deposit (here, 8ML thick, a similar spectrum is obtained for 5ML Co). This spectrum is similar to that of a Co foil and is therefore demonstrating that the Co layer is metallic with no sizeable trace of oxidation. The spectrum measured after oxidation of the 5 ML Co film (black) is very different from that of the metal film, with a significant edge shift towards higher energies. It is very similar to that obtained for Cobalt oxides in **chapter 3** (see

below), suggesting that the metallic layer has been converted into an oxide. In comparison, the spectrum of the anodized 8ML Co layer (blue) presents a higher pre-edge contribution and almost no EXAFS oscillations, suggesting that metallic cobalt remains under the oxide. This is confirmed by XRD characterizations. **Fig. 5.3** displays the Bragg peaks of Co(001) before (left) and after anodic oxidation (right). In the case of the 5ML Co film (panels a-b), the XRD Bragg peak disappears once the anodic oxide is formed. On the contrary for the 8ML Co film, a weak XRD Bragg peak is still found after oxidation. The XANES spectrum of the anodized 8ML Co layer (blue) can be described by a linear combination of Co metal (40%) and Co_3O_4 (60%) XANES spectra, suggesting that ~5ML of metal have been oxidized over 8 ML. Moreover, different Co anodic oxides obtained by oxidation of Co deposits of different thicknesses have been studied, and for deposits thicknesses below 5ML, no traces of Co metal XRD peak was found after oxidation, showing that a complete oxidation occurs whenever the layer is as thin or thinner than 5 ML.

The XRD and XAS data are therefore consistent: the anodic oxide formed on a 5ML Co film consumes all Co atoms; while in the 8ML case, a metal contribution can still be distinguished. These characterizations are thus a way to check that the electrodeposition took place properly and that the anodic oxidation was efficient enough to oxidize the whole metal film. Based on the result of **Figure 5.3**, we choose to investigate 5ML thick films that can be fully oxidized and are thick enough for them to be stable during the measurement's timescale.



Characterization of Co and Fe anodic oxides

No oxide XRD peak was found after oxidation of Co and Fe deposits. This suggests that the oxides are X-ray amorphous, and if they are composed of crystallites, their characteristics sizes are too small to be detected. The as-formed oxides are characterized by XAS in the following. **Figure 5.4a** compares the XANES spectra at Co K-edge of an anodic Co oxide obtained by oxidation of a 5 ML Co film (black) with those of Co_3O_4 (red) and $CoOOH$ (blue) prepared by direct electrodeposition on Au(111) (presented in **chapter 3**). Co anodic XANES spectrum is very similar to that measured for these oxides both in terms of EXAFS oscillations and edge energy position. At $0.97V_{RHE}$, we measure an oxidation state of 2.71 for 5ML Co anodic oxide, against 2.62 for Co_3O_4 and 3.02 for $CoOOH$. These observations suggest that Co environment in the anodic oxide is probably not too different from that in Co_3O_4 . The as-formed Co anodic oxide may also be a $CoOOH$ rich mixture of disordered $CoOOH$ and $Co(OH)_2$ as mentioned in [14] or an homogeneous CoO_xH_y phase where Co arrangement is not too different from that in Co_3O_4 and $CoOOH$.

In **Fig. 5.4b** are shown the spectra at Fe K-edge of an anodic Fe oxide obtained by oxidation of a 5 ML Fe film (black), together with XANES spectra of $\text{Fe}_3\text{O}_4/\text{Au}(111)$ and Fe_2O_3 reference powder (blue) (from **chapter 4**). The main edge energy of the Fe anodic oxide is close to that of Fe_3O_4 , however the amplitude of the spectrum EXAFS oscillations is lower than for Fe_3O_4 and Fe_2O_3 and the pre-edge intensity higher. At 0.97V, an oxidation state of 2.67 is found for Fe anodic oxide, very close to 2.65 determined for $\text{Fe}_3\text{O}_4/\text{Au}(111)$. This may indicate that the Fe anodic oxide is a Fe_3O_4 -like phase, as often mentioned in the literature [18,23,24]. However, it would likely be more disordered than Fe_3O_4 , with Fe atoms having a low order at short distance as suggest the shape of the spectrum.

To simplify notations, Co and Fe anodic oxides will be referred as CoO_y and FeO_y in the following.

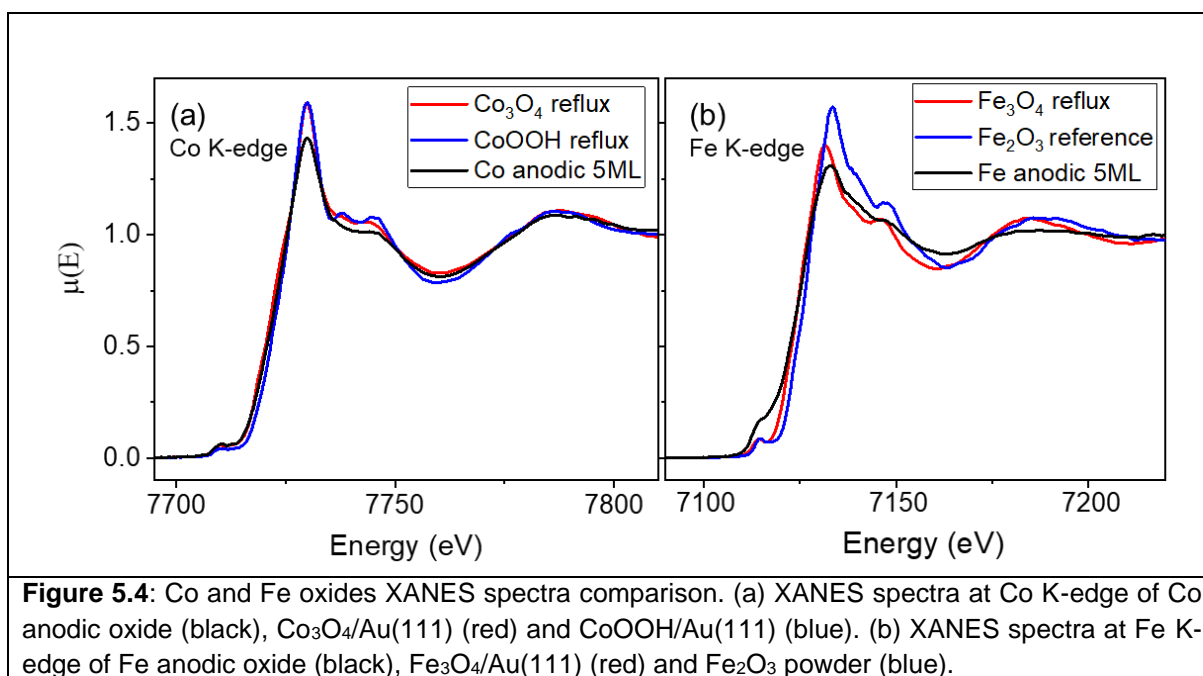


Figure 5.4: Co and Fe oxides XANES spectra comparison. (a) XANES spectra at Co K-edge of Co anodic oxide (black), $\text{Co}_3\text{O}_4/\text{Au}(111)$ (red) and $\text{CoOOH}/\text{Au}(111)$ (blue). (b) XANES spectra at Fe K-edge of Fe anodic oxide (black), $\text{Fe}_3\text{O}_4/\text{Au}(111)$ (red) and Fe_2O_3 powder (blue).

Characterizations of alloys films and oxides

Alloys composition

In the case of CoFe alloys, we follow the same procedure as the one described for Co and Fe depositions. This time, the electrolyte is composed of: $\frac{100-x}{100}$ mM of Co salt plus $\frac{x}{100}$ mM of Fe salt, and three compositions have been investigated: $x = 25$; $x = 50$ and $x = 75$. From each electrolyte, we deposit 5ML of metals. **Figure 5.5a** shows the raw XANES spectra (not normalized) measured at Fe and Co K-edges obtained after electrodeposition from each of the three electrolyte compositions. For all deposits, we measure a signal at both edges meaning that both Co and Fe are present in the deposits. We also observe that the intensity amplitude of the spectra varies with the electrolyte composition. Indeed, the absolute fluorescence

intensity difference between the beginning and the end of the main K-edge jump of non-normalized XAS spectra at a given element edge is proportional to the amount of this element in the material. The Co/Fe ratio in each deposit can therefore be retrieved from the ratio of these intensity differences at Co and Fe K-edges, if the measurements conditions are taken into account for each spectrum (attenuators, dead times). **Figure 5.5b** shows the iron percentage in the alloy determined from XAS spectra versus the iron percentage in the electrolyte solution. Red points correspond to iron content determined from alloys XANES spectra and black points the one estimated from corresponding oxides XANES spectra. The dashed line shows the 1 to 1 correlation between x and y axis. The plot indicates that the iron percentage from XAS spectra shows a good agreement with the Fe content in the electrodeposition solution, both for the alloys and oxides. The exact compositions are given in **Table 5.1**, together with the deposit thickness expected from the electrodeposition calibration. The biggest difference to the expected Fe content is measured for the 25% Fe electrolyte where the iron content is found at 16% in the alloy and increases to 20.5% in the oxide. Otherwise, the compositions are similar within a 4% error. The measured values between alloy and oxide are also in good agreement the one with the other. Overall, this analysis indicates that the alloys composition is close to that of the Co and Fe salts in the electrolyte solution, suggesting that Co and Fe deposition rates are similar in our deposition conditions. According to CVs in the potential window where the alloys are electrodeposited (see section 1 of **chapter 2**), both Co^{2+} and Fe^{2+} electrodepositions are limited by mass transport, which may explain why no preferential deposition of one of the species occurs. For the sake of simplicity, in the following the three alloy deposits will be named after the electrolyte composition: $\text{Co}_{75}\text{Fe}_{25}$, $\text{Co}_{50}\text{Fe}_{50}$ etc, and $\text{Co}_{100-x}\text{Fe}_x$ in general.

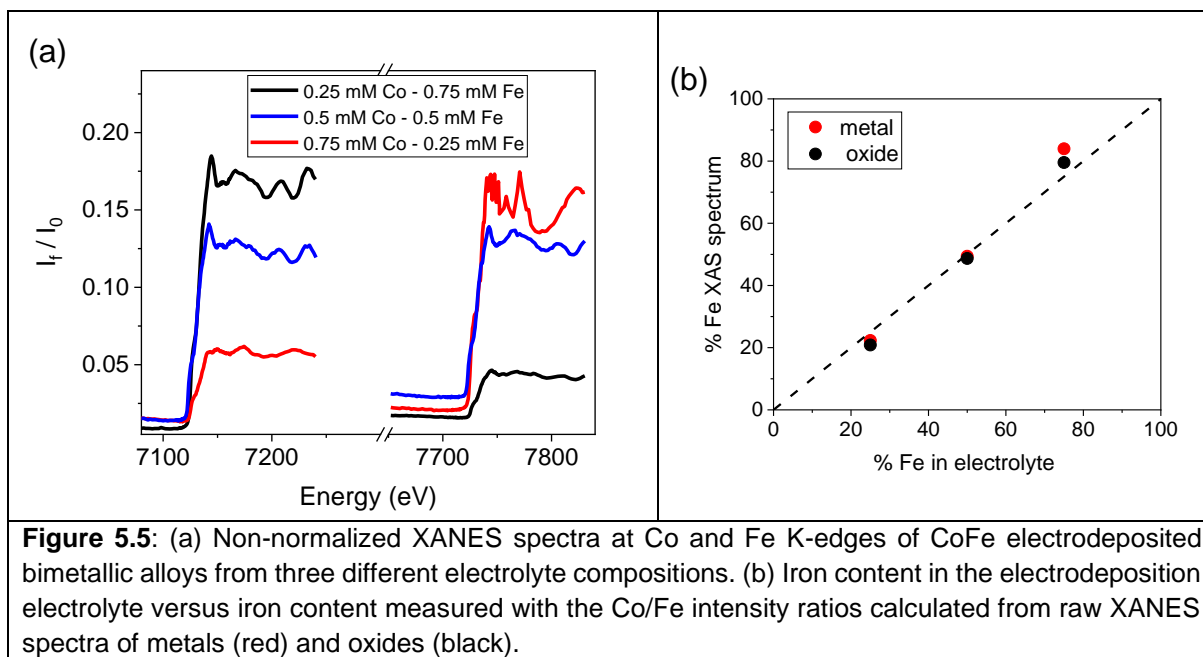


Table 5.1: Alloys composition. For each deposit the electrolyte composition is given (in M of Co^{2+} and Fe^{2+} salts), together with the metal and oxides composition obtained with the fluorescence intensity of non-normalized XANES spectra at Co and Fe K-edges. The deposition thickness is the expected metal thickness obtained for a calibrated deposition time. Co and Fe deposits shown in the previous section are added for comparison.

Electrolyte composition	Alloy composition (XAS)		Oxide composition (XAS)		Deposition thickness
	Co	Fe	Co	Fe	
1 mM Co	100%	0%	100%	0%	5 ML
0.75 mM Co 0.25 mM Fe	77.7%	22.3%	79.1%	20.9%	5 ML
0.5 mM Co 0.5 mM Fe	50.6%	49.4%	51.3%	48.7%	5 ML
0.25 mM Co 0.75 mM Fe	16.1%	83.9%	20.5%	79.5%	5 ML
1 mM Fe	0%	100%	0%	100%	5 ML

Alloys structure

As mentioned above, pure Co films electrodeposited on Au(111) in these conditions grow as hexa-Co(001), while Fe films grow as bcc-Fe(110) and we did find these XRD peaks for the corresponding deposits. For the three CoFe alloys described in **Table 5.1**, we looked for hexa-CoFe(011), bcc-FeCo(110) and fcc-CoFe(111) since Fe may also have a fcc structure [2]. The structure found for the alloys is given in **Table 5.2**, together with the detector angles (δ, γ) corresponding to the XRD peak found. Additional structural characterizations (phi scans across the diffraction peak) are shown in **Appendix 5.1**. Fe-rich alloys ($\text{Co}_{25}\text{Fe}_{75}$ and $\text{Co}_{50}\text{Fe}_{50}$) remain

in the bcc structure of Fe(110) and δ increases with increasing Co content. From the cubic Fe(110) and CoFe(110) peak positions measured at 7.24 keV, the unit cell parameter of the alloy may be retrieved as : $a_{CoFe} = \frac{\lambda \sqrt{h^2+k^2+l^2}}{|q|}$. For Fe metal, a unit cell parameter of 2.88 Å is found, in good agreement with the value of 2.87 Å that is expected. a_{CoFe} decreases slightly upon increasing Co content in the film, which has been reported in the literature [11], and attributed to the fact that incorporating smaller atoms (Co radius (0.104nm) < Fe radius (0.11 nm)) in the lattice would shrink it. For the cobalt rich alloy Co₇₅Fe₂₅, two XRD peaks were found: one weak hexa-CoFe(001) peak and one strong fcc-CoFe(111) peak. In the case of fcc-Co₇₅Fe₂₅ (111), a unit cell parameter of 3.61 Å is determined.

The difference of structure measured for Fe rich and Co rich alloys is consistent with the reported structure of electrodeposited CoFe alloys [9,10]. Kakuno et al. [9] found that the structure of Co_{1-x}Fe_x films electrodeposited on Cu(100) depends on x : the films present a bcc structure for x>0.3, followed by a transition from cubic to hcp structure for x<0.3, together with the existence of a fcc structure for x in 0.1-0.05. A transition from bcc to fcc was also found by Nakamura et al. [10] for x = 0.8. Since XAS spectra analysis (**Table 5.1**) gives a cobalt content of 83% in Co₇₅Fe₂₅ alloy, the fcc-structure found for this alloy is in line with the literature transition values. The fact that a hcp component also exists for this alloy is also consistent with the findings of reference [9].

To characterize the deposit structure, 2D detector images of Co_{100-x}Fe_x XRD peaks (see **Appendix 5.2**) were recorded and analysed in order to estimate the height (d_{\perp}) and width (d_{\parallel}) of metal crystallites. The results are shown in **Table 5.2**: the lateral size of the crystallites is ~ 10 to 20 nm and their height is in between 2.6 and 3.8 nm, which is ~ 3 to 4 times higher than 5ML of Co or Fe (0.7 to 1 nm). This difference is most probably due to the 3D shape of the Bragg peak (vertically elongated ellipsoid) and to the measurement's conditions (large detector height or δ angle). The 2D detector image corresponds thus to a cut of the Bragg peak with a tilt compared to the vertical cut yielding a peak FWHM significantly smaller than that expected from a vertical cut which gives the real film thickness. Consequently, the measurement is limited by the smaller horizontal width of the Bragg peak and estimated d_{\perp} is larger than the actual film thickness. The important point is that the lateral size of the crystallite is consequently larger than their vertical sizes, suggesting a smooth morphology.

Table 5.2: Structural parameters of bimetallic $\text{Co}_{100-x}\text{Fe}_x$ deposits, including the structure, the (Co)Fe(110), or CoFe(111) peak positions measured at 7.24 keV and an incident angle of 4° , the unit cell parameter derived from it, and Co(Fe)(001) peak position measured at 7.83 keV, together with the crystallite width (d_{\parallel}) and height (d_{\perp}) derived from XRD peak analysis.

Sample	structure	delta	gamma	a (Å)	d_{\parallel}	d_{\perp}
Co	Hexa-Co(001)	21.96°	45.0°	-	15.4 nm	3.5 nm
Co₇₅Fe₂₅	Hexa-CoFe(001)	21.95°	44.5°	-	14.7 nm	3.4 nm
	+ fcc-CoFe(110)	15.14°	47.48°	3.61 (fcc)		
Co₅₀Fe₅₀	bcc- CoFe(110)	25.19°	45.98°	2.86	9.9 nm	2.6 nm
Co₂₅Fe₇₅	bcc- CoFe(110)	24.96°	46.28°	2.87	14.0 nm	3.8 nm
Fe	bcc- CoFe(110)	24.71°	46.18°	2.88	18.2 nm	2.7 nm

XANES spectra of $\text{Co}_{100-x}\text{Fe}_x$ are shown in **Figure 5.6a** at Co K-edge and **Figure 5.6b** at Fe K-edge. Comparison of these spectra the ones with the others also reflects the structural differences found by XRD since at Fe K-edge the spectra of Fe, $\text{Co}_{25}\text{Fe}_{75}$ and $\text{Co}_{50}\text{Fe}_{50}$ overlap over the entire energy range, with very similar oscillations frequency and amplitude in the EXAFS region. On the contrary, $\text{Co}_{75}\text{Fe}_{25}$ presents completely different EXAFS features. At Co K-edge, Fe rich alloys spectra are also nearly identical, and those of Co and $\text{Co}_{75}\text{Fe}_{25}$ seem to have similar features but the data quality of $\text{Co}_{75}\text{Fe}_{25}$ spectrum is not good enough to make a strong affirmation. For each bcc $\text{Co}_{25}\text{Fe}_{75}$ and $\text{Co}_{50}\text{Fe}_{50}$ alloys, the EXAFS oscillations measured at Co and Fe K-edges of a same deposit overlap well (see **Appendix A5.3**). Since fcc and bcc environments yield different EXAFS oscillations, this overlap indicates that both Co and Fe are in a bcc environment, meaning that the alloys are solid solutions with a bcc structure.

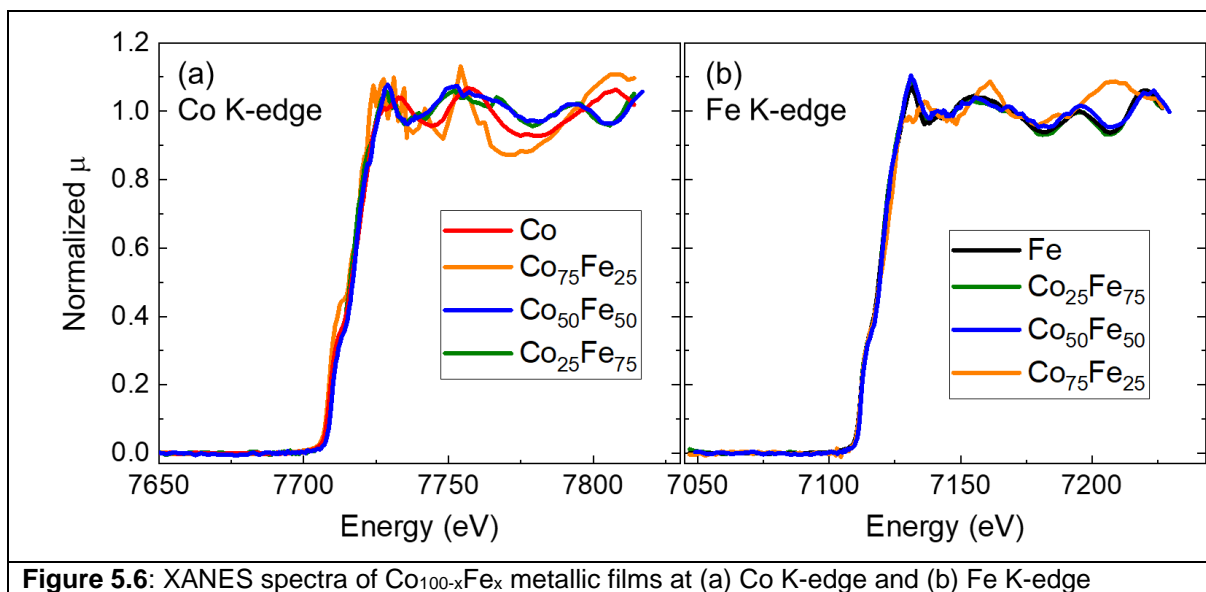


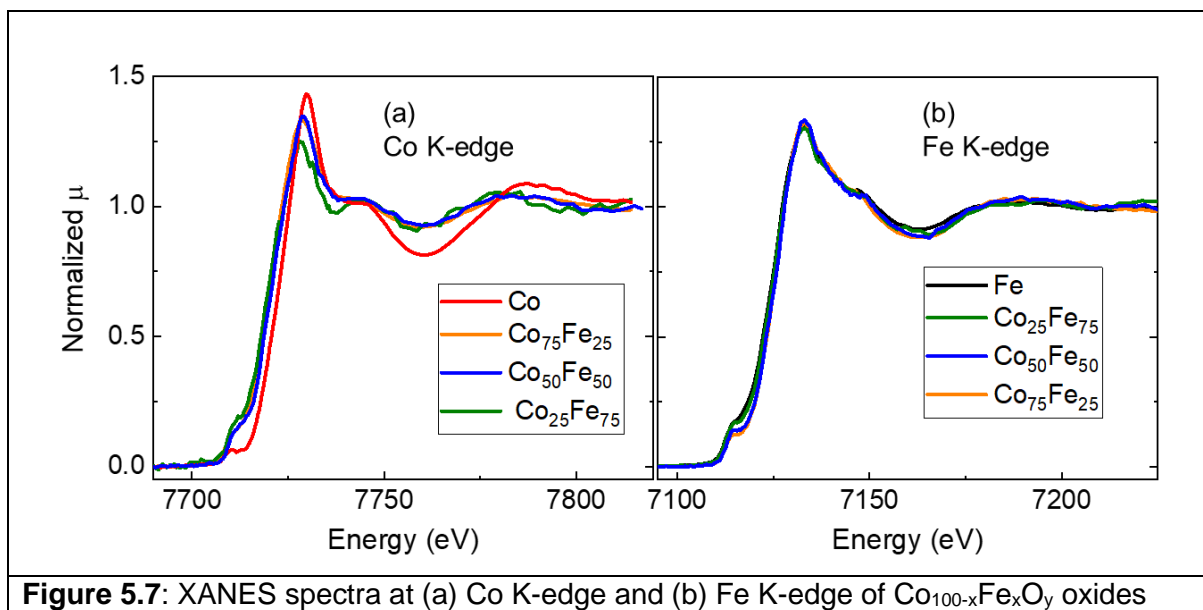
Figure 5.6: XANES spectra of $\text{Co}_{100-x}\text{Fe}_x$ metallic films at (a) Co K-edge and (b) Fe K-edge

Co and Fe oxidation states in anodic alloy oxides

Figure 5.7a and **b** show XANES spectra at Co and Fe K-edges respectively of anodic oxides formed after oxidation of $\text{Co}_{100-x}\text{Fe}_x$ deposits. The XANES spectra of Co and Fe anodic oxides are also shown for comparison. The spectra were recorded in 0.1M NaOH electrolyte at 1.4V_{RHE}, just after anodic oxidation. The anodic alloy oxides will be referred as $\text{Co}_{100-x}\text{Fe}_x\text{O}_y$ in the following.

At Co K-edge, XANES spectra of $\text{Co}_{100-x}\text{Fe}_x\text{O}_y$ are rather similar the one to the others. Compared to CoO_y , their main edge is shifted towards lower energies, they show low amplitude in EXAFS oscillations and their pre-edge is more intense. These observations first indicate that Co in anodic alloy oxides has a lower oxidation state than in CoO_y . The small EXAFS oscillations amplitude also suggests a lower order at short distance compared to CoO_y , meaning that alloy oxides would be more disordered than Co oxide. However, we cannot exclude that the high pre-edge and the low EXAFS oscillations amplitude observed for the alloy oxides would result from a contribution of remaining CoFe alloy after oxidation. Even though no XRD metal peak is visible anymore, it might be present in too little proportion to be detectable.

At Fe K-edge, all spectra look very similar in terms of shape, main edge energy and EXAFS oscillations, which suggest that both Fe oxidation state and Fe environment are close in FeO_y and $\text{Co}_{100-x}\text{Fe}_x\text{O}_y$.



The Co and Fe oxidation state of the oxides are determined with the XANES spectra of **Figure 5.7**, the main edge energy being calculated for $\mu > 0.35$ in order not to take into account the pre-edge contribution. The obtained $\alpha_{Co}(1.4V)$ and $\alpha_{Fe}(1.4V)$ values for each oxide are shown in **Table 5.3**. In anodic alloys, $\alpha_{Co}(1.4V)$ is in between 2.0 and 2.2, significantly smaller than in CoO_y , while $\alpha_{Fe}(1.4V)$ is higher, and increases with increasing Co content, from 2.67 in FeO_y to 2.83 in $Co_{75}Fe_{25}O_y$,

Table 5.3 also gives the charge measured during anodic oxidation of each of the deposits which may be compared to the oxidation state of Co and Fe. Indeed, all Co/Fe atoms are oxidized in the deposits and that their amount in the deposits is known from the structure as well as the thickness of the films. The oxidation charge is related to x , the number of electrons exchanged during the reaction $M \rightarrow M^{x+} + x e^-$ (M being Co, Fe or both) and the amount of Co/Fe atoms in the film. Estimating x yields values in between 3.4 and 3.6, which is larger than the oxidation states measured here (between 2.2 and 2.85), which suggests that a side reaction takes places during the anodic oxidation process.

As a comparison with spinel oxides where the mean cations oxidation state in the material is 2.66, the mean cations oxidation state obtained in the anodic alloy oxides is also given in **Table 5.3** (last column). It is obtained by weighting Co and Fe oxidation states measured with XANES spectra by their content in the film. The mean cation oxidation state is 2.5 – 2.6 in $Co_{50}Fe_{50}O_y$ and $Co_{25}Fe_{75}O_y$ which is not too far from what is expected in spinel oxides. However, in $Co_{75}Fe_{25}O_y$ it is 2.25, which departs more from the value in spinel oxides. Overall the Fe and Co oxidation states measured in the alloy oxides have some similarities with Co rich spinel oxides $Co_{1-x}Fe_xO_y$ presented in **chapter 4**, since Fe oxidation state is higher than the one of Co (Fe^{3+} and $Co^{2.5+}$). However, the preparation method forced Fe to be present as Fe^{3+} , which

makes it difficult to establish relevant comparisons between the oxides. It is also not easy to conciliate the oxidation state measured with a known CoFe oxide type. The lower mean oxidation state of $\text{Co}_{75}\text{Fe}_{25}\text{O}_y$ could for instance result from the fact that the oxide is a mixed of different oxide types ($\text{CoFe}(\text{OH})_2$ and Co_2FeO_4 for example). This may also be the case of the other alloy oxides in a smaller proportion.

Table 5.3: Spectroscopic parameters (Co, Fe and global metal oxidation states) of the oxides (5 ML thick) derived from XANES spectra recorded at $1.4V_{\text{RHE}}$ in 0.1M NaOH after metals/alloys oxidation. The anodic oxidation charge as well as the mean cations oxidation state in the film derived from αCo and αFe .

Sample	αCo (1.4V)	αFe (1.4V)	Oxidation charge	Mean α cations
CoO_y	2.8	-	5.07 mC/cm ²	2.8
$\text{Co}_{75}\text{Fe}_{25}\text{O}_y$	2.09	2.83	4.96 mC/cm ²	2.25
$\text{Co}_{50}\text{Fe}_{50}\text{O}_y$	2.21	2.80	5.36 mC/cm ²	2.50
$\text{Co}_{25}\text{Fe}_{75}\text{O}_y$	2.0	2.72	5.28 mC/cm ²	2.57
FeO_y	-	2.67	5.36 mC/cm ²	2.67

Catalytic properties of $\text{Co}_{100-x}\text{Fe}_x\text{O}_y$ films

The catalytic activity towards OER of the anodic oxides has been investigated in the closed XAS/XRD cell with the polymer membrane inflated, using cyclic voltammograms at 5mV/s in 0.1M NaOH. **Figure 5.8a** shows the CVs of CoO_y , $\text{Co}_{75}\text{Fe}_{25}\text{O}_y$, $\text{Co}_{25}\text{Fe}_{75}\text{O}_y$ and FeO_y samples, all formed on the same Au(111) substrate. $\text{Co}_{50}\text{Fe}_{50}\text{O}_y$ is not shown because it was formed on another Au(111) substrate and the electrochemical characterizations only go until 1.57V. The current density is given versus the substrate's geometrical surface area. The corresponding Tafel plots are shown in **Fig. 5.8b**. The OER activity follows the trend $\text{CoO}_y > \text{Co}_{75}\text{Fe}_{25}\text{O}_y > \text{Co}_{25}\text{Fe}_{75}\text{O}_y > \text{FeO}_y$. The overpotential measured at a current density of 0.2mA/cm² as well as the current density at 1.63V are given in **Table 5.4**. It confirms that FeO_y is the least OER active of oxides [3,4], as was the case for Fe_3O_4 in **chapter 4**. The surprising observation is the lower overpotential of CoO_y compared to CoFe oxides, while the addition of iron to Co oxides is generally thought to improve OER activity [5]. However, the overpotential of $\text{Co}_{75}\text{Fe}_{25}\text{O}_y$ is very close to that of CoO_y and they become almost equal around 1mA/cm². This suggests that $\text{Co}_{75}\text{Fe}_{25}\text{O}_y$ might be a better catalyst than CoO_y for higher current densities. **Table 5.4** also gives the Tafel slopes: all mixed CoFe anodic oxides exhibit a similar Tafel slope of ~ 65 mV/decade, while that of CoO_y and FeO_y is 75 mV/decade. This may indicate that the OER reaction proceeds with a similar mechanism on all mixed CoFe oxides and that it differs from the one taking place at CoO_y and FeO_y surfaces.

For this catalytic activity comparison, we have assumed that all oxides have a similar electrochemical surface area. Previous in situ STM imaging have shown that Fe and Co metal films electrodeposited in these conditions are two dimensional and atomically flat [2,32], and the oxides formed after their anodic oxidation are expected to maintain a rather similar smooth morphology. Therefore, a strongly different ECSA from the substrate surface area is not anticipated.

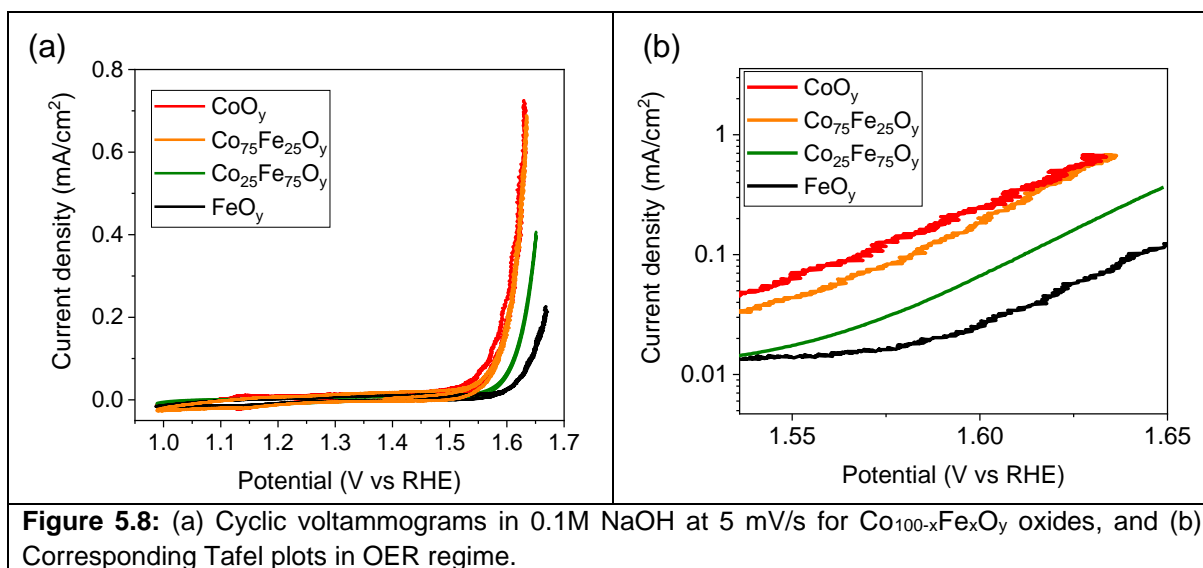


Table 5.4: Catalytic properties of Co_{100-x}Fe_xO_y samples measured during CV in 0.1M NaOH electrolyte. The current density at 1.63V_{RHE}, the overpotential at 0.2 mA/cm² and the Tafel slopes are given.

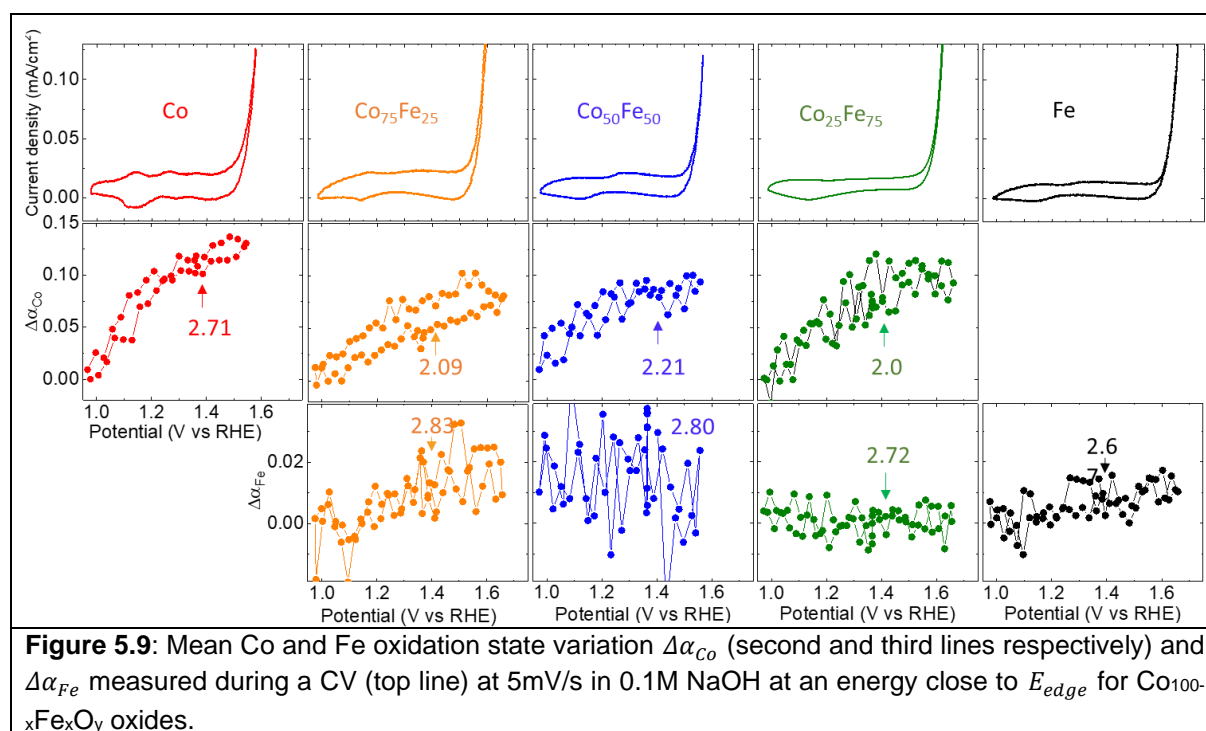
Sample	j at 1.63V (mA/cm ²)	η (mV)	b (mV/decade)
CoO _y	0.66	361	75
Co ₇₅ Fe ₂₅ O _y	0.63	377	67
Co ₅₀ Fe ₅₀ O _y	n.a.	n.a.	64
Co ₂₅ Fe ₇₅ O _y	0.19	401	66
FeO _y	0.07	430	75

Potential induced spectroscopic changes

The mean variations of Co and Fe oxidation state with potential $\Delta\alpha_{Co}(U)$ (second line) and $\Delta\alpha_{Fe}(U)$ (third line) are presented in **Figure 5.9** for CoO_y (red), Co₇₅Fe₂₅O_y (orange), Co₅₀Fe₅₀O_y (blue), Co₂₅Fe₇₅O_y (green) and FeO_y (black). They were measured during CVs at 5mV/s in 0.1M NaOH (top line), by recording the fluorescence intensity variations when the sample is illuminated by an X-ray beam which energy is close to E_{edge} at Co and Fe K-edges. The Fe and Co oxidation states measured at 1.4V for each oxide are given on the

corresponding plots. The CVs in **Fig. 5.9** are focused in the pre-OER regime. One cathodic wave around 1.1-1.15V is present in all CVs. Almost at the same potential, an anodic wave is visible for Co and Co₇₅Fe₂₅, while an anodic peak can be seen around 1.27V for Co₅₀Fe₅₀, and around 1.3V for Co₂₅Fe₇₅. It may be attributed to Co²⁺/Co³⁺ redox transition [5,7,8]. Anodic waves are difficult to distinguish in the CV of FeO_y.

The Co mean oxidation state variations $\Delta\alpha_{Co}$ occur before the OER, i.e. between 0.97V and 1.57V: $\Delta\alpha_{Co} \sim 0.1$ for CoFeO_y oxides, and 0.13 for CoO_y. Except for Co₇₅Fe₂₅, the increase is steep in [0.97V – 1.4V], then it slows down and almost saturates for Co₂₅Fe₇₅O_y. In the case of Fe, one also observes variations of $\Delta\alpha_{Fe}$ in pre-OER regime with, however, with a smaller amplitude. $\Delta\alpha_{Fe} \sim 0.02$ measured for Co₇₅Fe₂₅O_y, and is 0.01 for FeO_y. For Co₅₀Fe₅₀O_y and Co₂₅Fe₇₅O_y, $\Delta\alpha_{Fe}(U)$ is constant. If some measurements show higher noise than other, like $\Delta\alpha_{Fe}$ for Co₅₀Fe₅₀, this is probably due to experimental conditions (thickness of electrolyte layer on top the sample for example). These measurements show a systematic increase of Co oxidation state in [0.97 – 1.67V], that are a little higher for CoO_y than for CoFeO_y. In the same potential window, Fe oxidation state does not change in Fe rich CoFeO_y, and it increases only slightly in FeO_y and Co₇₅Fe₂₅O_y.



5.4 Discussion

Oxidation of Co_{100-x}Fe_xO_y oxides

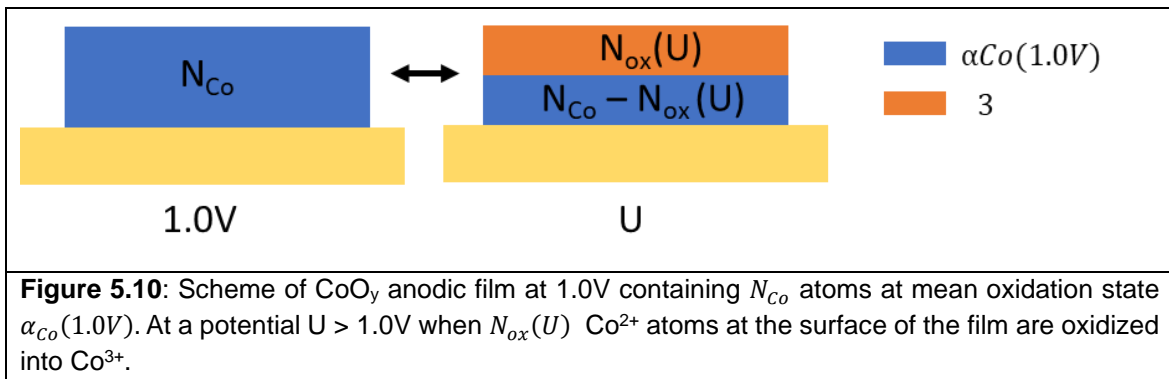
In this section, we aim at quantifying the potential induced variations of Co and Fe oxidation states shown in **Figure 5.9**. For this purpose, one may draw a comparison with Co₃O₄(111) in

chapter 3: namely we assume that the Co^{2+} atoms in the near surface region of the oxide's crystallites are oxidized into Co^{3+} upon increasing potential, while the Co atoms in the remaining of the oxide layer keep the same mean oxidation state. Let us take the example of CoO_y , illustrated with **Figure 5.10**. At 1.0V, the oxide film has a mean oxidation state $\alpha_{\text{Co}}(1.0\text{V})$ and contains N_{Co} Co atoms per nm^2 . When it is polarized at a potential $U > 1.0\text{V}$, $N_{\text{ox}}(U)$ Co atoms have been oxidized into Co^{3+} while $N_{\text{Co}} - N_{\text{ox}}(U)$ Co "bulk" remain Co^{2+} . We want to determine $N_{\text{ox}}(U)$ for each anodic oxide shown in **Figure 5.9**.

Following the model of CoO_y in **Figure 5.10**, $N_{\text{ox}}^{\text{Co}}(U)$ is related to $\Delta\alpha_{\text{Co}}(U)$ by the relation:

$$N_{\text{ox}}^{\text{Co}}(U) = \frac{N_{\text{Co}} * \Delta\alpha_{\text{Co}}(U)}{(3 - \alpha_{\text{Co}}(1.0\text{V}))} \quad (5.1)$$

In the 5 ML thick Co metallic deposit, the Co density per nm^2 is $N_{\text{Co}} = 5 * \rho_{\text{ML}}$ (see **section 5.2**). If we assume that no metal dissolution occurs while oxidizing the deposit, the amount of Co atoms in the as-formed oxide is the same as in the metal.



The same reasoning applies to obtain $N_{\text{ox}}^{\text{Fe}}(U)$ from potential induced oxidation state changes measured at Fe K-edge. The same method also applied for the alloys except that $N_{\text{Co}} = 5 * \rho_{\text{ML}} * \frac{(100-x)}{100}$ and $N_{\text{Fe}} = 5 * \rho_{\text{ML}} * \frac{x}{100}$.

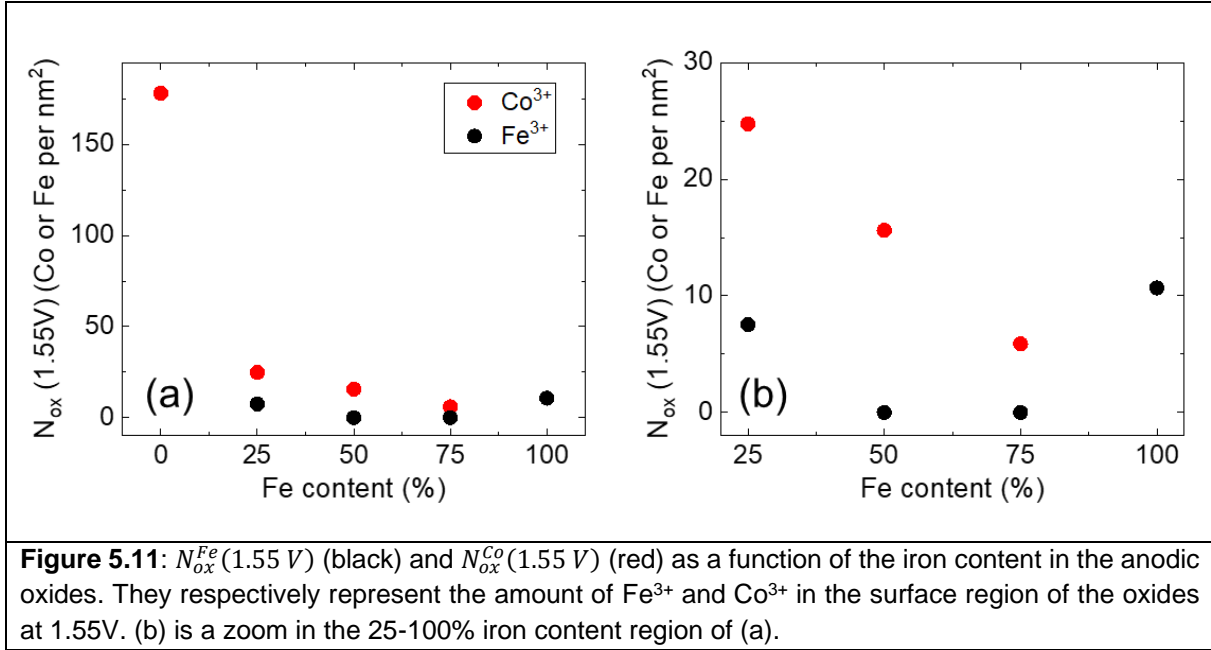
Table 5.5 gathers the different values used to determine $N_{\text{ox}}^{\text{Fe}}(1.55\text{V})$ and $N_{\text{ox}}^{\text{Co}}(1.55\text{V})$ for each anodic oxide, including N_{Co} , N_{Fe} , $\alpha_{\text{Co}}(1.0\text{V})$, $\alpha_{\text{Fe}}(1.0\text{V})$, $\Delta\alpha_{\text{Co}}(1.55\text{V})$ and $\Delta\alpha_{\text{Fe}}(1.55\text{V})$. This potential is chosen for two reasons: (i) not all measurements go beyond this potential and (ii) [0.97-1.5V] is the potential region where the largest Co oxidation states are measured since $\Delta\alpha_{\text{Co}}(U)$ seems to saturate above this potential.

Table 5.5: Spectroscopic and structural parameters used to compute $N_{\text{ox}}^{\text{Fe}}(1.55\text{V})$ and $N_{\text{ox}}^{\text{Co}}(1.55\text{V})$ for each anodic oxide. $\alpha_{\text{Co}}/\text{Fe}(1.0\text{V})$ are Co and Fe oxidation state at 1.0V, $\Delta\alpha_{\text{Co}}/\text{Fe}(1.55\text{V})$ are the amplitude of variations of $\Delta\alpha$ between 1.0V and 1.55V, determined from **Figure 5.9**. $d_{\text{eq}}(1.55\text{V})$ is the skin layer thickness formed at the surface of the anodic

oxides considering that their density is that of Co_3O_4 or Fe_3O_4 . As comparison, one Co_3O_4 monolayer (Co-O-Co distance) is 0.2 nm thick.

Sample	N_{Co} (Co/nm ²)	N_{Fe} (Fe/nm ²)	α_{Co} (1.0V)	α_{Fe} (1.0V)	$\Delta\alpha_{\text{Co}}$ (1.55V)	$\Delta\alpha_{\text{Fe}}$ (1.55V)	$d_{eq}(1.55V)$
CoO_y	397.5	-	2.71	-	0.13	-	0.80 nm
$\text{Co}_{75}\text{Fe}_{25}\text{O}_y$	300.2	79.8	2.03	2.82	0.08	0.017	0.13 nm (Co) 0.13 nm (Fe)
$\text{Co}_{50}\text{Fe}_{50}\text{O}_y$	154.3	148.3	2.16	2.82	0.085	0	0.10 nm
$\text{Co}_{25}\text{Fe}_{75}\text{O}_y$	63.6	239.0	1.92	2.72	0.10	0	0.07 nm
FeO_y	-	302.5	-	2.66	-	0.012	0.04 nm

$N_{ox}^{Fe}(1.55V)$ and $N_{ox}^{Co}(1.55V)$ are shown in **Figure 5.11** for all $\text{Co}_{100-x}\text{Fe}_x\text{O}_y$. The first observation is that $N_{ox}^{Co}(1.55V)$ is much larger in CoO_y than in alloy oxides: there is a factor 7 with $N_{ox}^{Co}(1.55V)$ in $\text{Co}_{75}\text{Fe}_{25}\text{O}_y$ and a factor 25 with that in $\text{Co}_{25}\text{Fe}_{75}\text{O}_y$. The second observation that highlights **Figure 5.11b** is the decrease of $N_{ox}^{Co}(1.55V)$ with increasing Fe content in the alloy. By comparing $N_{ox}^{Co}(1.55V)$ to N_{Co} , we can estimate that the oxidized surface layer (equivalent skin layer) corresponds to half of CoO_y initial film, while in the case of CoFeO_y oxides it is $\sim 10\%$ of the Co atoms in the film (all anodic films have similar thickness). In the case of FeO_y , $N_{ox}^{Fe}(1.55V)$ is low compared to CoO_y , which was expected from the only slight $\Delta\alpha_{Fe}(U)$ increase for this oxide. It indicates that $\sim 4\%$ of Fe atoms in the film are oxidized upon increasing potential. $N_{ox}^{Fe}(1.55V)$ in $\text{Co}_{75}\text{Fe}_{25}\text{O}_y$ is also not negligible since it corresponds to $\sim 10\%$ of Fe atoms in the film, just as for $N_{ox}^{Co}(1.55V)$ in this oxide. Overall this indicates that the presence of Fe in the anodic oxides has an appreciable impact on the amount of Co^{3+} atoms that are present on the surface layer region.



To compare these results with the thickness of skin layers measured by XRD in the case of Co_3O_4 , Fe_3O_4 and $Co_{1-x}Fe_xO_y$ (**chapters 3 and 4**), we will estimate the equivalent thickness called $d_{eq}(U)$ that $N_{ox}^{Fe}(1.55V)$ and $N_{ox}^{Co}(1.55V)$ represent. For this, the Co density in the anodic films will be approximated by Co density in Co_3O_4 ($\rho_{Co_3O_4} = 45.4 Co/nm^3$) and by that of Fe_3O_4 for Fe anodic oxide ($\rho_{Co_3O_4} = 42.9 Fe/nm^3$). For Co atoms, $d_{eq}(U)$ is for instance expressed:

$$d_{eq}(U) = \frac{N_{ox}^{Co}(U) * c_{ML}}{\rho_{Co_3O_4} * \left(\frac{100-x}{100}\right)} \quad (5.2)$$

The values of $d_{eq}(1.55V)$ are given in **Table 5.5** for each sample. For comparison, one Co monolayer in $Co_3O_4(111)$ (Co-O-Co distance) is 0.2 nm. $d_{eq}(1.55V)$ is 0.8 nm for CoO_y which is rather comparable with the skin layer thickness on $Co_3O_4(111)$ (0.5 – 1.0 nm). In the case of the CoFe anodic oxides, $d_{eq}(1.55V)$ is around 0.1 nm which is smaller than the skin layer thickness measured on $Co_{1-x}Fe_xO_y(111)$ (0.15-0.45 nm). In addition, $d_{eq}(1.55V)$ decreases with increasing iron content, which was also measured in **chapter 4** for mixed spinel oxides. In the case of FeO_y , $d_{eq}(1.55V)$ is 0.04 nm which is at least half of what we measured for the skin layer on $Fe_3O_4(111)$ (0.1-0.2 nm). For $Co_{25}Fe_{75}O_y$, the equivalent skin layer thickness is the same considering Fe^{3+} and Co^{3+} amounts, which suggests that the surface layer region may homogeneously contain both Co^{3+} and Fe^{3+} . For the two other alloys, this region may be composed of Co^{3+} and mainly Fe^{3+} since Fe oxidation state is around 2.8, however some Fe^{2+} remain.

Hence, the general trend in d_{eq} is $\text{CoO}_y > \text{CoFeO}_y > \text{FeO}_y$, which is similar to the trend found electrodeposited spinel oxide layers. The values of d_{eq} for FeO_y and CoFeO_y are smaller than that expected with spinel oxides (**chapter 4**). This may be due to a wrong estimation of Co/Fe density in the anodic oxides. For example, Co density in CoOOH is 1.5 times lower than in Co_3O_4 . Using CoOOH Co density would therefore increase $d_{eq}(1.55V)$ and make it closer to what was measured in **chapter 4**. However, since the data are in fair agreement between spinel and anodic oxides, this justifies the use of the skin layer model (see **Figure 5.10**) to determine the data presented above for anodic oxides.

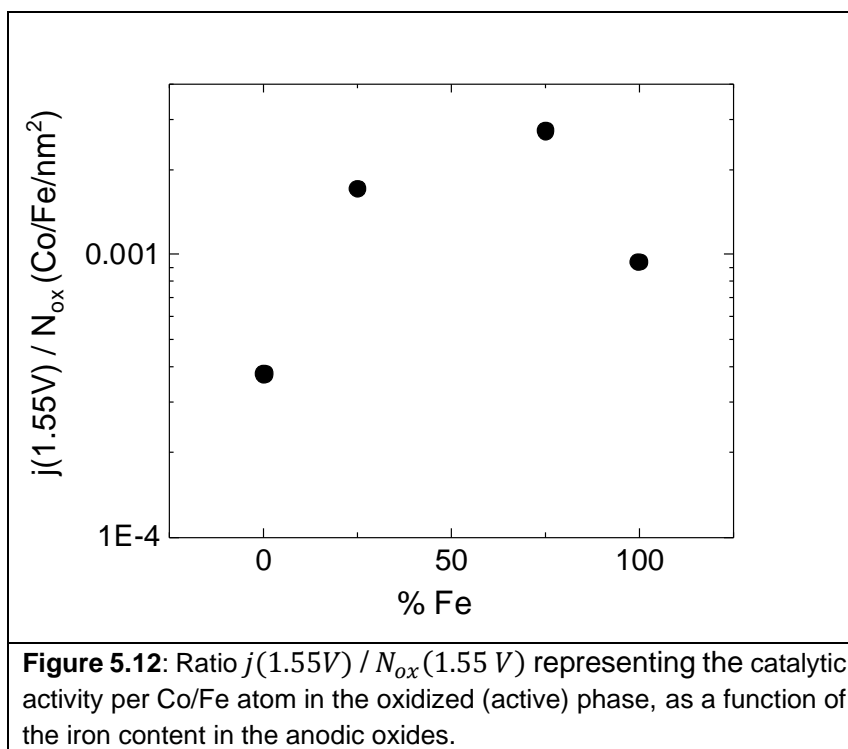
OER activity and amount of $\text{Co}^{3+} / \text{Fe}^{3+}$ in the surface region

In light of the above analysis, we will compare the OER activities of the different oxides. **Figure 5.12** shows the ratio $j(1.55V) / N_{ox}(1.55V)$ that represents the current density per atom in the active (oxidized) phase, as a function of the iron content in the anodic oxides.

We observe that the ratio $j(1.55V) / N_{ox}(1.55V)$ is smaller for pure oxides (FeO_y and CoO_y) compared to mixed oxides $\text{Co}_{75}\text{Fe}_{25}\text{O}_y$ and $\text{Co}_{25}\text{Fe}_{75}\text{O}_y$. This means that the catalytic activity per atom in the “skin layer” is higher for mixed oxides. In addition, the figure shows that the catalytic activity per Fe atom in FeO_y is higher than that measured per Co atom in CoO_y . This is surprising since Co oxides are very often considered as better catalysts than Fe oxides, and at the scale of the complete catalyst, we indeed measured that the OER activity of CoO_y is higher than that of FeO_y (see **Fig 5.8**). The present graph however seems to indicate that for our anodic oxides, the catalytic activity per active site in FeO_y is higher than that in CoO_y , but since FeO_y active (oxidized) phase contains fewer active sites than that of Co oxide, its global OER activity is lower. This is in line with the conclusion drawn in **chapter 4** from the comparison of spinel Co_3O_4 and Fe_3O_4 .

In the same way, one can see that CoO_y global OER activity (**Fig 5.8**) is higher than that of mixed oxides CoFeO_y while its activity per Co atom (**Fig 5.12**) is lower than in mixed oxides. Indeed, the amount of Co^{3+} in CoO_y active phase is consequently higher than for in mixed oxides. For example, it is ~ 7 times higher than in $\text{Co}_{75}\text{Fe}_{25}\text{O}_y$ while $\text{Co}_{75}\text{Fe}_{25}\text{O}_y$ and CoO_y global OER activity at 1.63V are not very different (0.66 and 0.63 mA/cm^2). A first explanation for such differences would be that only a fraction of Co^{3+} within the skin layer of CoO_y are OER active. However, this seems improbable because a correlation between OER activity and amount of Co^{3+} in the surface layer was found for CoO_y anodic oxides of varying thicknesses (see **Appendix A5.4**), which suggests that a higher amount of Co^{3+} in the skin layer is associated to a higher OER activity, and therefore all Co^{3+} within the skin layer would be OER active. A second explanation would be that due to Fe presence, the catalytic scheme is different for CoFeO_y and CoO_y : it does not require as much Co^{3+} at CoFeO_y surface as it does

for CoO_y to obtain a similar OER activity. This would be supported by the different Tafel slope measured for CoO_y (~75 mV/dec) and CoFeO_y (~65 mV/dec). In addition, a similar observation was made for spinel $\text{Co}_{1-x}\text{Fe}_x\text{O}_y$ and Co_3O_4 oxides in **chapter 4**.

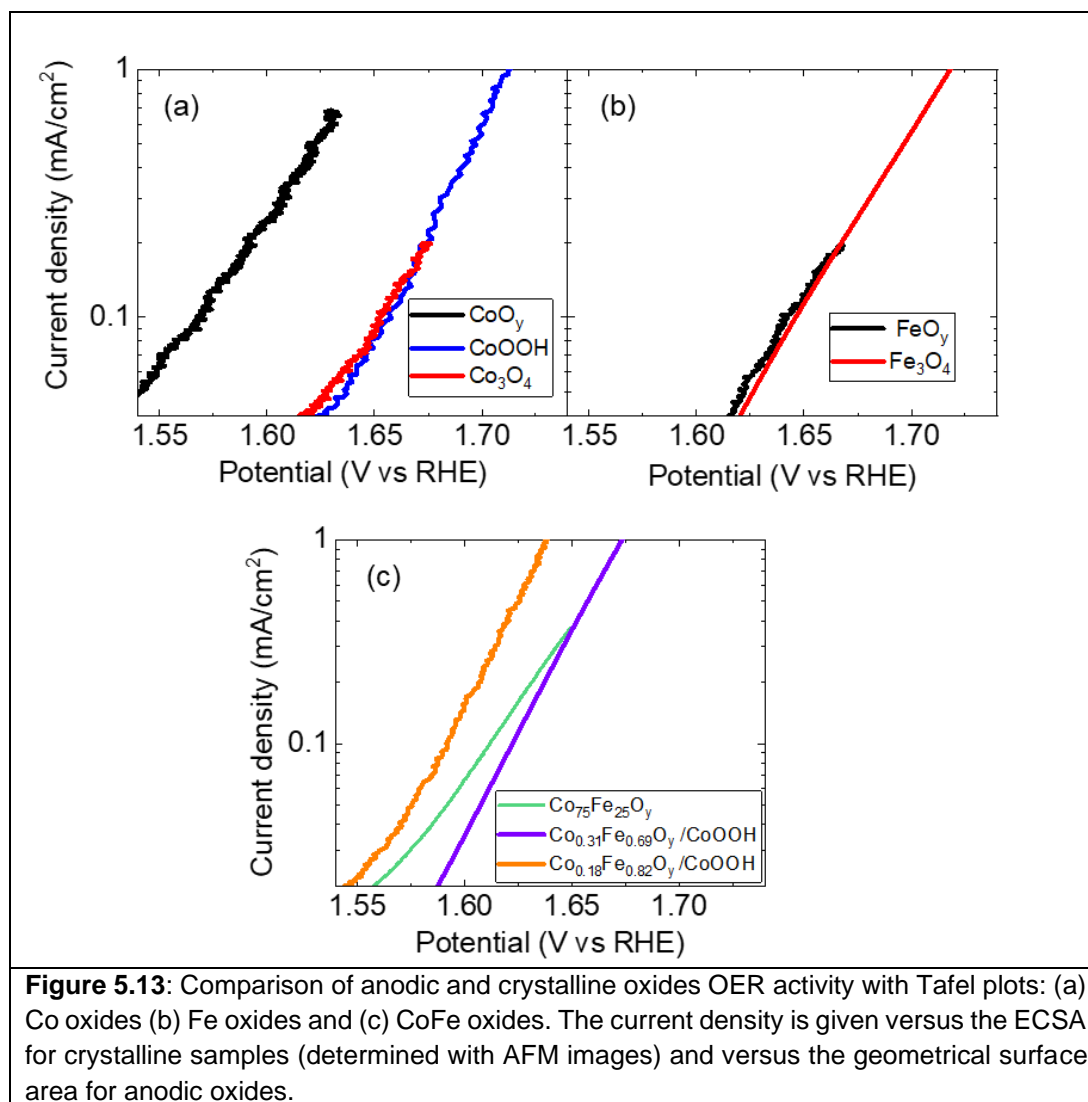


Comparison of anodic and crystalline oxides:

As evoked along this chapter, spinel and anodic oxides differ regarding their structure, thickness and redox states, and we will now compare their OER activity and surface redox state at OER potential.

Figure 5.13 compares the catalytic activity of anodic and spinel oxides in 0.1M NaOH. In the latter case the current density is normalized to the ECSA (we used AFM images to determine the roughness factor of the oxide surface, see **chapter 3** for more details). For anodic oxides, the geometrical surface area of the substrate is used since the oxides are grown on atomically flat metallic films. First, FeO_y and Fe_3O_4 (111) exhibit very similar overpotential and Tafel slopes, suggesting that the OER mechanisms is the same for the two types of Fe oxides. On the contrary, CoO_y is unambiguously a better catalyst than Co_3O_4 (111) and $\text{CoOOH}(001)$ samples, with an overpotential 70-80 mV lower. However, CoO_y has a higher Tafel slope than crystalline oxides (75 mV/decade against 55-60 mV/decade), which suggests that the rate determining step might be different for anodic and spinel oxides. However, operando characterizations suggest that the amount of Co^{3+} in the active phase are probably not too different for both types of oxides. A higher number of defects within the non-crystalline CoO_y

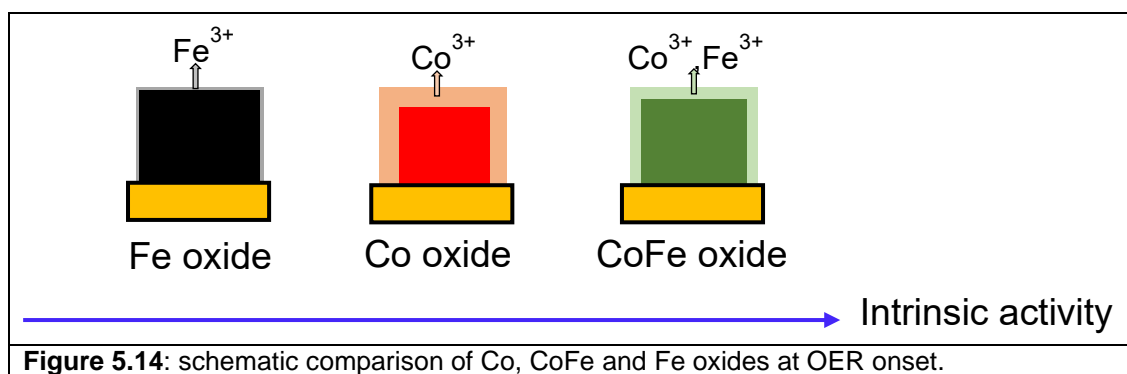
anodic oxide may account for its higher catalytic activity compared to $\text{Co}_3\text{O}_4(111)$, since defect sites such as oxygen vacancies are believed to be the most active for OER [12].



In both types of mixed CoFe oxides, a significant increase of Co oxidation state and almost no change in Fe oxidation state are measured in operando conditions. The exception is $\text{Co}_{75}\text{Fe}_{25}\text{O}_y$ in which αFe increases slightly, which is probably facilitated by the fact that there are Fe^{2+} centers in the anodic oxides. Therefore, a redox transition $\text{Fe}^{2+} \rightarrow \text{Fe}^{3+}$ is possible, unlike in $\text{Fe}_3\text{O}_4(111)$ films. These observations are interpreted as the formation of a skin layer at the surface of mixed oxides, mainly composed of Co^{3+} and Fe^{3+} . In both types of mixed oxides, we also saw that the catalytic activity of the films was related to the thickness of the skin layer formed at OER potential, which decreases with increasing Fe content. **Fig.5.13c** compares the OER activity of $\text{Co}_{75}\text{Fe}_{25}\text{O}_y$, $\text{Co}_{0.31}\text{Fe}_{0.69}\text{O}_y/\text{CoOOH}$ and $\text{Co}_{0.18}\text{Fe}_{0.82}\text{O}_y/\text{CoOOH}$. The current density measured for the spinel oxides is normalized to the ECSA. The difference in overpotential are not very large between the three oxides (30 mV gap maximum), the anodic

oxide having a low overpotential especially at low current densities. The crystalline oxides have smaller Tafel slopes than anodic oxides (45-55 mV/decade and ~65 mV/decade respectively), which suggests a difference in the OER mechanism taking place at the surface of each type of oxide. These observations may be interpreted as: for a similar Fe content in the oxides, a similar number of active sites are involved during OER at their surface, but the active site(s) on which OER proceeds may not be the same(s).

To summarize, a schematic comparison of Co, CoFe and Fe oxides surfaces at OER onset is shown in **Figure 5.14**. Globally, for either crystalline or amorphous oxides, a “thick” skin layer, made of Co^{3+} mainly is formed at the surface of Co oxides, while that of CoFe is smaller, containing Co^{3+} and Fe^{3+} principally and an even thinner Fe^{3+} containing skin layer is formed at the surface of Fe_3O_4 . The large-scale transformations (structural and redox) undergone by each oxide type are similar whether they are crystalline or amorphous. However, the local atomic environment differs between crystalline and disordered oxides, corresponding to different OER mechanisms especially for Co containing oxides. This leads to the common idea that disordered samples are more active than the crystalline ones, for which we only find strong evidence in the case of pure Co oxide.



5.5 Conclusion

In this chapter, anodic oxides formed by oxidation of a metal or alloy films have been prepared and characterized in situ by SXRD and XAS. Since the structure of the initial metal film is known, the density of Co and Fe atoms within the as-formed oxide film can be estimated, as well as the redox states of Co and Fe. Their potential induced changes in pre-OER and OER regimes can therefore be quantified and show similar trends for mixed oxides, with an increase of OER activity linked to a higher amount of Co^{3+} in a surface region formed in pre-OER regime. Even though more Co^{3+} are present on the skin layer of CoO_y than in $\text{Co}_{75}\text{Fe}_{25}\text{O}_y$, both oxides have a similar OER activity, which suggests the existence of different active sites for mixed oxides, more efficient. Comparison of potential induced redox changes and catalytic activity between crystalline (chapters 3 and 4) and anodic oxide samples of similar metal composition

yields common large-scale features for both amorphous and crystalline samples, and suggests differences of mechanisms at the atomic scale especially for Co containing oxides.

5.6 Bibliography

- [1] Reikowski, F.; Maroun, F.; Di, N.; Allongue, P.; Ruge, M.; Stettner, J.; Magnussen, O. M. In situ surface X-ray diffraction study of ultrathin epitaxial Co films on Au(111) in alkaline solution. *Electrochim. Acta* **2016**, *197*, 273–281. <https://doi.org/10.1016/j.electacta.2016.01.052>.
- [2] Jurca, H. F.; Damian, A.; Gougaud, C.; Thiaudière, D.; Cortès, R.; Maroun, F.; Allongue, P. Epitaxial Electrodeposition of Fe on Au(111): Structure, Nucleation, and Growth Mechanisms. *J. Phys. Chem. C* **2016**, *120* (29), 16080–16089. <https://doi.org/10.1021/acs.jpcc.5b12771>.
- [3] Morales-Guio, C. G.; Liardet, L.; Hu, X. Oxidatively Electrodeposited Thin-Film Transition Metal (Oxy)Hydroxides as Oxygen Evolution Catalysts. *J. Am. Chem. Soc.* **2016**, *138* (28), 8946–8957. <https://doi.org/10.1021/jacs.6b05196>.
- [4] Burke, M. S.; Kast, M. G.; Trotochaud, L.; Smith, A. M.; Boettcher, S. W. Cobalt-Iron (Oxy)hydroxide Oxygen Evolution Electrocatalysts: The Role of Structure and Composition on Activity, Stability, and Mechanism. *J. Am. Chem. Soc.* **2015**, *137* (10), 3638–3648. <https://doi.org/10.1021/jacs.5b00281>.
- [5] Smith, R. D. L.; Pasquini, C.; Loos, S.; Chernev, P.; Klingan, K.; Kubella, P.; Mohammadi, M. R.; Gonzalez-Flores, D.; Dau, H. Spectroscopic Identification of Active Sites for the Oxygen Evolution Reaction on Iron-Cobalt Oxides. *Nat. Commun.* **2017**, *8* (1). <https://doi.org/10.1038/s41467-017-01949-8>.
- [6] Maurice, V.; Marcus, P. Passive Films at the Nanoscale. *Electrochim. Acta* **2012**, *84*, 129–138. <https://doi.org/10.1016/j.electacta.2012.03.158>.
- [9] Kakuno, E. M.; Mosca, D.M.; Mazzaro, I.; Mattoso, N.; Schreiner, W. H.; Gomes, M.A.B. Structure, Composition, and Morphology of Electrodeposited Co_xFe_{1-x} Alloys. *J. Electrochem. Soc.* **1997**, *144* (9), 3222–3226. <https://doi.org/10.1149/1.1838059>.
- [10] Nakamura, A.; Takai, M.; Hayashi, K.; Osaka, T. Preparation and Magnetic Properties of CoNiFe Thin Film by Electrodeposition. *Surf. Finish. Soc. Japan* **1996**, *47* (11), 934–938. <https://doi.org/10.4139/sfj.47.934>
- [11] Qiang, C.; Xu, J.; Xiao, S.; Jiao, Y.; Zhang, Z.; Liu, Y.; Tian, L.; Zhou, Z. The Influence of PH and Bath Composition on the Properties of Fe-Co Alloy Film Electrodeposition. *Appl. Surf. Sci.* **2010**, *257* (5), 1371–1376. <https://doi.org/10.1016/j.apsusc.2010.08.070>.
- [12] Bergmann, A.; Jones, T. E.; Martinez Moreno, E.; Teschner, D.; Chernev, P.; Gliech, M.; Reier, T.; Dau, H.; Strasser, P. Unified Structural Motifs of the Catalytically Active State of Co(Oxyhydr)Oxides during the Electrochemical Oxygen Evolution Reaction. *Nat. Catal.* **2018**, *1* (9), 711–719. <https://doi.org/10.1038/s41929-018-0141-2>.
- [13] Foelske, A.; Kunze, J.; Strehblow, H. H. Initial Stages of Hydroxide Formation and Its Reduction on Co(0 0 0 1) Studied by in Situ STM and XPS in 0.1 M NaOH. *Surf. Sci.* **2004**, *554* (1), 10–24. <https://doi.org/10.1016/j.susc.2003.12.059>.
- [14] Han, Y.; Axnanda, S.; Crumlin, E. J.; Chang, R.; Mao, B.; Hussain, Z.; Ross, P. N.; Li, Y.; Liu, Z. Observing the Electrochemical Oxidation of Co Metal at the Solid/Liquid Interface Using

Ambient Pressure X-ray Photoelectron Spectroscopy. *J. Phys. Chem. B* **2018**, *122* (2), 666–671. <https://doi.org/10.1021/acs.jpcc.7b05982>.

[15] Zeng, Z.; Chan, M. K. Y.; Zhao, Z. J.; Kubal, J.; Fan, D.; Greeley, J. Towards First Principles-Based Prediction of Highly Accurate Electrochemical Pourbaix Diagrams. *J. Phys. Chem. C* **2015**, *119* (32), 18177–18187. <https://doi.org/10.1021/acs.jpcc.5b03169>.

[16] Risch, M.; Ringleb, F.; Kohlhoff, M.; Bogdanoff, P.; Chernev, P.; Zaharieva, I.; Dau, H. Water Oxidation by Amorphous Cobalt-Based Oxides: In Situ Tracking of Redox Transitions and Mode of Catalysis. *Energy Environ. Sci.* **2015**, *8* (2), 661–674. <https://doi.org/10.1039/c4ee03004d>.

[17] Behl, W. K.; Toni, J. E. Anodic Oxidation of Cobalt in Potassium Hydroxide Electrolytes. *J. Electroanal. Chem.* **1971**, *31* (1), 63–75. [https://doi.org/10.1016/S0022-0728\(71\)80043-8](https://doi.org/10.1016/S0022-0728(71)80043-8).

[18] Fujii, H.; Wakabayashi, Y.; Doi, T. Early Stages of Iron Anodic Oxidation: Defective Growth and Density Increase of Oxide Layer. *Phys. Rev. Mater.* **2020**, *4* (3), 1–7. <https://doi.org/10.1103/PhysRevMaterials.4.033401>.

[19] Freire, L.; Nóvoa, X. R.; Montemor, M. F.; Carmezim, M. J. Study of passive films formed on mild steel in alkaline media by the application of anodic potentials. *Mater. Chem. Phys.* **2009**, *114* (2–3), 962–972. <https://doi.org/10.1016/j.matchemphys.2008.11.012>.

[20] Díez-Pérez, I.; Gorostiza, P.; Sanz, F.; Müller, C. First Stages of Electrochemical Growth of the Passive Film on Iron. *J. Electrochem. Soc.* **2001**, *148* (8), B307. <https://doi.org/10.1149/1.1381073>.

[21] Allongue, P.; Maroun, F.; Jurca, H. F.; Tournerie, N.; Savidand, G.; Cortès, R. Magnetism of Electrodeposited Ultrathin Layers: Challenges and Opportunities. *Surf. Sci.* **2009**, *603* (10–12), 1831–1840. <https://doi.org/10.1016/j.susc.2008.11.040>.

[22] Allongue, P.; Cagnon, L.; Gomes, C.; Gündel, A.; Costa, V. Electrodeposition of Co and Ni/Au(1 1 1) Ultrathin Layers. Part I: Nucleation and Growth Mechanisms from in Situ STM. *Surf. Sci.* **2004**, *557* (1–3), 41–56. <https://doi.org/10.1016/j.susc.2004.03.016>.

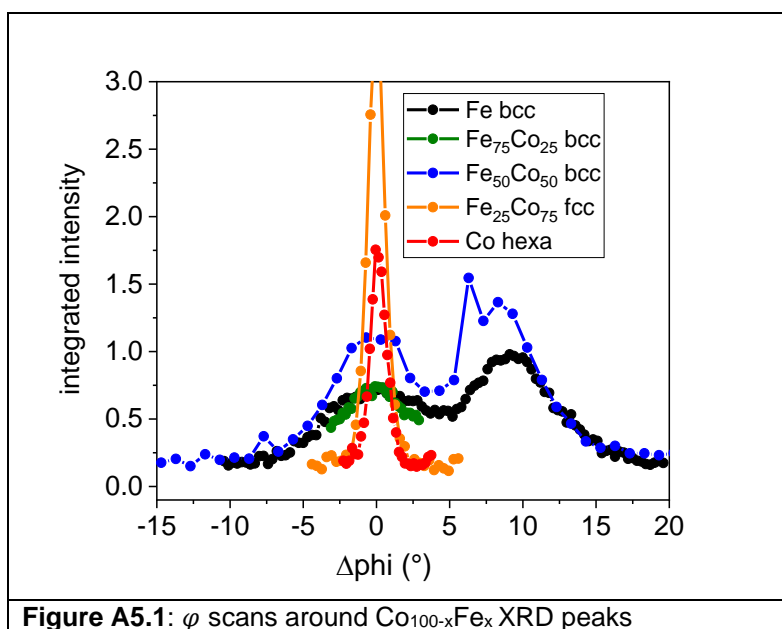
[23] Allongue, P.; Joiret, S. Structure Sensitive in Situ Raman Study of Iron Passive Films Using SERS-Active Fe/Au(111) Substrates. *Phys. Rev. B - Condens. Matter Mater. Phys.* **2005**, *71* (11), 1–7. <https://doi.org/10.1103/PhysRevB.71.115407>.

[24] Davenport, A. J.; Oblonsky, L. J.; Ryan, M. P.; Toney, M. F. The Structure of the Passive Film That Forms on Iron in Aqueous Environments. *J. Electrochem. Soc.* **2000**, *147* (6), 2162. <https://doi.org/10.1149/1.1393502>.

5.7 Appendix

A5.1 Additional structural characterizations of electrodeposited films: phi scans

Additional structural characterizations of electrodeposited metal and alloy films include φ -scans around the CoFe(011), (111) and Co(001) peak. Such scans are shown in **Fig.A5.1** for all $\text{Co}_{100-x}\text{Fe}_x$ samples. For metals with a bcc structure, a pair of broad Bragg peaks are found, separated by $\Delta\varphi \sim 9^\circ$ (Fe) and $\Delta\varphi \sim 7^\circ$ ($\text{Co}_{50}\text{Fe}_{50}$). The appearance of these peaks is expected for bcc-Fe(110), for which the formation of two distinct peak contributions was measured for deposits as or more thick than 5ML [2]. For 5ML Fe deposit, $\Delta\varphi$ was found close to 8.5° , which is line with our measurements. Hexa-Co(011) and fcc- $\text{Co}_{75}\text{Fe}_{25}$ (111) exhibit narrow and intense peaks.



A5.2 Example of metals and alloys XRD peak

Figure A5.2 presents the $\text{Co}_{100-x}\text{Fe}_x$ XRD diffraction peaks from which structural information given in **Table 5.2** are determined. They were recorded in pH 13 electrolyte at a potential where the metal phase is stable. They are broad Bragg peaks corresponding to thin metal films, which do not appear anymore after anodic oxidation of the films, as the second line of **Fig. A5.2** shows.

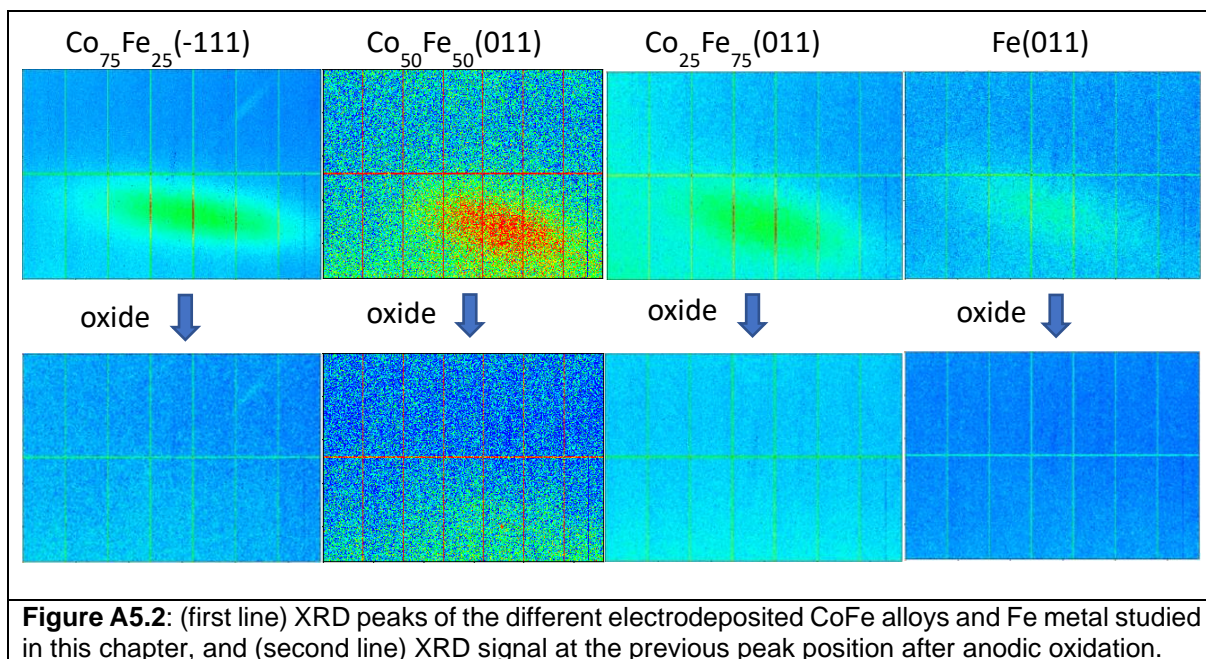


Figure A5.2: (first line) XRD peaks of the different electrodeposited CoFe alloys and Fe metal studied in this chapter, and (second line) XRD signal at the previous peak position after anodic oxidation.

A5.3 Comparison of XAS spectra of alloys at Co and Fe K-edges

Figure A5.3 shows the superposition of Co and Fe K-edges XAS spectra measured for a same alloy. Co K-edge spectrum is shown in red and Fe K-edge in black. In (a) and (b) are the spectra of bcc $\text{Co}_{25}\text{Fe}_{75}$ and $\text{Co}_{50}\text{Fe}_{50}$ for which the EXAFS oscillations overlap almost completely between Co and Fe spectra, except a slight difference in the very first oscillation. Since fcc and bcc environment yield different EXAFS oscillations, this overlap indicates that both Co and Fe are in a bcc environment, meaning that the alloys are solid bcc solutions. In the case of $\text{Co}_{75}\text{Fe}_{25}$ (c), the comparison is more difficult because of the quality of the spectrum at Co K-edge.

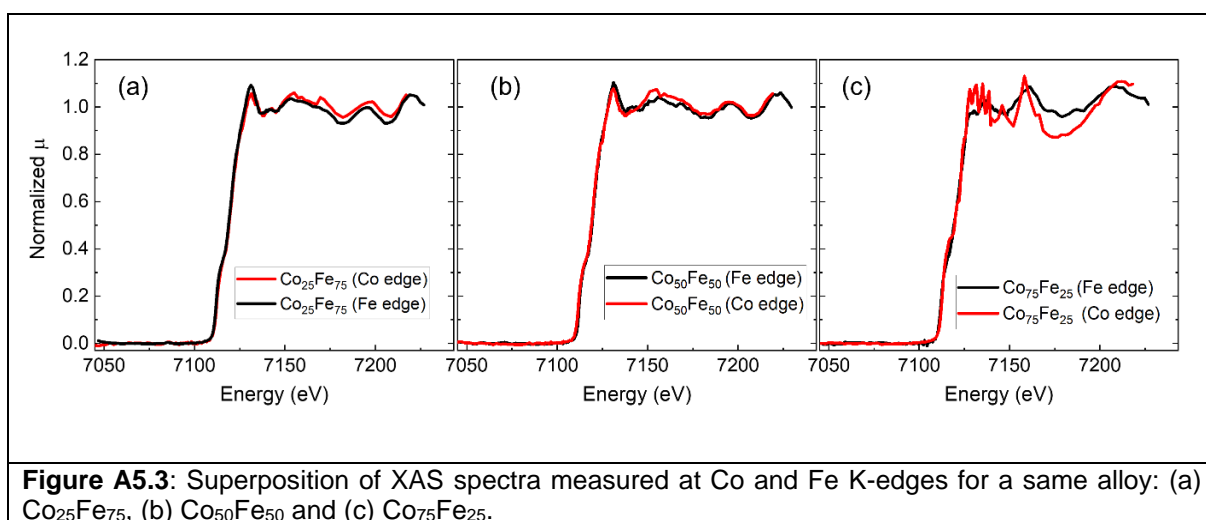
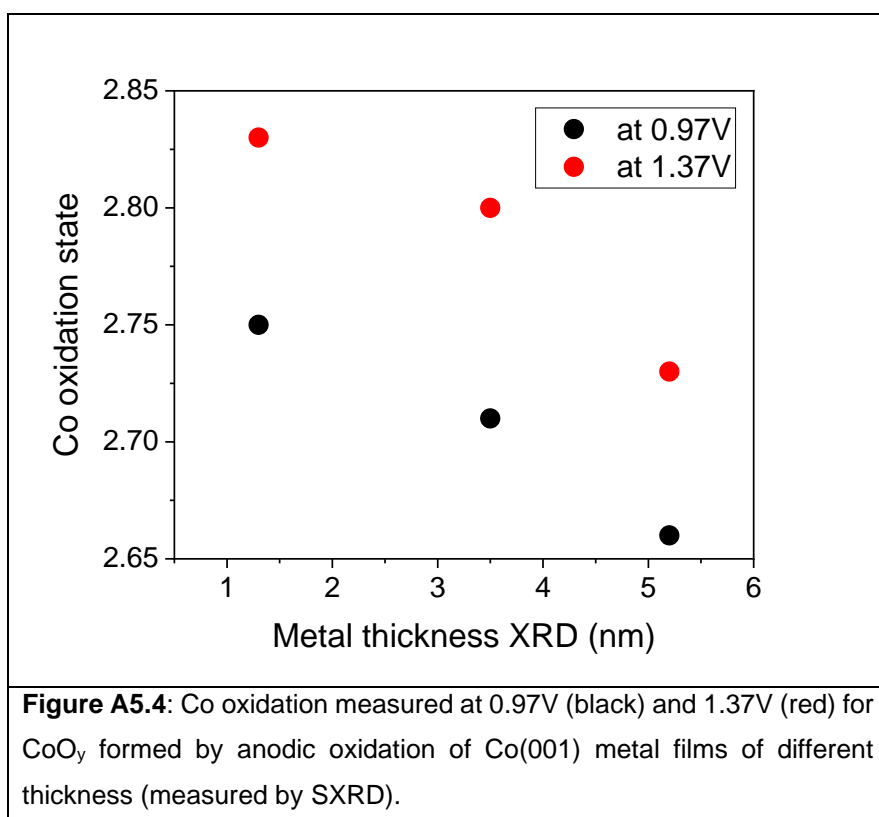


Figure A5.3: Superposition of XAS spectra measured at Co and Fe K-edges for a same alloy: (a) $\text{Co}_{25}\text{Fe}_{75}$, (b) $\text{Co}_{50}\text{Fe}_{50}$ and (c) $\text{Co}_{75}\text{Fe}_{25}$.

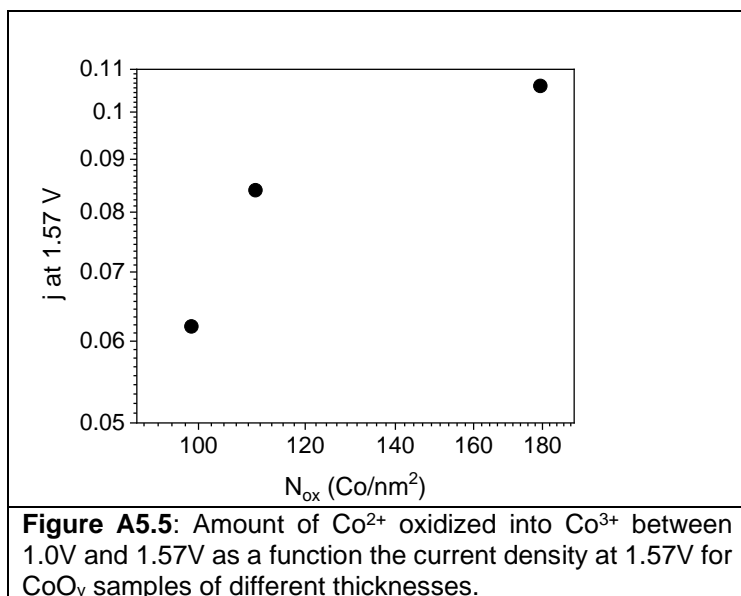
A5.4 Anodic Co oxides of different thickness

As mentioned in 5.3, we have studied CoO_y oxides obtained from anodic oxidation of $\text{Co}(001)$ films of different thickness. **Fig.A5.4** shows the dependence of Co oxidation state determined by XAS spectra analysis with the thickness of the initial $\text{Co}(001)$ film measured with SXRD. At both 0.97V and 1.37V (within the pre-OER regime), α_{Co} decreases with increasing thickness of the initial metal film. This indicates that thinner CoO_y tend to have a higher Co oxidation state than thicker ones. The oxidation states we measure are lower than 3 even for thin samples at OER potential, and higher than 2.65 for samples that we consider as fully oxidized (no metal contribution remaining in the XRD signal). If we assume that the oxide is composed of two layers, one containing Co(II) and one with Co(III) , this means that the Co(II) phase is more consequent for thicker oxides. In this case and even if CoO_y is seen as an homogeneous phase of oxidation state α_{Co} , this dependence with the $\text{Co}(001)$ thickness could be explained by the fact that oxidizing $\text{Co}(0)$ to Co(II) is easier than $\text{Co}(0)$ to Co(III) , and the oxidation is all the more facilitated than the number of Co atoms is small. Thinner layers would therefore be more readily oxidized into Co(III) than thicker ones where the oxidation would be more difficult, making more Co remaining Co(II) .



In **Fig. A5.5**, the catalytic activity of CoO_y films of different thickness (see **A5.4**) is compared to the amount of Co^{2+} oxidized in Co^{3+} before OER, between 0.97V and 1.55V. This amount is given in Co per nm^2 (according to Eq. (5.1)). A higher amount of oxidized Co atoms is

associated to a higher current density at 1.57V. Thicker oxides (less Co^{3+} rich) also tend to form thicker skin layers, allowing higher OER activity. This is in line with the work of Du et al. [16] who have shown a dependence of OER activity with the volume of electrodeposited CoCat catalyst. A combined volume and surface activity would therefore also exist in our CoO_y catalysts.



General conclusion and perspectives

In this thesis, we investigated the operando behaviour of different metal oxide catalysts for water splitting using both surface X-ray Diffraction and X-ray Absorption Spectroscopy. This aims at developing a better understanding of the oxygen evolution reaction mechanism taking place at their surface, which is required for developing efficient OER catalysts. We chose to study cobalt, iron and mixed cobalt iron oxides which are amongst the best earth abundant catalysts for water oxidation into oxygen in alkaline electrolyte. Especially, for our studies we used model catalysts which present well-defined morphologies, structures and compositions. These are epitaxial oxide thin films obtained by electrodeposition methods. The use of model catalysts enables to correlate the electrochemical response of the catalysts, measured versus a known electrochemical surface area with the structure and chemical state of the catalysts measured under operating conditions. We prepared thin films of Co, Fe and CoFe oxides adapting preparation methods in the literature. We also devised a new preparation method for Co rich CoFe oxides. In the latter case, we were able to obtain very flat films by performing the electrodeposition on CoOOH(001)/Au(111) buffer layers. We also devised another method for preparing Co, Fe and CoFe oxides based on the anodic oxidation of metal films. We used operando structural characterizations using XRD consist in monitoring changes of crystallites sizes and lattice parameters during potential sweeps until the OER regime. We additionally developed a procedure to simultaneously track the Co oxidation state using the XAS fluorescence signal emitted by the material at a chosen incident energy.

In the case of Co_3O_4 , we evidence the transformation a sub-nanometre thick surface layer of the crystallites into a disordered phase which mean oxidation state is 3. This surface layer, referred as skin layer is the active phase for OER and is formed upon the oxidation of Co^{2+} in the near surface to Co^{3+} . For CoOOH, the active phase is the (001) basal plane, which undergoes potential induced deprotonation, leaving a ~ 50% protonated surface at OER onset, where Co^{3+} are mainly present. In both cases, we found no evidence for the presence of Co^{4+} on the surface during OER. The Co^{3+} surface termination of both oxides is consistent with their similar OER activities. The surface crystallinity and roughness do not seem to play an important role in the OER activity.

We then extended the study to crystalline mixed CoFe oxides ($\text{Co}_{1-x}\text{Fe}_x\text{O}_y$) and iron oxide Fe_3O_4 . Fe is present as Fe^{3+} in the mixed oxides, and Co oxidation state is ~ 2.5. We evidence the potential induced formation of a skin layer on the Fe containing oxide's surfaces, just like for Co_3O_4 . Its thickness decreases with increasing Fe content, ranging from ~ 0.4nm in Co rich

oxides to ~ 0.1 nm in Fe_3O_4 . We find a mean Co oxidation state in the skin layer of 3.2 - 3.3, which is higher than for Co_3O_4 , while Fe oxidation state remains unchanged. We measure that the OER activity of Co_3O_4 and $\text{Co}_{1-x}\text{Fe}_x\text{O}_y$ is similar, while that of Fe_3O_4 is clearly lower. To rationalize this, we show that the number of active sites in the skin layer as well as its Co oxidation state should be considered. At equal OER activity, $\text{Co}_{1-x}\text{Fe}_x\text{O}_y$ skin layer contains less active sites than that of Co_3O_4 , and a higher Co mean oxidation state. We show that Co oxidation state and catalytic activity per active site are related. The intrinsic activity of $\text{Co}_{1-x}\text{Fe}_x\text{O}_y$ active sites is therefore higher than that of Co_3O_4 but the skin layer of the latter contains more active sites, globally resulting in a similar activity. Finally, almost no skin layer is formed at the surface of Fe_3O_4 , therefore containing little active sites, which may explain their lower OER activity.

In the last part of this work, we introduced another preparation method with which oxides films one order of magnitude thinner (1-2 nm) can be obtained. It consists in the anodic oxidation of an ultrathin metal or alloy epitaxial layers electrodeposited on Au(111). We could grow using this new method CoFe alloys with a wide composition range. These oxide films are not crystalline but their low thickness enables to track the potential induced oxidation state changes with high sensitivity. We found that the Co and Fe oxidation states in the corresponding anodic oxides are slightly higher than those of Co_3O_4 and Fe_3O_4 but remain less than 3. In the case of alloy oxides, Co oxidation state is lower than that of Fe (2 - 2.2 against 2.7 - 2.8). Considering the same potential induced oxidation model described for spinel oxides, we could conclude that Co anodic oxides do not catalyse as efficiently the OER reaction as the anodic alloy oxides do.

Overall, we have evidenced a general pattern amongst cobalt, cobalt-iron and iron oxides in pre-OER regime: the potential induced formation of a 3D reaction zone containing high valency cations. This is the active phase for OER, it is thicker on Co oxides compared to Fe oxides, and has an intermediate thickness for mixed CoFe oxides.

Beyond the work presented here, more investigations would however be required in order to get a more comprehensive understanding of the results we obtained.

Regarding the skin layer of spinel oxides, even though we have been able to determine the metal oxidation state within it, we could not resolve the complete chemical composition of the skin layer with our measurements. Doing EXAFS characterizations at OER potential could provide more insights into the Co local environments in the skin layer, which would be useful to understand the similarities in OER activity of Co_3O_4 and CoOOH . In the case of CoFeO_y spinel oxides, this could also help understanding why is Co more oxidized in $\text{Co}_{1-x}\text{Fe}_x\text{O}_y$ skin

layer than in Co_3O_4 , and therefore get more insights into the possible difference of OER mechanism between them. For these mixed oxides, even though we are confident in the results obtained by operando XAS-XRD measurements, performing additional measurements on other samples of different compositions would be interesting especially to investigate how the Co oxidation state within the skin layer might change with the oxide composition, and get stringer correlation with OER activity.

In addition, there are several experimental conditions that may have an influence on our results, which would require more investigations. For example, we found that the substrate on which the oxide is grown, the morphology of the oxide, or the pH of the electrolyte can influence both OER activity and potential induced structural changes of $\text{Co}_3\text{O}_4(111)$. Moreover, our operando characterizations would benefit of being performed in experimental conditions closer to that of commercial electrolyzers, for example at higher temperature (70°C) and in more concentrated electrolytes. The stability of the oxides during long term catalytic use is also an interesting parameter to look at. This includes investigating the stability of their catalytic performances and their structural stability (is amorphization becoming definitive, is the catalyst dissolving?).

Regarding anodic oxides presented in **chapter 5**, more knowledge about their exact composition, atomic arrangement and morphology would be required to get a more comprehensive understanding of their operando spectroscopic behaviour. Additional in situ characterizations using STM or XPS could be interesting in this regard. Since these samples are only characterized in situ, studying their stability in air with XAS, XRD and AFM characterizations would also be interesting. This might also help understand the OER activity differences between spinel and anodic oxides. We have also seen in the case of Co anodic oxides that the thickness of the oxide can influence its oxidation state. The influence of this parameter and how it may impact the operando behaviour of the oxides should therefore be investigated in the case of the other oxides. Repeating the XAS measurements with thinner alloy oxides could help also determine if residual metal is present or not in the alloy oxide films. Moreover, in order to have a broader understanding of the correlations between catalytic properties and potential induced redox changes in the anodic alloys, the resulted of chapter 5 should be consolidated by additional measurements including more alloy compositions distributed on the whole composition range.

Titre : Etudes in operando par diffraction et spectroscopie d'absorption des rayons X de catalyseurs modèles pour la décomposition de l'eau

Mots clés : caractérisations operando, structure, électrochimie, oxydes, degré d'oxydation

Résumé: La décomposition électrochimique de l'eau en oxygène et hydrogène est un moyen énergétiquement efficace de convertir et stocker l'électricité issue d'énergies renouvelables. Pour cette technologie, l'utilisation de catalyseurs est nécessaire afin d'optimiser le rendement de conversion. Les oxydes du groupe fer (Fe, Ni, Co) sont parmi les meilleurs matériaux présents en abondance sur terre pour la catalyse de la réaction d'oxydation de l'eau en oxygène. Le développement de catalyseurs efficaces implique leur synthèse et la compréhension des mécanismes réactionnels ayant lieu à leur surface. Dans ce travail, nous cherchons à développer une meilleure connaissance de la structure atomique et de l'état chimique des catalyseurs en conditions réactionnelles.

Pour cela, nous avons synthétisé des catalyseurs modèles – des couches d'oxydes très minces avec une morphologie idéalement plane électrodéposés sur un substrat – et utilisé le rayonnement synchrotron pour sonder, en conditions operando, la structure atomique et le degré d'oxydation des cations métalliques. L'utilisation de catalyseurs modèles permet une interprétation approfondie des observations faites. Les corrélations établies, entre propriétés structurales et variations de degré d'oxydation, sont utilisées pour identifier la phase active pour la réaction d'oxydation de l'eau et discuter de son mécanisme réactionnel.

Title: Model catalysts for water splitting studied operando using X-ray Diffraction and X-ray Absorption Spectroscopy

Keywords: operando characterizations, structure, electrochemistry, oxides, oxidation state

Abstract: Water splitting into oxygen and hydrogen is a promising route for renewable energies conversion and storage. For this technology, the use of catalysts is mandatory in order to optimize the conversion efficiency. Iron group oxides (Fe, Ni, Co) are amongst the best earth abundant materials for the catalysis of water oxidation into oxygen reaction. The development of efficient catalysts involves their synthesis and understanding the mechanisms of this reaction at the surface of such materials. In this work we aim at developing a better knowledge of the atomic structure and chemical state of the catalysts under reaction conditions.

For this purpose, we prepared model catalysts – very thin layers with ideally flat morphology electrodeposited on a substrate - and used synchrotron radiation to probe, in operando conditions, their atomic structure and the oxidation state of the metal cations. The use of model catalysts allows a deeper interpretation of observations. The established correlation between structural properties and oxidation state changes are used to identify the active phase for water oxidation reaction and discuss its reaction mechanism.